



The University of
Nottingham

**Hydrothermal Synthesis and
Characterisation of $\alpha\text{-Fe}_2\text{O}_3$
Nanorods**

By

Trevor Almeida, MEng

A thesis submitted to the University of Nottingham
for the degree of Doctor of Philosophy

2010

Abstract

The hydrothermal synthesis (HS) of α -Fe₂O₃ nanorods (NRs) is investigated using a combination of complementary analytical techniques. The construction of an HS ‘process map’ as a function of temperature, time and phosphate (PO₄³⁻) concentration provides insight into the nature of intermediate β -FeOOH NR precipitation, dissolution and subsequent α -Fe₂O₃ growth, along with the effect of PO₄³⁻ anion concentration on the development of α -Fe₂O₃ particle shape. An HS processing temperature of 200°C and an Fe³⁺ : PO₄³⁻ molar ratio of 31.5 yielded crystalline acicular α -Fe₂O₃ NRs with an aspect ratio of ~ 7 (~ 420 nm long, ~ 60 nm wide). The additional effects of FeCl₃ concentration, pH, stage of phosphate addition and α -Fe₂O₃ seed content on the growth of α -Fe₂O₃ NRs is investigated.

The development of a novel valve-assisted pressure autoclave is described, facilitating the rapid quenching of hydrothermal suspensions into liquid nitrogen, providing ‘snapshots’ closely representative of the *in situ* physical state of the synthesis reaction products. Examination of the samples acquired as a function of reaction time and known reaction temperature provides fundamental insight into the anisotropic crystal growth mechanism of the acicular α -Fe₂O₃ NRs. It is considered that the release of Fe³⁺ ions back into solution through intermediate β -FeOOH dissolution supplies the nucleation and growth of primary α -Fe₂O₃ nanoparticles (NPs) (< 10 nm) which subsequently coalesce through a mechanism of oriented attachment (OA) with increasing temperature, into larger, acicular α -Fe₂O₃ NRs.

Fourier transform infra-red spectroscopy investigation of the quenched reaction products provides evidence for PO₄³⁻ absorption on the α -Fe₂O₃ NPs, in the form of mono or bi-dentate (bridging) surface complexes, on surfaces normal and parallel to the crystallographic α -Fe₂O₃ c-axis, respectively. The balance between bi-dentate and mono-dentate phosphate absorption is considered to be critical in mediating the acicular shape of the α -Fe₂O₃ NRs.

A feasibility study on the incorporation of ferromagnetic cobalt, Co₃O₄ NPs or CoFe₂O₄ NPs into α -Fe₂O₃ NRs during HS is presented. In all cases, there is no evidence for the incorporation of cobalt within the α -Fe₂O₃ NRs or the formation of hetero-nanostructures with the Co₃O₄ or CoFe₂O₄ NPs.

The overall growth mechanism of single crystalline acicular α -Fe₂O₃ NRs involves the anisotropic growth and dissolution of intermediate β -FeOOH NRs, governed by its crystallographic structure, and the OA of primary α -Fe₂O₃ NPs, mediated by the preferential absorption of phosphate surfactant.

Publications

1. **Almeida, T. P.**, Fay, M. W., Zhu, Y. Q., Brown, P. D., Process map for the hydrothermal synthesis of α -Fe₂O₃ nanorods, *Journal of Physical Chemistry C*, 2009, 113, pp. 18689-18698.
2. **Almeida, T. P.**, Fay, M. W., Zhu, Y. Q., Brown, P. D., A valve-assisted snapshot approach to understand the hydrothermal synthesis of α -Fe₂O₃ nanorods, *CrystEngComm*, 2010, 12, pp. 1700-1704.
3. **Almeida, T. P.**, Fay, M. W., Zhu, Y. Q., Brown, P. D., Hydrothermal growth mechanism of α -Fe₂O₃ nanorods derived by near *in situ* analysis, *Nanoscale*, 2010, 2, pp. 2390 - 2399.
4. **Almeida, T. P.**, Fay, M. W., Zhu, Y. Q., Brown, P. D., Effect of phosphate on the morphology of hydrothermally synthesised β -FeOOH and α -Fe₂O₃ particles, *Journal of Physics: Conference Series*, 2010, 241, DOI:10.1088/1742-6596/241/1/012045.
5. **Almeida, T. P.**, Fay, M. W., Zhu, Y. Q., Brown, P. D., Complementary RHEED and XRD investigation of β -FeOOH and α -Fe₂O₃ nanoparticles, *Journal of Physics: Conference Series* 2010, 241, DOI:10.1088/1742-6596/241/1/012087.
6. **Almeida, T. P.**, Fay, M. W., Zhu, Y. Q., Brown, P. D., *In situ* TEM investigation of β -FeOOH and α -Fe₂O₃ nanorods, *Physica E*, (in press).
7. **Almeida, T. P.**, Fay, M. W., Zhu, Y. Q., Brown, P. D., Hydrothermal synthesis and characterisation of single crystal α -Fe₂O₃ nanorods, 2 page extended abstract, *European Microscopy Conference*, Aachen, Germany, September 2008.
8. **Almeida, T. P.**, Fay, M. W., Zhu, Y. Q., Brown, P. D., Growth Mechanism of α -Fe₂O₃ Nanorods Derived by Near *In Situ* Analysis, 2 page extended abstract, *International Microscopy Congress*, Rio de Janeiro, Brazil, September 2010.

Presentations

1. **Almeida, T. P.**, Fay, M. W., Zhu, Y. Q., Brown, P. D., Hydrothermal synthesis and characterisation of α -Fe₂O₃ nanorods, oral presentation, *Electron and Microscopy and Analysis Group Conference*, Sheffield, September 2009.
2. **Almeida, T. P.**, Fay, M. W., Zhu, Y. Q., Brown, P. D., Hydrothermal growth mechanism of α -Fe₂O₃ nanorods derived by near *in situ* analysis, oral presentation, *Nottingham Nanotechnology and Nanoscience Centre Researcher Forum*, November 2009.
3. **Almeida, T. P.**, Fay, M. W., Zhu, Y. Q., Brown, P. D., Growth mechanism of α -Fe₂O₃ nanorods derived by near *in situ* analysis, poster presentation, *International Microscopy Congress*, Rio de Janeiro, Brazil, September 2010.
4. **Almeida, T. P.**, Fay, M. W., Zhu, Y. Q., Brown, P. D., Hydrothermal growth mechanism of 1D nanostructures derived by near *in situ* analysis, poster presentation, *European Materials Research Society Spring Meeting*, Strasbourg, France, June 2010.
5. **Almeida, T. P.**, Zhu, Y. Q., Brown, P. D., Complementary RHEED and XRD investigation of β -FeOOH and α -Fe₂O₃ nanoparticles, poster presentation, *Electron and Microscopy and Analysis Group Conference*, Sheffield, September 2009.
6. **Almeida, T. P.**, Fay, M. W., Zhu, Y. Q., Brown, P. D., Hydrothermal synthesis and characterisation of single crystal α -Fe₂O₃ nanorods, poster presentation, *European Microscopy Conference*, Aachen, Germany, September 2008.

Table of Contents

Abstract	i
Publications	ii
Presentations	iii
Table of Contents	iv
Acknowledgements	ix
List of Abbreviations	x
Chapter 1 Introduction	1
Chapter 2 Literature review	4
2.1 Introduction	4
2.2 Nanoparticles.....	4
2.2.1 Effect of NP size on physical properties	5
2.3 Overview of one-dimensional nanostructures.....	10
2.3.1 Growth mechanisms and applications of 1D nanostructures	10
2.3.2 Aqueous / solvent manufacturing methods	11
2.4 Overview of hydrothermal synthesis	15
2.4.1 Temperature, pressure and boiling point of liquids	15
2.4.2 Fundamental chemistry	16
2.4.3 Instrumentation for hydrothermal processing.....	18
2.4.4 Continuous hydrothermal synthesis	19
2.5 Iron oxide	22
2.5.1 Precipitation from FeCl ₃ aqueous solution.....	23
2.5.2 Akaganéite - β-FeOOH	24
2.5.3 Hematite - α-Fe ₂ O ₃	24
2.6 Surfactants	26
2.6.1 Effect of surfactants on α-Fe ₂ O ₃ morphology	26
2.6.2 Effect of phosphate ions on α-Fe ₂ O ₃ morphology	27

Table of Contents

2.6.3	Effect of phosphate ions on the development of α -Fe ₂ O ₃	28
2.7	Overview	29
2.8	Summary	30
Chapter 3 Experimental methodology		31
3.1	Introduction	31
3.2	Hydrothermal synthesis.....	31
3.2.1	Basis of HS.....	31
3.2.2	Pressure autoclaves	31
3.2.2.1	Standard pressure autoclave	31
3.2.2.2	Valve-assisted pressure autoclave.....	32
3.2.3	Materials and processing conditions	34
3.2.3.1	Fabrication of β -FeOOH and α -Fe ₂ O ₃ nanostructures.....	34
3.2.3.2	Fabrication of Co ₃ O ₄ and CoFe ₂ O ₄ NPs	34
3.3	Material characterisation techniques.....	36
3.3.1	Sample handling.....	36
3.3.1.1	Standard pressure autoclave	36
3.3.1.2	Valve-assisted pressure autoclave.....	36
3.3.2	Material characterisation	37
3.3.2.1	Interaction of waves with crystal structures.....	37
3.3.2.2	X-ray diffractometry	38
3.3.2.3	Electron microscopy.....	40
3.3.2.4	Interaction of high energy electrons with matter	40
3.3.2.5	Transmission electron microscopy.....	41
3.3.2.6	Selected area electron diffraction.....	44
3.3.2.7	Reflection high energy electron microscopy.....	46
3.3.3	Chemical analysis.....	46
3.3.3.1	Energy dispersive X-ray analysis.....	46
3.3.3.2	X-ray photoelectron spectroscopy.....	47
3.3.3.3	Fourier transform infra-red spectroscopy.....	48

3.3.4	Data handling	48
3.4	Summary	50
Chapter 4 Hydrothermal synthesis of β-FeOOH and α-Fe₂O₃ nanostructures ... 51		
4.1	Introduction	51
4.2	Effect of HS processing conditions.....	51
4.2.1	Results	53
4.2.1.1	Effect of reaction temperature.....	53
4.2.1.2	Effect of phosphate surfactant concentration	55
4.2.1.3	Effect of reaction temperature for a fixed surfactant concentration and reaction time	57
4.2.1.4	Effect of reaction time.....	59
4.2.1.5	NR crystal orientation and chemical analysis	60
4.2.1.6	Reaction product summary and process map.....	63
4.2.2	Discussion	65
4.2.2.1	Process map.....	65
4.2.2.2	Morphology and phase analysis	65
4.2.2.3	Effect of phosphate surfactant.....	67
4.2.2.4	Growth mechanism	68
4.3	Effect of FeCl ₃ precursor concentration on α -Fe ₂ O ₃ NR growth for fixed Fe ³⁺ : PO ₄ ³⁻ molar ratio	69
4.3.1	Results and discussion.....	69
4.4	Effect of pH on α -Fe ₂ O ₃ NR growth.....	71
4.4.1	Results and discussion.....	71
4.5	Effect of stage of phosphate addition.....	73
4.5.1	Results and discussion.....	73
4.6	Effect of α -Fe ₂ O ₃ NPs (seeds) on α -Fe ₂ O ₃ NR growth.....	77
4.6.1	Results and discussion.....	77
4.7	RHEED / XRD comparison	79
4.7.1	Results	80
4.7.1.1	Effect of HS reaction temperature.....	80

Table of Contents

4.7.1.2	Effect of phosphate surfactant.....	81
4.7.2	Discussion	82
4.8	Summary	84
Chapter 5 HS growth mechanism derived from analysis of quenched samples .		85
5.1	Introduction	85
5.2	Effect of reaction time on α -Fe ₂ O ₃ NR growth.....	86
5.2.1	Results	86
5.2.2	Discussion	89
5.3	Effect of (known) reaction temperature on α -Fe ₂ O ₃ NR growth ..	92
5.3.1	Results	93
5.3.1.1	Transmission electron microscopy.....	93
5.3.1.2	X-ray photoelectron spectroscopy.....	98
5.3.1.3	Fourier transform infrared spectroscopy.....	99
5.3.2	Discussion	100
5.3.2.1	Overview	100
5.3.2.2	Stages of growth.....	100
5.3.2.3	Growth and dissolution of β -FeOOH.....	102
5.3.2.4	Form of the phosphate surfactant.....	103
5.3.2.5	Role of the phosphate surfactant.....	105
5.3.2.6	Growth Mechanism.....	106
5.4	<i>In situ</i> TEM investigation of α -Fe ₂ O ₃ NR growth	108
5.4.1	Results	108
5.4.1.1	<i>i</i> TEM investigation of β -FeOOH	108
5.4.1.2	<i>i</i> TEM investigation of α -Fe ₂ O ₃	109
5.4.2	Discussion	110
5.5	Summary	112
Chapter 6 HS of α-Fe₂O₃ NRs in the presence of CoCl₂, Co₃O₄ and CoFe₂O₄...		113
6.1	Introduction	113
6.2	Effect of CoCl ₂ salt on the growth of α -Fe ₂ O ₃ NRs.....	113

Table of Contents

6.2.1	Results and discussion.....	115
6.3	Effect of Co_3O_4 NPs on the growth of $\alpha\text{-Fe}_2\text{O}_3$ NRs	118
6.3.1	Results and discussion.....	118
6.4	Growth of CoFe_2O_4 NPs	121
6.4.1	Results and discussion.....	121
6.5	Effect of CoFe_2O_4 NPs on the growth of $\alpha\text{-Fe}_2\text{O}_3$ NRs	124
6.5.1	Results and discussion.....	124
6.6	Reaction product summary and process map	127
6.7	Summary	129
Chapter 7 Discussion		130
7.1	Introduction	130
7.2	Hydrothermal synthesis and effect of processing conditions.....	130
7.3	Effect of phosphate surfactant on $\beta\text{-FeOOH}$, $\alpha\text{-Fe}_2\text{O}_3$ and CoFe_2O_4 nanostructures	133
7.4	Nucleation and growth theory	135
7.5	Growth mechanism of $\beta\text{-FeOOH}$ and $\alpha\text{-Fe}_2\text{O}_3$ NRs	138
7.6	Summary	141
Chapter 8 Summary and conclusions		142
Chapter 9 Future work.....		145
References.....		146
Appendix.....		164

Acknowledgements

I would like to express my deepest gratitude to Prof. Yanqiu Zhu and Prof. Paul D Brown for their continued support and guidance during my PhD studies. Their attitude, enthusiasm, patience and encouragement regarding my education and personal development are greatly appreciated.

I would like to thank the technical staff in Advanced Materials Group. Special thanks to Mr Keith Dinsdale and Dr Nigel Neate for their constant help and expertise using a range of characterisation techniques, in particular TEM and XRD. I would like to thank Mr Thomas Buss and Mr Martin Roe for their assistance using FTIR and XPS characterisation techniques, respectively. I would also like to thank Mrs Julie Thornhill for help and training in developing TEM images. I am very grateful for the friendship and help from the group members Dr Ifikhar Ahmad, Mr Hamed Parham, Mr Charlie Carpenter, Mr Shibin Sun, Mrs Fang Xu and many others.

I would like to thank to Dr Michael Fay from the Nottingham Nanoscience and Nanotechnology Centre (NNNC), University of Nottingham, United Kingdom for performing HRTEM characterisation and his assistance throughout.

I would also like to take this opportunity to thank the EPSRC and the Doctoral Training Account at the University of Nottingham for the research grant and the provision of a studentship.

List of Abbreviations

1D	One-dimensional
BF	Bright field
CCD	Charge couple device
CNT	Carbon nanotube
CTAB	Cetyltrimethylammonium bromide
CVD	Chemical vapour deposition
DM	Digital micrograph
DF	Dark field
EDX	Energy dispersive X-ray spectroscopy
FFT	Fast Fourier transform
FTIR	Fourier transform infrared spectroscopy
GIF	Gatan imaging filter
GRIGC	Grain-rotation-induced grain coalescence
HRTEM	High resolution transmission electron microscopy
HS	Hydrothermal synthesis
IR	Infra-red
<i>i</i> TEM	<i>In situ</i> transmission electron microscopy
JCPDS	Joint committee on powder diffraction standard
JPEG	Joint photographic experts group
LSPR	Localised surface plasmon resonance
MS	Microsoft
MWCNT	Multi-walled carbon nanotube
NP	Nanoparticle
NR	Nanorod
NT	Nanotube
NW	Nanowire

List of Abbreviations

OA	Oriented attachment
PZC	Point of zero surface charge
SAED	Selected area electron diffraction
RHEED	Reflection high energy electron diffraction
scWHS	Super-critical water hydrothermal synthesis
SEM	Scanning electron microscopy
SWCNT	Single-walled carbon nanotube
TEM	Transmission electron microscopy
UXD	URLBase URL Database
XPS	X-ray photoelectron spectroscopy
XRD	X-ray diffractometry

Chapter 1 Introduction

Nanostructured materials have attracted considerable research interest over recent decades due to their potential applications in the fields of engineering, science and technology. However, developments in nanotechnology are dependent on the availability of new materials, and the ability to design and synthesise new nanostructured materials. Nano-materials are defined as materials of less than 100 nm in one or more dimension and exhibit novel physical properties that are not possessed by their bulk forms. Consequently, the synthesis, characterisation and application of nano-materials have been widely investigated in recent years. However, significant challenges remain regarding the preparation of well-crystallised nano-materials with definitive size and morphology.

One-dimensional (1D) nanostructures represent a group of nano-materials with highly anisotropic morphologies and have received much attention since the discovery of carbon nanotubes (CNTs) in 1991.¹ Controlled nucleation and growth in a particular crystallographic direction is considered the basis for the formation of a 1D nanostructure. However, the growth mechanisms by which anisotropic development occurs can differ depending on the nano-material and its method of production.

Weakly-ferromagnetic α -Fe₂O₃ (hematite) is of particular interest as a cheap, environmentally friendly and thermodynamically stable iron oxide, and 1D α -Fe₂O₃ nanorods (NRs) have been studied for a wide range of applications because their magnetic properties are greatly dependent on NR size and shape. NRs are capable of exhibiting much higher coercivities than their isotropic counterparts because of the effect of shape anisotropy.²

Aqueous iron (III) chloride (FeCl₃) solution is well established as a simple precursor for the formation of monodispersed α -Fe₂O₃ nanoparticles (NPs), and needle-shaped β -FeOOH (akaganeite) NPs are known to form as an intermediate phase which gradually diminishes as the α -Fe₂O₃ NPs develop.³ Further, a small addition of phosphate (PO₄³⁻) anions has been shown to mediate the anisotropic growth of α -Fe₂O₃, leading to the development of acicular NRs.³

To date, α -Fe₂O₃ nanostructures have been produced using a variety of techniques including sol-gel processing, microemulsion, forced hydrolysis,

hydrothermal synthesis (HS) and chemical precipitation. In particular, HS offers effective control over the size and shape of nanostructures at relatively low reaction temperatures and short reaction times, providing for well-crystallised reaction products with high homogeneity and definite composition. Indeed, the technique of continuous and high throughput HS has become a viable method for the commercial synthesis of nanostructures.⁴⁻⁶

However, a gap in knowledge remains with regards to the distinct stages of the HS growth of α -Fe₂O₃ nanostructures. *Ex situ* investigations of the phase transformation of β -FeOOH to α -Fe₂O₃ under HS conditions, along with α -Fe₂O₃ shape control within phosphate environments, can provide valuable insights into the growth of α -Fe₂O₃ NRs.⁷ Nevertheless, improved understanding of the *in situ* mechanistics of α -Fe₂O₃ NR growth is required in order to control fully the functional properties of these 1D nanostructures. The use of HS reaction vessels under conditions of high temperature and pressure creates an aspect of inaccessibility which limits direct investigation. Indeed, even *in situ* synchrotron and energy dispersive X-ray diffraction methods are sensitive only to bulk crystal phase transformations.⁸⁻¹⁰ Consequently, analysis of HS nanostructures to date on the localised scale has been restricted to post-synthesis reaction products isolated following cool down under equilibrium conditions, with possibility of loss of *in situ* constituent evidence demonstrating the specific mechanistics of growth.

In this context, the focus of this project is to investigate the HS growth mechanism of high aspect ratio α -Fe₂O₃ NRs. A comprehensive HS ‘process map’ is presented, providing insight into the nature of β -FeOOH precipitation, dissolution and subsequent α -Fe₂O₃ growth, as well as the effect of PO₄³⁻ anion concentration on the development of α -Fe₂O₃ particle shape. Further, the development of a novel, valve-assisted, Teflon-lined, hydrothermal pressure autoclave which allows for the rapid quenching of hydrothermal products is reported. It is considered that the reaction products obtained from this autoclave are closely representative of the *in situ* physical state of the developing iron oxide nanostructures due to the large cooling rate experienced during quenching. Hence, detailed analysis of quenched hydrothermal reaction solutions provides for better understanding of α -Fe₂O₃ NR growth.

Examination of the HS reaction products using the combined complementary characterisation techniques of conventional and *in situ* transmission electron microscopy (TEM), selected area electron diffraction (SAED), energy dispersive X-

ray (EDX) analysis, Fourier transform infrared (FTIR) spectroscopy, X-ray diffractometry (XRD), X-ray photoelectron spectroscopy (XPS) and reflection high energy electron diffraction (RHEED) has led to a detailed description of the fundamental growth mechanism of acicular α -Fe₂O₃ NRs.

The thesis has been organised into nine chapters. Chapter 1 introduces the motivation, objectives and organisation of the thesis. Chapter 2 presents the research background and literature review for isotropic and 1D nanostructures, HS and iron oxides. Chapter 3 describes the pressure autoclaves and chemical solutions used during the HS process, as well as the characterisation techniques employed to examine the reaction products. Chapter 4 presents the development of β -FeOOH and α -Fe₂O₃ nanostructures using a wide range of HS processing conditions, and emphasis is given to the construction of a comprehensive HS ‘process map’. Chapter 5 demonstrates the use of the novel valve-assisted pressure autoclave to provide descriptions of the localised development of the acicular α -Fe₂O₃ NRs. Chapter 6 presents a feasibility study on the incorporation of ferromagnetic cobalt within α -Fe₂O₃ NRs for the purpose of improving their magnetic performance. In Chapter 7, the HS process, phosphate surfactant, nucleation of nanostructures and growth mechanism of the β -FeOOH and α -Fe₂O₃ NRs are discussed. The conclusions of this thesis are summarised in Chapter 8 and prospects for future development of this research activity are presented in Chapter 9.

Chapter 2 Literature review

2.1 Introduction

This chapter provides the context for the themes explored within this thesis. The underlying aspects are nanostructures, their synthesis techniques, iron oxides, their structures, surfactants, morphology, functional properties and applications. Emphasis is placed upon the size effect of NPs and their corresponding physical properties, providing a benchmark from which nanostructures with various morphologies can be discussed. In particular, focus is given to 1D nanostructures and the advantages offered by their shape effect. Several methods of nano-material production are available and HS is identified as a favourable technique, offering good control over the size and morphology of nanostructures. Iron oxides are multifunctional materials and easily produced using HS; hence their various phases and structures are outlined. Further, the hydrothermal fabrication of β -FeOOH and α -Fe₂O₃ nanostructures from a FeCl₃ precursor solution is described. Small additions of PO₄³⁻ based surfactants have been shown to increase the α -Fe₂O₃ nanostructure aspect ratio and their effect on the α -Fe₂O₃ shape is considered.

2.2 Nanoparticles

A particle which exhibits one or more dimensions on the nano-scale (< 100 nm) is considered a *nanoparticle (NP)*.¹¹ The scientific community is in general agreement with this definition. However, sub-micron sized particles are often regarded, mistakenly, to fall within this particular group of materials. Figure 2.1 illustrates the context of the NP size domain compared to the size of some well known objects.¹²

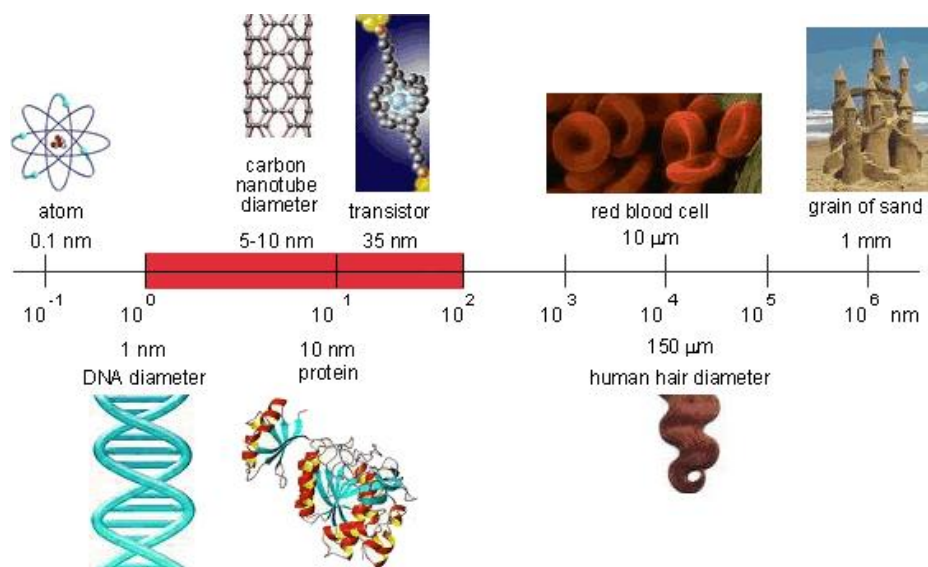


Figure 2.1 Schematic diagram showing the nano-scale domain (red) relative to some common physical and biological objects.¹²

2.2.1 Effect of NP size on physical properties

NPs have attracted considerable attention because they act as an effective bridge between bulk materials and atomic or molecular structures. Bulk materials exhibit constant physical properties, irrespective of their size and mass. However, NPs possess unique size dependent properties due to the significant proportion of atoms existing on their surface in relation to the bulk, resulting in a large specific surface area, as demonstrated in Figure 2.2.¹³ In view of this, the electronic, optical and magnetic properties of materials are found to change as their size decreases towards the nano-scale. Accordingly, the size control of NPs is of particular interest due to the possibility of influencing their functional properties. The additional physicochemical properties of NPs that dictate their microscopic and macroscopic behaviours are summarised in Figure 2.3.¹⁴

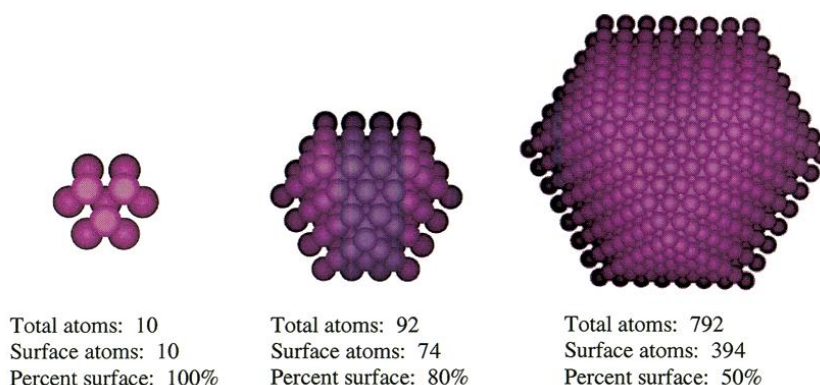


Figure 2.2 Schematic diagrams showing the scaling of 'surface to bulk' atoms to illustrate the size-related effect of NPs.¹³

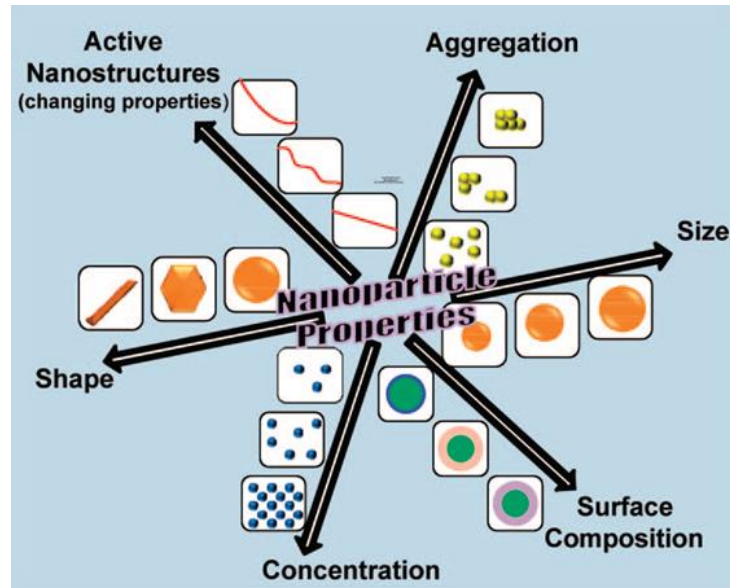


Figure 2.3 Schematic diagram showing the dependence of microscopic and macroscopic behaviours on NP size, shape, concentration, surface composition, and aggregation for passive and active nanostructures.¹⁴

In terms of thermodynamics, total free energy of a NP is the sum of the free energy of the bulk and the surface of the NP:

$$G_{nanoparticle} = G_{surface} + G_{bulk} \quad (2.1)$$

For a NP, the surface free energy becomes a large component of the total free energy and an important component of its overall phase stability.¹⁵⁻¹⁷

The electronic properties of NPs are dependent on their size. For example, the electronic band gap, E_g , for semiconductor NPs can be estimated for a spherical particle as:¹⁸

$$E_g \approx \left(\frac{\pi^2 \hbar^2}{2R^2} \frac{1}{\mu} \right) - \frac{1.8e^2}{\epsilon R} \quad (2.2)$$

where \hbar is Planck's constant, R is the particle radius, μ is the reduced mass of the electron-hole pair, e is the electric charge and ϵ is the dielectric constant of the semiconductor. The Fermi energy level (E_F) is the highest occupied energy level of the system in its ground state, as shown in Figure 2.4.¹⁹ The band gap of such systems is the difference in energy between the highest occupied and lowest unoccupied energy states. A change in band gap influences many properties of NPs, including

surface reactivity. The Kubo gap, denoted by δ , is the average spacing between these energy levels.

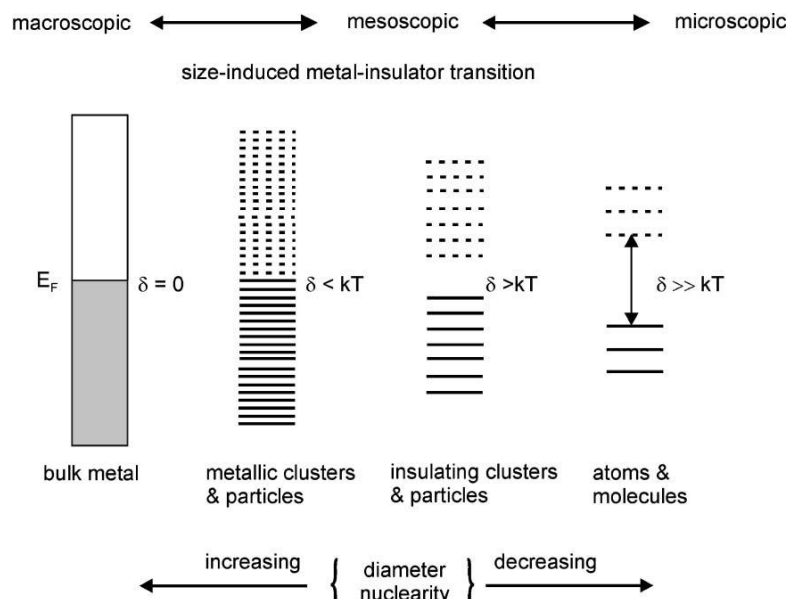


Figure 2.4 Evolution of the band gap and the density of states as the number of atoms in a system increases (from right to left). E_F is the Fermi energy level and δ is the so-called Kubo gap.¹⁹

The optical properties of NPs also can differ greatly as a function of their size. For example, if a small spherical metallic NP is irradiated by light, the accompanying incident electric field induces the conduction electrons to oscillate coherently, as shown in Figure 2.5.²⁰

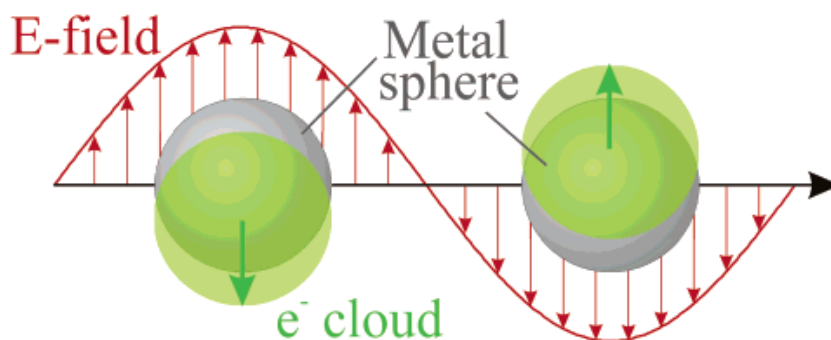


Figure 2.5 Schematic of a plasmon oscillation for a NP, showing displacement of the conduction electron charge cloud relative to the atomic nuclei.²⁰

This oscillation induces a displacement of the electron cloud relative to the atomic nuclei, prompting a restoring force between electrons and nuclei (Coulombic attraction). As a result, further oscillation of the electron cloud relative to the nuclear framework takes place. The overall electron oscillation is termed the dipole plasmon resonance. Depending on their size, the localised surface plasmon resonance (LSPR)

of *e.g.* gold NPs can occur throughout the visible region of the spectrum. For example, Figure 2.6 demonstrates the relationship between the size of gold NPs and their corresponding luminescence.²¹

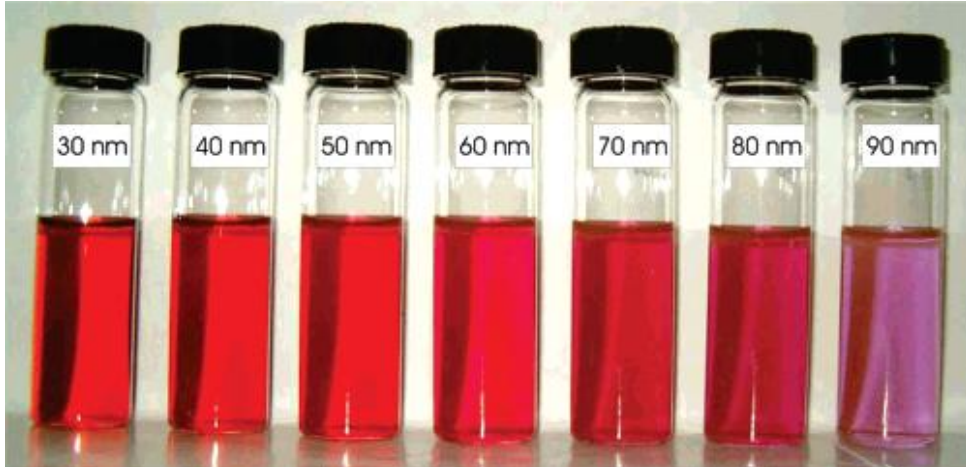


Figure 2.6 Photograph showing the varied luminescence of *e.g.* gold NPs, providing evidence for the scaling of the semiconductor band gap with particle size.²¹

Similarly, the magnetic properties of NPs can also be size-dependent. The balance between exchange energy and magnetocrystalline anisotropy energy results in typical magnetic domain wall widths of ~ 100 nm.² These energies depend on the NP size and below a critical radius, r_c (~ 100 nm), it becomes energetically unfavourable to form domain walls. As a result, single-domain NPs are produced. The magnetisation of a single-domain NP lies along an ‘easy direction’, which is determined by the NP shape and magnetocrystalline anisotropy, as illustrated, for example, for an Fe_3O_4 crystal in Figure 2.7.²²

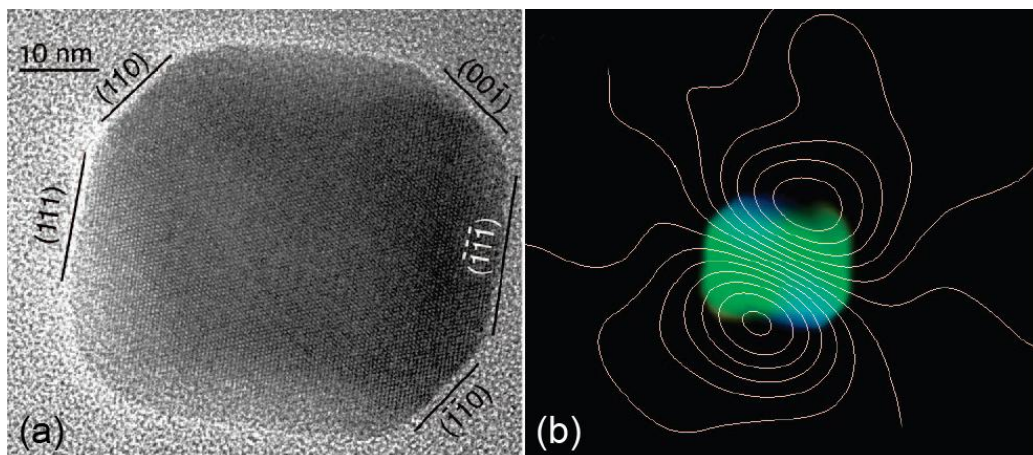


Figure 2.7 (a) HRTEM image of an isolated faceted 50 nm diameter magnetite (Fe_3O_4) crystal; (b) magnetic induction map recorded using off-axis electron holography from the same particle, showing remnant magnetic states at room temperature.²²

In addition to its size, the shape of a nanostructure greatly affects their functional properties. Before application of an external field, the magnetisation of a single-domain NR lies along the easy direction (Figure 2.8a). When an external field is applied in the opposite direction, the NR is unable to respond by domain wall motion, and instead the magnetisation must rotate through the hard direction (Figure 2.8b), to the new easy direction (Figure 2.8c). The anisotropy forces which hold the magnetisation in an easy direction in NRs are stronger than isotropic NPs, and thus the coercivity is large.² For this reason, 1D nanostructures are desirable for magnetic storage media applications.

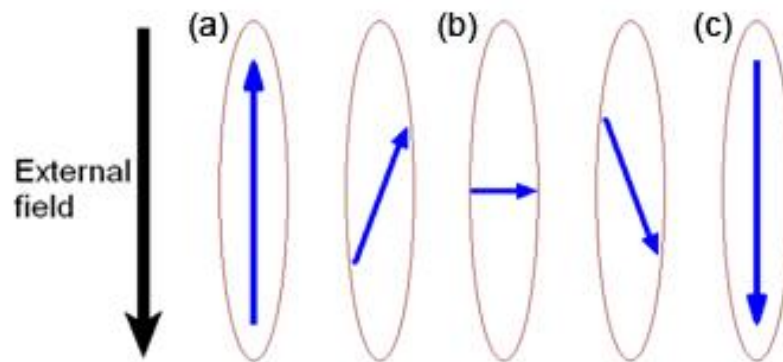


Figure 2.8 Schematic of the magnetisation rotation in single domain NRs.

A more detailed review of 1D nanostructures will be presented in the next section.

2.3 Overview of one-dimensional nanostructures

1D nanostructures represent a group of nano-materials with highly anisotropic morphologies. Typical examples include wires (aspect ratio > 10), rods (aspect ratio < 10), belts, ribbons and tubes (hollow interior). They exhibit unique functional properties because of their shape anisotropy, and their growth, characterisation and application invoke all disciplines of science and engineering. Further, 1D nanostructures are considered ideal model systems for investigating the dependence of optical, electrical, magnetic and mechanical properties on size and morphology. Accordingly, NRs, nanowires (NWs) and nanotubes (NTs) are regarded promising for applications in electronics,^{23,24} photonics,²⁵⁻²⁷ hierarchical biologically inspired nanocomposites,²⁸⁻³⁰ (bio)chemical sensing and imaging^{31,32} and drug delivery.^{33,34}

2.3.1 Growth mechanisms and applications of 1D nanostructures

Table 2.1 summarises many examples of 1D nanostructures fabricated using a wide range of production techniques, putting into context the diversity and potential applications of the various NRs, NR arrays, NWs and NTs currently available. Understanding their growth mechanisms is critical in mediating their development, thereby controlling their sizes, morphologies and dispersity. In recent years, a variety of chemical methods have been identified for generating 1D nanostructures, offering different levels of control over their dimensional parameters. Figure 2.9 schematically illustrates some of the growth mechanisms identified.³⁵

The growth mechanism is governed by the material, production technique and environment, and may change drastically with slight variation in the processing conditions used. Hence, understanding the effect of each process variable on the development of 1D nanostructures is required to fully control their size, shape, phase and, by implication, their functional properties. For example, 1D nanostructures can be produced with relative ease through aqueous / solvent methods of manufacturing and will be discussed in the next section.

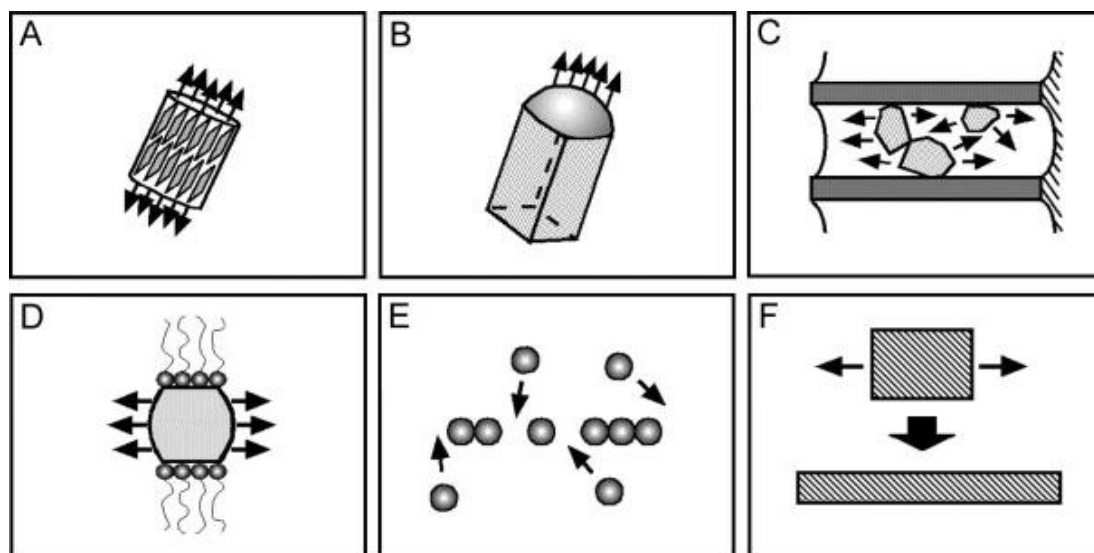


Figure 2.9 Schematic illustrations of different growth mechanisms for achieving 1D nanostructures: (a) dictated by the anisotropic crystallographic structure of a solid; (b) confinement by a liquid droplet as in the vapour-liquid-solid process; (c) direction as controlled through the use of a template; (d) kinetic control provided by a capping reagent; (e) self-assembly of NPs; and (f) size reduction of a 1D microstructure.³⁵

2.3.2 Aqueous / Solvent Manufacturing Methods

Metal and metal oxide NPs and 1D nanostructures can be synthesised using various wet chemical methods: *i.e.* sol-gel processes,³⁶⁻³⁸ microemulsions,³⁹⁻⁴² chemical coprecipitation,⁴³⁻⁴⁵ solvo-⁴⁶⁻⁴⁹ or hydrothermal⁵⁰⁻⁵³ synthesis and the forced hydrolysis of precursors.⁵⁴⁻⁵⁷ These methods make use of precipitation processes within a solution to create a colloid. Solutions comprising different ions can be mixed under controlled temperatures and pressures to form insoluble precipitates. NPs of various sizes and morphologies can be produced by controlling their nucleation processes, further assisted by sono-chemical effects⁵⁸ and growth kinetics.

The co-precipitation technique is a simple chemical pathway to obtain NPs, usually prepared by ageing a stoichiometric mixture of salts in an aqueous medium. When weak aqueous solutions have no effect, strong acids or bases can be added to act as a catalyst to ‘force’ the hydrolysis. In this context, the sol-gel process is based on the hydroxylation and condensation of molecular precursors in solution, creating a ‘sol’ of metal oxide NPs. A micro-emulsion is generally defined as a thermodynamically stable, isotropic dispersion of two relatively immiscible liquids, consisting of micro-domains of one or both liquids stabilised by an interfacial film of surface active molecules.^{59,60} Solvo- and HS offers functional control over the size and shape of the NPs at relatively low reaction temperatures and short reaction times,

providing for well-crystallised reaction products with high homogeneity and definite composition.⁶¹

In view of this, the aqueous route and HS in particular (as shown in Table 2.1), allows the production of 1D nanostructures with dimension close to the critical single magnetic domain range. Accordingly, the HS approach will be discussed in more detail in the next section.

Chapter 2 Literature review

Material	Synthesis	Morphology	Length	Diameter	Growth mechanism	Applications	Ref.
MoS ₂	redox reaction in aqueous solution	NRs	50 – 150 nm	20 – 40 nm	epitaxial growth on a template	anti-wear and friction reduction	62
CNT	fluid bed CVD	S / MWCNT	0.02 – 60 μm	3 – 11 / 5 – 200 nm (inner / outer diameter)	bulk or surface diffusion and precipitation on a catalyst	optoelectronics, structural materials, biosensors and energy-storage devices	63
LnVO ₄ (Ln=La, Nd, Sm, Eu, Dy)	HS	NRs	50 – 200 nm	10 – 50 nm	crystalline nuclei formation and growth through Ostwald ripening	efficient phosphor, a low-threshold laser	64
BN	boron oxide CVD	NTs	10 μm	50 nm	catalytic growth parallel to (1010) planes	host and a polariser material	65
Eu ₂ O ₃	simple precipitation with subsequent calcination	NRs	200 nm	10 – 30 nm	crystalline Eu(OH) ₃ nuclei formation and anisotropic growth in <001> direction, followed by calcination in air into Eu ₂ O ₃	luminescence activator	66
CdS	wet chemical method	NRs	< 64 nm	< 25 nm	dipole moment assisted OA of preformed quasi-spherical particles along the dipole faceted direction <002> followed by coalescence	photo-electronic applications	67
ZnO	wet chemical method	NR array	1 – 5 μm	20 – 200 nm	nucleation and anisotropic growth of aligned ZnO NRs along the c-axis on a ZnO _f / Si substrate	electronic and optoelectronic devices	68
TiO ₂	sol-gel processing / electrophoretic deposition	NW array	10 μm	180 nm	nucleation and growth of TiO ₂ NRs in a sol, followed by the sol being drawn into a polycarbonate membrane by capillary action	electronic devices, sensors, and actuators	69
Si	laser ablation	NWs	> 100 μm	3 – 43 nm	laser ablated material from the Fe / Si target collides with inert gas molecules and condenses in the gas phase, resulting in Fe-Si nanodroplets, which act as seeds for vapour-liquid-solid Si NW growth	nano-electronics and sensors	70

Table 2.1 Overview of 1D nanostructures and their fabrication methods, morphologies, dimensions, growth mechanisms and applications.

Chapter 2 Literature review

Material	Synthesis	Morphology	Length	Diameter	Growth mechanism	Applications	Ref.
FePt	solvothermal synthesis	NWs	5 μm	30 – 50 nm	coarsening and ripening of aggregates into well defined NWs	high-density data storage and high performance permanent magnets	71
W ₁₈ O ₄₉	solvothermal synthesis	NWs	5 μm	bundles of 2 – 5 nm NWs	alignment of ultra-thin NWs that grow anisotropically in the <010> direction	gas sensors	72
PbCrO ₄	facile aqueous solution	NRs	< 2.5 μm	> 150nm	PbCrO ₄ NPs nucleate and grow up to 50 nm, agglomerate and crystallise into NRs	dielectric materials, humidity sensing resistor, pigment, solid lubricants	73
CdS	sonochemical synthesis	NRs / NWs	1.3 μm	80 nm	ultrasound expels S ²⁻ and Cd ²⁺ and strong penta-dentate ligand complexing action mediates CdS NR formation along <001> direction	laser light-emitting diodes and optical devices based on nonlinear properties	74
Bi ₂ O ₃	metalorganic CVD	NRs	1 μm	40 – 250 nm	self-catalytic process characteristic of vapour-solid growth process	gas sensors	75
SnO ₂	thermal evaporation	NWs	2 μm	20 – 60 nm	self-catalytic process characteristic of vapour-solid growth process	gas sensor, solar cell and transparent electrodes	76
Ge	CVD	NWs	1.2 μm	40 nm	catalytic Ge growth in <111> direction from gold NPs deposited on Si substrate	3-D electronics	77
PbTe	alkaline reducing chemical route	NRs	0.3 – 2 μm	50 – 200 nm	PbTe nucleates on Te NR templates and grows by consuming Te NRs	high-efficiency thermoelectric micro-devices	78
GaN	radio frequency magnetron sputtering	NWs	10 μm	100 – 400 nm	decomposition of Ga ₂ O ₃ and NH ₃ and subsequent formation of GaN micrograins through diffusion - laying foundation for GaN NRs	optoelectronic material and high-temperature / high-power electronic devices	79
BaTiO ₃	pulsed laser deposition	NTs	200 – 1000 nm	5 – 20 / 20 – 150 nm (inner / outer diameter)	laser ablated material from target grows epitaxially on ZnO template	non-volatile memories, piezoelectric optoelectronic devices	80
VO _x	HS	NTs	50 – 140 nm	15 – 45 nm	amine surfactant is directly intercalated into the precursor V ₂ O ₅ layers, promoting anisotropic growth	catalysis and as electrochemical devices	81

Table 2.1 continued...

2.4 Overview of hydrothermal synthesis

The term ‘hydrothermal’ is of geological origin and has undergone several changes from the original Greek words ‘hydros’ and ‘thermos’ meaning water and heat, respectively. It was first used by the British geologist, Sir Roderick Murchison (1792-1871), to describe the action of water at elevated temperature and pressure, leading to the formation of various rocks and minerals in the earth’s crust.⁶¹

2.4.1 Temperature, pressure and boiling of liquids

A liquid boils at the temperature at which its vapour pressure equals the surrounding pressure. The standard boiling point is defined as the temperature at which the liquid boils under a pressure of 1 bar.⁸² Increasing the pressure of the system allows a liquid to contain more thermal energy whilst remaining in a saturated state, thereby increasing the boiling point. This temperature of saturation can increase with pressure to a critical point at which its gas and liquid properties become identical, and cannot increase further, as shown for water in Figure 2.10. Likewise, the boiling point decreases with decreasing pressure until a triple point is reached at which it cannot be further reduced. Moreover, when a non-volatile solute is added to a solvent the boiling point of the solution will be higher than the solvent.⁸³ This colligative property, *i.e.* dependent on the presence of dissolved particles and their number, irrespective of their identity, is called boiling point elevation.

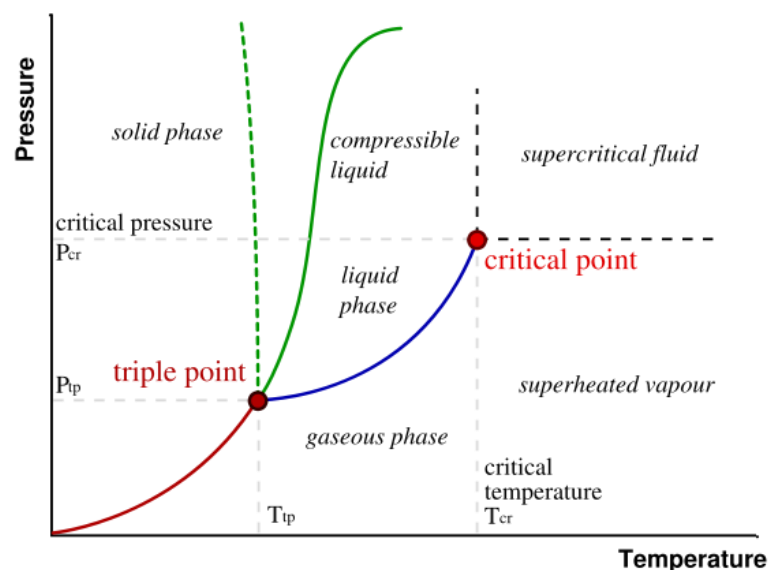


Figure 2.10 Pressure – Temperature diagram showing the phase change boundaries of water.⁸⁴

In thermodynamic terms, boiling point elevation is entropic and can be explained in terms of the chemical potential of the solvent, as shown in Figure 2.11. Chemical potential is the change in energy of a species in a system if an additional particle *of that species* is introduced, with the entropy and volume held fixed. At the boiling point, the liquid and vapour phase have the same potential, *i.e.* they are energetically equivalent. When a non-volatile solute is added, the chemical potential of the solvent in the liquid phase is decreased by dilution, whilst the chemical potential of the solvent in the vapour phase is not affected. Hence, the equilibrium established between a liquid and the vapour phase is at a higher temperature in a solution than a pure solvent.

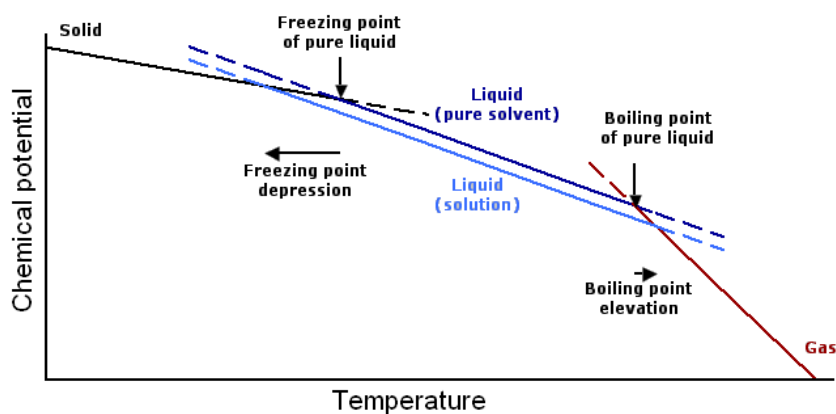


Figure 2.11 Schematic of change in the chemical potential of a solution illustrating boiling point elevation.⁸⁵

2.4.2 Fundamental chemistry

Hydrothermal processing can be defined as any heterogeneous reaction in an aqueous solvent (or non-aqueous solvent for *solvothermal* processing) under high pressure and temperature conditions, which induces the dissolution and recrystallisation of materials that are relatively insoluble under ordinary conditions. Figure 2.12 shows a pressure / temperature map of HS in relation to other material processing techniques.⁸⁶ In comparative terms, the hydrothermal processing of materials is considered environmentally benign. Further, the hydrothermal technique offers the highly controlled diffusivity of strong solvent media in a closed system. In the context of nanotechnology, the hydrothermal technique provides an ideal method for producing ‘designer particulates’, *i.e.* mono-dispersed particles with high purity, high crystallinity and controlled physicochemical characteristics. Such particles are in great demand by industry.

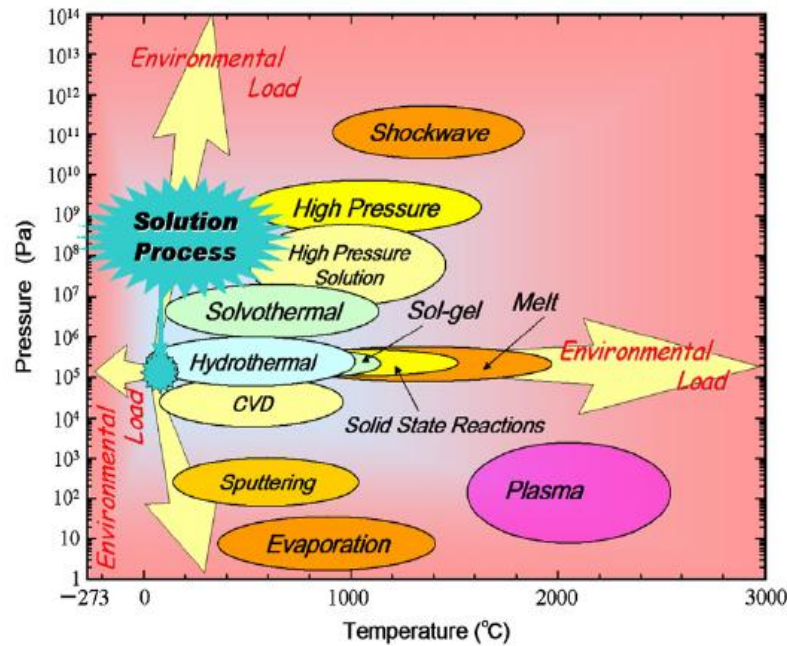


Figure. 2.12 Pressure / temperature map of material processing techniques.⁸⁶

Figure 2.13 shows the major differences in particle products obtained by ball milling, sintering / firing and hydrothermal methods.⁸⁷ For example, ball milling involves breaking down bulk material into small irregular shaped particles, and hence is considered a crude fabrication method in comparison to the controlled growth provide by HS. The hydrothermal product particle size can range from a few nanometres up to several microns, depending on temperature, nucleation seed content, pH and solvent concentration.

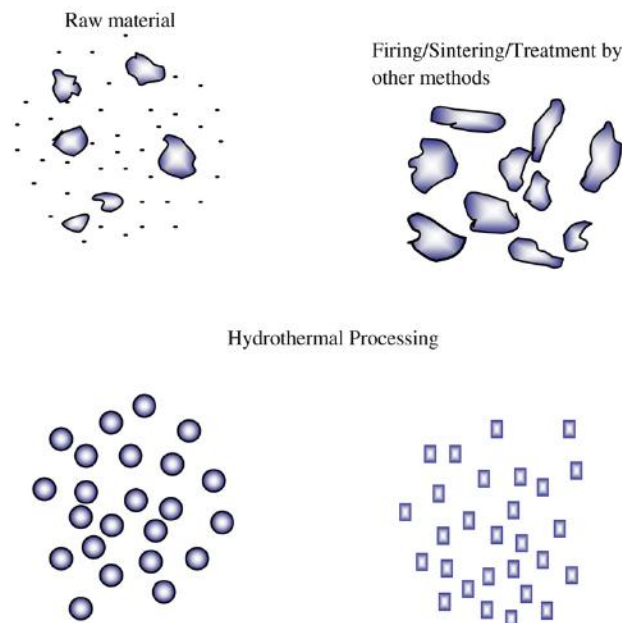


Figure 2.13 Particle processing by conventional and hydrothermal techniques, producing irregular shaped particles and ‘designer particulates’, respectively.⁸⁷

The behaviour of solvents under hydrothermal conditions allows the development of crystal structures under sub- and supercritical states (along with pH variations, viscosity, coefficient of expansion and density, *etc.*) to be understood in terms of varying pressure and temperature. Similarly, thermodynamic studies provide valuable information on the behaviour of solutions with respect to varying pressure and temperature conditions. Some commonly studied aspects are solubility, stability, yield and dissolution / precipitation reactions, *etc.* However, fundamental understanding of the kinetics during hydrothermal crystallisation is limited. This is due to an absence of data relating to the formation of intermediate phases and the inaccessibility of direct *in situ* investigation techniques under conditions of high pressure and temperature.

2.4.3 Instrumentation for hydrothermal processing

Hydrothermal materials processing requires a vessel capable of containing a highly corrosive solvent, operating under extreme pressure and temperature conditions. The hydrothermal apparatus, commonly known as an autoclave, reactor, pressure vessel or high pressure bomb, must meet a variety of objectives, processing conditions and tolerances. A generic hydrothermal autoclave should be:

- 1) Leak-proof under high pressure / temperature conditions.
- 2) Easily assembled / disassembled.
- 3) Inert to acids, bases and oxidising agents.
- 4) Resilient to high pressure and temperature experiments, so that no machining or treatment is needed after each experimental run.

In view of the above requirements, autoclaves are generally fabricated from thick glass or quartz cylinders and high strength alloys, such as austenitic stainless steel, iron, nickel, cobalt-based super alloys or titanium and its alloys.⁶¹ The primary parameters to be considered in the selection of a suitable reactor are the experimental temperature and pressure conditions, including corrosion resistance in the pressure / temperature range for a given solvent. Materials processing from aqueous phosphoric acid media or other highly corrosive media, *i.e.* extreme pH conditions, require the use of an un-reactive Teflon lining, as shown in Figure 2.14,⁸⁷ or inert tubes (platinum, gold or silver) to protect the autoclave body from corrosion.



Figure 2.14 General purpose pressure autoclave and white Teflon lining used for HS.⁸⁷

In order to gain insight into the distinct stages and growth mechanism of nanostructure development as a function of various HS processing conditions, a standard 125 ml capacity Teflon-lined stainless steel pressure autoclave and novel 50 ml capacity valve-assisted Teflon-lined stainless steel pressure autoclave, developed for the purpose of rapid quenching of hydrothermal suspensions in liquid nitrogen, was used during this research (discussed in more detail in Section 3.2.2).

2.4.4 Continuous hydrothermal synthesis

HS has been shown to be a relatively simple, efficient and cheap process for the fabrication of nanostructures. However, the quantity of reaction product produced is dependent on the amount of precursor chemicals and the capacity of the autoclave used. For this reason, there has been much incentive to make the process continuous.⁸⁸⁻⁹⁰ The continuous production of metal oxide NPs may be achieved by mixing a metal salt aqueous solution with a preheated water stream, often supercritical, fed from separate inlet lines. For example, mixed oxide $Ce_{1-x}Zr_xO_2$ NPs were obtained continuously by the hydrolysis of mixtures of $[NH_4]_2[Ce(NO_3)_6]$ and $[Zr(acetate)_4]$ in near-critical water (ncH_2O) using the reactor setup shown in Figure 2.15.⁹¹

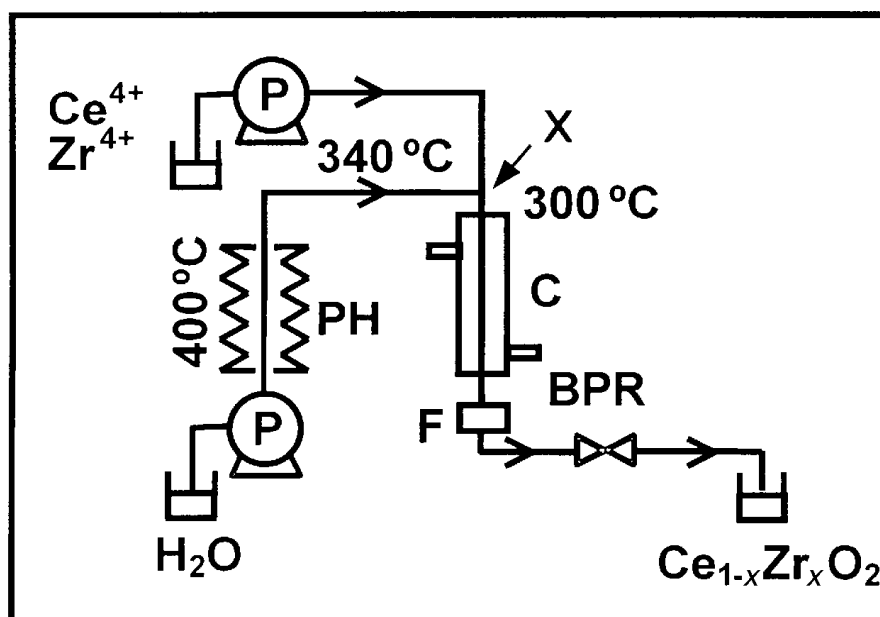


Figure 2.15 Diagram of the flow reactor for the synthesis of metal oxide powders and solid solutions in $n\text{CH}_2\text{O}$. A solution of Ce^{4+} and Zr^{4+} salts at room temperature is mixed with a stream of H_2O heated up to 400°C by the preheater (PH). The mixture is cooled immediately after the mixing point (X) by water cooling (C) and is then passed through a filter (F) (to remove any large aggregates) and a back-pressure regulator (BPR). Particles are then collected as a suspension. P denotes pumps.⁹¹

However, this method requires significant improvement before being applied industrially due to issues of reliability, reproducibility and process control. Consequently, a new reactor design was developed specifically to: (a) handle unusual mixing environments efficiently; (b) establish appropriate flow properties that could manage the particulate product; and (c) produce a greatly improved heat transfer profile. This particular reactor design for supercritical water HS (scWHS) known as the Nozzle Reactor,⁹² is illustrated in Figure 2.16.⁹³ The arrangement comprises an internal pipe, with an open-ended nozzle and attached cone, positioned within an external pipe that contains the metal salt aqueous solution. The supercritical water is fed downwards through the internal pipe and out of the end of the nozzle, where it makes contact with the aqueous metal salt stream, fed upwards through the outer pipe. The reactor outlet for the resulting nanostructures, dispersed in solution, is situated upwards through the outer pipe. However, nanostructure development using continuous scWHS processes mostly involves nucleation with limited growth, restricting their particle size.

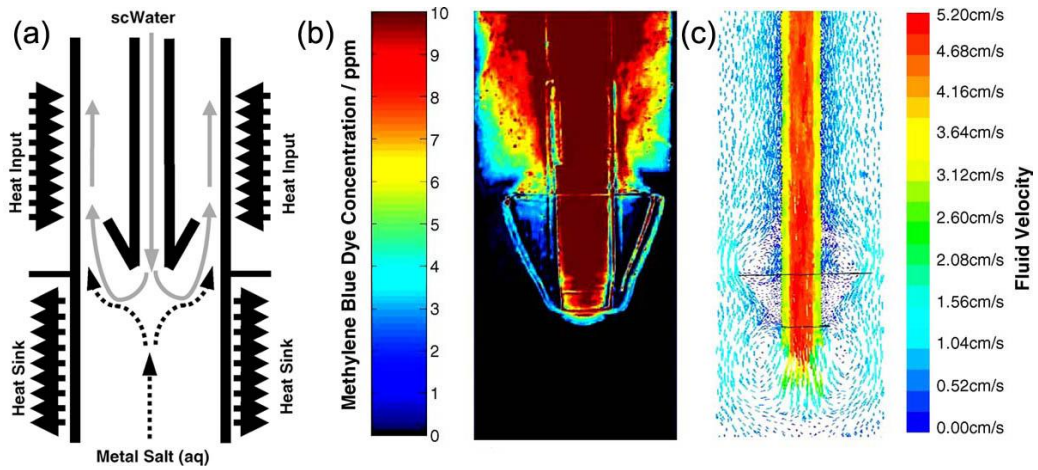


Figure 2.16 (a) Schematic of the Nozzle Reactor design for scWHS with ideal heating / cooling profile; (b) Steady state concentration map of the Nozzle Reactor and (c) steady state computational fluid dynamics simulation.⁹³

Before outlining the critical issues for the development of the HS process, a brief overview of the crystallography of iron oxide is now given in advance of a review of the use of surfactants to mediate growth.

2.5 Iron oxide

Iron is abundant in the Earth's crust and an important element in our environment. It is present in soils as oxides⁹⁴ and easily mobilised in natural waters in the form of molecular complexes and colloids. There are a number of iron oxides, hydroxides and oxy-hydroxides, as summarised in Table 2.2. For simplicity, this group of iron oxo((oxy)hydroxi)des is often referred to as *iron oxide*.

Oxides	Hydroxides	Oxy-hydroxides
FeO, iron(II) oxide, (wüstite)	iron(II) hydroxide (Fe(OH) ₂)	goethite (α -FeOOH),
Fe ₃ O ₄ , iron(II,III) oxide, (magnetite)	iron(III) hydroxide (Fe(OH) ₃), (bernalite)	akaganéite (β -FeOOH),
Fe ₂ O ₃ , iron(III) oxide		lepidocrocite (γ -FeOOH)
α -Fe ₂ O ₃ , hematite		feroxyhyte (δ -FeOOH)
β -Fe ₂ O ₃		ferrhydrite (Fe ₅ HO ₈ ·4H ₂ O approx.)
γ -Fe ₂ O ₃ , maghemite		
ϵ -Fe ₂ O ₃		

Table 2.2 List of iron oxides, hydroxides and oxy-hydroxides.

The structural chemistry of these compounds is diverse, reflecting the large number of atomic structures, as summarised in Figure 2.17.⁹⁴⁻⁹⁶ Almost all these phases can be formed from chemical solution, alluding to a complicated chemistry of formation.^{94,97,98} In particular, the diversity of physicochemical conditions present in the environment (*e.g.* acidity, redox conditions, temperature, salinity, presence of organic or inorganic ligands, *etc.*) suggests, practically, all the iron oxide phases can be found naturally. The high versatility of iron chemistry in an aqueous medium originates from two factors: the occurrence of two oxidation states, Fe²⁺ and Fe³⁺, which are stable over a large range of acidity, and the high reactivity of iron complexes towards acid-base and condensation phenomena.⁹⁶

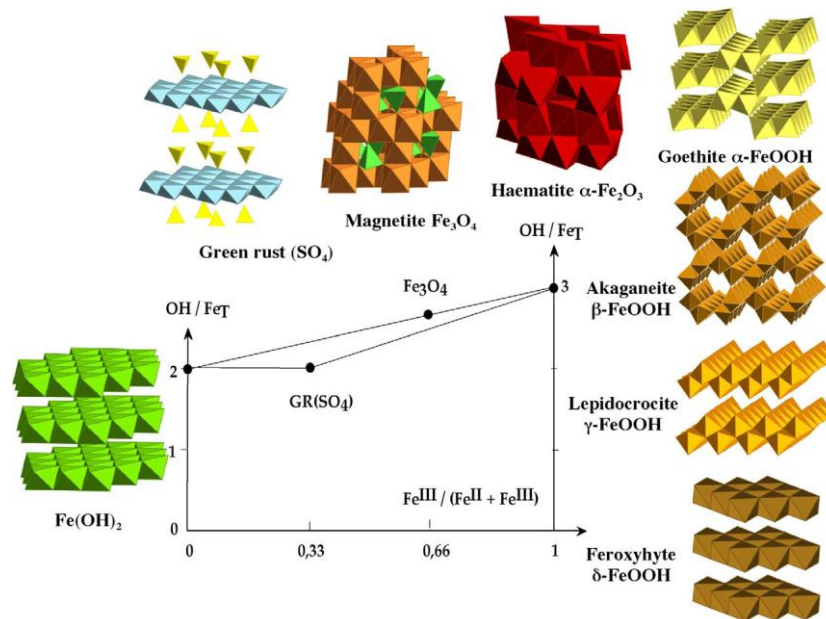


Figure 2.17 The many different phases of iron oxi((oxy)hydroxi)des formed as a function of hydroxylation ratio and composition in the ferrous–ferric system.⁹⁶

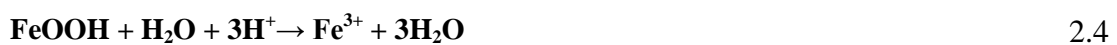
2.5.1 Precipitation from FeCl_3 aqueous solution

Several experimental routes can be employed to produce iron (III) oxide. *E.g.* the slow or forced hydrolysis of Fe (III) salts; crystallisation from iron (III) hydroxide gels; the oxidation of $\text{Fe}(\text{OH})_2$ in aqueous suspension at various pH values; and crystallisation from mixed $\text{Fe}(\text{OH})_2:\text{Fe}(\text{OH})_3$ gels.⁹⁹ Solid reaction products are easily formed through the hydrolysis of Fe^{3+} ions under hydrothermal conditions by the dissociation of an iron salt. The precipitation of $\beta\text{-FeOOH}$ and $\alpha\text{-Fe}_2\text{O}_3$ from FeCl_3 solution, shown in the simple chemical equations below, is a good example of the involvement of Fe^{3+} ions with aqueous media. Generally, the process of precipitation of such iron oxides, as well as particle sizes and morphologies, is dependent on the concentration of the iron salt, the presence of foreign ions and molecules, pH, temperature and the time of crystallisation.¹⁰⁰

Precipitation of $\beta\text{-FeOOH}$



Dissolution of $\beta\text{-FeOOH}$



Precipitation of $\alpha\text{-Fe}_2\text{O}_3$



2.5.2 Akageneite – β -FeOOH

Akaganéite, β -FeOOH, is named after the Akagane mine in Iwate, Japan, where the mineral was first discovered.¹⁰¹ β -FeOOH is a typical product of the hydrolysis of dilute or concentrated ferric chloride solution at low pH value, and the subject of numerous studies due to its sorption, ion exchange, and catalytic properties.¹⁰²⁻¹⁰⁶ β -FeOOH exists in the environment as a fine-grained material with a large specific surface area, which increases significantly with decreasing particle size. β -FeOOH was first recognised by Weiser and Milligan,¹⁰⁷ who distinguished it from other members of the Fe–O–H–Cl system by means of powder diffraction. The crystal structure of β -FeOOH (Figure 2.18) was shown by Mackay¹⁰⁸ to be related to the hollandite structure, with additional chloride anions occupying channels parallel to the crystallographic c-axis. β -FeOOH exhibits a monoclinic crystal structure with space group I4/m (tetragonal symmetry), $a = 10.480 \text{ \AA}$, $b = 10.480 \text{ \AA}$ and $c = 3.023 \text{ \AA}$.

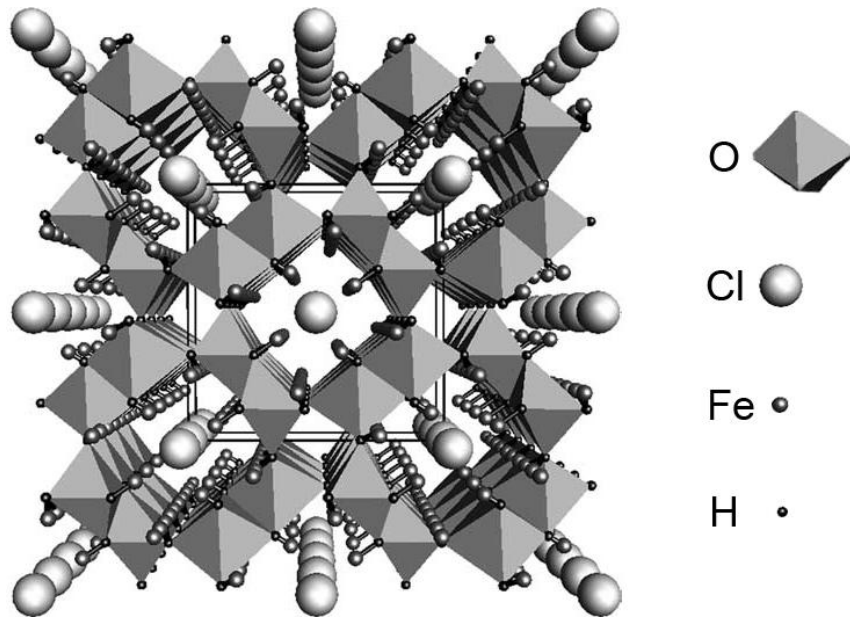


Figure 2.18 The crystal structure of β -FeOOH viewed down the c-axis. Large spheres represent chlorine atoms which regularly occupy channels in the β -FeOOH lattice.¹⁰⁹

2.5.3 Hematite – α -Fe₂O₃

Mineral hematite, α -Fe₂O₃, formerly spelt haematite, is derived from the Greek *haimatite* meaning ‘blood-like’, referring to its powder’s shade of red.¹¹⁰ In bulk compact form, it is coloured black or silver-grey. Hematite is mined as the main ore for producing iron. The structure of α -Fe₂O₃ (Figure 2.19a), determined by Pauling and Hendricks in 1925, is isostructural with corundrum, α -Al₂O₃.¹¹¹ The space group

is R3c (rhombohedral symmetry) and the lattice parameters given in the hexagonal cell, shown in Figure 2.19b, are: $a = b = 5.0346 \text{ \AA}$ and $c = 13.752 \text{ \AA}$.¹¹²

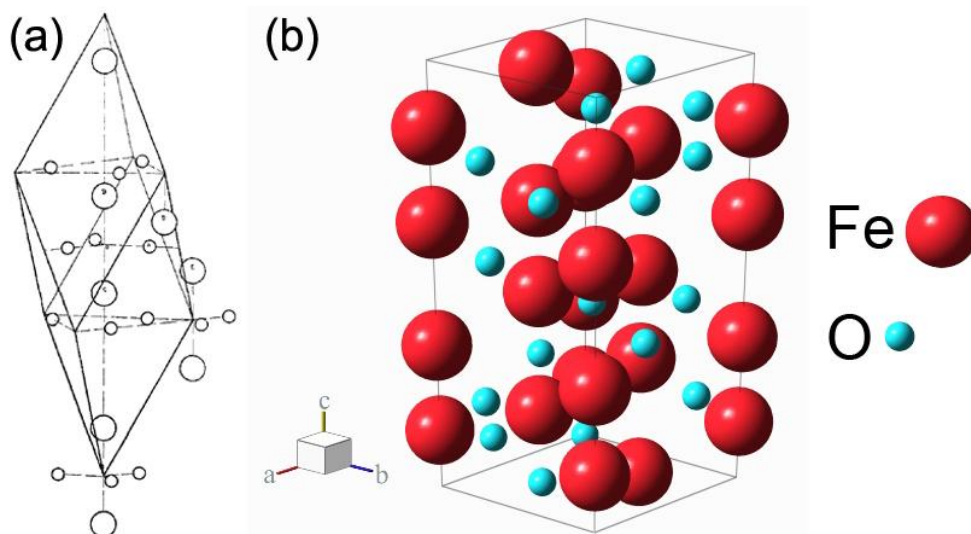


Figure 2.19 (a) The arrangement of atoms in the structure of hematite (and corundum); small and large atoms represent oxygen and iron (or aluminium), respectively.¹¹¹ (b) Model of the hematite unit cell.

Nanostructured $\alpha\text{-Fe}_2\text{O}_3$ is the most thermodynamically stable iron oxide phase and is of particular interest because of its high resistance to corrosion, low processing cost and non-toxicity.¹¹³ This multifunctional material has therefore been investigated extensively for a variety of applications including photo-catalysis,¹¹⁴ gas sensing,^{115,116} magnetic recording,¹¹⁶ drug delivery,¹¹⁷ tissue repair engineering¹¹⁸ and magnetic resonance imaging,¹¹⁹ along with its use in lithium-ion batteries,¹¹⁶ spin electronic devices¹²⁰ and pigments.¹²¹ In particular, the magnetic properties of $\alpha\text{-Fe}_2\text{O}_3$ have attracted much interest over the past decades. In the 1950s it was found to be canted antiferromagnetic (weakly ferromagnetic) at room temperature, antiferromagnetic below the Morin transition temperature of 250 K and paramagnetic above its Néel temperature of 948 K.

As mentioned in Section 2.2.1, 1D nanostructures exhibit higher magnetic coercivities than NPs. Accordingly, surfactants which promote the anisotropic growth of $\alpha\text{-Fe}_2\text{O}_3$ nanostructures will be discussed in the next section.

2.6 Surfactants

Surface active compounds used in practical applications are commonly known as *surfactants*.¹²² These are usually organic compounds that are amphiphilic, meaning they contain both hydrophobic and hydrophilic groups. Surfactants are employed in a variety of technologies including detergency, emulsification, dispersion, coating, wetting, flotation, petroleum recovery, lubrication and adhesion.¹²³⁻¹²⁷ However, surfactants can also be used to control the size and shape of nanostructures grown from chemical solution. For example, cetyltrimethylammonium bromide (CTAB) binds preferentially to side faceted gold NPs.¹²⁸ Such binding stabilises the {100} crystal faces, promoting material addition along the [110] common axis on the {111} faces, resulting in anisotropic growth, as demonstrated in Figure 2.20.

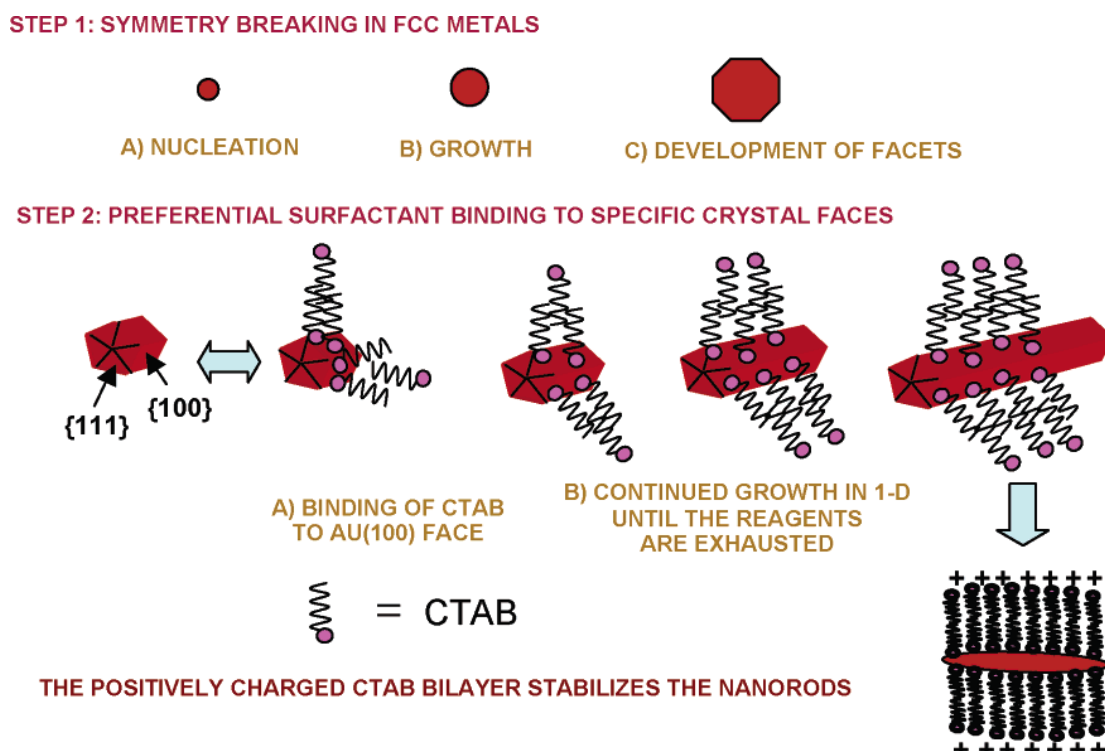


Figure 2.20 Proposed mechanism of surfactant-directed Au NR growth. The single crystalline seed particles have facets that are differentially blocked by the surfactant. Subsequent addition of metal ions and weak reducing agent lead to metallic growth at the exposed particle faces.¹²⁸

2.6.1 Effect of surfactants on α -Fe₂O₃ morphology

Similarly, several surfactants have been shown to affect the morphology of α -Fe₂O₃ nanostructures produced through HS, resulting in various shapes including cubes,^{129,130} rods,^{131,132} tubes,^{132,133} rings,^{134,135} sheets,¹³² hollow spheres,^{135,136} pines¹³⁷ and snowflakes.¹³⁸ Some examples of α -Fe₂O₃ nanostructures with these

morphologies are shown in Figure 2.21. Chloride, hydroxide, sulphate and phosphate anions have been shown to significantly change the α -Fe₂O₃ particle shape.¹³⁹⁻¹⁴⁶ In particular, phosphate anions have been widely used to obtain a variety of well defined α -Fe₂O₃ nanostructures. However, the mechanism by which these anions mediate α -Fe₂O₃ particle growth is not fully understood and can differ depending on solution temperature, pH and concentration.

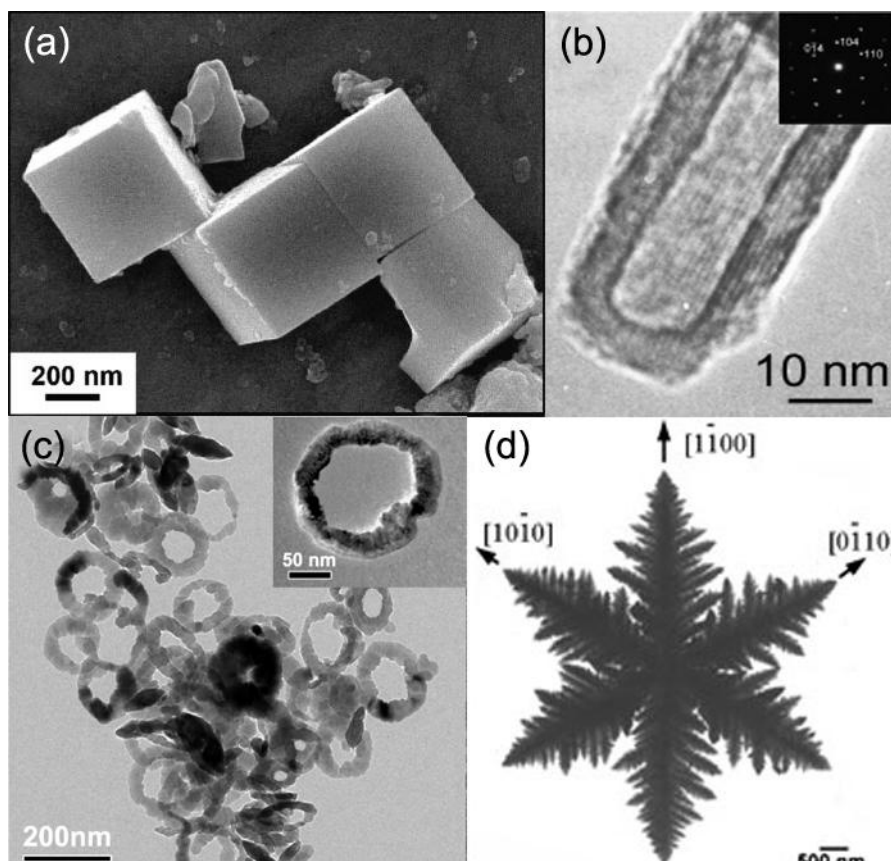


Figure 2.21 (a) SEM micrograph of α -Fe₂O₃ cubes,¹²⁹ (b) BF TEM images of α -Fe₂O₃ NT with SAED (inset);¹³² (c) nanorings;¹³³ and (d) snowflakes.¹³⁸

2.6.2 Effect of phosphate ions on α -Fe₂O₃ morphology

Kratohvil *et al* investigated the iron oxide hydrothermal precipitation process from FeCl₃-NaH₂PO₂ aqueous solution at 245°C,¹⁴⁷ reporting the formation of particles of various shapes and a reduction of Fe³⁺ to Fe²⁺ which had an additional effect on the precipitation process. Ozaki *et al* showed that small additions of phosphate or hypophosphite ions to ferric chloride solution similarly had a significant effect on α -Fe₂O₃ particle shape, resulting in ‘spindle-type’ colloidal particles.³ Since then, many surfactant compounds containing PO₄³⁻ anions have been used to promote anisotropic growth of α -Fe₂O₃ nanostructures from chemical solution.^{148,149} However, the exact

role of PO_4^{3-} anions in mediating the ‘spindle-type’ or acicular $\alpha\text{-Fe}_2\text{O}_3$ particle shape is not fully understood.

2.6.3 Effect of phosphate ions on the development of the $\alpha\text{-Fe}_2\text{O}_3$

Surfactants often restrict crystal growth in certain directions through preferential absorption, thereby promoting increased relative growth on other crystal faces. This surface interference through absorption can also affect the phase composition of the resultant precipitates. For example, increased phosphate additions may induce $\beta\text{-FeOOH}$ to become the dominant phase, as opposed to $\alpha\text{-Fe}_2\text{O}_3$, during precipitation from FeCl_3 solutions, with small amounts of $\alpha\text{-FeOOH}$ present, depending on pH.¹⁵⁰ Suppressed $\beta\text{-FeOOH}$ dissolution through surface phosphate absorption is considered to inhibit subsequent $\alpha\text{-Fe}_2\text{O}_3$ precipitation. $\alpha\text{-Fe}_2\text{O}_3$ NPs may form after prolonged periods of processing due to the dependence of HS kinetics on phosphate concentration. Very fine iron (III) phosphate particles or iron (III) phosphate complexes are also thought to serve as nuclei or templates for the growth of $\alpha\text{-Fe}_2\text{O}_3$ particles in suspension.¹⁵¹ Further, phosphorus atoms may become incorporated into the $\alpha\text{-Fe}_2\text{O}_3$ structure during precipitation and inhibit growth.

2.7 Overview

In summary, the critical issues regarding the HS of 1D α -Fe₂O₃ nanostructures that will be addressed in this thesis are:

- The effect of HS processing conditions on the reaction products.
- Acquiring evidence closely representative of the localised development of HS reaction products to allow for detailed descriptions of their growth.
- In depth account of the β -FeOOH to α -Fe₂O₃ phase transformation.
- The effect of phosphate surfactant on the phase and morphologies of β -FeOOH and α -Fe₂O₃ nanostructures.
- A detailed description of the hydrothermal growth mechanism of single crystal acicular α -Fe₂O₃ NRs.

2.8 Summary

In this chapter, the dependence of the physical properties of various nanostructures, in particular 1D nanostructures, on their size and morphology have been outlined. HS is identified as an effective method for the production of monodispersed nanostructures with high purity, high crystallinity and controlled physicochemical characteristics. From literature, iron oxides are considered relevant, multifunctional materials with a wide range of potential applications. Heating of an FeCl_3 precursor solution under hydrothermal conditions results in the formation and dissolution of an intermediate β - FeOOH phase, prior to precipitation of the more thermodynamically stable α - Fe_2O_3 phase. Addition of a PO_4^{3-} containing surfactant can result in adsorption onto β - FeOOH and α - Fe_2O_3 crystals, mediating their shape control, as well as affecting both the β - FeOOH dissolution and α - Fe_2O_3 crystal growth. In this context, the research in this thesis is aimed at gaining fundamental understanding of the hydrothermal growth mechanism of single crystalline acicular shaped α - Fe_2O_3 NRs. Details concerning the relationship between the nanostructures' phase, morphology, structure, *etc.*, and the hydrothermal processing conditions will be documented. Further, in depth discussion on the intricate details related to phase transformation of β - FeOOH to α - Fe_2O_3 , and the critical role of the phosphate surfactant, made possible by a novel valve-assisted pressure autoclave, will be presented. In addition, a feasibility study on the incorporation of ferromagnetic cobalt into α - Fe_2O_3 NRs for the purpose of improving their magnetic properties is presented. Finally, the main aspects concerning the hydrothermal growth of acicular single crystalline α - Fe_2O_3 NRs are discussed.

Chapter 3 Experimental methodology

3.1 Introduction

The experimental procedures used for the fabrication and characterisation of the nanostructures presented in this thesis will be discussed in this chapter. The first section concerns the technique of HS, including the equipment and chemical precursors used. The second section covers the complementary chemical, structural and surface characterisation techniques used to appraise the acquired nanostructures.

3.2 Hydrothermal synthesis

3.2.1 Basis of HS

As outlined in Section 2.4, HS involves the nucleation of precipitates from an aqueous precursor solution under conditions of high temperature and pressure. The pressure autoclave needs to remain resistant to corrosion under hydrothermal conditions and provide reaction products with consistent size, phase and morphology. Accordingly, this section aims to provide detailed information on the hydrothermal vessels used in this research, with emphasis placed on the development of a novel valve-assisted Teflon-lined stainless steel pressure autoclave which allows for rapid quenching of the hydrothermal suspension in liquid nitrogen. The various precursor chemicals, solutions, phosphate surfactant and associated processing conditions are also discussed.

3.2.2 Pressure autoclaves

3.2.2.1 Standard pressure autoclave

For the purpose of conventional HS and producing consistent reaction products, a standard 125 ml capacity stainless steel pressure autoclave was purchased from Parr Instruments, as shown in Figure 3.1a. The chemical equation (2.3) presented in Section 2.5.1 showed the formation of a corrosive HCl reaction product. Hence, the chemical precursor solution was poured into an un-reactive Teflon liner positioned within the pressure autoclave, as shown in Figure 3.1b. The bolts on the cap of the

autoclave were tightened to seal the solution within the vessel, as illustrated by an image of the cross section of the system (Figure 3.1c). The autoclave was inserted into a temperature controlled furnace at reaction temperature and placed onto a steel grid to allow uniform heating from all sides. After the reaction time, the autoclave, once removed from the furnace, was allowed to cool down to room temperature naturally.

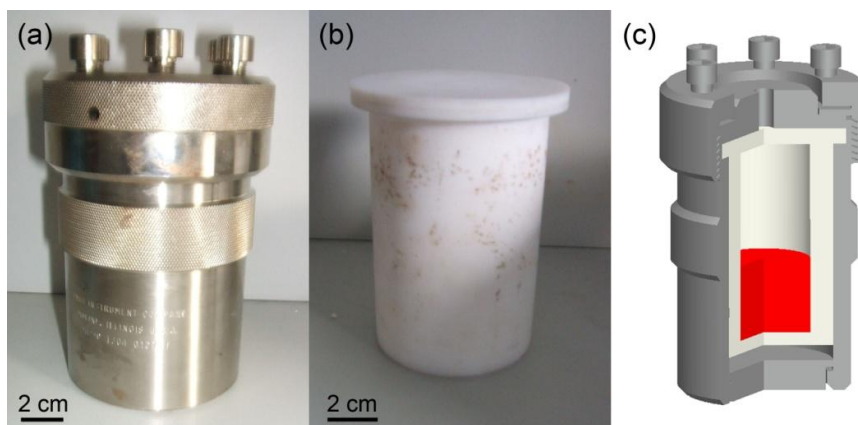


Figure 3.1 Images of (a) stainless steel pressure autoclave and (b) 125ml Teflon liner used for HS. (c) Schematic diagram illustrating the chemical solution (red) within the white Teflon liner of the pressure autoclave.

3.2.2.2 Valve-assisted pressure autoclave

A novel 50 ml capacity valve-assisted Teflon-lined stainless steel pressure autoclave (Figure 3.2) was developed for the purpose of rapid quenching of hydrothermal suspensions in liquid nitrogen. The approach facilitated ‘snapshot’ descriptions closely representative of the *in situ* physical state of the HS reaction product. The large cooling rate experienced during quenching from the reaction temperature is considered to restrict possible atom / ion transport, thereby locking-in the morphology of the nanostructures. Hence, this ‘snapshot’ approach is thought to provide valuable insight into the development of nanostructures grown by HS. The autoclave was fabricated by machining the main body and lid from a section of stainless steel cylinder. The lid incorporated a release channel, extending from the reaction solution and attached to a stainless steel 1/8" needle valve. The autoclave also included a Teflon liner, machined from a section of Teflon cylinder into the main lining and lid. The Teflon lid incorporated a hole to allow for the release channel and was sealed with Teflon tape. The autoclave was sealed with six 6 mm bolts inserted through holes drilled in the lid and flange of the main body. The release channel also allowed for the insertion of a thermo-couple for the purpose of time lapse HS solution temperature measurement.



Figure 3.2 Image of the valve-assisted Teflon-lined stainless steel pressure autoclave.

Again, the autoclave was inserted into a temperature controlled furnace at reaction temperature and placed onto a steel grid to allow uniform heating from all sides. As illustrated in Figure 3.3, the autoclave was removed from the furnace at the reaction temperature and immediately transferred to a tripod support for stability, where the valve was opened and closed, as quickly as practically possible, for the release of sufficient hydrothermal product suspension into liquid nitrogen for the purpose of rapid quenching. It is recognised that cooling rate is dependent on the reaction solution pressure and thus the associated solution expulsion rate from the valve. At low pressures, it is considered that the quenching time might be in the range of tenths of a second, whilst at high pressures, the cooling rate is thought to be significantly higher. The resultant suspension comprised frozen droplets, from a few tens of micrometres up to a few millimetres in diameter, with pale orange to reddish / brown appearance.

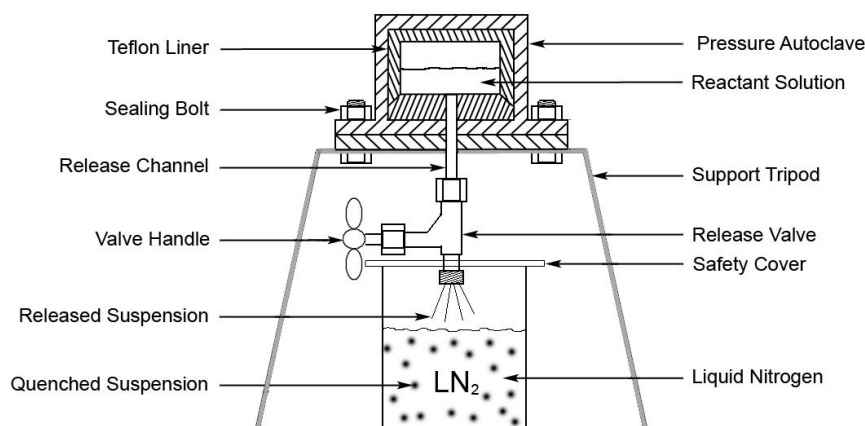


Figure 3.3 Schematic diagram of the valve-assisted Teflon-lined stainless steel pressure autoclave. The hydrothermal suspension is released into liquid nitrogen and quenched to allow characterisation of the reaction products.

3.2.3 Materials and processing conditions

3.2.3.1 Fabrication of β -FeOOH and α -Fe₂O₃ nanostructures

For the purpose of constructing an HS ‘process map’, 0.2 ml of iron (III) chloride aqueous solution (45% pure FeCl₃; Riedel-de Haen, Germany), further diluted in 40 ml distilled water and mixed with and without an ammonium dihydrogen-phosphate (99.999% NH₄H₂PO₄; Sigma-Aldrich, UK) surfactant, was mechanically stirred in the standard 125 ml Teflon-lined stainless steel pressure autoclave. The controlling parameters of reaction temperature (100 to 240°C), time (30 to 120 minutes) and surfactant concentration (0 to 5 mg phosphate addition) were varied in a systematic fashion to demonstrate the relationship between HS processing conditions and reaction products. Some additional experiments were performed to explore the effect of FeCl₃ aqueous solution concentration, pH, stage of NH₄H₂PO₄ addition and α -Fe₂O₃ seed content on the development of β -FeOOH and α -Fe₂O₃ nanostructures.

To allow for rapid quenching of HS reaction products, 0.1 ml FeCl₃ aqueous solution, further diluted in 20 ml of distilled water and mixed with 1.5 mg of NH₄H₂PO₄, was mechanically stirred in the 50 ml capacity valve-assisted Teflon-lined stainless steel pressure autoclave. Initial experiments were performed as a function of discrete reaction time (20, 30, 40 or 50 minutes) at 200°C. However, time lapse temperature measurements later confirmed the reaction solution only reached the desired temperature after ~ 80 minutes of processing. Accordingly, further experiments were performed as a function of known reaction temperature (100 to 200°C) for a reaction time of 80 minutes.

3.2.3.2 Fabrication of Co₃O₄ and CoFe₂O₄ NPs

To produce Co₃O₄ NPs, CoCl₂ powder (20 and 100 mg) was added to 40 ml distilled water and mechanically stirred in the standard 125 ml Teflon-lined stainless steel pressure autoclave. For the fabrication of the CoFe₂O₄ NPs, CoCl₂ powder (25 and 50 mg) and FeCl₃ (0.05, 0.1 and 0.2 ml) were added to 40 ml distilled water, mixed with and without NH₄H₂PO₄ and mechanically stirred in the standard 125 ml Teflon-lined stainless steel pressure autoclave. NaOH solution was added drop-wise to adjust the pH of the precursor solution to ~ 8 and 12, for Co₃O₄ and CoFe₂O₄ NPs, respectively. In both cases, the sealed autoclave was then heated at 200°C for 120 minutes.

The precursor concentrations, processing variables and HS autoclaves used for the samples investigated throughout this thesis are summarised in Table 3.1.

Experiment set	Sample	FeCl ₃ / ml	NH ₄ H ₂ PO ₄ / mg	pH (approx.)	Temperature / °C	Time / min	α-Fe ₂ O ₃ seeds / mg	CoCl ₂ / mg	HS autoclave
Process map (RHEED / XRD)	S1 (S32)	0.2		2	100	120			S
	S2 (S33)	0.2		2	120	120			S
	S3 (S34)	0.2		2	140	120			S
	S4 (S35)	0.2		2	160	120			S
	S5	0.2		2	200	120			S
	S6 (S36)	0.2	1	2	160	120			S
	S7 (S37)	0.2	2	2	160	120			S
	S8 (S38)	0.2	3	2	160	120			S
	S9 (S39)	0.2	4	2	160	120			S
	S10	0.2	5	2	160	120			S
	S11	0.2	3	2	120	120			S
	S12	0.2	3	2	140	120			S
	S13	0.2	3	2	180	120			S
	S14	0.2	3	2	200	120			S
	S15	0.2	3	2	220	120			S
	S16	0.2	3	2	240	120			S
	S17	0.2	3	2	200	30			S
	S18	0.2	3	2	200	60			S
	S19	0.2	3	2	200	90			S
Effect of FeCl ₃ conc.	S20	0.15	2.25	2	200	120			S
	S21	0.1	1.5	2	200	120			S
	S22	0.05	0.75	2	200	120			S
Effect of pH value	S23	0.2	3	2.5	200	120			S
	S24	0.2	3	3	200	120			S
	S25	0.2	3	4	200	120			S
Stage of phosphate addition	S26	0.2	3	2	110	120			S
	S26*			1.5	200	120			S
	S27	0.2		2	110	120			S
	S27*		3	1.5	200	120			S
Effect of α-Fe ₂ O ₃ seeds	S28						Is sample		
	S29	0.2	3	2	200	120	1		S
	S30	0.2	3	2	200	120	3		S
	S31	0.2	3	2	200	120	5		S
Effect of reaction time	Q20	0.1	1.5	2	200	20			V
	Q30	0.1	1.5	2	200	30			V
	Q40	0.1	1.5	2	200	40			V
	Q50	0.1	1.5	2	200	50			V
Effect of reaction temperature	Q100	0.1	1.5	2	100	80			V
	Q120	0.1	1.5	2	120	80			V
	Q140	0.1	1.5	2	140	80			V
	Q160	0.1	1.5	2	160	80			V
	Q180	0.1	1.5	2	180	80			V
	Q200	0.1	1.5	2	200	80			V
Effect of CoCl ₂ / Co ₃ O ₄ NPs	S14*			8	200	120		100	S
	C1	0.2	3	2	200	120		100	S
	C2			8	200	120		20	S
	C2*	0.2	3	2	200	120			S
Effect of CoFe ₂ O ₄ NPs	F1	0.2		12	200	120		50	S
	F2	0.1		12	200	120		25	S
	F3	0.1		12	200	120		50	S
	F4	0.05		12	200	120		25	S
	F5	0.05	3	12	200	120		25	S
	F6	0.05	6	12	200	120		25	S
	F6*	0.2	3	2	200	120			S

Table 3.1 HS precursor concentrations, processing variables and HS autoclaves used. * Denotes a secondary HS process for selected samples. S and V signify the use of standard and valve-assisted pressure autoclaves, respectively.

3.3 Material characterisation techniques

To appraise fully the nanostructures grown during HS, it is appropriate to use a combination of complementary chemical, structural and surface characterisation techniques. This section aims to provide a brief background on the analytical techniques used during this research programme, including sample preparation, X-ray diffractometry (XRD), secondary electron microscopy (SEM), transmission electron microscopy (TEM), reflection high energy electron diffraction (RHEED), energy dispersive X-ray (EDX) analysis, X-ray photoelectron spectroscopy (XPS) and Fourier transform infrared spectroscopy (FTIR).

3.3.1 Sample handling

3.3.1.1 Standard pressure autoclave

For a comprehensive appraisal of the standard HS process, characterisation was carried out on the HS suspension taken directly from the autoclave, following ultrasonic dispersion. The ultrasonic method was used to separate out the nanostructures that may have settled during cooling, providing for an evenly dispersed suspension. The reaction products were deposited onto single crystalline Si substrates for the purpose of surface characterisation using XPS and RHEED, and bulk characterisation using XRD. For the purpose of survey TEM investigation, the HS product suspensions were deposited straight onto lacey carbon / copper mesh support grids (Agar Scientific Ltd., U.K.) for a generalised appraisal of the reaction products present. For the purpose of high level TEM and EDX analysis of individual nanostructures, the HS product suspensions were centrifuged for 6 min at 6000 rpm, cleaned with acetone, and dispersed using an ultrasonic bath before deposition onto the support grids. For the purpose of FTIR investigation, a few drops of the HS suspension were deposited onto the FTIR diamond sensor, where it was dried at 80°C using the heating stage and subsequently clamped.

3.3.1.2 Valve-assisted pressure autoclave

Frozen droplets of the quenched reaction suspension were removed from the liquid nitrogen using tweezers. For the purpose of XPS analysis, they were allowed to melt in a pipette at room temperature and deposited onto single crystalline Si substrates. For the purpose of TEM investigation, the frozen droplets were deposited straight

onto lacey carbon/copper mesh support grids and allowed to melt at room temperature prior to TEM investigation. For FTIR analysis, the frozen droplets were allowed to melt in a pipette at room temperature, deposited directly onto the FTIR diamond sensor, dried at 80°C using the heating stage and subsequently clamped.

3.3.2 Material characterisation

Diffraction provides evidence for the identification of a nanostructure's crystallographic structure, which is governed by its arrangement of atoms. This section provides a brief background to the fundamental concepts underpinning the structural characterisation techniques of XRD and electron microscopy used during this research.

3.3.2.1 Interaction of waves with crystal structures

A wave is a disturbance or variation that travels through a medium and transfers energy. An example of a transverse wave with a wavelength (λ) is shown in Figure 3.4a. According to Huygens' Principle, a wave can be thought of as spreading spherically at every point along its wave-front. These spherical 'wavelets' are constantly interacting to maintain a planar wave-front. However, if the wave-front is interrupted by an obstacle, the wavelets spread spherically from the points of obstruction. These wavelets interfere with each other and several wavelets in phase result in constructive interference, as shown in Figure 3.4b.

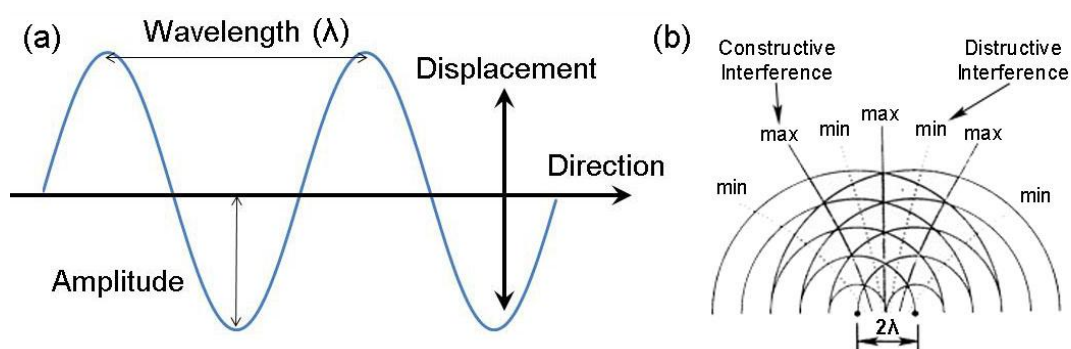


Figure 3.4 Schematic diagram of (a) a transverse wave and (b) interaction of waves with an obstacle, resulting in constructive and destructive interference.

For the case of X-rays, the incident waves may be scattered by atoms in the crystal lattice. The interference of waves scattered from different atoms form a distinct pattern of constructive and destructive interference (reconstructed intensities),

providing information on the atomic structure of the material. The structure factor, F , describes the way in which the incident wave is scattered by atoms of a crystal unit cell, obtained by summation of the waves scattered by the individual atoms. If a unit cell contains atoms 1, 2, 3, ..., N , with fractional coordinates $u_1v_1w_1$, $u_2v_2w_2$, $u_3v_3w_3$, ... then the structure factor for an hkl reflection is given by:¹⁵²

$$F_{hkl} = \sum_1^N f_n e^{2\pi i(hu_n + kv_n + lw_n)} \quad (3.1)$$

The amplitude of each scattered wave is given by the appropriate atomic scattering factor, f , which depends on the type of incident radiation, typically X-ray, electron or neutron.

3.3.2.2 X-ray diffractometry

XRD is commonly used for the determination of bulk crystallographic structure and the grain size of nanostructured materials. When a monochromatic beam of X-rays is directed towards a crystalline material, the incident X-ray photons interact with the electrons that surround the atoms. The electron clouds scatter the X-rays in all directions. However, at certain angles (θ) the distance travelled by the incident and scattered X-rays differ by a complete number (n) of wavelengths, as illustrated by Figure 3.5. Consequently, the scattered X-rays remain in phase, known as constructive interference.¹⁵²

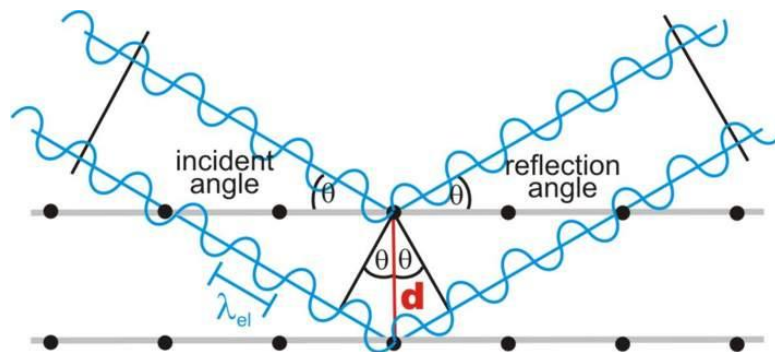


Figure 3.5 Schematic diagram illustrating the constructive interference of scattered waves (maxima and minima are superimposed).¹⁵³

X-ray diffraction occurs when the following equation, also known as Bragg's law, is satisfied:

$$n\lambda = 2d \sin\theta \quad (3.2)$$

where d is the lattice spacing, λ is the X-ray wavelength and θ is the angle of diffraction.

Samples were examined by plotting the angular positions (2θ) and their reconstructed intensities, resulting in diffraction patterns characteristic to individual or mixed phases. Information content from diffraction patterns is available from peak position, intensity and profile. XRD investigations were performed using a Siemens D500 X-ray diffractometer operating at 40 kV and 25 mA, using a $\text{CuK}\alpha$ radiation source ($\lambda = 0.154$ nm). Analysis was carried out at a 2θ step rotation of 0.01° with a dwell time of 1.5 sec at room temperature ($\sim 25^\circ\text{C}$). Crystalline phase features were identified using DIFFRAC^{plus} computer software (Bruker Advanced X-ray Solutions).

The particle size of nanostructures were determined by measuring peak breadth in an X-ray diffraction pattern, and applying the Scherrer equation:¹⁵²

$$\beta_{hkl} = \frac{K\lambda}{L_{hkl} \cos\theta_{hkl}} \quad (3.3)$$

where β is the peak width at half maximum intensity in radians, K is a constant ($0.89 < K < 1$), θ is the peak position and L is the crystallite size. The value of β can increase through instrumental broadening, which depends on the geometry of the diffractometer and spectral characteristics of the incident beam. Instrumental broadening can be corrected by subtracting the β value of a standard reference sample, assumed to comprise infinitely thick particles, from the measured β .

3.3.2.3 Electron microscopy

Electron microscopy makes use of a beam of highly energetic electrons to examine materials on the very fine scale. Information *e.g.* sample crystallography, morphology and elemental composition can all be acquired. This section briefly outlines the underpinning concepts associated with the interaction of high-energy electrons with matter that are fundamental to electron microscopy. Consideration is then given to the TEM, selected area electron diffraction (SAED), high resolution TEM (HRTEM) and RHEED.

3.3.2.4 Interaction of high energy electrons with matter

The electron beam may be treated as both a succession of particles and a series of waves. According to de Broglie's theory of wave-particle duality, the wavelength of a high energy electron is given by:

$$\lambda = \frac{h}{\left[2m_0eV \left(1 + \frac{eV}{2m_0c^2}\right)\right]^{1/2}} \quad (3.4)$$

where h is Planck's constant, m_0 is the rest mass of an electron, e is the electron charge, V is the potential difference through which the electron is accelerated and c is the velocity of light.

Electrons may be scattered by both electrons and the nuclei in an atom. During scattering, the electron beam is capable of ejecting inner-shell electrons from the attractive field of a nucleus in an atom. Consequently, a wide range of secondary signals can be produced, as summarised in Figure 3.6. Many of these signals can be used for imaging, *e.g.* secondary electrons and backscattered electrons in SEM or elastically scattered electrons in TEM; or chemical analysis, *e.g.* characteristic X-rays in EDX analysis. Elastic electron-electron interactions usually result in a relatively low scattering angle, while electron-nucleus interactions cause higher-angle scattering. For TEM investigation, elastically scattered electrons are essential for the construction of diffraction patterns and diffraction contrast images.

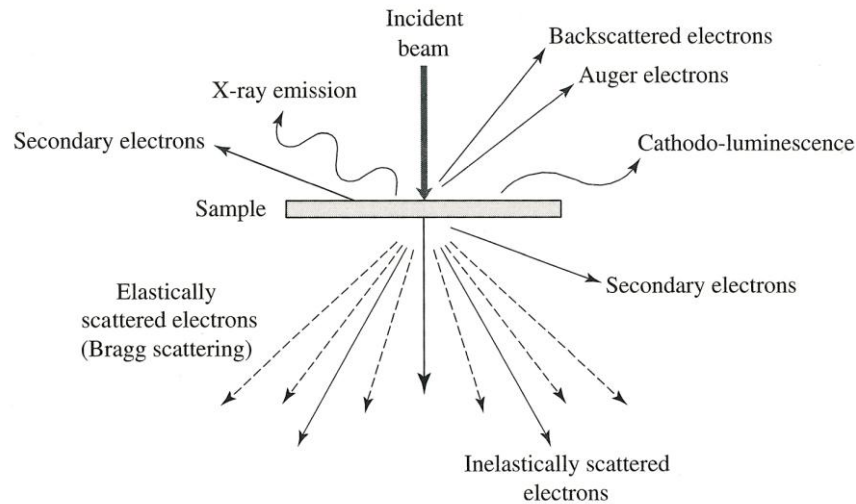


Figure 3.6 Electron scattering and secondary signal generation when a beam of high-energy electrons interacts with a thin specimen.

3.3.2.5 Transmission electron microscopy

TEM allows electron transparent specimens (< 100 nm thick) to be examined at a resolution approaching the atomic scale. In principle, resolution is only limited by the wavelength (λ) of the incident electron beam. However, in practice, resolution is dependent on the aberrations associated with the electron optics. A conventional TEM consists of a number of electron-optical components, as illustrated in Figure 3.7. Electrons produced by thermionic emission from a W or LaB₆ filament, or by field emission from a single crystal W filament gun, are accelerated towards the anode at a high energy, typically between 100 and 400 kV. A series of condenser lenses focus the electrons into a probe and are responsible for varying the spot size. The condenser aperture filters out electrons far from the optic axis and controls the number of electrons incident on the specimen. The electron beam is transmitted through the specimen, generally inserted on a plane normal to the optic axis and situated close to the focal plane of the objective lens. The objective aperture, located in the back focal plane of the objective lens, blocks any transmitted electrons with a large scattering angle, thereby enhancing the contrast of the projected image. The image is projected onto an electron sensitive florescent screen or a charged couple device (CCD) camera by the projector lens. Images can be recorded on photographic film or digitised to be stored on computer.

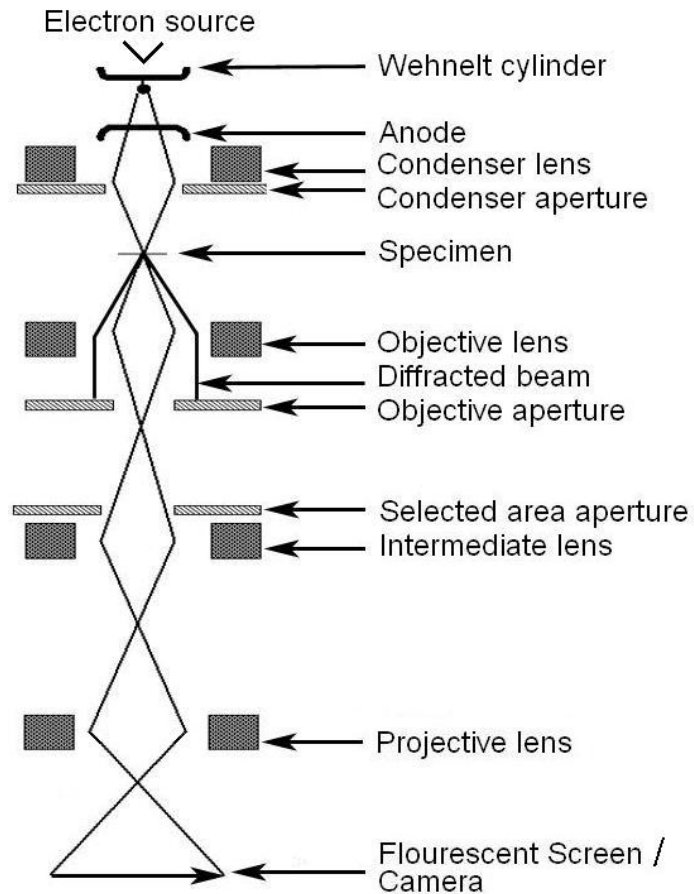


Figure 3.7 Schematic diagram of the basic electron-optical components of a TEM.

For electron diffraction pattern formation, the objective aperture is removed and a selected area aperture is inserted into the intermediate image plane, and the projector optics are focused on the back focal plane of the objective lens. This allows a smaller area of the specimen to be selected for defining the electron diffraction pattern. The different optics for the formation of images and electron diffraction patterns within a TEM are illustrated in Figure 3.8.

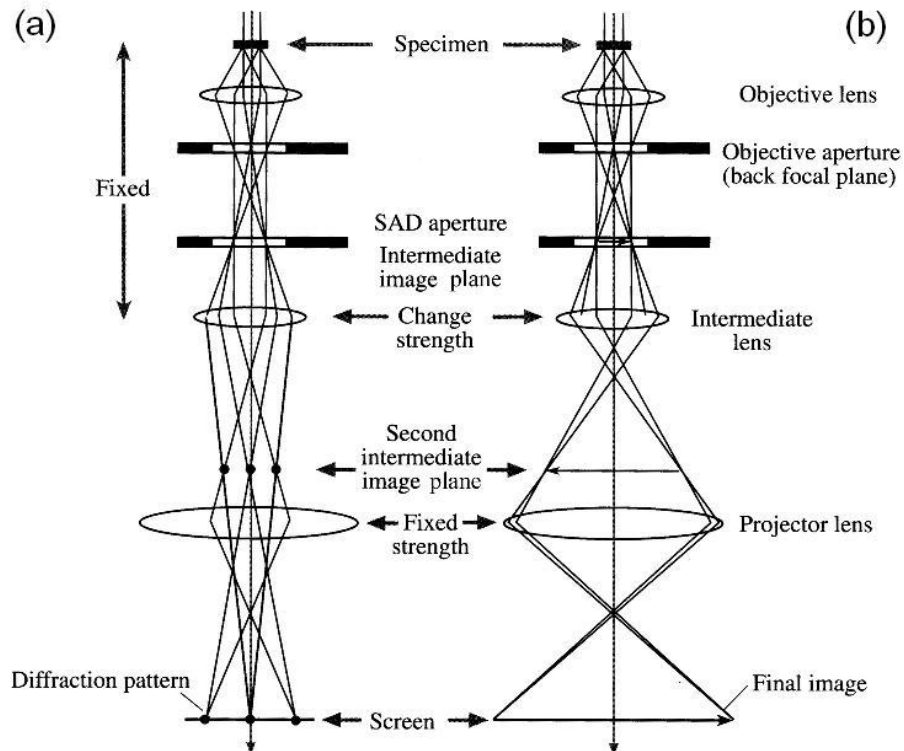


Figure 3.8 Schematic diagram showing the optics for the formation of (a) electron diffraction patterns and (b) images within a TEM.¹⁵⁴

Images in TEM can be formed either using directly transmitted or scattered electrons. The electrons are selected by inserting an aperture into the back focal plane of the objective lens, thus blocking out most of the diffraction pattern. If the central spot is chosen, a bright field image is formed using directly transmitted electrons, as shown in Figure 3.9a. There are three modes of contrast formation in TEM images. In amorphous samples, thicker regions of the sample and areas with a higher atomic number appear dark, due to mass-thickness contrast. Low index crystalline orientations of crystalline samples that satisfy Bragg diffraction also appear dark, termed diffraction contrast. Further, if the objective aperture is removed, images with contrast arising from constructive and destructive interference of the electron waves, termed phase contrast, can reveal lattice with atomic resolution, known as HRTEM. In all cases, regions imaged with the transmitted beam are termed bright field (BF). Alternatively, by aligning a diffracted beam down the optic axis of the microscope, a dark field (DF) image may be formed, as shown in Figure 3.9b. Most of the conventional imaging and EDX analysis was performed on Jeol 2000fx with a LaB₆ filament operating at 200 kV. A Jeol 2100F equipped with a Gatan Imaging Filter (GIF) and Gatan double tilt heating holder was used for HRTEM imaging and *in situ* TEM (*i*TEM) investigations.

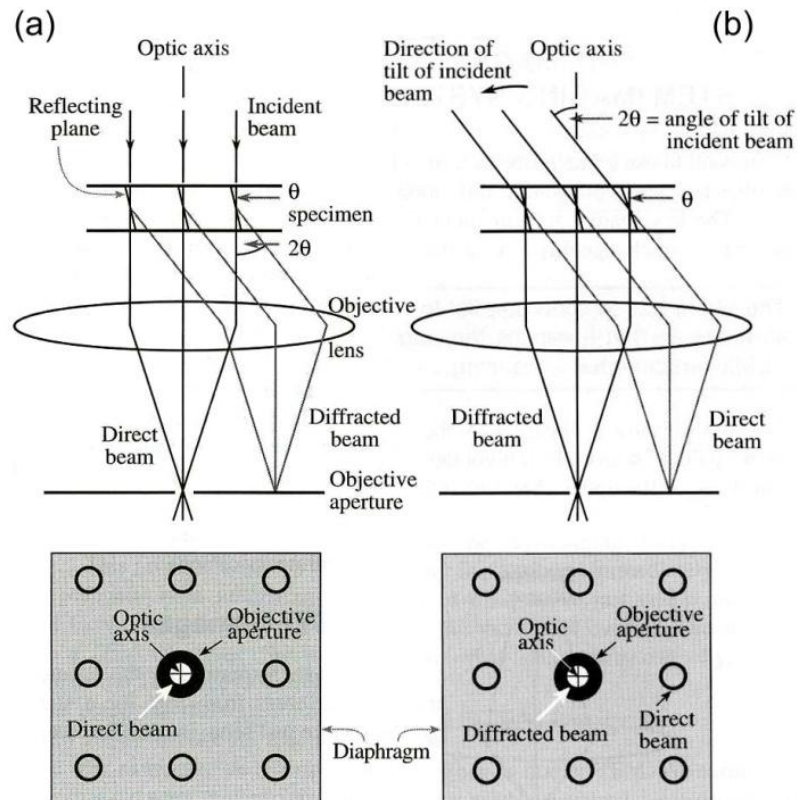


Figure 3.9 Schematic diagram showing the formation of (a) a BF diffraction contrast image using the direct transmitted beam and a (b) a centred DF diffraction contrast image, with the incident beam tilted so that the scattered beam remains on the optic axis.¹⁵⁴

3.3.2.6 Selected area electron diffraction

SAED can provide information on the crystallography and crystal orientation of an individual NR. The angle of diffraction (θ) in SAED is very small because of the very small wavelength of high energy electrons (as compared with the wavelength of X-rays) resulting in small distances between the transmitted electron beam and diffracted spots, R_{hkl} , as illustrated in Figure 3.10.

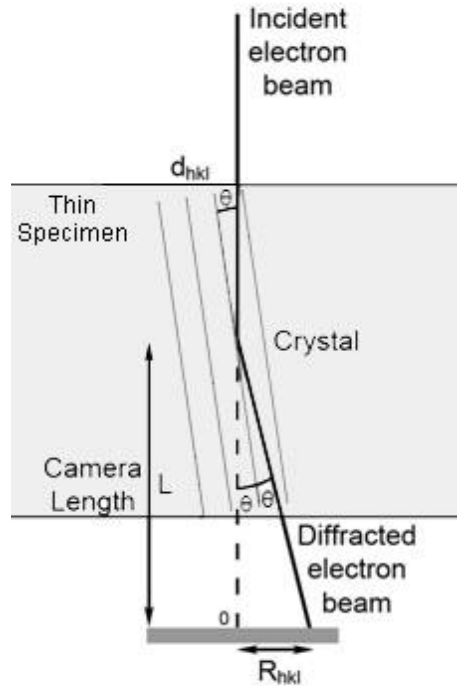


Figure 3.10 Schematic diagram to illustrate the concept of the camera constant in TEM.

In view of this, the Bragg equation can be simplified:

Since $\sin\theta \approx \theta$ for small θ (in radians)

$$\lambda = 2d_{hkl}\theta \quad (3.5)$$

From Figure 3.10, the geometric equation is obtained:

$$\tan 2\theta = \frac{R_{hkl}}{L} \approx 2\theta = \frac{R_{hkl}}{L} \quad (3.6)$$

where L is the camera length, the effective distance between the specimen and the recording plane.

Combining equations 3.5 and 3.6 gives:

$$\lambda L = R_{hkl}d_{hkl} \quad (3.7)$$

λL is termed the camera constant and can be obtained using a reference sample of known lattice parameter under the same electron-optic conditions. By using this equation, crystal plane spacings, d_{hkl} , of an unknown material can be calculated and associated diffraction spots indexed.

3.3.2.7 Reflection high energy electron diffraction

The variant technique of RHEED within the TEM utilises the diffraction of electrons from the top few atomic layers of a sample, providing information on near surface crystal structure, preferred orientation and roughness.¹⁵⁵ The sample is situated on a dedicated stage positioned directly below the projector lens of the Jeol 2000fx. The stage (Figure 3.11) allows for tilt, rotation and translation of the sample on three axes to access any zone axis within the surface plane.¹⁵⁶ During the RHEED process, the incident electron beam interacts with a surface area of $\sim 1 \text{ mm}^2$ at a glancing angle of $\sim 1^\circ$

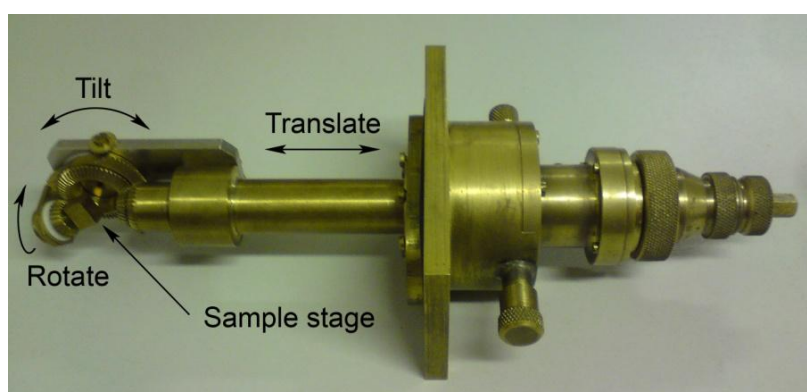


Figure 3.11 Photograph of the RHEED stage and its 3 axes of movement (labelled).¹⁵⁶

3.3.3 Chemical analysis

In addition to structural characterisation, the identification of chemical elements and bonding associated with a nanostructured material is necessary to fully understand its growth. This sections aims to provide a brief background on the concepts applied in the chemical analyses techniques of EDX analysis, XPS and FTIR.

3.3.3.1 Energy dispersive X-ray analysis

EDX analysis is a standard method for local identification of elements within a sample in an SEM or TEM. As mentioned previously, the interaction with the inner most electron shell of an atom by the high energy electron beam will lead to the ejection of a photoelectron. Consequently, an electron from an outer orbiting shell jumps into the core level vacancy, and emits energy in the form of an X-ray photon. The energy of the X-rays arises from the difference in energy between the shells, is characteristic to the atomic number, and therefore can be used to ascertain the

elemental composition of a sample. The relationship between atomic number and energy for a given X-ray is given by Moseley's Law:

$$\sqrt{E} = C_1 (Z - C_2) \quad (3.8)$$

where E is the energy of the emission line for a given X-ray series (*e.g.* K_α , K_β , L_α , M_α , *etc.*), Z is the atomic number and C_1 , C_2 are constants.

In this work, EDX analysis was performed using an *Oxford Link Isis* package on a Jeol 2000fx TEM operated at 200 kV. This provided quantitative elemental compositions for individual nanostructures.

3.3.3.2 X-ray photoelectron spectroscopy

XPS is a widely used technique for surface compositional analysis.¹⁵⁷ The sample is illuminated with monochromatic X-rays resulting in the emission of core shell photoelectrons. Their low kinetic energies (0 - 1500 eV) limit the depth from which they can emerge, hence the technique is sensitive only to the top few atomic layers (~ 30 Å). The kinetic energies of the photoelectrons determine their binding energies (Figure 3.12). The binding energy, which is the energy required to remove an electron from its orbital, is unique to the element and its particular atomic orbital. A spectrum of emission intensity (in counts per second) versus binding energy of the characteristic photoelectron peaks may be plotted to identify the elements present and their quantity. High spectral resolution XPS studies can detect small shifts in the elemental binding energies and therefore also provide information about the chemical state of the surface elements. In this work, the samples were investigated using VG 58 Scientific ESCALAB Mark II and Kratos AXISULTRA X-ray photoelectron spectrometers configured with monochromated Al_K X-ray sources. The XPS spectra were analysed using *CasaXPS* software.

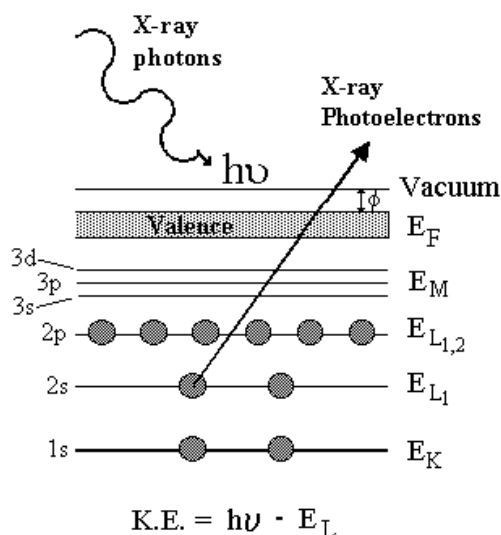


Figure 3.12 Schematic diagram showing the irradiation of a surface with monochromatic X-rays and the emission of photoelectrons at a certain kinetic energy (K.E). $h\nu$ is the photon energy from the X-ray source and E_L is the binding energy of the photoelectron from the inner core shell.

3.3.3.3 Fourier transform infrared spectroscopy

Infrared (IR) spectroscopy uses the infrared region of the electromagnetic spectrum to identify covalent bonding present within materials. IR radiation is passed through the sample and absorbed by covalently bonded molecules at their resonant frequency of vibration. A molecule has many *vibrational modes* that are only considered "IR active" if they result in an associated change in permanent dipole. These vibration modes can be symmetrical, asymmetrical or scissoring. In FTIR, the IR radiation is collected by an interferometer, which measures all IR frequencies to produce an 'interferogram'. The data-processing technique of Fourier transformation converts the interferogram into a spectrum, a plot of wavenumber (wavelength) against absorbance or transmittance, signatures of which are characteristic to the covalent bonding present.¹⁵⁸ In this research, IR spectra were recorded using a Bruker Tensor FTIR spectrometer and analysed using *OPUS* and *CasaXPS* software.

3.3.4 Data handling

The data acquired from each materials characterisation technique underwent some degree of processing for presentation. The raw data of the XRD spectra were converted to UXD format, which is compatible with *Microsoft (MS) Excel*. EDX spectra collected with the TEM using an Oxford Link Isis package were exported into *MS Notepad* in TXT format. XPS and FTIR spectra were analysed using *CasaXPS*

software, where specific regions of the spectra were deconvoluted into their individual spectral components. The EDX, FTIR and XPS data were rendered presentable using *MS Excel*. All data was subsequently imported into worksheets in *Microcal (TM) Origin* ® software, where the spectra were reconstructed, labelled and saved in JPEG format.

TEM images taken with the Jeol 2000fx were recorded on photographic film, developed and fixed. The plate negatives were then rinsed in water, dried at room temperature and scanned using an EPSON scanner. In all cases, the films were scanned as black and white negatives, at a resolution of 1200 dpi, and saved in JPEG format. TEM images taken on the Jeol 2100f were recorded using a CCD camera, processed using Gatan Digital Micrograph (DM) software and saved in both DM3 and JPEG formats. Measurements carried out on TEM images were performed using *ImageJ* software. For the purpose of magnification scale calibration, BF phase contrast images of graphitised carbon and gold film reference samples, with known lattice plane fringe spacings, were collected from the Jeol 2000fx and 2100F microscopes, respectively. SAED patterns were collected from a reference aluminium foil sample to calibrate the camera constant, λL , of the Jeol 2000fx microscope using equation 3.7. Measurement of R_{hkl} values from SAED patterns allowed d_{hkl} values to be calculated and matched with reference indices and indexed. Fast Fourier transform (FFT) processing was performed also on phase contrast images using *ImageJ* to investigate reciprocal space.

For the purpose of crystal structure modelling, reference crystal data was downloaded from the Inorganic Crystal Structure Database and rendered using *CaRine Crystallographie* and *Balls & Sticks* software. Appraisal of the relationship between crystallographic orientation and nanostructure morphology was achieved through correlation of BF images and real and modelled (*CaRine*) SAED patterns.

All images and spectra were cropped, edited, labelled and compiled, *etc.*, using *Adobe Photoshop CS2* software.

3.4 Summary

The experimental procedures used for the fabrication and characterisation of the nanostructures in this research have been presented. A standard 125 ml Teflon-lined stainless steel pressure autoclave was used for production of HS reaction products over a range of processing conditions. Development of a novel 50 ml valve-assisted Teflon-lined stainless steel pressure autoclave for the purpose of rapid quenching HS reaction products in liquid nitrogen provided ‘snapshot’ descriptions closely representative of the *in situ* physical state. FeCl₃ aqueous solution was used for the production of β-FeOOH and α-Fe₂O₃ nanostructures, whilst NH₄H₂PO₄ was added as a phosphate surfactant. CoCl₂ aqueous solution was used for the formation of Co₃O₄ and CoFe₂O₄ NPs (in addition to FeCl₃). NaOH was added to precursor solutions to alter the pH value. A combination of complementary chemical, structural and surface characterisation techniques were used to examine the nanostructures. Diffraction techniques of XRD, RHEED and SAED allowed for the bulk, surface and localised structural characterisation of the nanostructures, respectively. TEM and HRTEM provided diffraction contrast and phase contrast imaging of crystalline nanostructures, respectively. TEM imaging and SAED used in conjunction with *CaRine* crystal modelling provided information on the crystal orientation of individual nanostructures. EDX and XPS analysis techniques were used for compositional analysis of nanostructures and their surface, respectively. FTIR provided information on the covalent bonding associated with nanostructures and the mode of surfactant absorption to their surface. The data retrieved from all characterisation techniques was handled appropriately and compiled for presentation.

Chapter 4 Hydrothermal synthesis of β -FeOOH and α -Fe₂O₃ nanostructures

4.1 Introduction

In this chapter, the development of β -FeOOH and α -Fe₂O₃ nanostructures using a wide range of HS processing conditions is presented. Systematic investigation of the effect of HS temperature, phosphate surfactant and reaction time on the β -FeOOH to α -Fe₂O₃ phase transformation, morphology and crystallinity provides a comprehensive HS ‘process map’ for their development, giving valuable insight into the nature of β -FeOOH precipitation, dissolution, and subsequent α -Fe₂O₃ growth. In particular, emphasis is given to the effect of PO₄³⁻ anion concentration on the mediation of α -Fe₂O₃ NP shape. In addition, the effects of FeCl₃ aqueous solution concentration, pH, stage of NH₄H₂PO₄ addition and α -Fe₂O₃ seeds on the β -FeOOH and α -Fe₂O₃ nanostructures are explored. The applicability of RHEED and XRD as techniques for the structural characterisation of β -FeOOH and α -Fe₂O₃ nanostructures is discussed and their relative merits highlighted.

4.2 Effect of HS process conditions

The hydrothermal processing of aqueous FeCl₃ solution enabled the synthesis of either, or both, β -FeOOH or α -Fe₂O₃ NPs with differing aspect ratios, depending on the HS reaction temperature, time and NH₄H₂PO₄ concentration. The range of HS experimental conditions investigated and the reaction products produced are summarised in Table 4.1; the evidence for which is now presented in detail.

Chapter 4 Hydrothermal synthesis of β -FeOOH and α -Fe₂O₃ nanostructures

Sample	NH ₄ H ₂ PO ₄ / mg	Molar ratio Fe ³⁺ : PO ₄ ³⁻	Temperature / °C	Process Time / min	Reaction product	Morphology	Dimension (l/w) / nm	Aspect Ratio Fe ₂ O ₃
S1	0	-	100	120	β -FeOOH	NRs	<60/20	-
S2	0	-	120	120	β -FeOOH + α -Fe ₂ O ₃	NRs + Pseudocubes	<60/20 + <60/55	1.1
S3	0	-	140	120	β -FeOOH + α -Fe ₂ O ₃	NRs + Pseudocubes	<60/20 + <125/115	1.1
S4	0	-	160	120	α -Fe ₂ O ₃	Pseudocubes	<150/140	1.1
S5	0	-	200	120	α -Fe ₂ O ₃	Agglomerated Pseudocubes	-	-
S6	1	94.4	160	120	α -Fe ₂ O ₃	Pseudocubes / Round / Ellipsoidal	<130/120 / <90 / <150/50	1.1/3
S7	2	47.2	160	120	α -Fe ₂ O ₃	Ellipsoidal NPs	<330/90	3.7
S8	3	31.5	160	120	β -FeOOH + α -Fe ₂ O ₃	NRs + Partial acicular NRs	<60/20 + <360/60	6
S9	4	23.6	160	120	β -FeOOH + α -Fe ₂ O ₃	NRs + Partial acicular NRs	<60/20 + <250/50	5
S10	5	18.9	160	120	β -FeOOH + α -Fe ₂ O ₃	NRs + Partial acicular NRs	<60/20 + <200/50	4
S11	3	31.5	120	120	β -FeOOH	NRs and NPs	<50/15	-
S12	3	31.5	140	120	β -FeOOH + α -Fe ₂ O ₃	NRs + Partial acicular NRs	<60/20 + <280/50	5.6
S13	3	31.5	180	120	α -Fe ₂ O ₃	Partial acicular NRs	<400/60	6.7
S14	3	31.5	200	120	α -Fe ₂ O ₃	Fully formed acicular NRs	<420/60	7
S15	3	31.5	220	120	α -Fe ₂ O ₃	Fully formed ellipsoidal NPs	<360/100	3.6
S16	3	31.5	240	120	α -Fe ₂ O ₃	Fully formed rectangular NPs	<240/70	3.4
S17	3	31.5	200	30	β -FeOOH	NRs and NPs	<50/15	-
S18	3	31.5	200	60	β -FeOOH + α -Fe ₂ O ₃	NRs + Partial acicular NRs	<60/20 + 280/50	5.6
S19	3	31.5	200	90	β -FeOOH + α -Fe ₂ O ₃	NRs + Partial acicular NRs	<60/20 + <400/60	6.7

Table 4.1 HS processing variables and a summary of the reaction products, morphologies, dimensions and aspect ratios of the α -Fe₂O₃ NPs.

4.2.1 Results

4.2.1.1 Effect of reaction temperature

The BF, diffraction contrast TEM images of Figures 4.1(a – e) illustrate the morphologies of the nano-materials grown in the absence of a surfactant, at temperatures from 100 to 200°C (Samples S1 – S5), for a reaction time of 120 minutes. The associated XRD patterns shown in Figure 4.1f, corresponding to Samples S1 to S4 for simplicity, chart the transformation from an intermediate phase of β -FeOOH to the well defined phase of α -Fe₂O₃ with increasing HS temperature. Indeed, Figure 4.1a illustrates the small (~ 60 nm long, ~ 20 nm wide) β -FeOOH NRs synthesised at 100°C, as compared with Figure 4.1d which shows the larger (~150 nm sized) rhombohedral α -Fe₂O₃ NPs synthesised at 160°C. The intermediate stages of growth of the α -Fe₂O₃ NPs can be seen at the reaction temperatures of 120°C and 140°C (Figures 4.1b & c), respectively. A small number of single crystal α -Fe₂O₃ NPs were identified in amongst the β -FeOOH NRs of Sample S2 (Figure 4.1b), but at a volume fraction beneath the detection limit of the XRD technique in this instance (Figure 4.1f). Inspection of Sample S5 synthesised at 200°C indicated that some of the α -Fe₂O₃ NPs had agglomerated at this highest reaction temperature (Figure 4.1e). An additional diffraction peak was present (~ 28°, Figure 4.1f) in the XRD patterns for Samples S1, S2 and S3.

SAED was used to chart the transformation of β -FeOOH to α -Fe₂O₃ on the localised scale. For example, Figures 4.2a & b present electron diffraction patterns recorded from Samples S1 and S4, respectively. The measured interplanar spacings were found to be in excellent agreement with database values for β -FeOOH (Figure 4.2a) and α -Fe₂O₃ (Figure 4.2b), respectively. No diffraction rings attributable to β -FeOOH were evident within the SAED patterns corresponding to α -Fe₂O₃ recorded from Sample S4, suggesting chemical transformation to be complete after 120 minutes at 160 °C. It is noted that the continuous distinct rings of Figure 4.2a and the interrupted intense rings of Figure 4.2b are consistent with the very small sizes of the β -FeOOH nanostructures as compared with the larger, more well-defined α -Fe₂O₃ NPs.

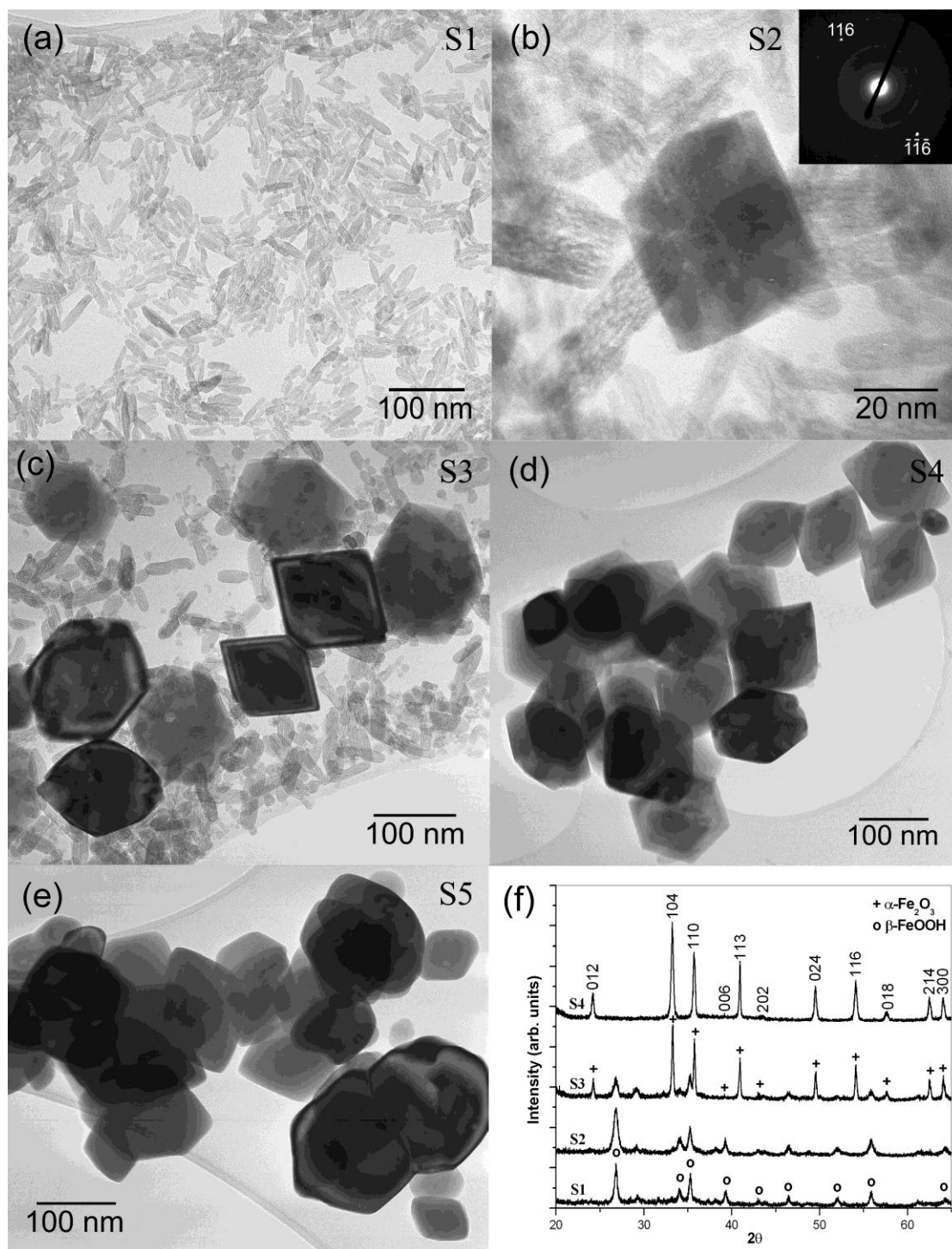


Figure 4.1 BF TEM images of the hydrothermal products synthesised in the absence of a surfactant, for a reaction time of 120 minutes. (a) 100°C; (b) 120°C with SAED inset; (c) 140°C; (d) 160°C; and (e) 200°C. (f) Associated XRD patterns corresponding to Samples S1 to S4 (with Miller indices corresponding to α -Fe₂O₃).

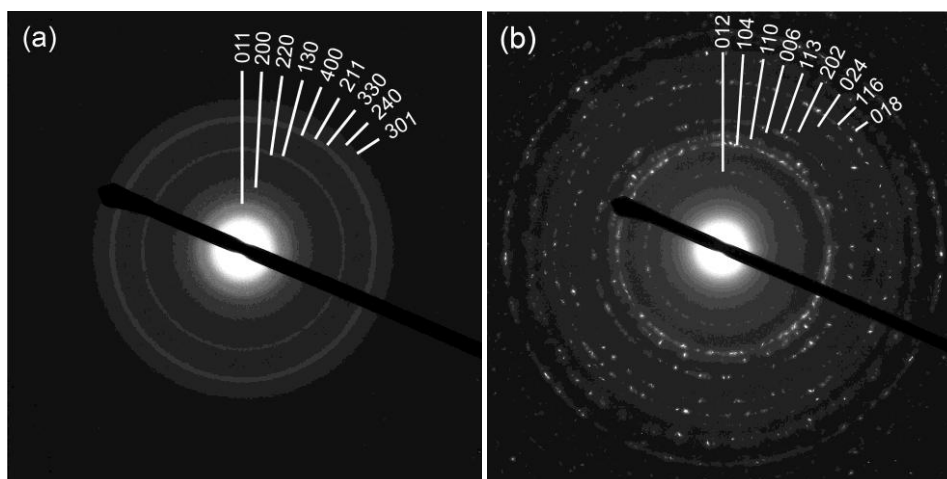


Figure 4.2 SAED patterns from (a) Sample S1, synthesised at 100°C, matching β -FeOOH (JCPDS 34-1266); and (b) Sample S4, synthesised at 160°C, matching α -Fe₂O₃ (JCPDS 72-469).

4.2.1.2 Effect of phosphate surfactant concentration

The BF TEM images of Figures 4.3a – e illustrate the influence of increasing additions (1 to 5 mg) of phosphate surfactant on the shape of α -Fe₂O₃ NPs synthesised for 120 minutes at 160°C (Samples S6 – S10; corresponding to Fe³⁺ : PO₄³⁻ molar ratios of (a) 94.4, (b) 47.2, (c) 31.5, (d) 23.6 and (e) 18.9, respectively). The associated XRD patterns of Samples S6 to S10 (Figure 4.3f), exhibited narrow, high intensity peaks characteristic of α -Fe₂O₃ at high molar ratios, with an ensuing loss in intensity, and by implication extent of crystallinity, with increasing PO₄³⁻ anion concentration. The emergence of a few small peaks characteristic of the β -FeOOH phase was evident in the XRD patterns for Samples S9 and S10. The first stages of the changing shape of the α -Fe₂O₃ NPs were revealed in the TEM investigation of Sample S6, corresponding to an Fe³⁺ : PO₄³⁻ molar ratio of 94.4, with a mixture of ‘pseudocubes’ and rounded and elliptical NPs (Figure 4.3a). Conversely, well defined acicular α -Fe₂O₃ NRs with an aspect ratio of 3.7 were evident within Sample S7, synthesised with a lower molar ratio of 47.2 (Figure 4.3b). Sample S8, synthesised using an Fe³⁺ : PO₄³⁻ molar ratio of 31.5 (Figure 4.3c), comprised partially crystalline, acicular α -Fe₂O₃ NRs exhibiting the highest aspect ratio of 6 for this Sample set. A further decrease in the extent of crystallinity and the acicular α -Fe₂O₃ NR aspect ratio, from 5 to 4, was associated with Samples S9 and S10 synthesised with molar ratios of 31.5 and 23.6, respectively (Figures 4.3d & e).

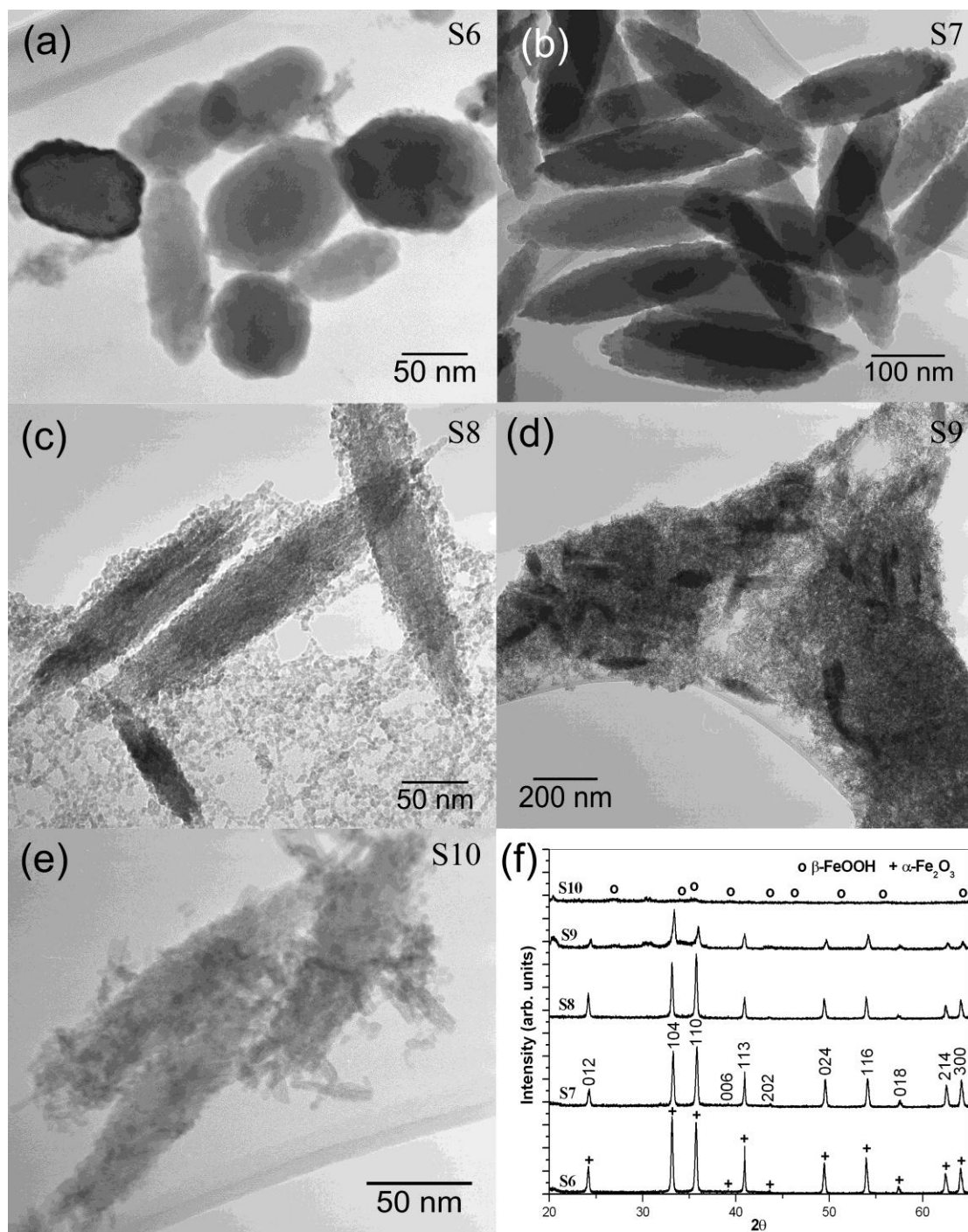


Figure 4.3 BF TEM images of hydrothermal products synthesised at 160°C, for a reaction time of 120 minutes, for increasing additions (1 - 5 mg) of phosphate surfactant, corresponding to Fe³⁺ : PO₄³⁻ molar ratios of (a) 94.4; (b) 47.2; (c) 31.5; (d) 23.6; and (e) 18.9, respectively. (f) Associated XRD patterns corresponding to Samples S6 to S10.

4.2.1.3 Effect of reaction temperature for a fixed surfactant concentration and reaction time

The BF TEM images of Figures 4.4a – f illustrate the effect of increasing HS temperature, from 120 to 240°C (Samples S11 – S16), on the shape of NPs synthesised with an Fe³⁺ : PO₄³⁻ molar ratio of 31.5 and a reaction time of 120 minutes. The associated XRD patterns (Figure 4.4h) again demonstrated a transformation from β -FeOOH to α -Fe₂O₃ with increasing processing temperature. However, it is noted that peaks attributable to α -Fe₂O₃ as identified in Sample S3 (Figure 4.1f), synthesised at 140°C in the absence of a surfactant were not present in the corresponding XRD pattern for Sample S12 (Figure 4.4h), demonstrating that the presence of the surfactant, whilst mediating the NP shape, acts to inhibit the formation and lower the relative abundance of α -Fe₂O₃, for a given processing temperature.

The BF TEM image of Figure 4.4a, corresponding to Sample S11 grown at 120°C, confirmed the presence of β -FeOOH NPs and NRs, similar to those identified in Sample S1 (Figure 4.1a) synthesised at 100°C, but smaller in size and without any of the rhombohedral α -Fe₂O₃ NPs, as identified in Sample S2 grown at 120°C (Figure 4.1b). Partially formed acicular α -Fe₂O₃ NRs and larger crystalline NRs were observed in Samples S12 and S13 (Figures 4.4b & c), synthesised at 140 and 180°C, respectively, whilst Sample S14 (Figure 4.4d) synthesised at 200°C showed the formation of fully crystalline acicular α -Fe₂O₃ NRs, exhibiting an aspect ratio of ~ 7, the highest for all the Samples investigated. Further, Samples S15 and S16 (Figures 4.4e & f) synthesised at 220 and 240°C, respectively, exhibited ellipsoidal and rectangular α -Fe₂O₃ NRs with aspect ratios on the scale of ~ 3.5.

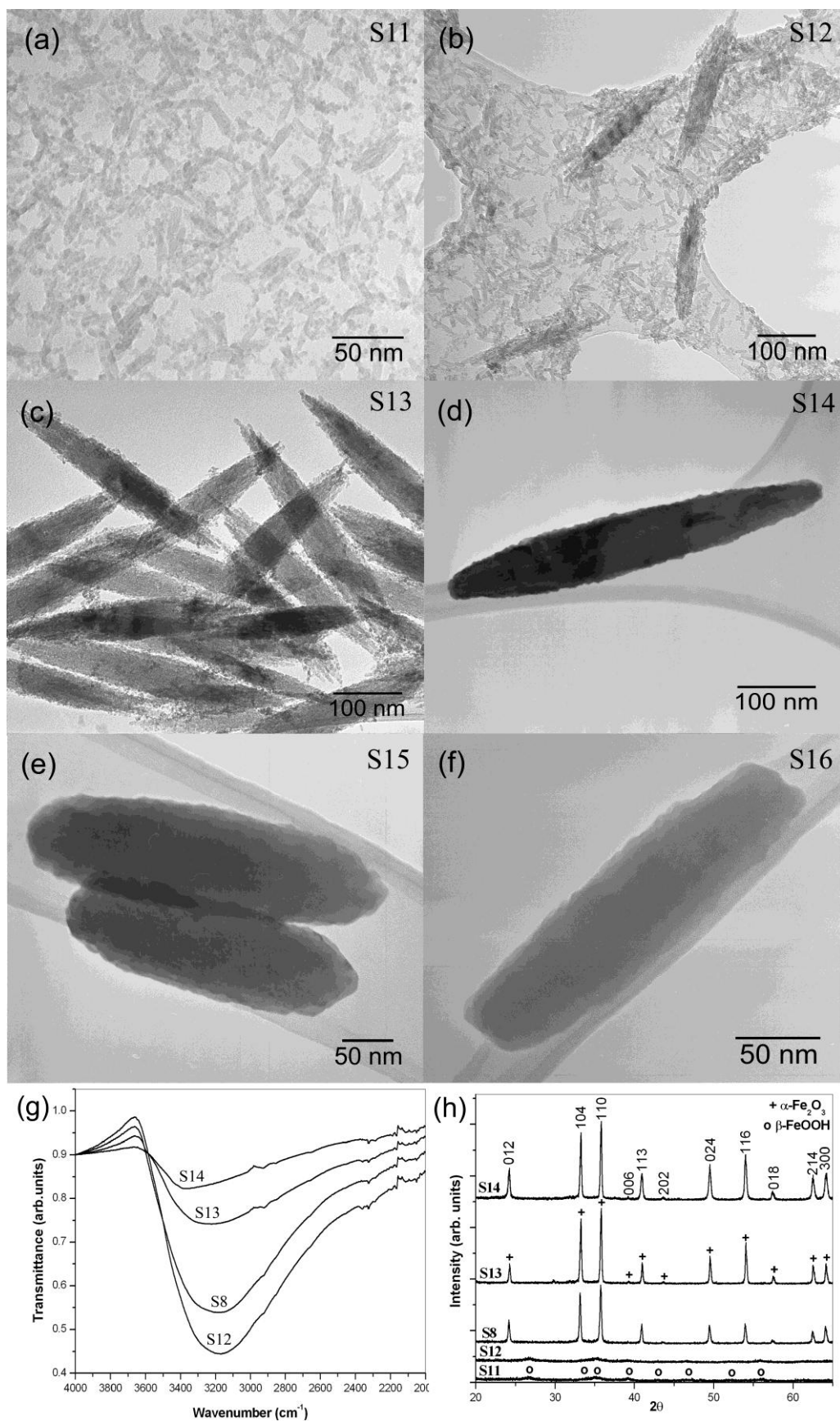


Figure 4.4 BF TEM images of the hydrothermal products synthesised for a reaction time of 120 minutes with a constant Fe³⁺ : PO₄³⁻ molar ratio of 31.5. (a) 120°C, (b) 140°C, (c) 180°C, (d) 200°C, (e) 220°C and (f) 240°C. (g) Associated FTIR spectra of the HS products (Samples S12, S8, S13 & S14) as a function of increasing processing temperature. (h) Associated XRD patterns (Samples S11, S12, S8, S13 & S14) charting the transition from β -FeOOH to α -Fe₂O₃ with increasing processing temperature.

4.2.1.4 Effect of reaction time

The BF TEM images of Figures 4.5a, c & e illustrate the effect of increasing reaction times of 30, 60 and 90 minutes, respectively, on the progressive growth of α -Fe₂O₃ NRs at a constant Fe³⁺ : PO₄³⁻ molar ratio of 31.5 and HS processing temperature of 200°C (Samples S17 – S19). Figure 4.5a, corresponding to Sample S17 grown for 30 minutes, confirmed the presence of β -FeOOH NPs and NRs, similar to those identified in Sample S11 (Figure 4.4a) after 120 minutes of synthesis at 120°C. A similar distribution of β -FeOOH NPs and NRs was found for Sample S18, synthesised for 60 minutes at 200°C, along with some partially crystallised acicular α -Fe₂O₃ NRs (Figure 4.5c). A higher proportion of partially formed acicular α -Fe₂O₃ NRs were observed within Sample S19 after 90 minutes of synthesis with some β -FeOOH NRs (Figure 4.5e), whilst the presence of fully formed α -Fe₂O₃ acicular NRs confirmed the reaction to be complete after 120 minutes of processing at 200°C (Sample S14, Figure 4.4d).

The EDX spectrum of Figure 4.5b (Sample S17), recorded using a spot size on the scale of an individual NR, indicated the presence of both phosphorus and chlorine, in addition to the expected signals for iron and oxygen (and a Cu artefact signal arising from the specimen support grid). In this case the specimen was not cleaned in acetone prior to chemical analysis.

The associated XRD patterns of Figure 4.5f again demonstrated a transformation from β -FeOOH to α -Fe₂O₃ with increasing HS processing time. Similar to the XRD pattern of Figure 4.1f, some additional diffraction peaks were present ($\sim 28^\circ$ to 31° , arrowed, Figure 4.5f) in the XRD patterns for Samples S17 and S18. Additional features were also discerned within some associated SAED patterns (*e.g.* Figure 4.5d, arrowed (Sample S18)), which were not attributable to either the β -FeOOH or α -Fe₂O₃ phase. These features were attributed to incomplete precipitation and the presence of some iron chloride hydrate or possibly preliminary formed FeOCl.¹⁰⁹

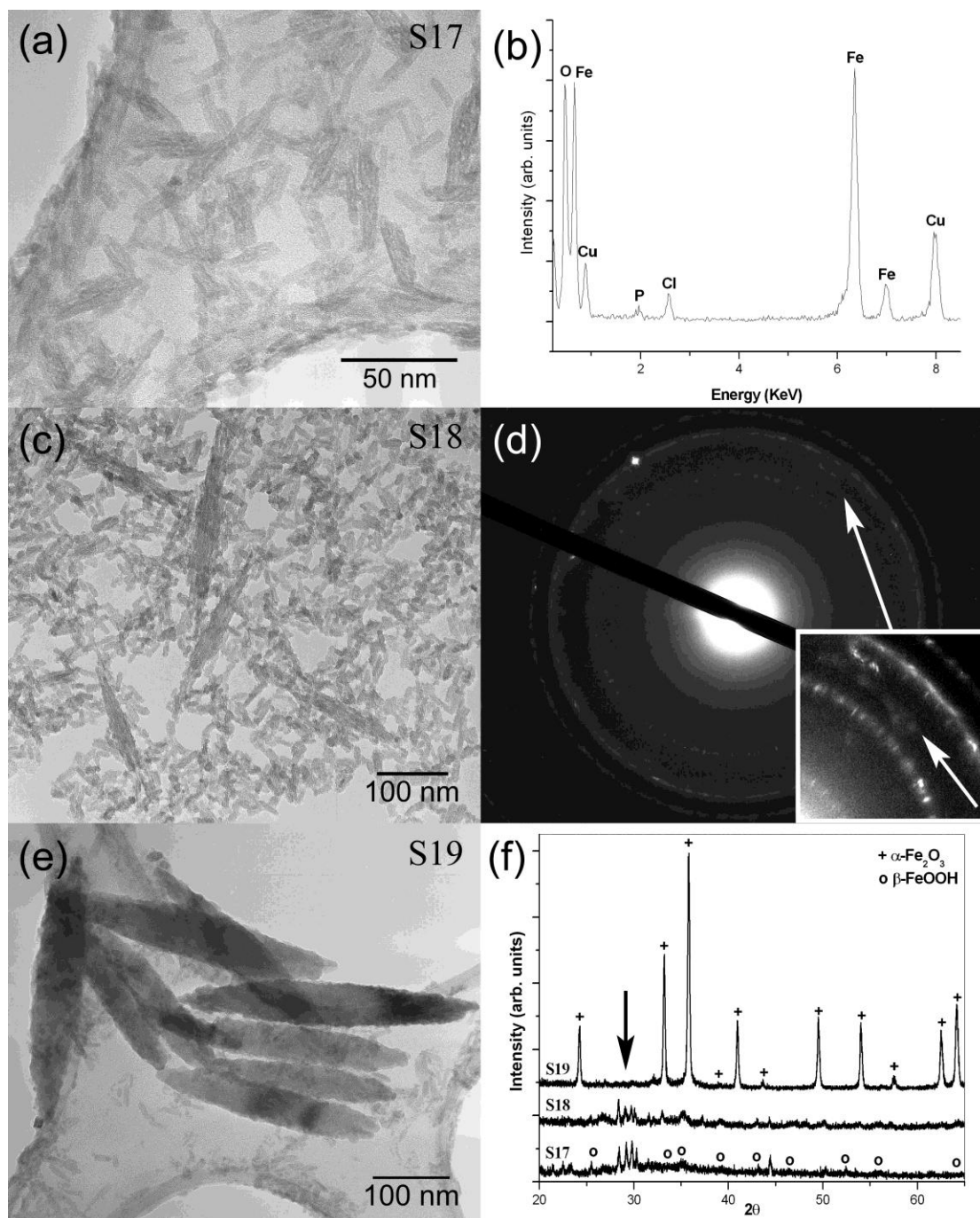


Figure 4.5 BF TEM images of the hydrothermal products synthesised at 200°C with a constant $\text{Fe}^{3+}:\text{PO}_4^{3-}$ molar ratio of 31.5 for reaction times of (a) 30 min, (c) 60 min and (e) 90 min. (b) Associated EDX spectrum acquired from Sample S17 shown in (a). (d) SAED from Sample S18 shown in (c) with magnified section inset showing additional diffraction features. (f) Associated XRD patterns from Samples S17 – S19, charting the transition from β -FeOOH to α -Fe₂O₃ with increasing processing time. The additional features (arrowed) are attributed to some iron chloride hydrate or preliminary formed FeOCl.

4.2.1.5 NR crystallographic orientation and chemical analysis

SAED used in conjunction with diffraction contrast TEM allowed the crystallographic and morphological relationship of individual α -Fe₂O₃ NRs (*e.g.* Sample S14) to be examined in detail. In all cases, the major axis of the well-defined, single crystal

structure NRs was found to be parallel to the $\langle 006 \rangle$ direction (Figure 4.6a), *i.e.* the NR major axis corresponded to the *c*-axis of the α -Fe₂O₃ unit cell, as illustrated by the computer model of the α -Fe₂O₃ crystal structure with simulated diffraction pattern inset (Figure 4.6b). Complementary EDX investigation of such individual NRs (Sample S14) indicated the presence of iron, oxygen and a small amount of phosphorus (*e.g.* Figure 4.6c), considered to be residual within the bulk of the α -Fe₂O₃ NR from the phosphate surfactant. In this instance, the specimen was cleaned in acetone prior to chemical analysis.

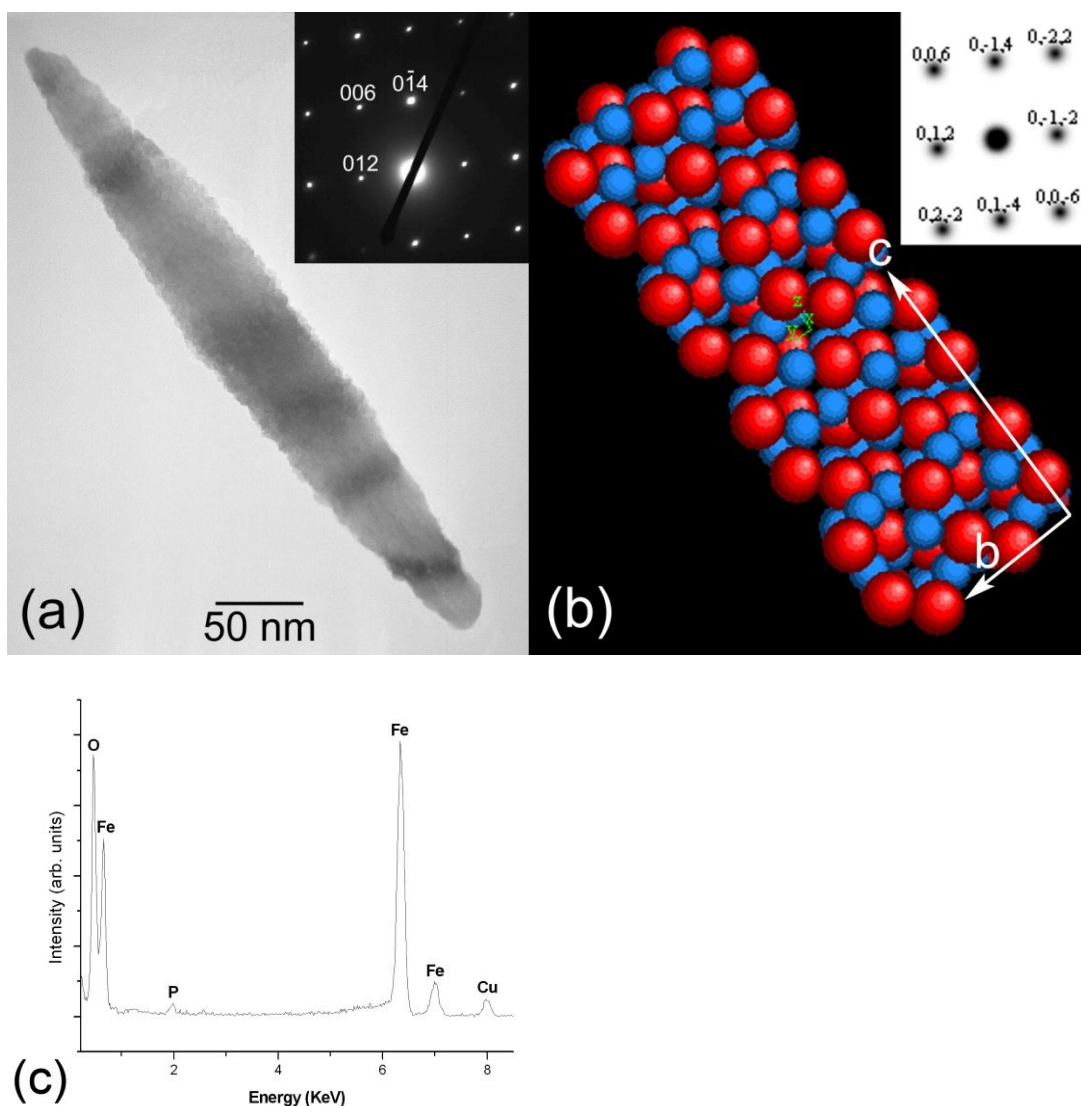


Figure 4.6 (a) BF TEM image and SAED pattern of an individual α -Fe₂O₃ NR (Sample S14) showing the NR major axis to be parallel to the $\langle 006 \rangle$ direction. (b) *CaRine* model of the α -Fe₂O₃ crystal structure (with simulated diffraction pattern inset), showing the NR major axis to be parallel to the *c*-axis of the α -Fe₂O₃ unit cell. (c) Associated EDX spectrum, demonstrating the presence of a small amount of phosphorus within such α -Fe₂O₃ NRs.

Complementary XPS survey scans providing details on the near surface chemistries of Samples S11 and S14, corresponding to pure β -FeOOH and α -Fe₂O₃ are presented in Figures 4.7a & b, synthesised with an Fe³⁺ : PO₄³⁻ molar ratio of 31.5 and a reaction time of 120 minutes, at temperatures of 120°C and 200°C, respectively. The Fe and O binding energy peaks are consistent with the presence of β -FeOOH and α -Fe₂O₃ NPs, but the spectra appear to be nearly identical, consistent with a lack of immediate discrimination between iron oxide and iron hydroxide using this technique. A slight ‘shake-up’ peak is present in the high resolution Fe 2p scan of α -Fe₂O₃ (Figure 4.7d) in comparison to β -FeOOH (Figure 4.7c) but is not considered definitive for phase identification. The presence of Cl 2s and 2p peaks (arrowed) are indicative of some residual surface FeCl₃, with slightly stronger Cl peaks being associated with β -FeOOH, as Cl is known to occupy channels within the β -FeOOH crystal structure.¹⁰⁹ It is noted that peaks characteristic to phosphorus are absent from both spectra, consistent with the suggestion that P does indeed become partitioned within the nanostructure, as indicated by EDX, rather than being residual on the surface.

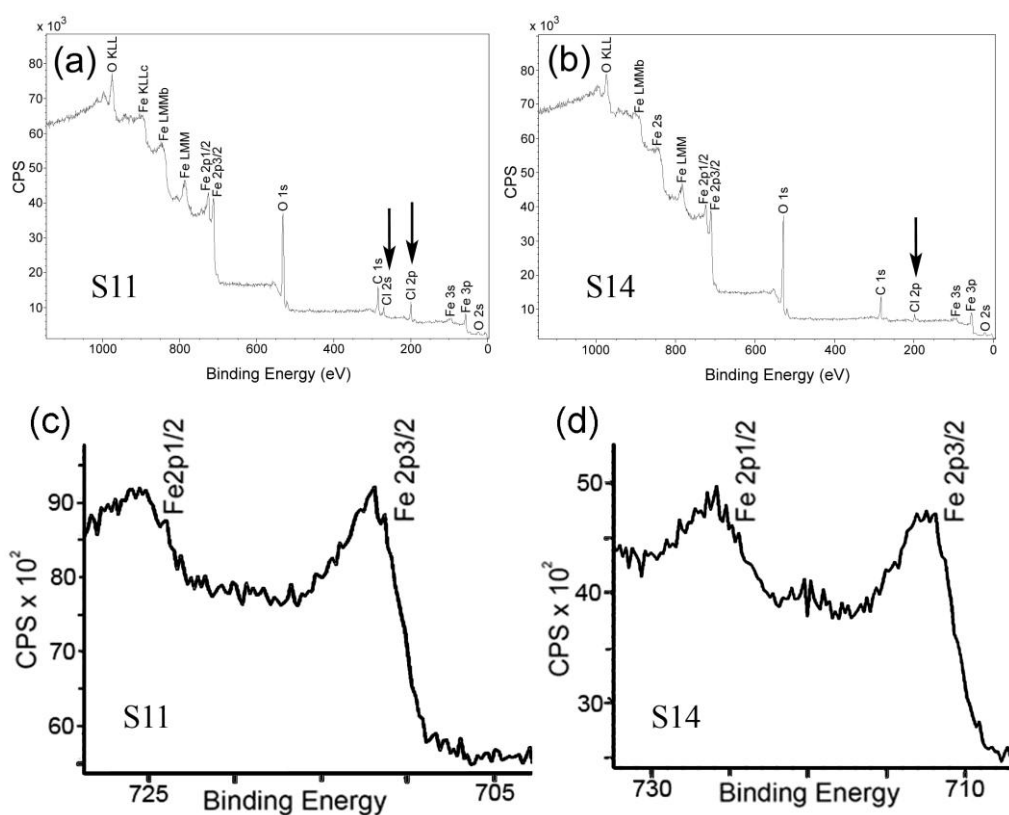


Figure 4.7 XPS survey spectra of the hydrothermal products synthesised with an Fe³⁺:PO₄³⁻ molar ratio of 31.5 for a reaction time of 120 minutes at (a) 120°C (β -FeOOH) and (b) 200°C (α -Fe₂O₃), respectively; both with high resolution spectra of Fe 2p peaks ((c) & (d), respectively).

4.2.1.6 Reaction product summary and process map

The complete HS process can be classified in three stages following the reactions introduced previously in Section 2.5.1, describing the generalised precipitation and dissolution of β -FeOOH and the subsequent precipitation of α -Fe₂O₃

Table 4.1 summarised the reaction products, morphologies, dimensions and aspect ratios of the α -Fe₂O₃ NPs as a function of the processing conditions investigated. The schematic diagram of Figure 4.8 constitutes a ‘process map,’ illustrating the development of the shape and phases of the HS reaction products as a function of temperature, time and surfactant concentration.

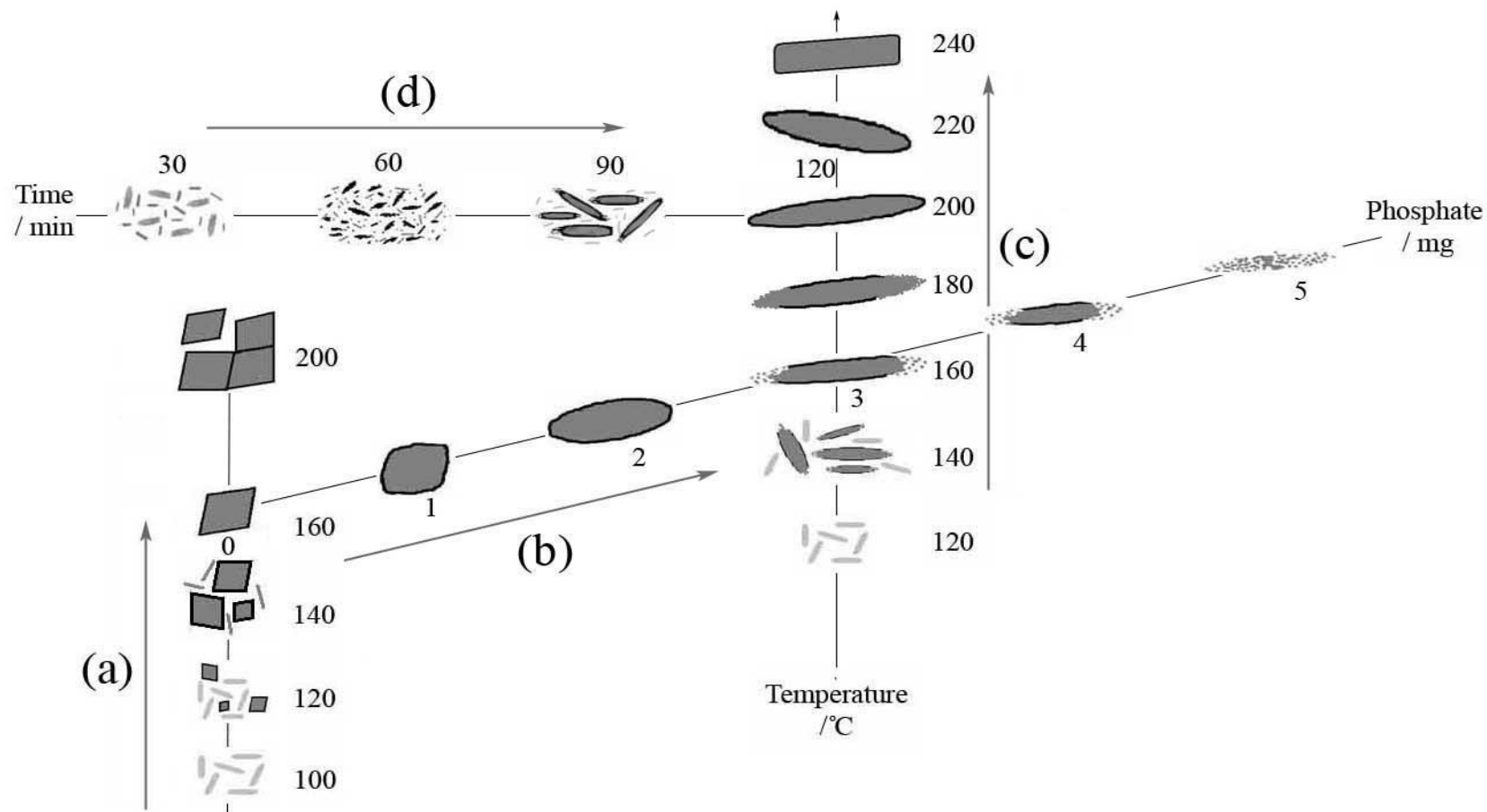


Figure 4.8 ‘Process map’ illustrating the development of the shape and phases of the hydrothermal products synthesised using 0.2 ml of 45% pure FeCl₃ in 40 ml water, as a function of temperature, time and phosphate concentration. The main trends shown are: (a) β -FeOOH precipitation and dissolution and subsequent α -Fe₂O₃ precipitation with increasing HS temperature, in the absence of a surfactant; (b) α -Fe₂O₃ shape change with increasing PO₄³⁻ concentration at an HS processing temperature of 160°C; (c) β -FeOOH precipitation and dissolution and subsequent α -Fe₂O₃ NR growth and shape change with increasing HS temperature at an Fe³⁺ : PO₄³⁻ molar ratio of 31.5 (3 mg NH₄H₂PO₄); and (d) β -FeOOH precipitation and dissolution and subsequent α -Fe₂O₃ NR precipitation and growth with increasing reaction time at an HS processing temperature of 200°C and an Fe³⁺ : PO₄³⁻ molar ratio of 31.5 (3 mg NH₄H₂PO₄).

4.2.2 Discussion

4.2.2.1 Process map

Figure 4.8 provides a generalised summary of the HS reaction products as a function of temperature, time and PO₄³⁻ anion concentration. The precipitation of β -FeOOH NRs from the FeCl₃ salt solution occurred after 120 minutes of synthesis at 100°C in the absence of a surfactant. Increasing the processing temperature promoted the dissolution of β -FeOOH and the nucleation and growth of equiaxed α -Fe₂O₃ NPs with rhombohedral morphology (Figure 4.8, axis (a)). The increasing addition of PO₄³⁻ anions at 160°C resulted in a shape change of the α -Fe₂O₃ NPs into acicular α -Fe₂O₃ NRs with increasing aspect ratio, but then with progressive inhibition of α -Fe₂O₃ phase formation (Figure 4.8, axis (b)). Increasing the synthesis temperature in the presence of 3 mg of NH₄H₂PO₄ was associated with the nucleation and growth of well defined single crystal, acicular NRs, with optimum size and aspect ratio at 200°C (Figure 4.8, axis (c)). Increasing the time of synthesis at 200°C in the presence of 3 mg NH₄H₂PO₄ was associated with the progressive formation and dissolution of β -FeOOH and the growth of well-defined acicular α -Fe₂O₃ NRs with optimum aspect ratio after 120 minutes (Figure 4.8, axis (d)). EDX chemical analysis indicated the presence of P within the bulk of the α -Fe₂O₃ NRs, whilst XPS suggested an absence of P at the developed α -Fe₂O₃ NR surfaces. Signatures due to Cl were tentatively attributed to residual iron chloride hydrate or FeOCl within the dispersed reaction product, but it is considered that Cl was not incorporated within the bulk of the α -Fe₂O₃ NRs.

4.2.2.2 Morphology and phase analysis

It is considered that the development of α -Fe₂O₃ NPs (Figure 4.8, axis (a)) is in accordance with the process of β -FeOOH phase precipitation, dissolution and subsequent α -Fe₂O₃ phase formation. The growth of α -Fe₂O₃ proceeds until the abundance of β -FeOOH is exhausted. Well-defined, rhombohedral α -Fe₂O₃ NPs with clear sharp facets were formed after 120 minutes of synthesis at 160°C. Rodriguez *et al*¹⁵⁹ showed how such dissimilarly oriented rhombohedral NPs can appear hexagonal in projection in TEM.¹⁵⁹ Increasing the HS processing temperature to 200°C led to agglomeration and the fusing together of these α -Fe₂O₃ NPs, consistent with the high surface energies associated with uncoated crystal surfaces formed in the absence of surfactant.

Synthesis at 160°C in the presence of increasing PO₄³⁻ concentration was associated with a significant variation in α -Fe₂O₃ shape and crystallinity (Figure 4.8, axis (b)). An Fe³⁺ : PO₄³⁻ molar ratio of 94.4 resulted in the production of α -Fe₂O₃ NPs with rounded, rough edges, whilst more ellipsoidal shaped α -Fe₂O₃ NPs were formed upon decreasing the Fe³⁺ : PO₄³⁻ molar ratio to 47.1. The largest aspect ratio of 6, corresponding to partially formed acicular α -Fe₂O₃ NRs, was achieved with an Fe³⁺ : PO₄³⁻ molar ratio of 31.5. Further decrease in the molar ratio to 23.6 and 18.9 was associated with the production of ill-defined α -Fe₂O₃ NRs with reduced aspect ratio and further reduced levels of crystallinity. Conversely, increasing the HS processing temperature allowed for the recovery of α -Fe₂O₃ NR crystallinity (Figure 4.8, axis (c)). At a constant Fe³⁺ : PO₄³⁻ molar ratio of 31.5 and an initial HS processing temperature of 120°C, small β -FeOOH NR and NPs were formed. Partial α -Fe₂O₃ NRs were identified at 140°C and these grew, at the expense of β -FeOOH, as the synthesis temperature increased. Indeed, FTIR investigation (Figure 4.4g) reinforced the view that increasing HS temperature acts to drive the dissolution of β -FeOOH and the subsequent precipitation of α -Fe₂O₃. As β -FeOOH dissolution occurs, OH bonds are broken and absorbed water is released, resulting in a steady increase in IR transmittance with increasing HS temperature and α -Fe₂O₃ precipitation. Well-defined crystalline α -Fe₂O₃ NRs with a maximum aspect ratio of 7 were synthesised at 200°C. Synthesis at even higher temperatures of 220°C and 240°C was associated with a truncation of the α -Fe₂O₃ NRs, with a reduction in length and becoming more ellipsoidal and rectangular in shape, suggesting a small degree of α -Fe₂O₃ NR dissolution at the tips at the higher temperatures.

A similar process of β -FeOOH precipitation, dissolution and α -Fe₂O₃ NR precipitation was demonstrated with increasing time of synthesis, at the elevated temperature of 200°C and a constant Fe³⁺ : PO₄³⁻ molar ratio of 31.5 (Figure 4.8, axis (d)). β -FeOOH NPs, partially formed α -Fe₂O₃ NRs and larger α -Fe₂O₃ NRs (with a few β -FeOOH NPs) developed after 30, 60 and 90 minutes of synthesis, respectively, again leading to the optimised case of well-defined crystalline α -Fe₂O₃ NRs after 120 minutes of synthesis. It is apparent that α -Fe₂O₃ NR growth in the presence of a surfactant proceeds through the nucleation, agglomeration and recrystallisation of smaller α -Fe₂O₃ NPs (Figure 4.3c), and will be discussed in detail in Chapter 5.

4.2.2.3 Effect of phosphate surfactant

It is considered that the surfactant is preferentially adsorbed on the faces parallel to the c-axis of α -Fe₂O₃, in view of the better matching of the O-O inter-atomic distance of PO₄³⁻ anions (2.50Å) with the Fe-Fe spacing parallel rather than perpendicular to this axis, thereby promoting the development of acicular shaped NRs.¹⁴² This will be discussed in more detail in Chapter 5. XRD investigations support this description, noting that the peak intensity from the {104} planes in the absence of PO₄³⁻ anions becomes slowly surpassed by the peak intensity of the {110} planes (nearly parallel to the c-axis) with increasing PO₄³⁻ anion addition, and then back again, as the aspect ratio of the acicular NRs increases and then decreases (Figure 4.3f).

Accordingly, it is recognised that surfactant PO₄³⁻ ions are critical in mediating the shape and crystallinity of α -Fe₂O₃ NRs. It is noted that the β -FeOOH NRs formed initially in the presence of PO₄³⁻ ions at 120°C (Sample S11) were smaller than those formed in the absence of the surfactant at the same temperature (Sample S2), as evidenced by direct TEM observations, supported by the broader, lower intensity peaks of the associated XRD patterns. Comparison of these two Samples also demonstrated that the presence of PO₄³⁻ ions was associated with a delayed onset of formation of α -Fe₂O₃ NRs with increasing synthesis temperature. In this context, it is noted that the pH of ~ 1.2 - 1.4 of the HS product solution was much lower than the PZC of solid β -FeOOH (pH ~ 8).¹⁶⁰ Hence, it is considered that strong electrostatic attraction, resulting in high PO₄³⁻ anion adsorption,¹⁶¹ acts to inhibit the size of the initial β -FeOOH NRs, whilst then stabilising the β -FeOOH NRs and decreasing their solubility at higher synthesis temperatures, particularly in a phosphate-rich environment, with consequent inhibition of subsequent α -Fe₂O₃ formation.

It is noted that Sugimoto and Muramatsu¹⁶² suggest that more phosphate anions can become incorporated into the tunnel-like structures of β -FeOOH during growth than are adsorbed onto the surface. This view is supported by EDX analysis which indicated that P was present within the bulk of the initially formed β -FeOOH NRs and the subsequently developed α -Fe₂O₃ NRs, whilst complementary XPS analysis indicated that P was absent from the developed NR surfaces.

4.2.2.4 Growth mechanism

The development of equiaxed α -Fe₂O₃ NPs with clear, sharp facets in a surfactant-free environment at 160°C suggests the direct deposition of Fe³⁺ species on to the NP surfaces. In the presence of a phosphate, it is considered that the incorporation of phosphate into the bulk of the initially formed β -FeOOH NRs would lead to a gradual liberation of PO₄³⁻ anions back into solution during subsequent β -FeOOH dissolution; in which case, a lower proportion of surfactant PO₄³⁻ anions would be available to promote the initial development of anisotropic α -Fe₂O₃ NRs, consistent with a near equiaxed shape for the case of synthesis under conditions of low surfactant concentration, developing gradually into a more acicular α -Fe₂O₃ NR shape with increasing surfactant concentration. In view of the observation that NR growth proceeds through the nucleation, agglomeration and recrystallisation of smaller α -Fe₂O₃ NPs (described in detail in Chapter 5), the stabilisation of these α -Fe₂O₃ NPs by the PO₄³⁻ surfactant would act to hinder their coalescence, explaining the increasingly rougher edges and partial crystallinity associated with α -Fe₂O₃ NRs developed under increasingly phosphate-rich conditions. Indeed, phosphate adsorbed to the small α -Fe₂O₃ NPs would become trapped within the bulk of the α -Fe₂O₃ NRs during crystallisation. This helps to explain why α -Fe₂O₃ NR formation becomes completely inhibited in the presence of even higher phosphate concentrations, and why it becomes necessary to increase the temperature of synthesis in order to recover the crystallinity of the α -Fe₂O₃ NRs. The development of the anisotropic α -Fe₂O₃ NRs is still evident at the higher HS temperatures of 220°C and 240°C, albeit with truncated shape. The growth mechanism of the high aspect ratio α -Fe₂O₃ NRs will be discussed in more detail in Chapter 5.

4.3 Effect of FeCl₃ precursor concentration on α -Fe₂O₃ NR growth for fixed Fe³⁺ : PO₄³⁻ molar ratio

FeCl₃ and NH₄H₂PO₄ have been identified as simple precursors for the hydrothermal growth of α -Fe₂O₃ NRs. The effect of FeCl₃ concentration on α -Fe₂O₃ NR growth and size is now explored now. As shown in section 4.2, the highest aspect ratio α -Fe₂O₃ NR of ~ 6.7 (Sample S14) was achieved with 0.2 ml FeCl₃ solution, further diluted in 40 ml water, 3mg NH₄H₂PO₄ (Fe³⁺ : PO₄³⁻ molar ratio of 31.5) and heated in the standard 125 ml Teflon-lined stainless steel pressure autoclave at 200°C for 2 hours. Here, the amounts of FeCl₃ and NH₄H₂PO₄ were altered proportionally to produce 75 %, 50 % and 25 % of the original concentration in 40 ml water, whilst keeping the Fe³⁺ : PO₄³⁻ molar ratio constant, as summarised in Table 4.2.

Sample	FeCl₃ / ml	NH₄H₂PO₄ / mg	% of Sample S14
S14	0.2	3	100
S20	0.15	2.25	75
S21	0.1	1.5	50
S22	0.05	0.75	25

Table 4.2 Quantity of FeCl₃ and NH₄H₂PO₄ hydrothermal precursors.

4.3.1 Results and discussion

The BF TEM images of Figure 4.9 demonstrate the change in α -Fe₂O₃ morphology with decreasing FeCl₃ precursor concentration. Sample S20 (Figure 4.9a) revealed large α -Fe₂O₃ NRs (~ 350 nm long, ~ 70 nm wide) as the primary morphology. A decrease in precursor concentration in Sample S21 resulted in the formation of some larger α -Fe₂O₃ NRs (~ 300 nm long, ~ 60 nm wide) and NPs (< 90 long, < 50 nm wide), as shown in Figure 4.9b. Sample S22 comprised α -Fe₂O₃ NPs < 70 nm in diameter (Figure 4.9c).

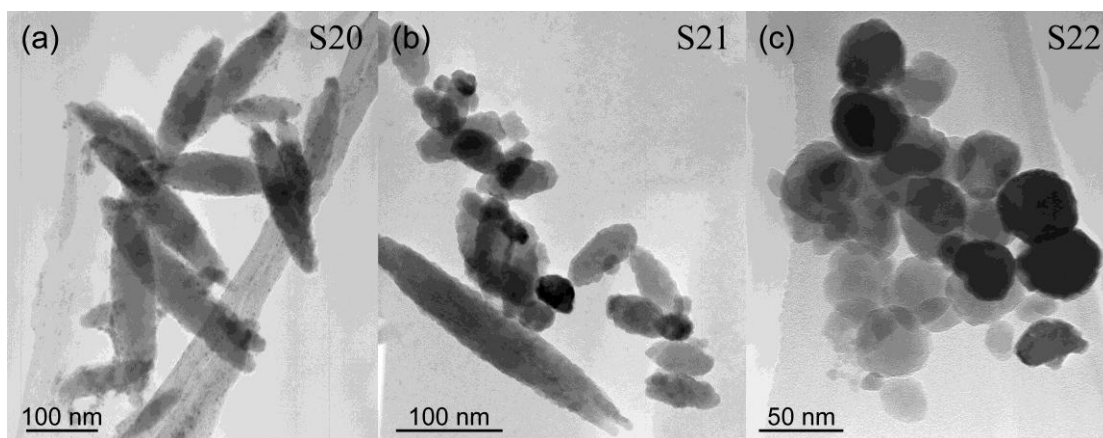


Figure 4.9 BF TEM images of hydrothermal products heated at 200°C for 2 hours with c) 0.15 ml FeCl₃ and 2.25 mg NH₄H₂PO₄; (b) 0.1 ml FeCl₃ and 1.5 mg NH₄H₂PO₄; and (a) 0.05 ml FeCl₃ and 0.75 mg NH₄H₂PO₄. (All corresponding to an Fe³⁺ : PO₄³⁻ molar ratio of 31.5)

It is evident that changing the FeCl₃ and NH₄H₂PO₄ precursor concentrations, whilst keeping the Fe³⁺ : PO₄³⁻ molar ratio constant, had a significant effect on the size and morphology of the associated α -Fe₂O₃ nanostructures. The decrease in precursor concentration resulted in a trend of forming primarily large α -Fe₂O₃ NRs (Sample S20), α -Fe₂O₃ NPs exhibiting a larger aspect ratio of ~ 2 amongst large α -Fe₂O₃ NRs (Samples S21) and α -Fe₂O₃ NPs (Sample S22). Hence, it is evident that the α -Fe₂O₃ particle size is dependent on precursor concentration, decreasing in both size and aspect ratio when lowering the FeCl₃ and NH₄H₂PO₄ concentration. Whilst the main objective was to investigate the effect of FeCl₃ concentration on particle size, the intention was for the α -Fe₂O₃ NRs to maintain their anisotropic morphology. Consequently, focus will be given to the original precursor concentration (0.2 ml FeCl₃ solution and 3mg NH₄H₂PO₄ further diluted in 40 ml water), resulting in the high aspect ratio α -Fe₂O₃ NRs, for the remainder of this Chapter.

4.4 Effect of pH on α -Fe₂O₃ NR growth

FeCl₃ solution is as an acidic salt solution with a low pH. Further, the synthesis equations in Section 2.5.1 show that HCl, a strong acid, is formed during the breakdown of the FeCl₃ precursor. For this reason, the precursor and α -Fe₂O₃ reaction product solutions generally exhibit low pH values of ≤ 2 . However, it is considered that the pH value of the hydrothermal solution affects the absorption of phosphate surfactant on to α -Fe₂O₃ surface. Accordingly, the pH value of the hydrothermal precursor solution is varied now, to investigate the subsequent effect on α -Fe₂O₃ morphology. Again, starting with the highest aspect ratio α -Fe₂O₃ NRs (Sample S14 with initial pH of ~ 2) was achieved with 0.2 ml FeCl₃ solution, further diluted in 40 ml water, 3mg NH₄H₂PO₄ (Fe³⁺ : PO₄³⁻ molar ratio of 31.5) and heated in the standard 125ml Teflon-lined stainless steel pressure autoclave at 200°C for 2 hours. Here, the pH value of the precursor solution was altered (prior to heating), to 2.5, 3.5 and 4 with NaOH solution, added drop-wise into the Teflon liner, whilst using a pH meter to measure the associated pH value, as summarised in Table 4.3.

Sample	pH
S14	2
S23	2.5
S24	3.5
S25	4

Table 4.3 pH values of precursor solutions.

4.4.1 Results and discussion

The BF TEM images of Figure 4.10 demonstrate the effect of precursor solution pH on the α -Fe₂O₃ morphology. Sample S23 consists of α -Fe₂O₃ NRs (< 270 nm long, < 60 nm wide) (Figure 4.10a). A slight increase in pH value for Sample S24 resulted in α -Fe₂O₃ NRs (< 150 nm long, < 70 nm wide) with a noticeable decrease in aspect ratio (Figure 4.10b). Sample S25 comprised α -Fe₂O₃ NPs, < 90 nm in diameter (Figure 4.10c).

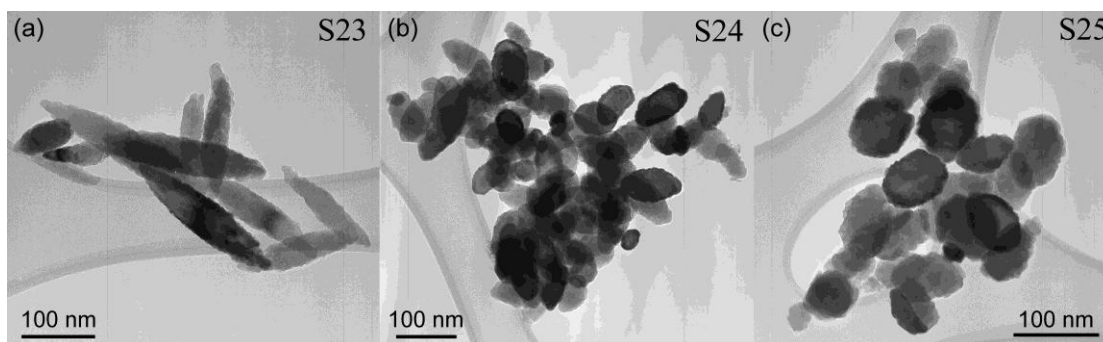


Figure 4.10 BF TEM images of hydrothermal products heated at 200°C for 2 hours with precursor solution of 0.2 ml FeCl₃ solution, further diluted in 40 ml water, 3mg NH₄H₂PO₄ with pH values, altered using NaOH, of (a) 2.5; (b) 3.5; and (c) 4.

It is evident that a small increase in pH has a marked effect on the resultant α -Fe₂O₃ morphology. A decrease in aspect ratio from ~ 4.5 to ~ 1 was observed for the α -Fe₂O₃ nanostructures present in Samples S23 and S25, respectively. The pH of the reaction product solution (~ 1) in Sample S23 was much lower than the PZC of solid α -Fe₂O₃ (pH ~ 8.5).^{163,164} Hence, it is considered that strong electrostatic attraction, which would result in high PO₄³⁻ anion adsorption, promotes the anisotropic α -Fe₂O₃ NR growth. However, an increase in precursor solution pH (Sample S25) is associated with a significant reduction in the α -Fe₂O₃ aspect ratio. Hence, it is suggested that a change in phosphate adsorption on the α -Fe₂O₃ surface takes place within this pH regime, and this will be addressed further in Chapter 5.

4.5 Effect of stage of phosphate addition

Phosphate anions have been shown to influence the growth of 1D α -Fe₂O₃ NRs, even at relatively low concentrations. However, little has been reported on the effect of phosphate on the initial development of β -FeOOH, in the context of the anisotropic growth of α -Fe₂O₃ nanostructures. The growth of β -FeOOH and α -Fe₂O₃ nanostructures is described now, with the phosphate surfactant added at different stages of the HS process, to appraise its effect on the morphology and growth of the reaction products. The reactant solution (0.2 ml FeCl₃ solution further diluted in 40 ml water) was mixed with and without 3 mg of NH₄H₂PO₄ surfactant (Samples S26 and S27, respectively), mechanically stirred in the standard 125 ml Teflon-lined stainless steel pressure autoclave, and then sealed and inserted into a temperature controlled furnace at a reaction temperature of 110°C for 2 hours. The experiment was repeated and after cooling, Sample S26 was reinserted into the furnace again at 200°C for 2 hours (Sample S26*), whilst 3 mg of NH₄H₂PO₄ was added to Sample S27 before resealing and reinsertion into the furnace at 200°C for 2 hours (Sample S27*). The processing conditions are summarised in Table 4.4.

Initial HS				Secondary HS		
Sample	FeCl ₃ / ml	NH ₄ H ₂ PO ₄ / mg	Temperature / °C	Sample	NH ₄ H ₂ PO ₄ / mg	Temperature / °C
S26	0.2	3	110	S26*	0	200
S27	0.2	0	110	S27*	3	200

Table 4.4 HS processing conditions demonstrating discrete stages of NH₄H₂PO₄ addition.

4.5.1 Results and discussion

Figure 4.11 presents a BF TEM image (with associated SAED pattern inset) and an associated XRD pattern from Sample S26*. The XRD pattern (Figure 4.11b) confirmed that the Sample comprised solely the α -Fe₂O₃ phase. TEM investigation confirmed the development of acicular α -Fe₂O₃ NRs, ~ 75 nm wide and ~ 450 nm in length, in this instance (Figure 4.11a). In all cases, the major axis of these well-defined, single crystalline NRs was found to be perpendicular to the {006} set of crystal planes (Figure 4.11a), consistent with section 4.2.1.5.

BF TEM images of Samples S26, S27 and S27* are presented in Figures 4.12a, b & c, respectively. The associated XRD patterns of Figure 4.12d confirmed all these samples to comprise β -FeOOH. Application of the Scherrer equation using the (310) diffraction peak suggested average grain size to be ~ 15 nm (S26), 19 nm (S27) and 24 nm (S27*), respectively, alluding to an increase in particle size. However, the Scherrer equation does not take into consideration particle morphology.

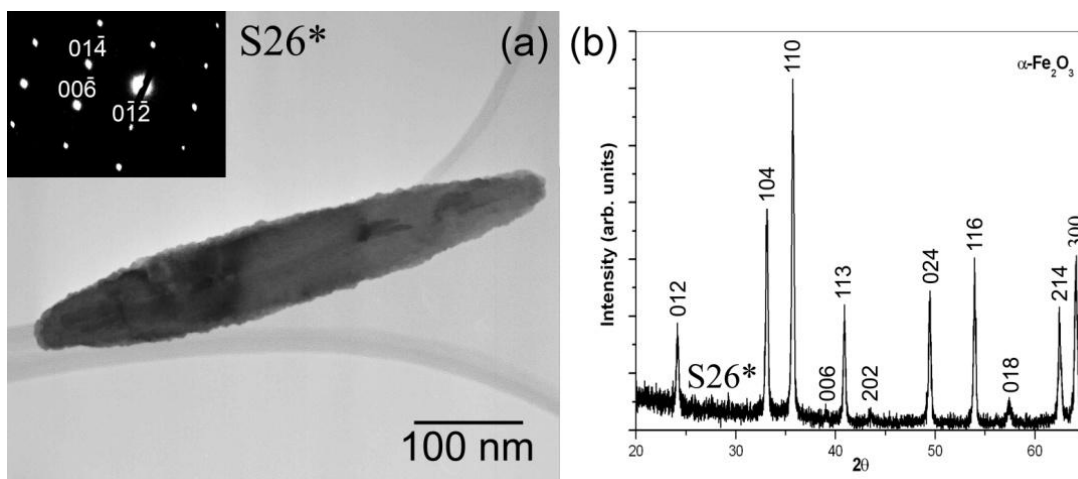


Figure 4.11 (a) BF TEM image (with SAED pattern inset) of an individual α -Fe₂O₃ NR (Sample S26*). (b) Associated XRD pattern from Sample S26*, confirming the presence of the α -Fe₂O₃ phase.

TEM investigation of Sample S26 confirmed this suspension to be a mixture of small and round, as well as larger rod-like, β -FeOOH NPs, up to ~ 15 nm wide and ~ 45 nm in length (Figure 4.12a). Conversely, Sample S27 (Figure 4.12b) exhibited only the β -FeOOH NRs (~ 20 nm wide and ~ 60 nm in length). Sample S27* displayed larger, well-crystallised β -FeOOH NRs, up to ~ 40 nm wide and ~ 120 nm in length (Figure 4.12c).

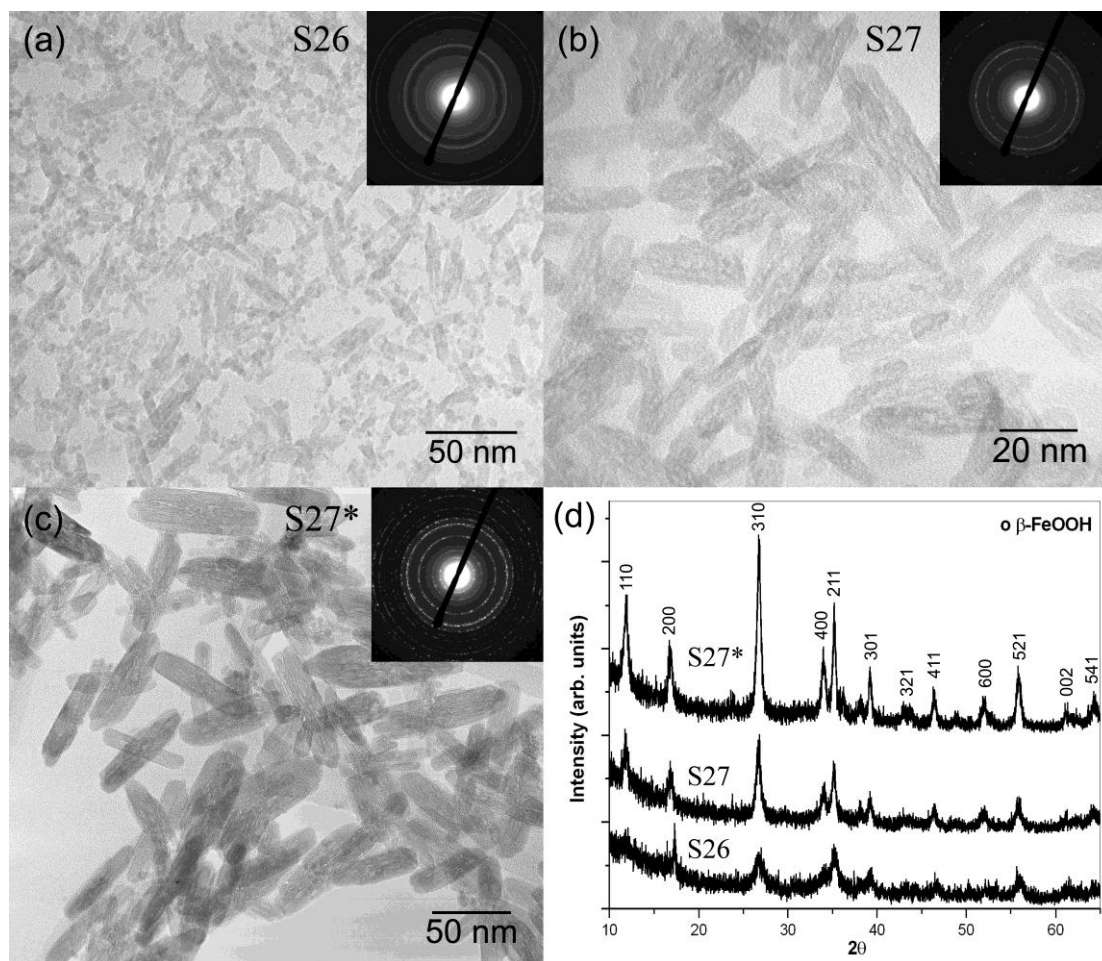


Figure 4.12 BF TEM images (with associated SAED patterns inset) of the hydrothermal products synthesised with (a) 3 mg $\text{NH}_4\text{H}_2\text{PO}_4$ and heated at 110°C (Sample S26); (b) no $\text{NH}_4\text{H}_2\text{PO}_4$ and heated at 110°C (Sample S27); and (c) 3 mg $\text{NH}_4\text{H}_2\text{PO}_4$ added to Sample S27 and heated at 200°C (Sample S27*). (d) Associated XRD patterns from Samples S26, S27 and S27* showing the formation of β -FeOOH.

This combined TEM and XRD investigation confirmed that Samples grown with and without phosphate at 110°C (Samples S26 & S27), and without phosphate at 110°C then with phosphate at 200°C (Sample S27*) all comprised the β -FeOOH phase, whilst only Sample S26* grown in the presence of phosphate throughout, at 110°C and then 200°C , comprised the α -Fe₂O₃ phase. Hence, it is evident that the stage at which the $\text{NH}_4\text{H}_2\text{PO}_4$ surfactant was added to the initial suspension had a dramatic effect on the crystalline phase of the reaction products synthesised at 200°C , *i.e.* the presence of the phosphate was required at the outset for the efficient formation and development of α -Fe₂O₃ NRs, via the intermediate β -FeOOH phase.

Sample S26 synthesised at 110°C in the presence of the surfactant comprised a mixture of small, rounded NPs and NRs. Sample S27, synthesised at 110°C in the absence of a surfactant, mainly consisted of slightly larger NRs, whilst TEM investigation of Sample S27*, synthesised at 200°C subsequent to the addition of

NH₄H₂PO₄ to Sample S27, revealed larger still, well-crystallised β -FeOOH NRs. Hence, it is apparent that the initial addition of surfactant to Sample S26 acted to inhibit the growth of the developing β -FeOOH NPs, as compared with Sample S27. It is noted that the precursor solution exhibited an initial pH of ~ 2 , being much lower than the PZC of β -FeOOH (pH 8),¹⁶⁰ and hence it is possible that the inhibition of particle growth arises from strong electrostatic attraction and the adsorption of high levels of PO₄³⁻ anions (as mentioned in Section 4.2.2.3).

Indeed, strong surface PO₄³⁻ anion adsorption onto the β -FeOOH NRs of Sample S27, after interruption of the HS process, is considered to stabilise these established β -FeOOH NRs at the elevated reaction temperature of 200°C. This delay to the timing of surfactant addition provides an element of control over the HS process, preventing the phase transformation of β -FeOOH in Sample S27* to α -Fe₂O₃, whilst also assisting with increasing the size of the β -FeOOH NRs.

4.6 Effect of α -Fe₂O₃ NPs (seeds) on α -Fe₂O₃ NR growth

It was suggested in Section 4.2 that α -Fe₂O₃ NR growth proceeds through the nucleation, agglomeration and recrystallisation of smaller α -Fe₂O₃ NPs. In this context, the effect of dispersing additional α -Fe₂O₃ NPs, called ‘seeds’, in the precursor solution, prior to HS, on α -Fe₂O₃ NR growth is investigated. The α -Fe₂O₃ seeds were previously synthesised through the scWHS of iron (III) nitrate nonahydrate using a dehydration temperature of 100°C (Sample S28).¹⁶⁵ Varied amounts of α -Fe₂O₃ seeds were dispersed ultrasonically in the precursor solution (0.2 ml FeCl₃ solution, further diluted in 40 ml water, 3mg NH₄H₂PO₄) and heated at 200°C for 2 hours, as summarised in Table 4.5.

Sample	α-Fe₂O₃ seeds / mg (Sample S28)
S29	1
S30	3
S31	5

Table 4.5 Amount of α -Fe₂O₃ seeds dispersed in the HS precursor solution.

4.6.1 Results and discussion

The BF TEM images of Figure 4.13b – d illustrate the effect of α -Fe₂O₃ seeds on the development of α -Fe₂O₃ NRs (Samples S29 – S31, respectively). Figure 4.13a shows the α -Fe₂O₃ seeds (Sample S28) to be < 10 nm in diameter. The α -Fe₂O₃ NRs in Figure 4.13a (Sample S29) are observed to be ~ 400 nm long and ~ 70 nm wide. TEM investigation of Samples S30 and S31 revealed α -Fe₂O₃ NRs ~ 300 nm long, ~ 60 nm wide (Figure 4.13c) and ~ 250 nm long, ~ 60 nm wide (Figure 4.13d), respectively.

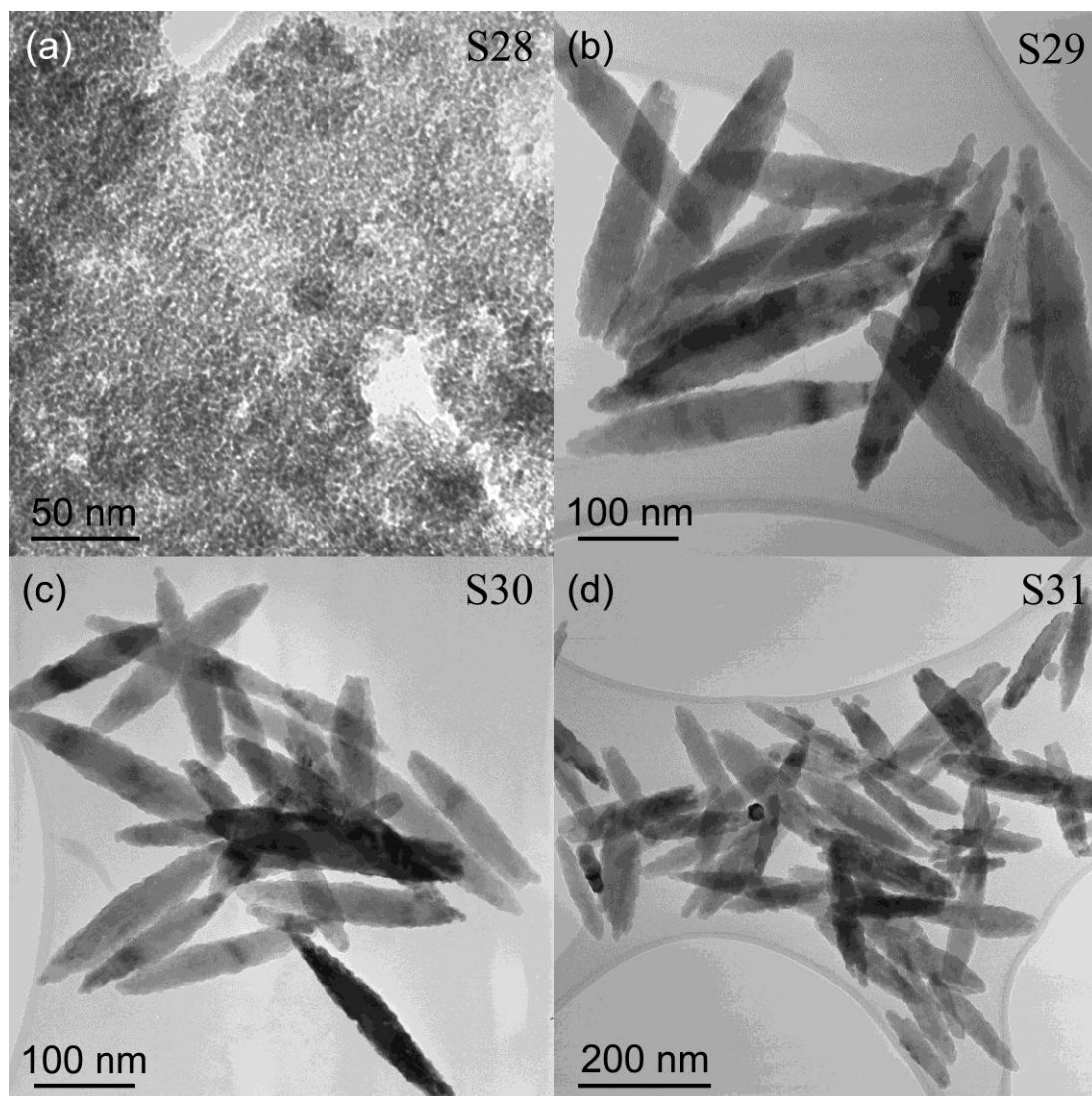


Figure 4.13 BF TEM images of (a) α -Fe₂O₃ seeds produced through the scWHS of iron (III) nitrate nonahydrate using a dehydration temperature of 100°C (Sample S28); (b) 1 mg, (c) 3mg and (d) 5 mg of α -Fe₂O₃ seeds, dispersed in 0.2 ml FeCl₃, 3 mg NH₄H₂PO₄, further diluted in 40 ml water.

The TEM investigation of Samples S29 – S31 revealed a trend of decreasing α -Fe₂O₃ NR size with increasing α -Fe₂O₃ seed content. The dispersed α -Fe₂O₃ seeds can be considered as additional centres of aggregation for the primary α -Fe₂O₃ NPs. Nevertheless, aggregation will still occur amongst the primary α -Fe₂O₃ NPs. The overall quantity of α -Fe₂O₃ NRs is dependent on the amount of discrete aggregation sites and is expected to increase with α -Fe₂O₃ seed content. However, additional NR growth sites imply a lower supply of primary α -Fe₂O₃ NPs to individual α -Fe₂O₃ NRs, reducing their size with increasing α -Fe₂O₃ seed content.

4.7 RHEED / XRD comparison

In sections 4.2, the use of appropriate material characterisation techniques allowed an HS ‘process map’ to be developed, providing an overall impression of the β -FeOOH and α -Fe₂O₃ phase transformation. In this section, the applicability of RHEED and XRD as techniques for the structural characterisation of nanostructured iron oxide are compared and their relative merits highlighted. The reactant solution consisting of 0.2 ml FeCl₃ and varied amounts of NH₄H₂PO₄ was mechanically stirred in the standard 125ml Teflon-lined stainless steel pressure autoclave, sealed and inserted into a temperature controlled furnace for 2 hours at reaction temperature, as specified in Table 4.6. Example RHEED patterns indexed to the phases of β -FeOOH and α -Fe₂O₃ are presented in Figures 4.14a & b, respectively, to assist with the interpretation of RHEED patterns recorded as a function of the HS processing conditions. Subtle differences in the spacings and intensities of the diffraction rings enabled the two distinct phases to be distinguished.

Sample	NH₄H₂PO₄ / mg	Temperature / °C	Sample	NH₄H₂PO₄ / mg	Temperature / °C
S32	0	100	S36	1	160
S33	0	120	S37	2	160
S34	0	140	S38	3	160
S35	0	160	S39	4	160

Table 4.6 HS processing conditions of increasing reaction temperature (Sample S22 to S35) and increasing NH₄H₂PO₄ (Samples S36 – S39).

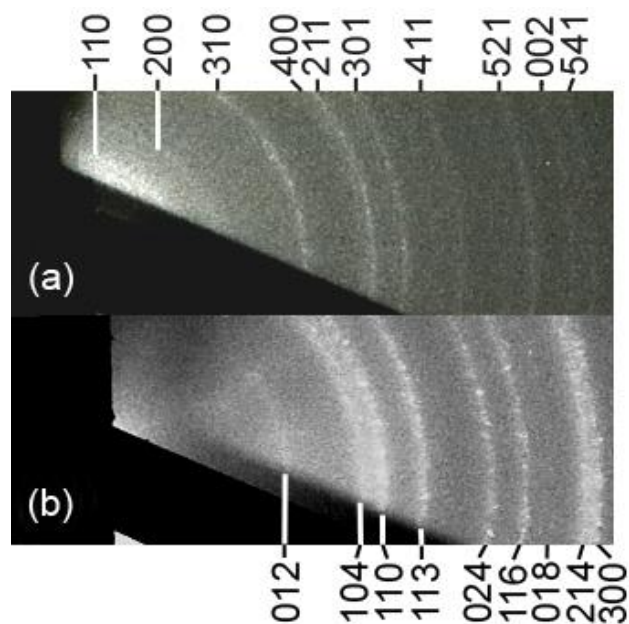


Figure 4.14 Example RHEED patterns indexed to (a) β -FeOOH and (b) α -Fe₂O₃.

4.7.1 Results

4.7.1.1 Effect of HS reaction temperature

Figure 4.15 presents XRD and RHEED patterns of the hydrothermal products synthesised at reaction temperatures of 100°C to 160°C, in the absence of a surfactant, accompanied by conventional BF TEM images showing the product morphologies (Samples S32 – S35). The XRD patterns corresponding to Samples S32 – S35 (Figure 4.15a) chart a transformation from an intermediate phase of β -FeOOH to a well defined phase of α -Fe₂O₃ with increasing HS temperature. Figures 4.15b & c show the associated RHEED patterns from Samples S32 and S33, respectively, with diffraction spacings corresponding to β -FeOOH. Conversely, the diffraction spacings from Sample S35 (Figure 4.15e) matched accurately with α -Fe₂O₃, whilst the RHEED pattern from Sample S34 exhibited rings attributable to β -FeOOH and additional, discrete diffraction spots attributable to α -Fe₂O₃ (Figure 4.15d). The associated TEM image of Figure 4.15f (Sample S32) shows the small β -FeOOH NRs, with varying aspect ratios, synthesised at 100°C, as compared with Figure 4.15i (Sample S35) which shows the larger rhombohedral / hexagonal α -Fe₂O₃ NPs synthesised at 160°C. The intermediate stages of α -Fe₂O₃ NP growth are seen at the reaction temperatures of 120°C and 140°C (Figures 4.15g, h).

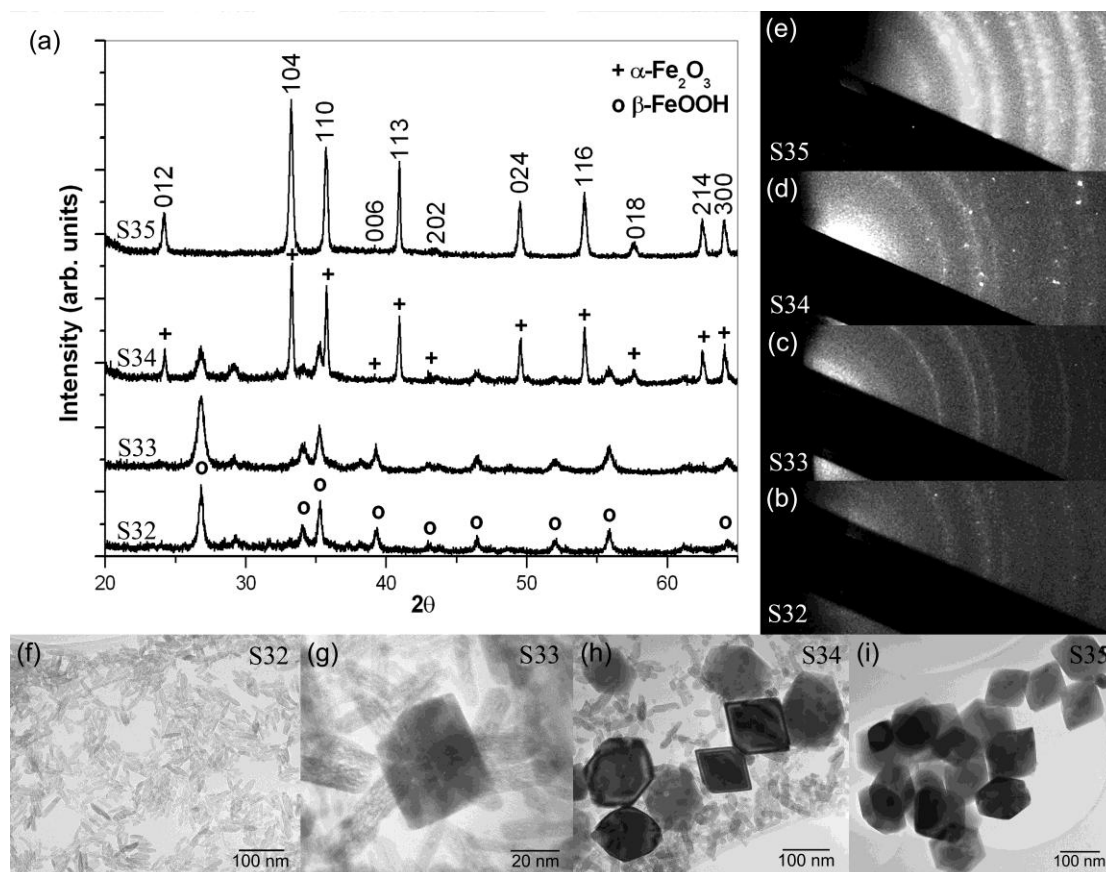


Figure 4.15 (a) XRD patterns of the HS reaction products synthesised from 0.2 ml FeCl₃ further diluted in 40ml and as a function of increasing temperature from 100 to 160°C (Samples S32 – S35, respectively) in the absence of a surfactant, with indices attributed to β -FeOOH and α -Fe₂O₃. Associated RHEED patterns and BF, diffraction contrast TEM images corresponding to Samples (b,f) S32; (c,g) S33; (d,h) S34 and (e,i) S35.

4.7.1.2 Effect of phosphate surfactant

Figure 4.16 presents associated XRD and RHEED patterns of the hydrothermal products synthesised at a reaction temperature of 160°C with surfactant additions of 1 to 4 mg phosphate, along with BF TEM images showing the reaction product morphologies (Samples S36 to S39). The XRD patterns of Figure 4.16a exhibit narrow, high intensity peaks characteristic of α -Fe₂O₃ at high Fe³⁺: PO₄³⁻ molar ratios, but with an ensuing loss in intensity, and by implication extent of crystallinity, with increasing PO₄³⁻ anion concentration. The associated RHEED patterns of Figures 4.16b – d (Samples S36 – S38) exhibit distinct, high intensity rings which reinforce the concept of superior crystallinity, as compared with Sample S39, corresponding to the highest phosphate concentration, which exhibits less distinct diffraction rings (Figure 4.16e). The TEM image of Figure 4.16f illustrates the mixture of ‘pseudocubes’ and rounded and elliptical α -Fe₂O₃ NPs comprising Sample S36. Conversely, well defined acicular α -Fe₂O₃ NRs with an aspect ratio of 3.7 were

evident within Sample S37 (Figure 4.16g). Sample S38 (Figure 4.16h) comprised partial acicular α -Fe₂O₃ NRs exhibiting the highest aspect ratio of 6 for this sample set. A further decrease in the extent of crystallinity and the acicular α -Fe₂O₃ NR aspect ratio was associated with Sample S39.

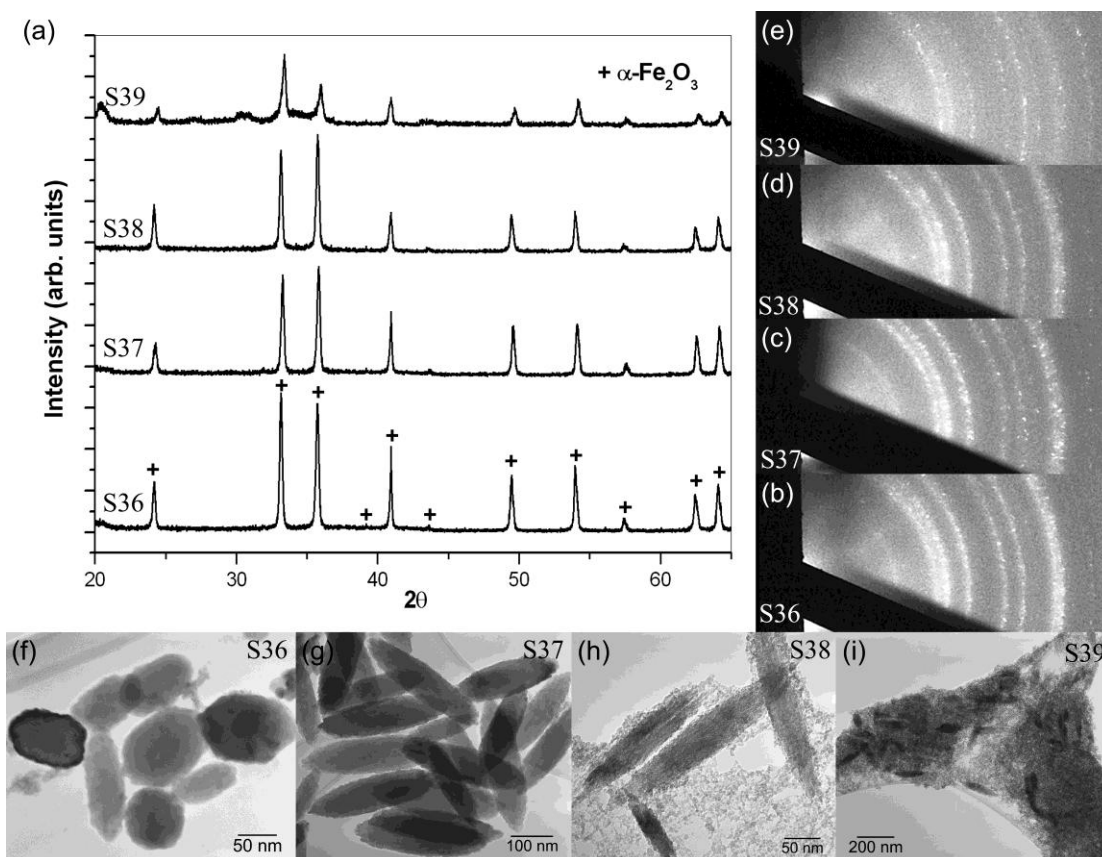


Figure 4.16 (a) XRD patterns of the HS reaction products synthesised from 0.2 ml FeCl₃ further diluted in 40ml at 160°C in the presence of increasing phosphate concentration from 1 to 4 mg NH₄H₂PO₄ (Samples S36 to S39, respectively). Associated RHEED patterns and BF TEM images corresponding to Samples (b,f) S36; (c,g) S37; (d,h) S38 and (e,i) S39.

4.7.2 Discussion

The data shows that both the XRD and RHEED techniques are capable of identifying and distinguishing between different β -FeOOH and α -Fe₂O₃ HS reaction products. For example, both the XRD and RHEED patterns for Samples S32 and S33 identify the β -FeOOH phase, synthesised at the relatively low reaction temperatures of 100 and 120°C. However, TEM investigation of Sample S33 revealed the additional presence of some small α -Fe₂O₃ NPs, suggesting that the volume fraction of α -Fe₂O₃ in this instance was beneath the detection limit of either diffraction technique.

The XRD pattern of Sample S34 demonstrates that α -Fe₂O₃ was the dominant phase at the intermediate temperature of 140°C, with a reduced β -FeOOH peak

intensity compared to Samples S32 and S33. TEM investigation reinforced this perception, with the presence of well developed α -Fe₂O₃ NPs up to 150 nm in size. However, the RHEED pattern of Sample S34 still showed continuous diffraction rings attributable to β -FeOOH with a few intense diffraction spots characteristic of α -Fe₂O₃. This reflects the surface sensitivity of the RHEED technique as compared with XRD. One possibility is that α -Fe₂O₃ NPs are terminated with a surface structure of β -FeOOH at this intermediate temperature of 140°C. Alternatively, there may be an issue for the separation of mixed phases from suspension. It is suggested that the denser and less soluble hexagonally closed-packed α -Fe₂O₃ crystals would settle comparatively quickly compared to the smaller body-centred tetragonal β -FeOOH NRs, during aqueous solution evaporation, leaving a higher β -FeOOH surface proportion which would dominate the RHEED in this instance. At the highest reaction temperature of 160°C (Sample S35), all three characterisation techniques of XRD, RHEED and TEM confirmed the sole presence of the α -Fe₂O₃ phase.

The XRD and RHEED data for Samples S36 to S39 similarly confirmed that α -Fe₂O₃ was the dominant phase at the reaction temperature of 160°C in the presence of a phosphate surfactant. TEM investigation demonstrated a variation in α -Fe₂O₃ NP aspect ratio with increasing concentration of PO₄³⁻ anions. This aspect ratio dependence is reflected in the relative peak intensities of the XRD patterns. Further, the suppression of α -Fe₂O₃ formation associated with Sample S39 was attributed to the hindrance of β -FeOOH dissolution, symptomatic of higher PO₄³⁻ anion concentration and hence, absorption. This observation is echoed in the both the reduced intensities of the XRD data (Figure 4.16a) and less distinct diffraction rings associated with the RHEED pattern of Figure 4.16e.

4.8 Summary

The development of β -FeOOH and α -Fe₂O₃ nanostructures using a wide range of HS processing conditions has been presented. A ‘process map’ for the HS of single crystalline α -Fe₂O₃ NRs from aqueous FeCl₃ was constructed, as a function of temperature, time and phosphate concentration. The ‘process map’ provided insight into the nature of intermediate β -FeOOH NR precipitation, dissolution and subsequent α -Fe₂O₃ growth, along with the effect of PO₄³⁻ anion concentration on the α -Fe₂O₃ particle shape. Increasing the processing temperature in the absence of a surfactant promoted the dissolution of initially formed β -FeOOH NRs and the nucleation and growth of equiaxed α -Fe₂O₃ NPs with rhombohedral morphology. Increasing additions of phosphate surfactant resulted in a shape change of the α -Fe₂O₃ NPs into acicular α -Fe₂O₃ NRs with increasing aspect ratio, but with progressive inhibition of α -Fe₂O₃ phase formation. Increasing the synthesis temperature in the presence of PO₄³⁻ anions was associated with the recovery of well-defined single crystal, acicular NRs. Increasing the time of synthesis in the presence of PO₄³⁻ anions was similarly associated with the progressive formation and dissolution of β -FeOOH and the growth of well-defined acicular α -Fe₂O₃ NRs. An HS processing temperature of 200°C and an Fe³⁺ : PO₄³⁻ molar ratio of 31.5 yielded optimal crystalline acicular α -Fe₂O₃ NRs with an aspect ratio of ~ 7. Additional effects of FeCl₃ aqueous solution concentration, pH, stage of NH₄H₂PO₄ addition and α -Fe₂O₃ seeds on the β -FeOOH and α -Fe₂O₃ nanostructures synthesised using the high aspect ratio conditions were explored. The α -Fe₂O₃ particle size was found to be dependent on precursor concentration, decreasing in both size and aspect ratio when lowering the FeCl₃ and NH₄H₂PO₄ concentration, whilst keeping the Fe³⁺ : PO₄³⁻ molar ratio constant. A small increase in pH from ~ 2.5 to ~ 4 resulted in marked reduction in the α -Fe₂O₃ aspect ratio. Addition of the surfactant after β -FeOOH precipitation prevented the phase transformation of β -FeOOH to α -Fe₂O₃ and assisted with increasing the size of the β -FeOOH NRs. XRD and RHEED techniques have both identified and distinguished between the different β -FeOOH and α -Fe₂O₃ HS reaction products. Subtle differences in the data arise from the surface sensitivity of the RHEED technique as compared with XRD. Investigation of the effect of the HS processing conditions has led to controlled growth of β -FeOOH to α -Fe₂O₃ nanostructures.

Chapter 5 Hydrothermal growth mechanism derived from analysis of quenched samples

5.1 Introduction

The use of HS reaction vessels under conditions of high temperature and pressure generally creates an aspect of inaccessibility which limits direct investigation. Consequently, the analysis of HS nanostructures in Chapter 4 was restricted to post-synthesis reaction products isolated following cool down under equilibrium conditions, with possibility of loss of *in situ* constituent evidence demonstrating the specific mechanistics of growth. In this chapter, use of a novel 50 ml valve-assisted Teflon-lined stainless steel pressure autoclave to facilitate ‘snapshot’ investigation of HS product suspensions rapidly quenched in liquid nitrogen is presented. This approach is considered to provide descriptions closely representative to the *in situ* physical state of the synthesis reaction products. In this context, the viability of this ‘snapshot’ approach to provide information on the localised development of high aspect ratio acicular α -Fe₂O₃ NRs as a function of reaction time is investigated. Consequently, a more detailed description of the development of 1D α -Fe₂O₃ nanostructures, as a function of known reaction temperature, providing for better understanding of the growth mechanism of α -Fe₂O₃ NRs, is presented. In particular, emphasis is given to the critical role of the PO₄³⁻ surfactant mediating their acicular shape. In addition, *in situ* TEM (*i*TEM) investigation of β -FeOOH and α -Fe₂O₃ NRs, providing fundamental insight into the localised growth of these nanostructures as a function of temperature, for comparison with the quenched HS reaction products is presented.

5.2 Effect of reaction time on α -Fe₂O₃ NR growth

A 50 ml valve-assisted Teflon-lined stainless steel pressure autoclave was constructed to investigate the *in situ* growth of α -Fe₂O₃ NRs, prepared through the hydrothermal reaction of the FeCl₃ precursor solution, (0.1 ml 45% pure FeCl₃ solution, further diluted in 20 ml water). Use of the valve-assisted pressure autoclave allowed snapshots of the synthesis to be obtained after 20, 30, 40 or 50 minutes ('Quenched' Samples, labelled Q20, Q30, Q40, and Q50, respectively, for simplicity) of processing, as summarised in Table 5.1. The autoclave was removed from the furnace at the reaction temperature and immediately transferred to a tripod support for stability, where the valve was opened and closed, as quickly as practically possible, for the release of sufficient hydrothermal product suspension into liquid nitrogen for the purpose of rapid quenching.

5.2.1 Results

Figures 5.1, 5.2 and 5.3 present TEM images that illustrate the development of the varied β -FeOOH and α -Fe₂O₃ reaction products on the atomic scale. The phases present were identified by the matching of diffraction spots within SAED patterns and the characteristic lattice fringe spacings revealed by phase contrast imaging, as summarised in Table 5.1.

Snapshot sample	NH ₄ H ₂ PO ₄ / mg	Temperature / °C	Reaction time / min	Reaction product	Morphology	Dimension (l/w) / nm
Q20	1.5	200	20	β -FeOOH	NRs and NPs	<50/15
Q30	1.5	200	30	β -FeOOH	NRs and NPs	<50/15
				α -Fe ₂ O ₃	NPs	<70
Q40	1.5	200	40	α -Fe ₂ O ₃	NRs	<150/25
				α -Fe ₂ O ₃	NPs	<10
Q50	1.5	200	50	α -Fe ₂ O ₃	NRs with tip filamentary features	<400/80

Table 5.1 Reaction times of 'snapshots' and a summary of the product phases, morphologies and sizes.

TEM investigation of Sample Q20, quenched after 20 minutes of processing, revealed β -FeOOH NRs ~ 50 nm in length, as identified by the associated SAED pattern (Figure 5.1, inset).

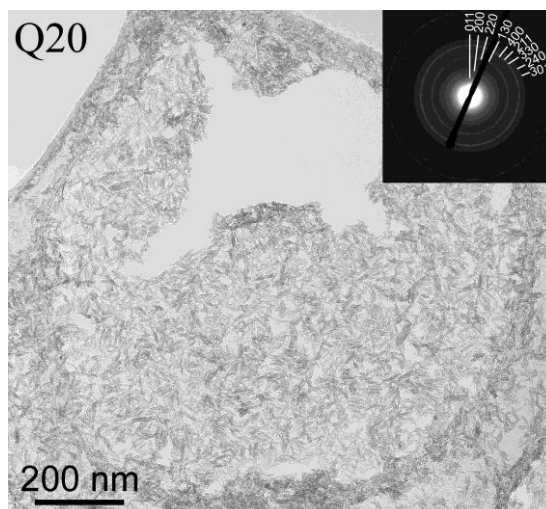


Figure 5.1 BF TEM images of ‘quenched’ hydrothermal products after 20 minutes of processing at 200°C (Sample Q20) and corresponding SAED pattern indexed to β -FeOOH (inset).

Figure 5.2a shows the fine details of the β -FeOOH NRs being readily distinguishable from the α -Fe₂O₃ phase because of their significantly larger lattice fringe spacings (Figure 5.2a, inset). A large number of small α -Fe₂O₃ NPs (< 10 nm in diameter) were also identified within the sample. Further, Figure 5.2b (boxed region) illustrates the development of a distinct, single crystalline α -Fe₂O₃ NP (~ 70 nm in diameter) exhibiting an irregular structure with rough edges.

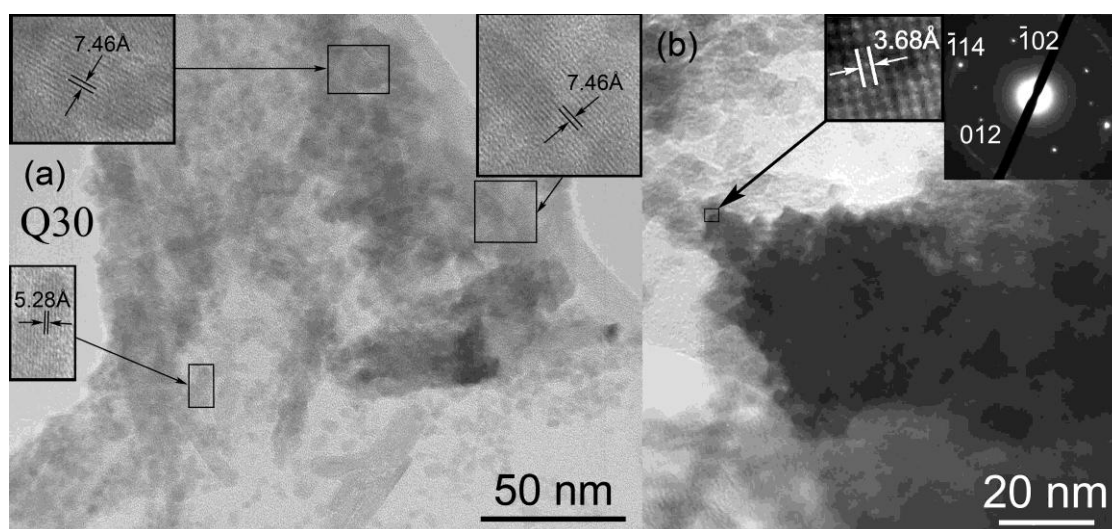


Figure 5.2 BF and phase contrast TEM images of ‘quenched’ hydrothermal products after 30 minutes of processing at 200°C (Sample Q30). (a) β -FeOOH, as identified by lattice fringes (inset) and (b) an α -Fe₂O₃ NP (boxed), identified by lattice fringes and corresponding SAED pattern (inset).

TEM investigation of the reaction products produced after 40 minutes of synthesis (Sample Q40) again indicated the presence of many small isotropic α -Fe₂O₃ NPs (< 10 nm in diameter) along with development of larger α -Fe₂O₃ acicular NRs (~ 150 nm long, ~ 25 nm wide), but without any noticeable evidence for the presence of the intermediate β -FeOOH phase (Figure 5.3). Higher magnification examination illustrated the close association between the smaller α -Fe₂O₃ NPs and the development of the single crystalline α -Fe₂O₃ NRs. Indeed, lattice fringes revealed by phase contrast imaging were consistent with the presence of only crystalline α -Fe₂O₃ (Figure 5.3e).

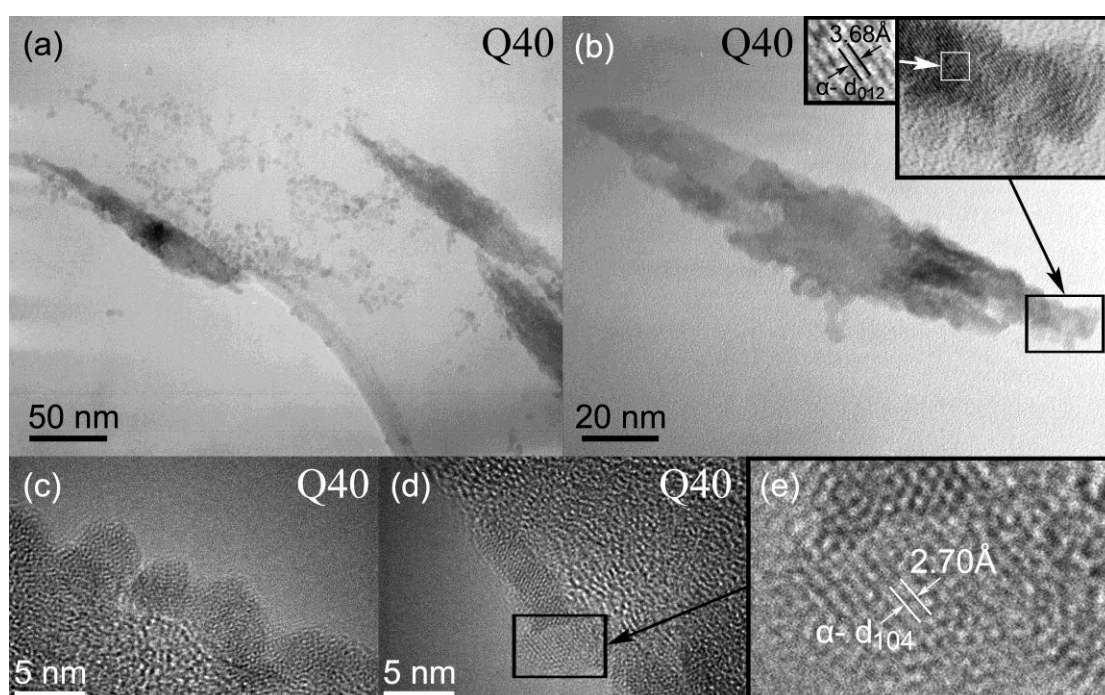


Figure 5.3 BF and phase contrast TEM images of the hydrothermal products after 40 minutes of processing at 200°C (Sample Q40). (a) Larger α -Fe₂O₃ NRs (~ 150 nm long, ~ 25 nm wide) amongst smaller α -Fe₂O₃ NPs (< 10 nm); (b) large α -Fe₂O₃ NR with smaller NPs attached (inset); (c) & (d) smaller NPs on the edge of the lacy carbon support; and (e) an individual α -Fe₂O₃ NP.

TEM investigation of Sample Q50 (Figure 5.4) revealed the presence of large well-defined, crystalline, acicular α -Fe₂O₃ NRs, again identified by their lattice fringe spacings and associated SAED patterns (Figure 5.4a, inset). Filamentary features observed at the ends of the developing NRs exhibited the same lattice fringe spacings (Figure 5.4b, inset), being crystallographically aligned with bulk crystal nanostructure.

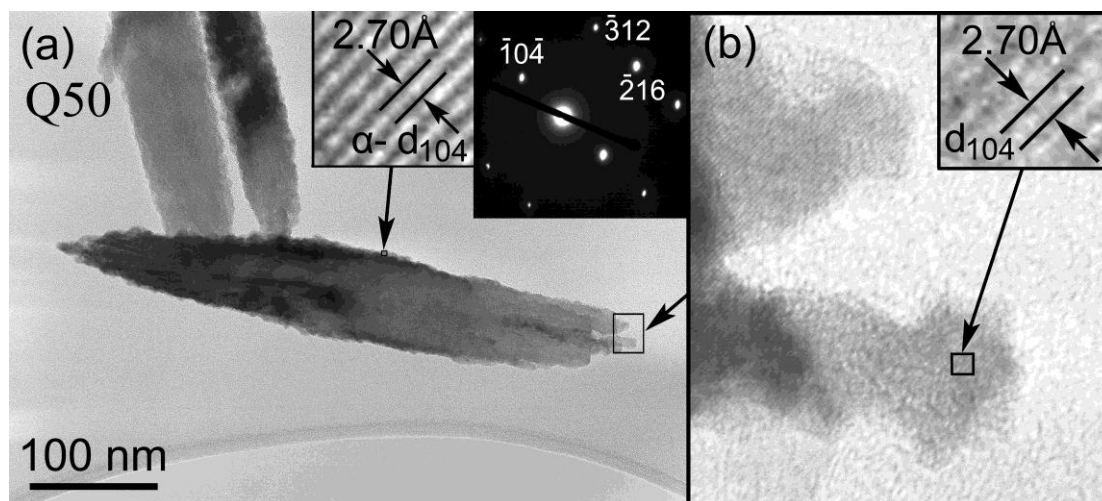


Figure 5.4 BF TEM image of (a) large acicular α -Fe₂O₃ NRs synthesised for 50 minutes at 200°C (Sample Q50), identified by lattice fringes and associated SAED pattern (*e.g.* inset) and (b) filamentary α -Fe₂O₃ feature at the tip of the developing NR.

5.2.2 Discussion

It is considered that the reaction products obtained from the valve-assisted pressure autoclave are closely representative of the *in situ* physical state of the developing iron oxide nanostructures, due to the large cooling rate experienced during quenching. This acts to restrict possible atom / ion transport, thereby locking-in the morphology of the nanostructures.

The dominant presence of β -FeOOH NRs after 30 minutes of processing (Sample Q30) confirms it to be an intermediate phase. A number of small (< 10 nm) α -Fe₂O₃ NPs were also observed, along with a few large crystalline α -Fe₂O₃ NPs (~ 70 nm in size) exhibiting irregular morphologies. It is noted that after 20 minutes of synthesis (Sample Q20), only β -FeOOH NRs were observed, as confirmed by SAED.

TEM investigation of the snapshot sample after 40 minutes of processing (Sample Q40) demonstrated the development of much larger α -Fe₂O₃ NRs (~ 150 nm in length), alongside many smaller (< 10 nm) α -Fe₂O₃ NPs, but with no evidence for the presence of any β -FeOOH nanostructures. This is consistent with the suggestion that the β -FeOOH NRs dissolve, supplying Fe³⁺ to support the growth of the α -Fe₂O₃ NRs, the development of which occurs through the consumption of smaller α -Fe₂O₃ NPs through a process of coarsening.¹⁶⁶ The Ostwald rule of stages, concerning the competition between kinetics, irreversible thermodynamics and equilibrium thermodynamics, implies that the energetic barrier for formation and dissolution of metastable β -FeOOH is lower and easier to overcome than the higher energetic barrier

associated with the precipitation of the more stable α -Fe₂O₃ phase, being driven by the enthalpy for bond formation at increasing hydrothermal temperatures.¹⁶⁶

The snapshot of Sample Q50 after 50 minutes of processing demonstrated a significant reduction in the number of the smaller α -Fe₂O₃ NPs, and the dominant presence of much larger (~ 400 nm in length), well-crystallised, acicular α -Fe₂O₃ NRs exhibiting distinctive filamentary features at their tips. Indeed, lattice fringes indicated these features to be crystallographically aligned with the bulk NRs. This confirms that the fundamental process defining the growth of the α -Fe₂O₃ NRs is that of agglomeration and re-arrangement of discrete α -Fe₂O₃ NPs, rather than one of dissolution and recrystallisation.

Further, the α -Fe₂O₃ filamentary features shown in Figure 5.4b suggest the preferential attachment of primary α -Fe₂O₃ NPs to faces normal to the α -Fe₂O₃ crystallographic c-axis, with reduction in surface energy driving subsequent coalescence and crystallisation, mediated by the phosphate surfactant, to produce such acicular shapes.

Thus, improved understanding of the reaction products synthesised using the standard pressure autoclave has been gained based on the insights provided by these fundamental valve-assisted synthesis experiments. In the case of conventional HS, as used in Chapter 4, it is considered that Fe³⁺ cations released through β -FeOOH dissolution may resort back to β -FeOOH during the process of cool down (< 120°C), thereby providing a slightly misleading representation of the *in situ* state of the hydrothermal reaction products.

This valve assisted HS approach offers a rapid route for fundamental investigation of the growth mechanisms of many interesting nanostructures, and those of complicated chemical composition in particular, simply by changing the reactant solution, coupled with some knowledge of the anticipated hydrothermal or solvo-thermal reaction products as a function of the processing conditions used. However, it is recognised that the cooling rate is dependent on the reaction solution pressure and thus the associated solution expulsion rate from the valve. At low pressures, it is considered that the quenching time might be in the range of tenths of a second, whilst at high pressures, there might be the possibility of some parasitic crystallisation and explosive nucleation caused by high supersaturation during quenching, as well as contamination artefacts. Nevertheless, it is believed that this data presents a markedly

more accurate representation of α -Fe₂O₃ NR hydrothermal growth compared to that obtained from the standard pressure autoclave used in Chapter 4.

In this context, it is noted that the technique of *in situ* synchrotron X-ray diffraction may also be used to investigate of the hydrothermal growth of nanostructured materials such as hematite,¹⁶⁷ but this approach is only sensitive to bulk crystal phase transformations. The advantage of the present snapshot valve-assisted HS approach, coupled with TEM, is that it facilitates the investigation of a sequence of *in situ* reaction products on the localised scale.

5.3 Effect of (known) reaction temperature on α -Fe₂O₃ NR growth

These initial experiments have demonstrated the viability of the ‘snapshot’ approach to provide detailed insight into the localised development of acicular α -Fe₂O₃ NRs, as a function of reaction time.¹⁶⁸ A more detailed investigation of the development of 1D α -Fe₂O₃ nanostructures, as a function of reaction temperature, using this 50 ml valve-assisted Teflon-lined stainless steel pressure autoclave, recognising that thorough understanding of the temperature response of each reaction vessel is needed to fully appraise the growth, is now presented. It is considered that detailed analysis of the quenched hydrothermal reaction solutions, acquired at known reaction temperatures, provides for better understanding of the development process of α -Fe₂O₃ NRs. In particular, emphasis is given to the critical role of the PO₄³⁻ surfactant mediating their acicular shape. The ‘snapshot’ samples were prepared through the hydrothermal reaction of the FeCl₃ precursor solution, as specified in Section 3.2.3.1. The time taken for the hydrothermal reaction solution to reach the furnace temperature (Table 5.2 – ‘quenched’ samples labelled Q100 – Q200, for simplicity) was monitored using an integrated thermal couple (Figure 5.5). This demonstrated that the autoclave, in this instance, required a dwell time of 80 minutes to achieve the desired hydrothermal reaction temperature, whilst the heating rate was dependent on the furnace temperature.

Snapshot sample	NH ₄ H ₂ PO ₄ / mg	Temperature / °C	Reaction time / min	Reaction product	Morphology	Dimension (l/w) / nm
Q100	1.5	100	80	β -FeOOH α -Fe ₂ O ₃	NRs and NPs NPs	<50/15 < 10
Q120	1.5	120	80	β -FeOOH α -Fe ₂ O ₃	NRs and NPs NPs	<50/15 < 10
Q140	1.5	140	80	β -FeOOH α -Fe ₂ O ₃ α -Fe ₂ O ₃	NRs NPs Acicular NRs	<50/15 <10 ~ 150/50
Q160	1.5	160	80	β -FeOOH α -Fe ₂ O ₃ α -Fe ₂ O ₃	Few NRs NPs Acicular NRs	< 40/15 <10 ~350/60
Q180	1.5	180	80	α -Fe ₂ O ₃ α -Fe ₂ O ₃	NPs Acicular NRs	<10 ~420/65
Q200	1.5	200	80	α -Fe ₂ O ₃	Acicular NRs	~ 450 / 80

Table 5.2 ‘Snapshot’ samples investigated as a function of increasing temperature and a summary of the product phases, morphologies and sizes.

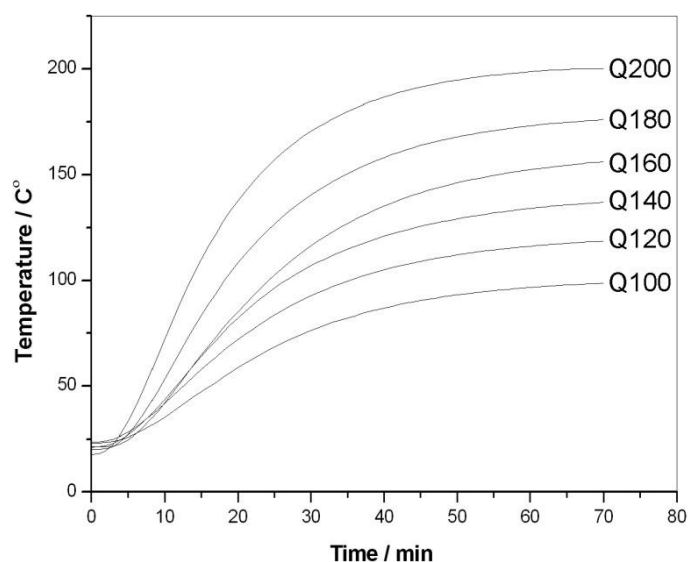


Figure 5.5 Hydrothermal reaction solution temperature plotted as a function of reaction time.

5.3.1 Results

Use of the valve-assisted pressure autoclave enabled investigation of the hydrothermal processing of aqueous FeCl_3 solution, for the synthesis of either $\beta\text{-FeOOH}$ or $\alpha\text{-Fe}_2\text{O}_3$ nanostructures, or both, depending on the HS reaction temperature. In this section, the valve-assisted pressure autoclave used to obtain snapshots of the synthesis after 80 minutes of processing, after the HS reaction solution had attained the target (furnace) temperature, the evidence for which is now presented in detail.

5.3.1.1 Transmission electron microscopy

The BF, diffraction contrast TEM images of Figures 5.6a – f illustrate the varied $\beta\text{-FeOOH}$ and $\alpha\text{-Fe}_2\text{O}_3$ reaction products, as a function of increasing HS temperature (Samples Q100 – Q200). The phases present were identified from associated SAED patterns (Figures 5.6a – f inset and summarised in Table 5.2). Sample Q100 (Figure 5.6a) showed the presence of $\beta\text{-FeOOH}$ needle-shaped NRs (< 50 nm long, 15 nm wide) and small $\alpha\text{-Fe}_2\text{O}_3$ NPs (< 10 nm in diameter). The same phases and particle morphologies were observed in Sample Q120 (Figure 5.6b), with the presence of slightly more of the small $\alpha\text{-Fe}_2\text{O}_3$ NPs. Conversely, Sample Q140 (Figure 5.6c) exhibited additional darker $\alpha\text{-Fe}_2\text{O}_3$ NRs (~ 200 long, ~ 50nm wide, as arrowed) amongst the previously observed $\beta\text{-FeOOH}$ and $\alpha\text{-Fe}_2\text{O}_3$ nanostructures. Further, Sample Q160 (Figure 5.6d) demonstrated an increased presence of the small isotropic $\alpha\text{-Fe}_2\text{O}_3$ NPs (< 10 nm in diameter), along with the development of larger $\alpha\text{-Fe}_2\text{O}_3$ acicular NRs (~ 350 nm long, ~ 60 nm wide) and a correspondingly marked reduction

in the presence of the intermediate β -FeOOH phase. The proportion and size of α -Fe₂O₃ NRs (~ 420 nm long, ~ 65 nm wide) was even greater in Sample Q180 (Figure 5.6e), without any noticeable evidence for the presence of the intermediate β -FeOOH phase amongst the remaining small α -Fe₂O₃ NPs. Sample Q200 exhibited the largest, most well-defined, crystalline acicular α -Fe₂O₃ NRs (~ 450 nm long, ~ 80 nm wide) (Figure 5.6f).

Phase contrast imaging of Sample Q100 revealed details of the initial development of β -FeOOH nanostructures, as identified by characteristic lattice fringes corresponding to {110} and {200} planes (Figures 5.7a and 5.7b, respectively). An embryonic β -FeOOH NP is shown in Figure 5.7a, whilst Figure 5.7b is representative of the first stages of development of a β -FeOOH NR, with characteristic {110} planes ($d_{110} = 7.47\text{\AA}$) lying parallel to the NR growth axis (Figure 5.7b).

The BF and phase contrast TEM images of Figure 5.8 present details of the initially formed α -Fe₂O₃ NPs, as identified in Sample Q160. Lattice fringes consistent with the development of crystalline α -Fe₂O₃ were identified (Figure 5.8d), and confirmed by associated Fast Fourier Transform (FFT) patterns (Figure 5.8e). The initially formed α -Fe₂O₃ NPs were all isotropic in shape and < 10 nm in diameter.

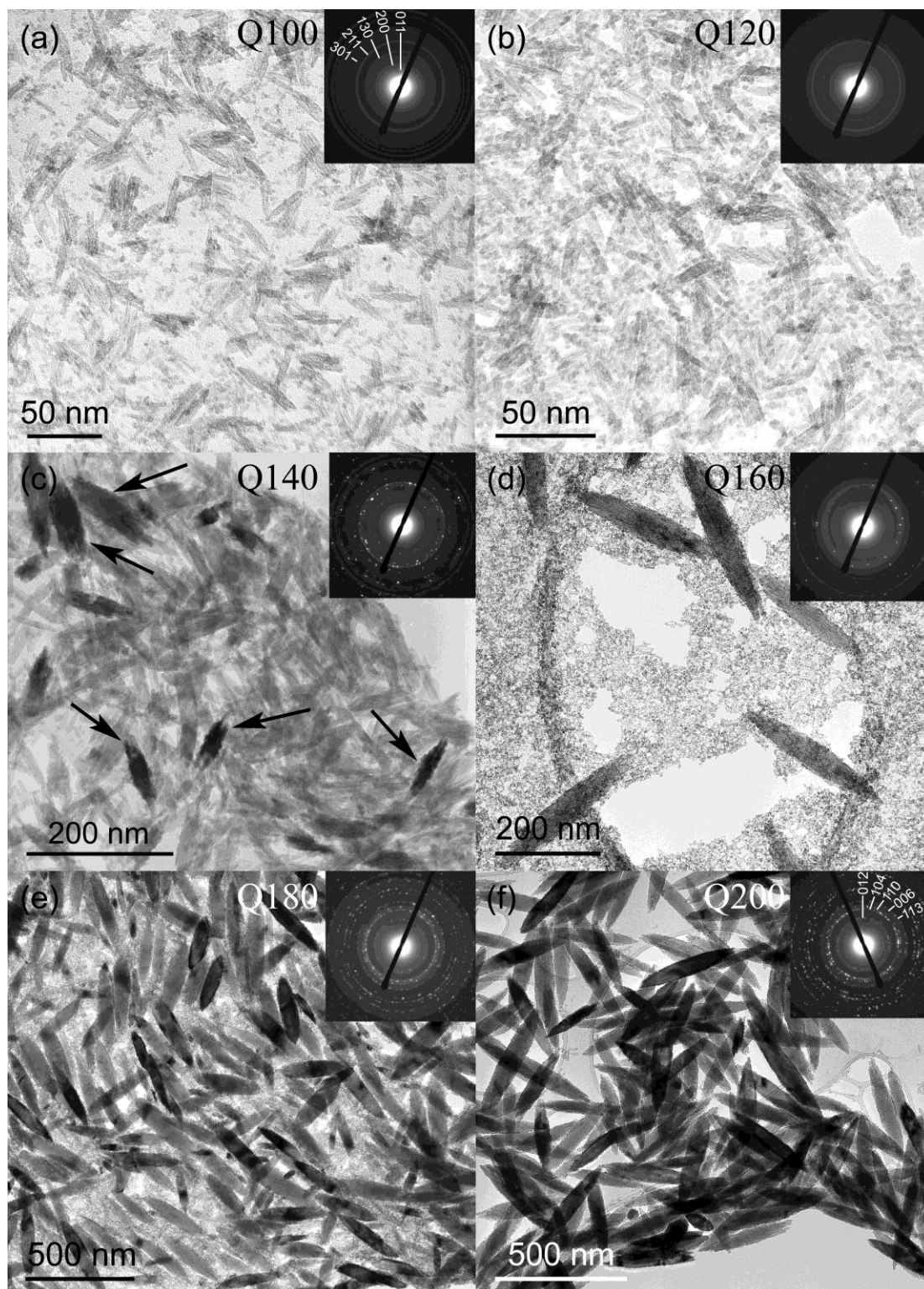


Figure 5.6 BF TEM images of ‘quenched’ hydrothermal products synthesised from 0.1 ml FeCl_3 , further diluted in 20 ml water, and 1.5 mg $\text{NH}_4\text{H}_2\text{PO}_4$, after 80 minutes of processing, having achieved temperatures of (a) 100, (b) 120, (c) 140, (d) 160, (e) 180 and (f) 200°C, respectively (Samples Q100 – Q200), with corresponding SAED patterns (inset – (a) and (f) are indexed to $\beta\text{-FeOOH}$ and $\alpha\text{-Fe}_2\text{O}_3$, respectively).

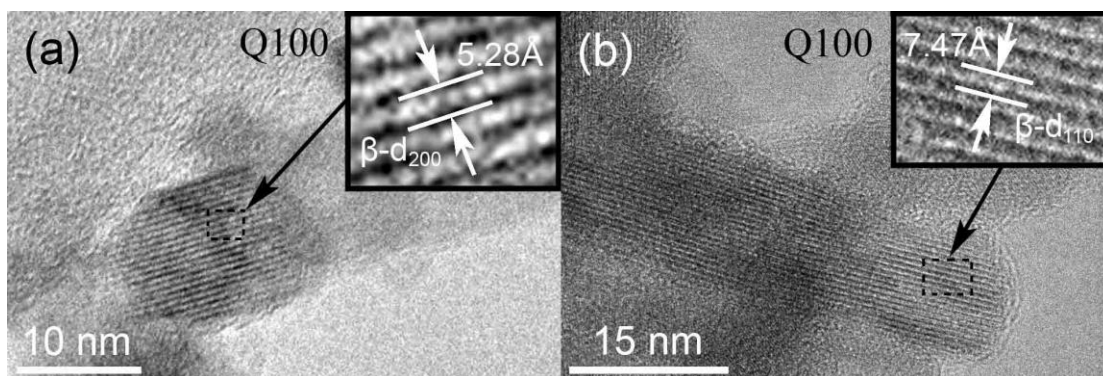


Figure 5.7 Phase contrast TEM images of the hydrothermal products synthesised from 0.1 ml FeCl_3 , further diluted in 20 ml water, and 1.5 mg $\text{NH}_4\text{H}_2\text{PO}_4$, at 100°C (Sample Q100). (a) Small $\beta\text{-FeOOH}$ NP (~ 15 nm in diameter); and (b) small developing $\beta\text{-FeOOH}$ NR (~ 50 nm long, ~ 15 nm wide); both identified by lattice fringes.

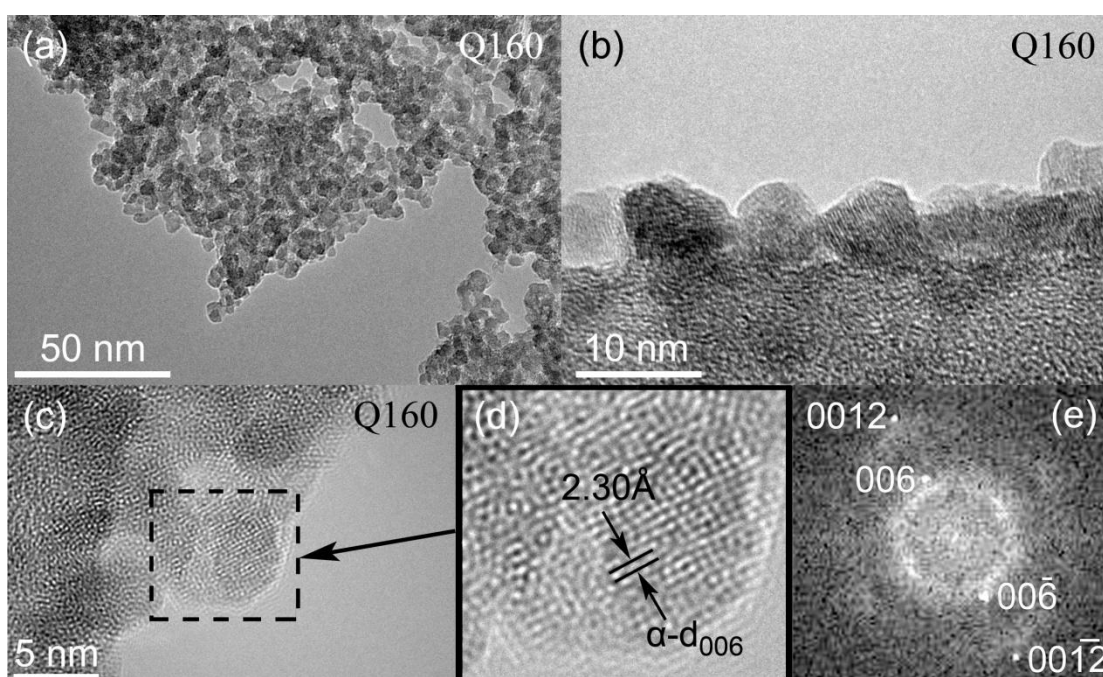


Figure 5.8 BF and phase contrast TEM images of the first stages of development of $\alpha\text{-Fe}_2\text{O}_3$ NPs, synthesised from 0.1 ml FeCl_3 , further diluted in 20 ml water, and 1.5 mg $\text{NH}_4\text{H}_2\text{PO}_4$, at 160°C (Sample Q160). (a) Small $\alpha\text{-Fe}_2\text{O}_3$ NPs (< 10 nm in diameter); (b) & (c) small $\alpha\text{-Fe}_2\text{O}_3$ NPs on the edge of the lacey carbon support; (d) an individual $\alpha\text{-Fe}_2\text{O}_3$ NP identified by lattice fringes and (e) corresponding FFT.

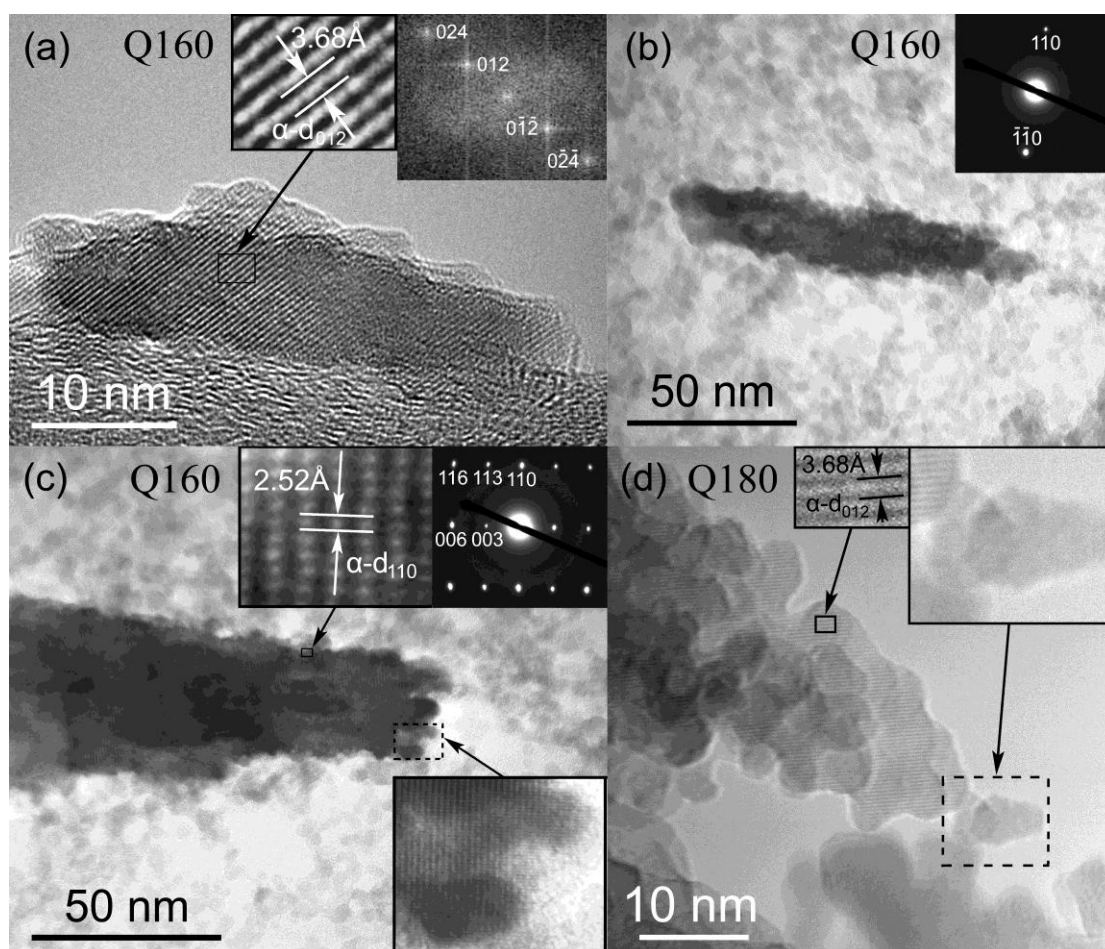


Figure 5.9 BF and phase contrast TEM images of the hydrothermal products processed at (a – c) 160°C and (d) 180°C, respectively. (a) Initially formed α -Fe₂O₃ NR (~ 40 nm long, ~ 12 nm wide), as identified by lattice fringes and associated FFT (both inset); (b) α -Fe₂O₃ NR (~ 120 nm long, ~ 25 nm wide) with corresponding SAED pattern (inset); (c) tip of an α -Fe₂O₃ NR, as identified by lattice fringes and SAED pattern (both inset), exhibiting filamentary features crystallographically aligned with the bulk NR (inset); and (d) tip of a developing α -Fe₂O₃ NR, as identified by lattice fringes (inset), with an irregular surface and uneven distribution of α -Fe₂O₃ NPs attached to the tip (inset).

TEM investigation of Samples Q160 and Q180 (Figures 5.9a – d) demonstrated the close association between the initially formed α -Fe₂O₃ NPs and the development of single crystalline α -Fe₂O₃ NRs. Figure 5.9a shows a small crystalline α -Fe₂O₃ NR (~ 40 nm long, ~ 12 nm wide), as identified by lattice fringe spacings and associated FFT. Figure 5.9b illustrates a slightly larger α -Fe₂O₃ NR (~ 120 nm long, ~ 25 nm wide), with an irregular surface. The developing tips of such α -Fe₂O₃ NRs exhibited filamentary features, comprising α -Fe₂O₃ NPs of similar size to those shown in Figure 5.8, with lattice fringes aligned with the NR bulk (Figure 5.9c, inset). Associated SAED patterns (Figure 5.9c inset) demonstrated the α -Fe₂O₃ NR growth axis to be parallel to $\langle 006 \rangle$. It is considered that the TEM image of Figure 5.9d reveals details of the initial stages of attachment of crystalline α -Fe₂O₃ NPs to a developing α -Fe₂O₃ NR, prior to their crystallographic alignment with the bulk NR.

5.3.1.2 X-ray photoelectron spectroscopy

Complementary XPS data from samples Q100 and Q160 (Figures 5.10a & b, respectively), showing details of Fe 2p and P 2p peaks, presented in Figures 5.10c & d, respectively. In Section 4.2.1.5, it was reported that Fe 2p and P 2p signatures from iron oxide and iron hydroxide grown by HS in a phosphate environment were nearly identical, limiting ease of discrimination between the surfaces of these phases using the technique of XPS.⁷ However, subtle differences in the near surface chemistries of these β -FeOOH and α -Fe₂O₃ nanostructures are revealed by the present data set.

Figure 5.10c shows Fe 2p_{3/2} binding energy peaks at 711.8 eV and 711.0 eV for samples Q100 and Q160, consistent with the presence of β -FeOOH and α -Fe₂O₃, respectively.^{169,170} Satellite peaks characteristic of Fe³⁺ were evident within both spectra, with differences in the binding energies between satellite and Fe 2p_{3/2} peaks being 7.60 eV and 4.50 eV for α -Fe₂O₃ and β -FeOOH, respectively. This observation is consistent with a recent report of an 8.0 eV separation between satellite peak and the Fe 2p_{3/2} binding energy for bulk α -Fe₂O₃.¹⁷¹ Further, Figure 5.10d showing P 2p peaks centred at 134.0 eV, 133.0 eV and 133.1 eV (Samples Q100, Q160 and Q200, respectively) is consistent with the presence of phosphate species on the surfaces of both β -FeOOH and α -Fe₂O₃ nanostructures.^{172,173}

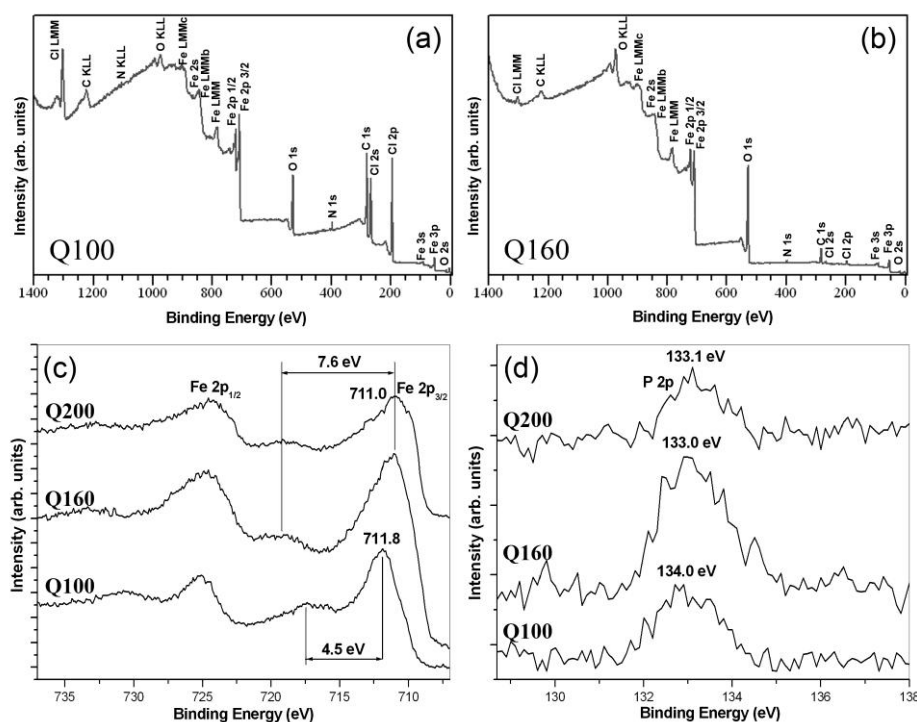


Figure 5.10 XPS survey spectra of (a) Sample Q100 and (b) Sample Q160. XPS data showing (c) Fe 2p and (d) P 2p signatures from Samples Q100, Q160 & Q200.

5.3.1.3 Fourier transform infrared spectroscopy

The nature of the covalent bonding of the surface phosphate species was investigated using FTIR spectroscopy. Phosphate stretching modes¹⁷⁴ were identified typically in the range of 900 - 1200 cm^{-1} . Figure 5.11a presents FTIR spectra obtained from Samples Q100, Q160 and Q200, as well as an additional spectrum from acetone cleaned Q200 (labelled Q200C). It is clear that the signal from Sample 200C is relatively small compared to Samples Q100, Q160 and Q200. For this reason, the signal from the original snapshot samples can be assigned to emission from surface species, as opposed to signal from the crystal bulk. Deconvolution of the Q100 and Q160 spectra into the individual spectral constituents was performed using *CasaXPS* software (Figures 5.11b and 5.11c / d, respectively). Sample Q100 demonstrated peaks at 1111, 1056 and 987 cm^{-1} (Figure 5.11b) whilst Sample Q160 showed peaks at 898, 934, 970, 1004, 1036, 1071 and 1149 cm^{-1} (Figure 5.11d).

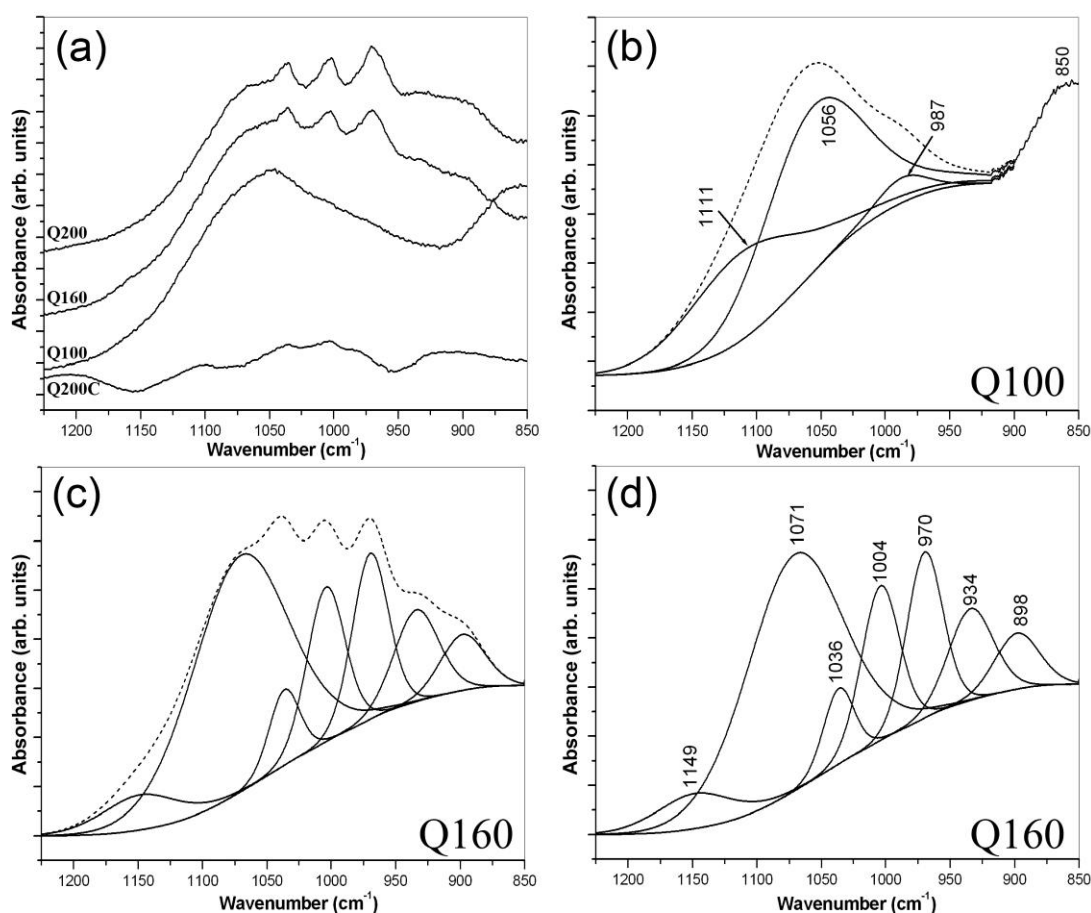


Figure 5.11 (a) FTIR spectra of phosphate species from Samples Q100, Q160, Q200 and Q200C; (b) deconvolution of Q100 showing labelled individual spectral constituents; (c) deconvolution of Q160 showing individual spectral constituents; and (d) labelled individual peaks (Sample Q160).

5.3.2 Discussion

5.3.2.1 Overview

It is considered that sequential snapshot characterisation of the hydrothermal reaction products as a function of processing temperature allows for direct realisation of the α -Fe₂O₃ NR growth mechanism. In this context, the present set of experiments chart the development of β -FeOOH and α -Fe₂O₃ reaction product phase and morphology as a function of stabilised temperature, attained using a valve-assisted pressure autoclave after 80 minutes of processing. Two considerations, however, should be noted. It is recognised that present set of experiments provides a series of steady-state observations as a function of known temperature, as distinct from a time dependent analysis of the development of reaction products, as described in Section 5.2. A lack of knowledge of the precise temperature during the time dependent heating stage in Section 5.2 prohibited direct association of HS temperature with nanostructure development.¹⁶⁸ Nevertheless, the overall growth sequence elucidated using the present snapshot approach at known temperature, now reported here, is found to match the trends of the original HS ‘process map’ (Figure 4.8) for the standard pressure autoclave, as shown in Chapter 4.2.2.1.⁷ Indeed, it is worth emphasising that the ‘process map’ explored a wider range of processing conditions, *i.e.* reaction time; temperature and phosphate concentration, and this focused the attention on the present series of snapshot experiments at known temperature, for the purpose of gaining improved understanding of the hydrothermal growth mechanism. Accordingly, embryonic β -FeOOH NPs and NRs, by way of intermediate phase (Sample Q100), led to the development of small (< 10 nm) α -Fe₂O₃ NPs (Sample Q120) which increased in proportion along with the development of small crystalline α -Fe₂O₃ NRs (Sample Q140). Maximisation of the quantity of small α -Fe₂O₃ NPs and corresponding reduction in the proportion of β -FeOOH NRs with increasing processing temperature (Sample Q160) led to further increase in the quantity and size of α -Fe₂O₃ NRs (Samples Q180 and Q200) at the expense of the α -Fe₂O₃ NPs.

5.3.2.2 Stages of growth

The development of large single crystalline α -Fe₂O₃ NRs can be considered as a two stage process: 1) the growth and dissolution of intermediate β -FeOOH nanostructures, alongside precipitation of α -Fe₂O₃ NPs; and 2) the agglomeration and coarsening of α -Fe₂O₃ primary NPs into α -Fe₂O₃ NRs.

β -FeOOH has been described as being slightly metastable and therefore kinematically accessible when precipitated from aqueous solution.¹⁶ However, due to the very small (< 50 nm) β -FeOOH NP and NR sizes, with positive surface energies by implication, the easily hydrated particle surfaces reduce their effective surface enthalpies by up to 0.1 J/m².¹⁰⁶ Consequently, β -FeOOH NPs become partially thermodynamically stabilised. As mentioned in the discussion of Section 5.2, the Ostwald rule of stages concerns the competition between kinetics, irreversible thermodynamics and equilibrium thermodynamics.¹⁶⁸ A decrease in total surface energy is considered to be the driving force for the crystal growth kinetics of β -FeOOH and α -Fe₂O₃. As the more thermodynamically stable α -Fe₂O₃ primary NPs nucleate and grow, driven by the enthalpy for bond formation at increasing hydrothermal temperatures, the equilibrium Fe³⁺ concentration at the surface of α -Fe₂O₃ becomes lower than that of β -FeOOH. The resulting concentration gradient leads to Fe³⁺ ions flowing from β -FeOOH to the newly formed α -Fe₂O₃ NPs, prompting β -FeOOH dissolution to restore the equilibrium Fe³⁺ concentration at the β -FeOOH surface. An illustration of β -FeOOH dissolution and α -Fe₂O₃ crystal growth based on the Ostwald rule of stages is shown in Figure 5.12a.¹⁶⁶

Further, it is considered that phosphate absorption on the α -Fe₂O₃ NP surfaces acts to stabilise the < 10 nm particle sizes,^{149,175} being distinct from the larger (< 150 nm) isotropic α -Fe₂O₃ NPs which form under surfactant-free conditions.⁷ These primary α -Fe₂O₃ NPs may be considered as ‘building blocks’ that collide and coalesce in an oriented fashion to form the single crystalline acicular α -Fe₂O₃ NRs. It is suggested that preferential phosphate absorption on specific α -Fe₂O₃ crystal faces is consistent with acting to promote the OA mechanism^{176,177} (Figure 5.12b). If the α -Fe₂O₃ NPs are not initially in compatible orientations at the point of coalescence (Figure 5.9d), they are still free to rotate to achieve structural coherence at a common interface (Figures 5.9a and 5.9c). It is considered that this grain-rotation-induced grain coalescence (GRIGC) mechanism^{178,179} acts to minimise the area of high energy interfaces, allowing low-energy configurations to become established, eliminating misoriented grain boundaries and forming coherent grain-grain boundaries in accordance with the model proposed by Zhang *et al.*¹⁷⁶ This OA mechanism appears to be equally applicable to the initial development of α -Fe₂O₃ NRs (Figure 5.9a), as to the attachment of α -Fe₂O₃ primary NPs to well-defined crystalline α -Fe₂O₃ NRs, creating the filamentary features observed at the NR tips (Figure 5.9c).

These two distinct stages of crystal growth will be now discussed in more detail, with emphasis on the pivotal role of the phosphate surfactant on the development of the acicular shape of the α -Fe₂O₃ NRs.

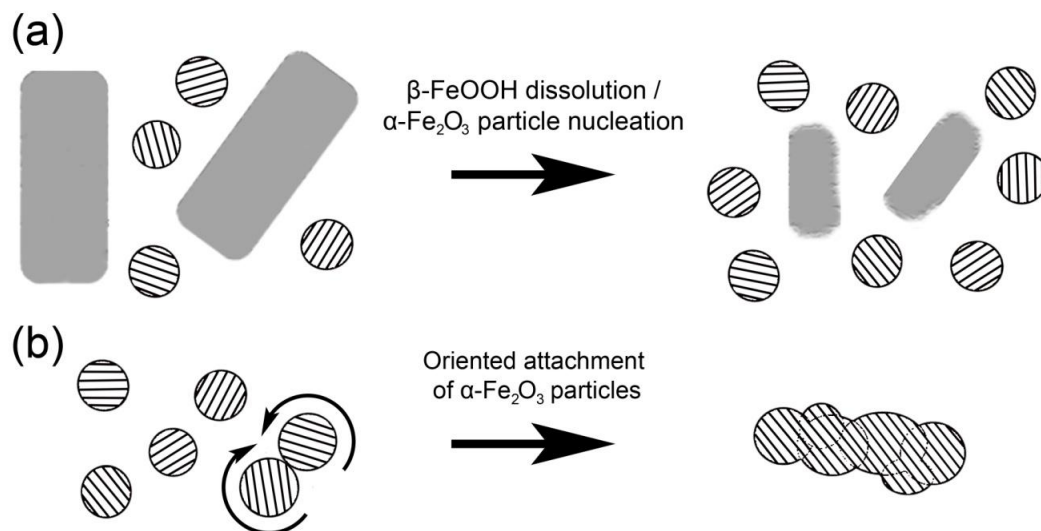


Figure 5.12 Schematic representation showing: (a) dissolution of intermediate β -FeOOH nanostructures (grey shading) alongside precipitation of α -Fe₂O₃ NPs (lined shading), based on the Ostwald rule of stages; and (b) agglomeration, rotation (arrowed) and coarsening of α -Fe₂O₃ primary NPs into an α -Fe₂O₃ NR, based on the OA mechanism.

5.3.2.3 Growth and dissolution of β -FeOOH

The evidence from Samples Q100 and Q120 is consistent with the initial formation of β -FeOOH NPs (~ 15 nm in diameter, Figure 5.7a) followed by the development of β -FeOOH NRs (~ 50 nm long, 15 nm wide, Figure 5.7b) with tetragonal crystal structure (Figure 5.13). The large channels associated with the principal growth *c*-axis (Figure 5.13c) are considered also to be energetically favourable for both growth and dissolution. It is suggested that chlorine and phosphate species occupy these channels, becoming incorporated within the β -FeOOH lattice during HS.^{109,162} It is likely that subsequent dissolution of β -FeOOH NRs occurs along the *c*-axis, with consequent release of any incorporated chemical species back into solution. The marked reduction in the number of β -FeOOH NRs and degradation into smaller β -FeOOH NPs with increasing temperature (Sample Q160), as evidenced by associated SAED patterns (Figure 5.6d), is consistent with this process of β -FeOOH dissolution alongside the development of α -Fe₂O₃ NPs. From a processing point of view, the control of phosphate concentration (combined with temperature and time) provides a mechanism to mediate the supply of Fe³⁺ ions used for the growth of α -Fe₂O₃.

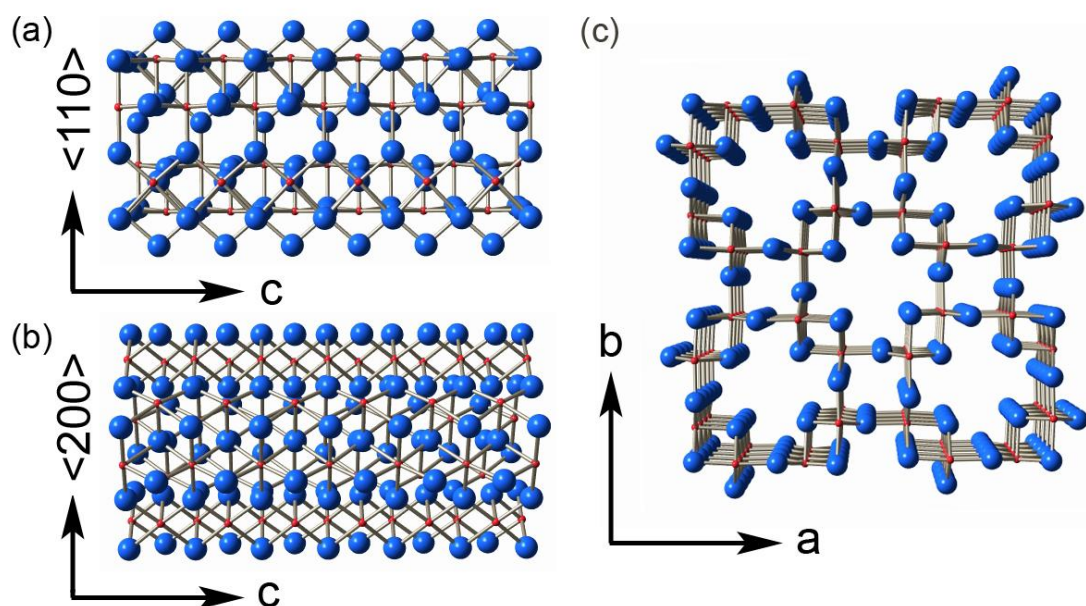


Figure 5.13 Schematic representation of the tetragonal β -FeOOH crystal structure showing: projections along the (a) $\langle 010 \rangle$ and (b) $\langle 110 \rangle$ zone axes; and (c) scaffold-like face normal to the c -axis revealing large channels. Small (red) and large (blue) atoms denote iron and oxygen, respectively. Terminal hydrogen atoms are not shown.

5.3.2.4 Form of the phosphate surfactant

Subtle differences in the Fe 2p data for β -FeOOH and α -Fe₂O₃ (Figure 5.10a) demonstrate that α -Fe₂O₃ (NPs and some NRs) had become the dominant phase by 160°C (Sample Q160), showing a similar XPS signature to that exhibited by fully formed acicular NRs synthesised at 200°C (Sample Q200). Further, noticeable P 2p peaks demonstrated the association of phosphorus, believed to be in the form of a phosphate complex, with both the β -FeOOH and α -Fe₂O₃ surfaces at all synthesis temperatures (Figure 5.10b). In a similar fashion to α -Fe₂O₃, it is considered that these phosphate species act to restrict the size of the β -FeOOH nanostructures (< 50 nm), as compared with β -FeOOH nanostructures (< 60 nm) synthesised in a phosphate-free environment.⁷ As mentioned in Section 4.2.2.3, phosphate complexes on iron hydroxide are known to depend on pH,¹⁸⁰⁻¹⁸² with a general increase in adsorption being associated with decreasing pH. The HS reaction product solution used here exhibited an initial pH < 2, whilst the PZC of β -FeOOH is ~ 8 .¹⁶⁰ Hence, it is again evident that the high phosphate absorption associated with electrostatic attraction acts to suppress both β -FeOOH growth and dissolution.¹⁶⁰

Further, the FTIR evidence presented here is consistent with the absorption of phosphate species on the iron atoms at the α -Fe₂O₃ surfaces, in the form of either mono or bi-dentate complexes. Hence, the form and the role of the phosphate ions

attached to α -Fe₂O₃ needs to be considered in more detail. Assignment of the peaks in the FTIR spectra of Figure 5.11 is made with reference to established literature.¹⁸³⁻¹⁸⁹ For example, Arai *et al*¹⁸³ applied FTIR spectroscopy to investigate surface phosphate complexes on FeOOH surfaces at low pH values, whilst Rose *et al*¹⁸⁴ and Wilhelmy *et al*¹⁸⁵ both suggested mono-dentate phosphate complexation with ferric ions at pH < 2 when using ferric chloride precursors under specific conditions. In this context, the single broad FTIR peak (Figure 5.11b) for Sample S100 at $\sim 1050\text{ cm}^{-1}$ can be deconvoluted into peaks at 997, 1056 and 1111 cm^{-1} and these ν_3 bands, consistent with C_{2v} symmetry or lower,¹⁸¹ are in good agreement with the three ν_3 band¹⁷⁴ splitting signatures of mono or bi-protonated mono-dentate mononuclear phosphate complexes (FeHPO₄²⁺ or FeH₂PO₄²⁺, both with C₁ symmetry).¹⁸⁵ The additional peak at $\sim 850\text{ cm}^{-1}$ is characteristic of the β -FeOOH phase.¹⁸⁶

In particular, the FTIR spectra from Samples Q160 and Q200 (Figure 5.11) provide valuable clues as to the nature of the phosphate complexes on the surfaces of both the α -Fe₂O₃ NPs and NRs. Elzinga *et al*¹⁸⁷ reported on IR spectra of phosphate complexes bonding in a bi-dentate (bridging) fashion with hematite surfaces at low pH values. Accordingly, it is considered that the hematite rich reaction products examined here (Samples Q160 – Q200, pH ~ 1) exhibited similar phosphate bi-dentate surface complexes. Deconvolution of the IR spectrum of Sample Q160 revealed strong peaks at 898, 934, 970, 1004, 1036, 1071 and 1149 cm^{-1} , (Figure 5.11d) which are all consistent with ν_3 bands, with the exception of one ν_1 band at 898 cm^{-1} .¹⁷⁴ The three ν_3 bands at 934, 1036 and 1071 cm^{-1} are assigned to the presence of H₂PO₄²⁻ surface species with C_{2v} symmetry or lower.¹⁸⁵ According to Borgnino *et al*,¹⁸⁸ this group of shifted H₂PO₄²⁻ vibrations are indicative of ‘inner-sphere surface complexes,’ attributable to the initial formation of the bi-dentate complex (FeO)₂PO₂.¹⁸⁹ It is reasonable to assume this complex becomes protonated ((FeO)₂P(OH)₂ with C_{2v} symmetry,¹⁸⁷ at the low pH conditions associated with the HS system examined here. However, the three ν_3 bands at 970, 1004 and 1136 cm^{-1} , also indicative of C_{2v} symmetry or lower, are attributable either to a mono-protonated bi-dentate complex (FeO)₂(OH)PO or protonated mono-dentate surface complex (FeO)(OH)₂PO (both with C₁ symmetry).¹⁸⁷⁻¹⁸⁹

5.3.2.5 Role of the phosphate surfactant

The coordination of phosphate species on the surface of α -Fe₂O₃ (NPs and NRs) may be considered in terms of the orientation of the crystal lattice. It was suggested in Section 4.2.2.3 that the surfactant is adsorbed preferentially on faces parallel to the c-axis of α -Fe₂O₃, in view of the better matching of the O-O inter-atomic distance of PO₄³⁻ anions (2.50Å) with the Fe-Fe spacing parallel rather than perpendicular to this axis.¹⁴² Modelling using *CaRine* software showed the smallest Fe-Fe distances within the α -Fe₂O₃ lattice oriented parallel and normal to the c-axis to be 2.88Å and 5.02Å, respectively (Figure 5.14). Hence, it is considered that the crystal structure of α -Fe₂O₃ surface parallel to the c-axis is favourable for the formation of bridging bi-dentate phosphate complexes, whilst such complex formation is not favourable on the c-plane. By implication, it is considered that mono-dentate mononuclear phosphate complex absorption is associated more closely with the c-plane. On this basis, configurations for the most strongly absorbed phosphate complexes on faces normal and parallel to the c-axis (without protonation) are proposed in Figures 5.14a and 5.14b, respectively. The association of the mono-dentate phosphate complex with the c-plane implies weaker absorption, as compared with the bi-dentate phosphate complex associated with planes parallel to the c-axis. This disparity is considered critical for mediating the attachment of the primary α -Fe₂O₃ NPs, and through the filamentary feature growth (Figure 5.9c), governs the acicular shape of the developing α -Fe₂O₃ NRs. The inference is that it is easier for such mono-dentate surfactant complexes to be displaced during α -Fe₂O₃ growth, as compared with bi-dentate complexes, consistent with the α -Fe₂O₃ crystal c-faces being favourable surfaces for OA.

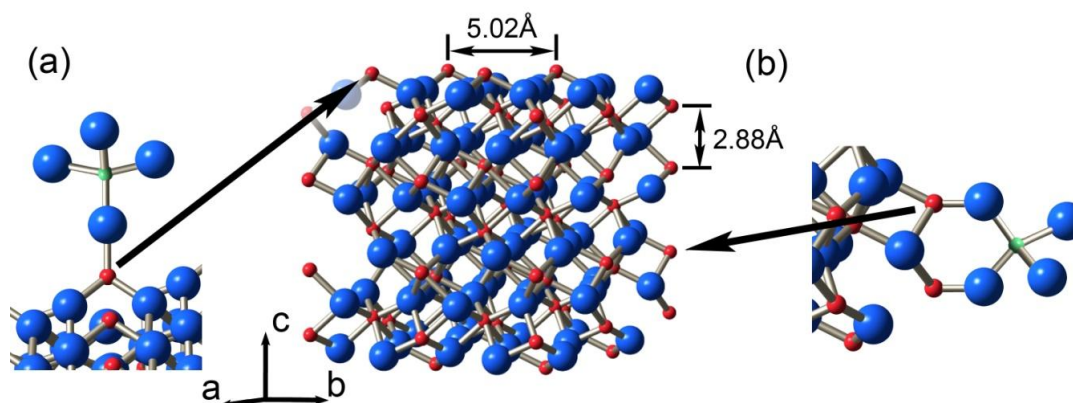


Figure 5.14 Schematic diagram of the hexagonal α -Fe₂O₃ crystal lattice showing (a) mono-dentate phosphate adsorption on the c-plane; and (b) bi-dentate phosphate adsorption on a faces parallel to the c-axis (Red (small), blue (large) and green (smallest) spheres correspond to iron, oxygen and phosphorus, respectively.)

5.3.2.6 Growth mechanism

The schematic diagram of Figure 5.15 summarises the results of this *in situ* ‘snapshot’ approach, as used to investigate the hydrothermal growth of α -Fe₂O₃ NRs as a function of known temperature. During Step 1 (100°C), HS promotes the initial precipitation of kinematically accessible β -FeOOH NPs and NRs and a few α -Fe₂O₃ NPs. Step 2 (120°C) illustrates the further nucleation of α -Fe₂O₃ NPs at increased temperature. During Step 3 (140°C), β -FeOOH dissolution begins to occur in response to the Fe³⁺ concentration gradient established with the additional nucleation of the more thermodynamically stable α -Fe₂O₃ NPs. This further increase in temperature also provides the driving force for the suggested OA of α -Fe₂O₃ NPs, mediated by the stronger adsorption of bi-dentate (bridging) phosphate inner sphere complexes to faces parallel to the α -Fe₂O₃ c-axis. Step 4 (160°C) illustrates the degradation of β -FeOOH NRs to a size similar to that of the α -Fe₂O₃ NPs, through dissolution of loosely packed c-planes. Thereafter, the α -Fe₂O₃ NRs grow and coarsen further during Steps 4 to 6 (160 - 200°C) through the OA mechanism, until the supply of the primary α -Fe₂O₃ NPs is exhausted. The highest hydrothermal temperature of 200°C, after a processing time of 80 minutes in this instance, results in the production of large, acicular, single crystalline α -Fe₂O₃ NRs.

Chapter 5 HS growth mechanism derived from analysis of quenched samples

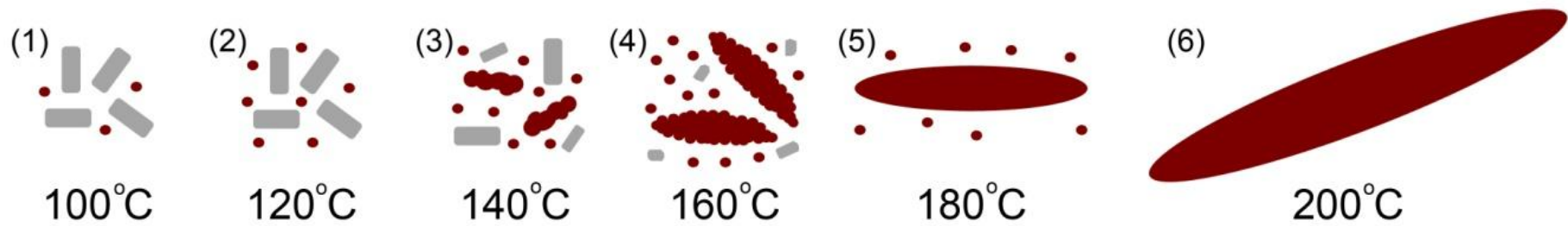


Figure 5.15 Schematic diagram summarising the HS growth mechanism for α -Fe₂O₃ NRs, as a function of increasing temperature: (1) precipitation of β -FeOOH NPs and NRs (grey), and α -Fe₂O₃ NPs (brown); (2) nucleation of additional α -Fe₂O₃ NPs; (3) dissolution of β -FeOOH NRs alongside oriented α -Fe₂O₃ NP attachment; (4) dissolution of β -FeOOH NRs into NPs and growth of α -Fe₂O₃ NRs; (5) growth and coarsening of α -Fe₂O₃ NRs; and (6) large, single crystalline α -Fe₂O₃ NRs.

5.4 *In situ* TEM investigation of α -Fe₂O₃ NR growth

It is recognised that examination of static reaction products, as seen in Sections 5.2 and 5.3, only presents snapshot evidence for the dynamic evolution of nanostructures. In this context, complementary *i*TEM investigation into the development of β -FeOOH and α -Fe₂O₃ NRs, providing fundamental insight into the growth of these nanostructures as a function of temperature, for comparison with the quenched HS reaction products, is presented. In this instance, ‘snapshot’ samples S100 and S160 from Section 5.3 allowed for *i*TEM investigation of the intermediate stages of β -FeOOH and α -Fe₂O₃ development as a function of temperature (room temperature to 450 °C at 50°C / min under vacuum), performed using a Gatan double tilt heating holder within the Jeol 2100F TEM.

5.4.1 Results

Use of the 50 ml valve-assisted Teflon-lined stainless steel pressure autoclave enabled investigation of the hydrothermal processing of aqueous FeCl₃ solution, for the synthesis of β -FeOOH and α -Fe₂O₃ nanostructures. The systematic investigation of quenched HS samples enabled a model describing the formation of α -Fe₂O₃ acicular NRs to be developed (Section 5.3.2.6), based on Ostwald’s rule of stages for the dissolution of β -FeOOH NRs and the formation of α -Fe₂O₃ NPs followed by a process of α -Fe₂O₃ NR growth based on the OA mechanism, as shown in Section 5.3.2.2. Further investigation of these samples using *i*TEM provided complementary dynamic information in support of this model, the evidence for which is now presented in detail.

5.4.1.1 *i*TEM investigation of β -FeOOH

Figure 5.16 presents BF diffraction and phase contrast TEM images of Sample Q100 acquired during the process of *in situ* heating within the TEM. When imaged at room temperature, Sample Q100 comprised small β -FeOOH NRs and small α -Fe₂O₃ NPs (Figure 5.16a). Indeed, fringes lying parallel to the major growth axis of the NRs within this sample were characteristic of the {200} β -FeOOH lattice planes (Figure 5.16d). Selected images from a time lapse series acquired during *in situ* heating of Sample S100 up to 450°C provided insight into the dynamic transformation of β -

FeOOH NRs into embryonic and developed α -Fe₂O₃ NPs with increasing temperature (Figures 5.16b&c, arrowed). The high magnification image of a NP in Figure 5.16e, showing {024} lattice fringes, confirmed these developed NPs to be α -Fe₂O₃.

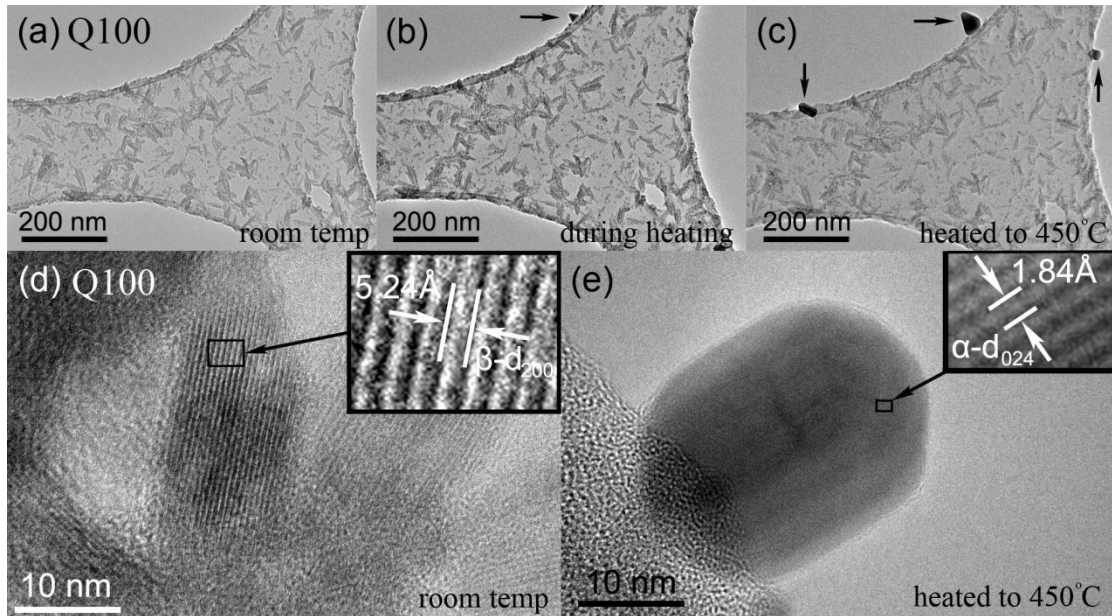


Figure 5.16 BF and phase contrast TEM images of Sample Q100 ‘quenched’ after 80 minutes of processing (a) examined at room temperature; (b) during *in situ* heating, revealing the formation of an α -Fe₂O₃ NP (arrowed); (c) heated *in situ* to 450°C, revealing the growth of α -Fe₂O₃ NPs (arrowed); (d) small developing β -FeOOH NR (~ 30 nm long, ~ 15 nm wide) identified by lattice fringes (inset); and (e) high magnification of an α -Fe₂O₃ NP grown during *in situ* heating, identified by lattice fringes (inset).

5.4.1.2 TEM investigation of α -Fe₂O₃

Figure 5.17 presents phase contrast images of Sample Q160 taken from a time lapse series during the process of *in situ* heating. Figure 5.17a shows the tip of a developing α -Fe₂O₃ NR, comprising small, loosely packed α -Fe₂O₃ NPs. Significant coarsening of the NR tip was evident following *in situ* heating up to 450°C (Figure 5.17b).

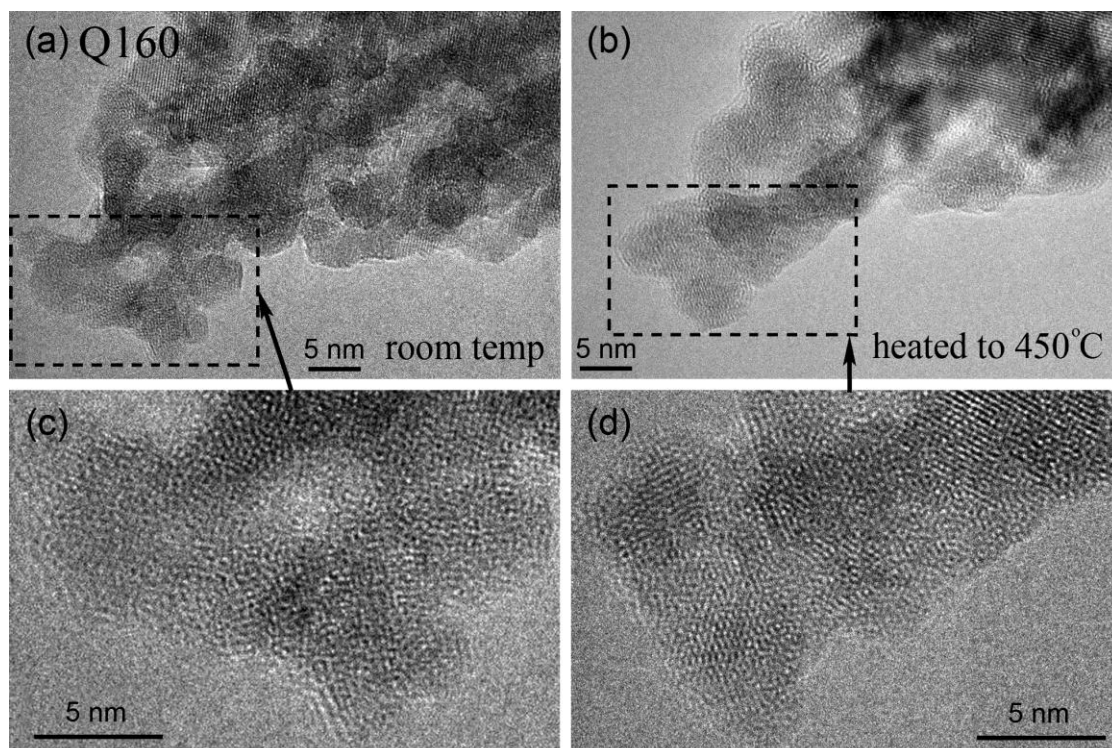


Figure 5.17 BF and phase contrast TEM images of Sample Q160 ‘quenched’ after 80 minutes of processing. (a) The tip of an individual α -Fe₂O₃ NR at room temperature, shown to comprise loosely packed α -Fe₂O₃ NPs (enlarged in (c)); (b) tip of the individual α -Fe₂O₃ NR shown in (a) after *in situ* heating to 450°C, observed to have undergone coarsening (enlarged in (d)).

5.4.2 Discussion

Direct observation of the transformation of β -FeOOH into α -Fe₂O₃ NPs (Figure 5.16) and the coarsening of the tips of α -Fe₂O₃ NRs through the consumption and coalescence of α -Fe₂O₃ NPs (Figure 5.17) was provided by time lapse imaging, during the *in situ* heating of quenched HS samples within the TEM. The caveat being that these transformations occurred in vacuum rather than within aqueous media in the presence of phosphate a surfactant. Nevertheless, the evidence demonstrates that β -FeOOH feeds the development of α -Fe₂O₃ NPs, which in turn feed the development of α -Fe₂O₃ NRs through a process of OA and coarsening, albeit at higher temperatures than those experienced during HS. It is noted that the developing α -Fe₂O₃ NPs adopt pyramidal and rhombohedral shapes in the absence of the mediating surfactant.

In the case of both HS processing and *i*TEM heating, it is evident that thermal energy is needed to promote the breakdown of the less thermodynamically stable β -FeOOH NRs (Figure 5.16a), releasing Fe³⁺ anions into the local ambient to supply the growth and development of the α -Fe₂O₃ NPs. Indeed, comparison of the HS sample Q160 (Figure 5.8) and the heat treated Sample Q100 (Figure 5.17c) indicates a

significant reduction in the proportion of β -FeOOH NRs along with an increase in the number of small α -Fe₂O₃ NPs, as a result of increasing temperature. Further, direct observation of the development of the tips of individual acicular α -Fe₂O₃ NRs during *in situ* TEM heating, with loosely packed small α -Fe₂O₃ NPs (Figure 5.17a) coarsening into well crystallised α -Fe₂O₃ NRs (Figure 5.17b) supports the model proposed for the formation of acicular α -Fe₂O₃ NRs, through the coalescence of primary α -Fe₂O₃ NPs by a mechanism of OA and coarsening, with increasing temperature.

5.5 Summary

Use of a novel valve-assisted pressure autoclave to facilitate ‘snapshot’ investigation of HS product suspensions rapidly quenched in liquid nitrogen has been presented. The approach gave descriptions closely representative to the *in situ* physical state of the HS reaction products, providing fundamental insight into the mechanisms of crystal growth. The viability of this ‘snapshot’ approach to provide information on the localised development of high aspect ratio acicular α -Fe₂O₃ NRs as a function of reaction time was investigated. A more detailed description of the development of 1D α -Fe₂O₃ nanostructures, as a function of known reaction temperature, provided for better understanding of the growth mechanism of α -Fe₂O₃ NRs. Dissolution of the β -FeOOH phase with increasing temperature, in accordance with Ostwald’s rule of stages, led to the release of Fe³⁺ anions back into solution to supply the growth of α -Fe₂O₃ NPs, which in turn coalesced to form acicular α -Fe₂O₃ NRs. The critical role of the PO₄³⁻ surfactant on mediating the acicular shape of the α -Fe₂O₃ NRs was emphasised. Strong phosphate anion absorption on α -Fe₂O₃ crystal surfaces stabilised the primary α -Fe₂O₃ NP size to < 10 nm. FTIR investigation of the quenched reaction products provided evidence for PO₄³⁻ absorption on the α -Fe₂O₃ NPs in the form of mono or bi-dentate (bridging) surface complexes on surfaces normal and parallel to the crystallographic α -Fe₂O₃ c-axis, respectively. Mono-dentate PO₄³⁻ absorption is considered weaker and hence easily displaced during growth, as compared to absorbed PO₄³⁻ bi-dentate species, which implies the α -Fe₂O₃ c-planes are favoured for the OA of primary α -Fe₂O₃ NPs, resulting in the development of filamentary features which act as the basis of growth, defining the shape of the acicular α -Fe₂O₃ NRs. *i*TEM investigation of β -FeOOH and α -Fe₂O₃ NRs, compared with the quenched HS reaction products, provided fundamental insight into the localised growth of these nanostructures as a function of temperature. The heating of quenched HS samples *in situ* within the TEM has provided direct evidence in support of the proposed mechanism for the formation of acicular α -Fe₂O₃ NRs.

Chapter 6 Hydrothermal synthesis of α -Fe₂O₃ NRs in the presence of CoCl₂, Co₃O₄ and CoFe₂O₄

6.1 Introduction

In this chapter, a feasibility study on the incorporation of ferromagnetic cobalt into α -Fe₂O₃ NRs for the purpose of improving their magnetic performance is presented. The effects of CoCl₂ salt addition on α -Fe₂O₃ NR growth and the formation of Co₃O₄ and CoFe₂O₄ NPs are investigated as a function of pH value. Further, the effect of FeCl₃ : CoCl₂ precursor ratio and phosphate surfactant on the phase purity and size of CoFe₂O₄ NPs is examined, respectively. The inclusion of Co₃O₄ and CoFe₂O₄ NPs during α -Fe₂O₃ NR growth is described. The range of HS experimental conditions investigated and the reaction products produced are summarised in Table 6.1; the evidence for which is now presented in detail.

6.2 Effect of CoCl₂ salt on the growth of α -Fe₂O₃ NRs

FeCl₃ acts a simple precursor for the formation of α -Fe₂O₃ NRs in the presence of phosphate. Likewise, CoCl₂ is a metal salt comprising a transition metal and chlorine, and hence is considered a potential precursor for the incorporation of elemental cobalt into α -Fe₂O₃ NRs because Co²⁺ ions are the only elemental addition to the solution. Accordingly, the effect of cobalt on the growth of α -Fe₂O₃ NRs was initially investigated, with the addition of 100 mg of CoCl₂ to the HS precursor solution (0.2 ml FeCl₃ solution, further diluted in 40 ml water, 3mg NH₄H₂PO₄) and heated at 200°C for 2 hours ('cobalt' sample labelled C1, for simplicity). Further, the possibility of α -Fe₂O₃ NRs as growth templates was investigated. 100 mg of CoCl₂ was added to a reaction product suspension of α -Fe₂O₃ NRs (Sample S14 from Chapter 4), already grown from the standard HS precursor solution (0.2 ml FeCl₃ solution, further diluted in 40 ml water, 3mg NH₄H₂PO₄, heated in the standard 125 ml Teflon-lined stainless steel pressure autoclave at 200°C for 2 hours), which were centrifuged, cleaned in acetone and ultrasonically dispersed in 40 ml water. In this case, the pH value of the suspension was altered using NaOH aqueous solution, added drop-wise until a pH of

Sample	CoCl ₂ / mg	FeCl ₃ / ml	Fe : Co	NH ₄ H ₂ PO ₄ / mg	pH	Reaction product	Morphology	Dimension (l/w) / nm
S14	-	0.2	-	3	2	α -Fe ₂ O ₃	Fully formed acicular NRs	<420/60
S14*	100	-	-	-	8	α -Fe ₂ O ₃ + Co ₃ O ₄	Fully formed acicular NRs + NPs	<420/60 + <100
C1	100	0.2	1:1	3	2	α -Fe ₂ O ₃	Fully formed acicular NRs	<950/130
C2	20	-	-	-	8	Co ₃ O ₄	NPs	<30
C2*	-	0.2	-	3	2	α -Fe ₂ O ₃ + Co ₃ O ₄	Fully formed acicular NRs + NPs	<420/60 + <30
F1	50	0.2	2:1	-	12	α -Fe ₂ O ₃ + CoFe ₂ O ₄	NPs	<50
F2	25	0.1	2:1	-	12	α -Fe ₂ O ₃ + CoFe ₂ O ₄	NPs	<50
F3	50	0.1	1:1	-	12	α -Fe ₂ O ₃ + CoFe ₂ O ₄	NPs	<50
F4	25	0.05	1:1	-	12	α -Fe ₂ O ₃ + CoFe ₂ O ₄	NPs	<50
F5	25	0.05	1:1	3	12	CoFe ₂ O ₄	NPS	<30
F6	25	0.05	1:1	6	12	CoFe ₂ O ₄	NPS	<20
F6*	-	0.2	-	3	2	α -Fe ₂ O ₃ + CoFe ₂ O ₄	Fully formed acicular NRs + NPs	<420/60 + <20

Table 6.1 HS processing variables and a summary of the reaction products, morphologies and dimensions. * Denotes a secondary HS process for selected samples. In all cases, HS was performed at a reaction temperature of 200°C for 2 hours.

~ 8 was reached. The modified HS suspension was then reheated at 200°C for 2 hours (labelled S14*, whereby * denotes a secondary HS process).

6.2.1 Results and discussion

The BF TEM images of Figure 6.1a & c illustrate the effect of adding 100 mg CoCl₂ to the FeCl₃ hydrothermal solution before (Sample C1) and after (Sample S14*) the formation of α -Fe₂O₃ NRs, respectively. Figure 6.1a illustrates the presence of a large acicular α -Fe₂O₃ NR (950 nm long, 130 nm wide) in Sample C1, as identified by the associated SAED. Smaller α -Fe₂O₃ NRs (450 nm long, 70 nm) and NPs (< 100 nm in diameter) were observed in Sample S14* (Figure 6.2c).

The EDX spectrum of Figure 6.1b (Sample C1), recorded using a spot size on the scale of the α -Fe₂O₃ NR (Figure 6.1a), indicated the presence of phosphorus in addition to the expected signals for iron and oxygen (and a Cu artefact signal arising from the specimen support grid). In this case the specimen was cleaned in acetone prior to chemical analysis.

The associated XRD patterns of Figure 6.1d confirmed the formation of α -Fe₂O₃ in both Sample C1 and S14*. However, additional diffraction peaks present in the XRD pattern of Sample S14*, found to be in excellent agreement with database values for the formation of Co₃O₄ (indexed appropriately, JCPDS 43-1003).

Even though the TEM image and associated SAED of Sample C1 (Figure 6.1a) shows the formation of large α -Fe₂O₃ NRs, a Co signal was not present in the associated EDX spectra, indicating the formation of α -Fe₂O₃ only. No evidence suggesting the formation or incorporation of cobalt within the α -Fe₂O₃ crystal lattice was obtained. The P signal was attributed to phosphorus from the surfactant trapped within the developing α -Fe₂O₃ NR, in a fashion akin to Sample S14.

Similarly, the NRs of Sample S14* were identified as being the α -Fe₂O₃ growth templates (similar in size to Sample S14) whilst the NPs were identified as Co₃O₄. There was no indication that these α -Fe₂O₃ NRs and Co₃O₄ NPs formed hetero-nanostructures, but had simply agglomerated during drying.

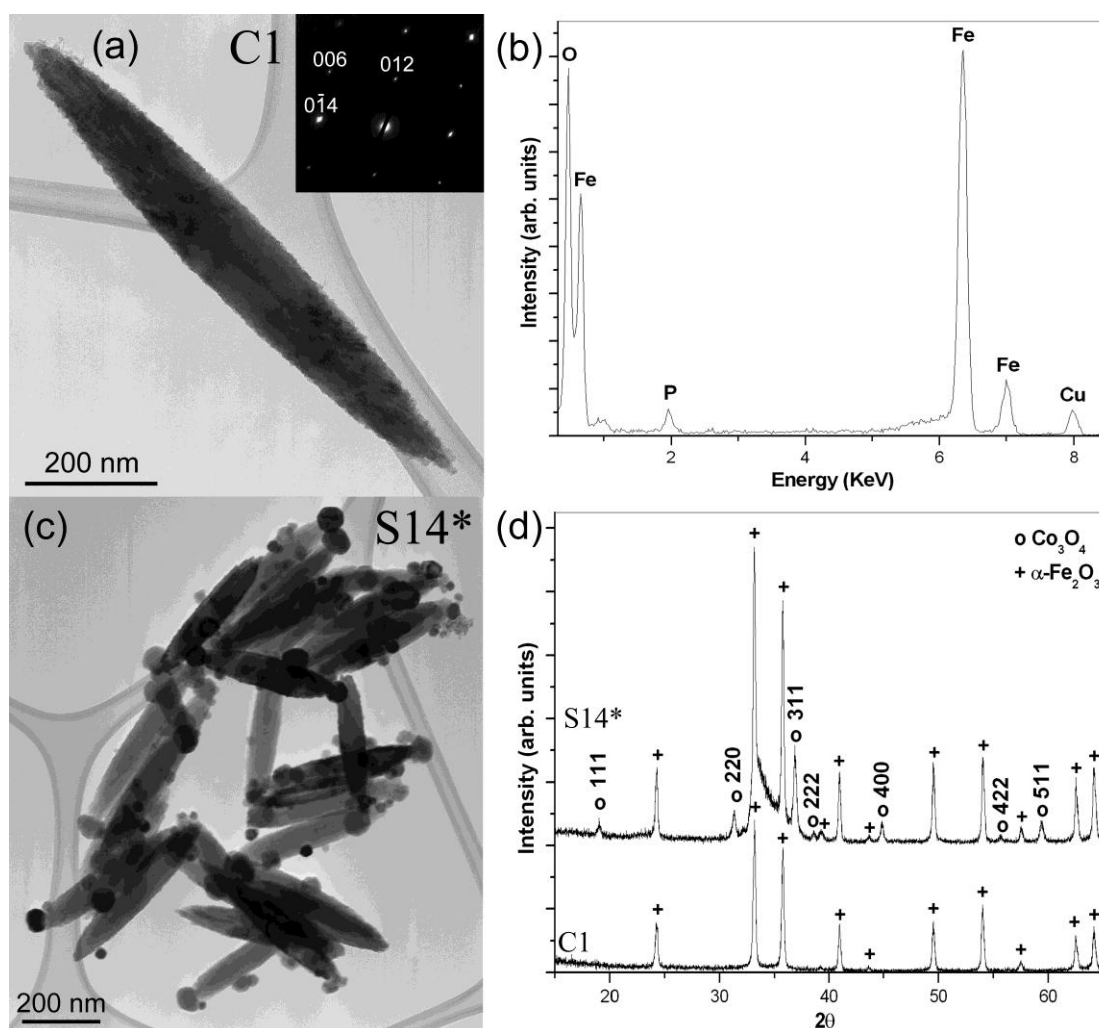


Figure 6.1 (a) BF TEM image of hydrothermal products with 100 mg CoCl₂ added to the FeCl₃ precursor solution before heating, with SAED inset. (b) Associated EDX spectrum acquired from Sample C1 shown in (a). (c) BF TEM image of hydrothermal products with 100 mg CoCl₂ added to α -Fe₂O₃ reaction product suspension after heating, pH altered to \sim 8 and reheated to 200°C for 2 hours. (d) Associated XRD patterns of Samples C1 and S14* showing the formation of α -Fe₂O₃; and a mixture of α -Fe₂O₃ and Co₃O₄ (indexed, JCPDS 43-1003), respectively.

No evidence of cobalt incorporation in α -Fe₂O₃ NRs in Sample C1 or the formation of Co₃O₄ implies the CoCl₂ remained in solution at low pH. It is considered that Co₃O₄ NPs could not form in the low pH (< 2) conditions exhibited by Sample C1 because atomic cobalt is too active to exist in acidic or neutral solutions,^{190,191} and therefore exists as cobaltous cations, Co²⁺. Also, it is noted that the α -Fe₂O₃ NRs of Sample C1 were significantly larger than the size of α -Fe₂O₃ NRs in Sample S14. It is speculated that the presence of Co²⁺ cations in Sample C1 has promoted the increase in size of the α -Fe₂O₃ NRs, possibly by hindering the OA of primary α -Fe₂O₃ NPs or increasing their size, resulting in fewer centres of aggregation, allowing a larger supply of primary α -Fe₂O₃ particles to feed the growth of individual α -Fe₂O₃ NRs,

explaining the increase in their size. Hence, Co²⁺ cations are considered to have the opposite effect on NR growth as compared with α -Fe₂O₃ seeds (Section 4.6).

NaOH addition was required to make Sample S14* basic (pH ~ 8) and promote Co₃O₄ NP precipitation, as expressed in the following simplified reaction equation:

Precipitation of Co₃O₄



No change in size or shape of the α -Fe₂O₃ NRs was apparent in Sample S14*. Hence the slightly basic contribution to the reaction product solution is not considered sufficiently corrosive to promote α -Fe₂O₃ dissolution. As shown in Sections 4.4 and 5.3.2.4, low pH values are needed for the anisotropic growth of the α -Fe₂O₃ NRs, mediated by bi-dentate phosphate absorption. It is recognised that α -Fe₂O₃ NRs and Co₃O₄ NPs cannot nucleate and grow at the same pH values. Accordingly, the next section concerns an investigation of the growth of α -Fe₂O₃ NRs in the presence of Co₃O₄ NPs.

6.3 Effect of Co₃O₄ NPs on the growth α -Fe₂O₃ NRs

It was found that Co₃O₄ NPs did not nucleate and grow in solution at low pH values (< 2) (Section 6.2). However, low pH values are required for the anisotropic growth of α -Fe₂O₃ NRs, involving the OA of primary α -Fe₂O₃ NPs, mediated by bi-dentate phosphate surface absorption, as shown in Chapter 5. Accordingly, the influence of preformed Co₃O₄ NPs on the development of α -Fe₂O₃ NRs was investigated. 20 mg CoCl₂ was diluted in 40 ml water (Samples C2), NaOH aqueous solution was added drop-wise until a pH ~ 8 was reached, before sealing in the standard 125 ml Teflon-lined stainless steel pressure autoclave and heating at 200°C for 2 hours. The resulting Co₃O₄ NPs of Sample C2 (Figure 6.2a) were centrifuged, cleaned with acetone and ultrasonically dispersed in the standard precursor solution for α -Fe₂O₃ NRs (0.2 ml FeCl₃ solution, further diluted in 40 ml water, 3mg NH₄H₂PO₄) in the standard pressure autoclave, which was again sealed and heated at 200°C for 2 hours (Sample C2*).

6.3.1 Results and discussion

The BF TEM image of Figure 6.2a illustrates the size of the Co₃O₄ NPs (the phase was identified by SAED), found to be < 30 nm (Sample C2), resulting from the HS of 20 mg of CoCl₂ in pH modified aqueous solution.

The TEM images of Figures 6.2b & c illustrate the effect of adding these Co₃O₄ NPs to the precursor solution on the α -Fe₂O₃ NR growth (Sample C2*). TEM surveying of Sample C2* demonstrated that the small Co₃O₄ NPs were attached to the surfaces of the α -Fe₂O₃ NRs (Figure 6.2b, arrowed), which were similar to these seen in Sample S14* (Figure 6.1c). Figure 6.2c (arrowed) shows examples of Co₃O₄ NPs situated at the tip of an individual α -Fe₂O₃ NR.

The associated XRD patterns of Figure 6.2d confirmed the formation of Co₃O₄ and α -Fe₂O₃ in Samples C2 and C2*, respectively.

The TEM image of Figure 6.2a (Sample C2, 20 mg CoCl₂ addition) when compared to Sample S14* (Figure 6.1c, 100 mg CoCl₂ addition, Section 6.2) demonstrated a decrease in Co₃O₄ NP size from < 100 nm to < 30 nm. This reduction in NP size with decreasing CoCl₂ concentration is similar to the decrease of α -Fe₂O₃

NP size with decreasing FeCl₃ concentration (Section 4.3). The smaller Co₃O₄ NPs of Sample C2 were considered potentially suitable for incorporation within α -Fe₂O₃ NRs during growth and were therefore dispersed in the α -Fe₂O₃ hydrothermal precursor solution.

The TEM images of Sample C2* (Figures 6.2b & c) shows the presence of Co₃O₄ NPs on the surface and tips of the α -Fe₂O₃ NRs. However, there was no evidence that the Co₃O₄ NPs were incorporated into the α -Fe₂O₃ NRs.

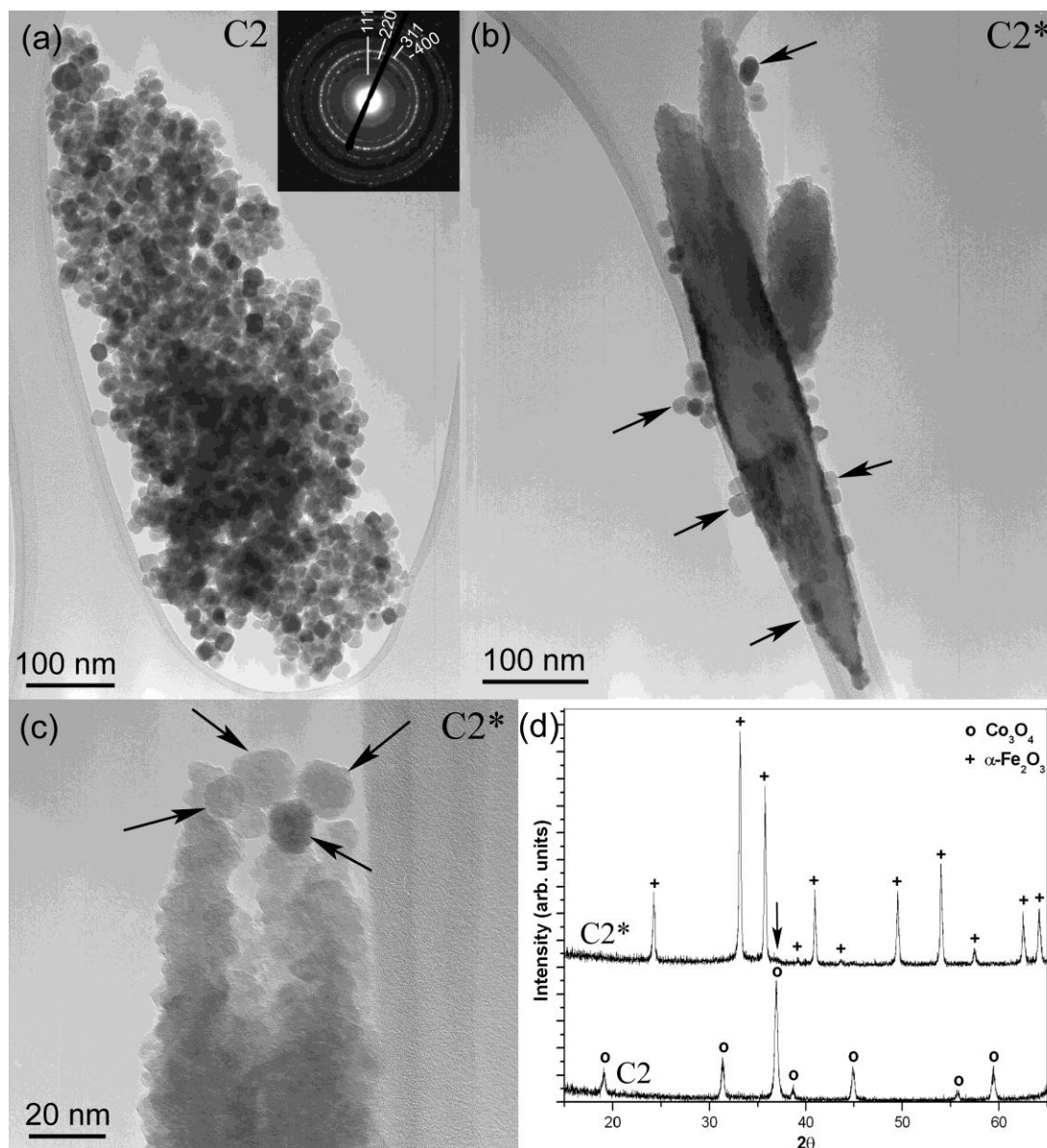


Figure 6.2 BF TEM images of (a) hydrothermal products synthesised with 20 mg CoCl₂, with corresponding SAED (inset – indexed to Co₃O₄); (b) α -Fe₂O₃ NRs synthesised with the addition of Co₃O₄ NPs (arrowed) from Sample C2; and (c) Co₃O₄ NPs (arrowed) at the tip of an individual α -Fe₂O₃ NR. (d) Associated XRD patterns of Sample C2 and C2* showing the formation of Co₃O₄ and α -Fe₂O₃, respectively, with a small peak corresponding to the {311} set of lattice planes of Co₃O₄ in the latter (arrowed).

The XRD pattern of Sample C2* confirmed the presence of the α -Fe₂O₃ phase. A small peak at $\sim 37^\circ$ (arrowed), positioned at the same 2θ value as the highest peak intensity of Sample C4, was attributed to the {311} set of Co₃O₄ lattice planes. The volume fraction of Co₃O₄ NPs in Sample C2* was extremely low, suggesting that the Co₃O₄ NPs had dissolved during α -Fe₂O₃ NR growth at this low pH. This is consistent with the inference that cobalt exists as Co²⁺ cations at low pH values,^{190,191} and dissolution of Co₃O₄ NPs would mediate against their incorporation into the α -Fe₂O₃ NRs.

6.4 Growth of CoFe₂O₄ NPs

HS of an aqueous solution comprising CoCl₂, FeCl₃ and NH₄H₂PO₄ surfactant in 40 ml water at pH ~ 12 (altered drop-wise using NaOH aqueous solution) led to the production of discrete batches of CoFe₂O₄, varying in phase purity (cobalt ‘ferrite’ samples labelled F1 – F6, for simplicity), as summarised in Table 6.1. The solution was sealed in the standard 125 ml Teflon-lined stainless steel pressure autoclave and heated at 200°C for 2 hours. The production of CoFe₂O₄ required the addition of a strong base in order to suppress the tendency of higher charge Fe³⁺ ions to precipitate out of solution at a lower temperature than the Co²⁺ ions. Alteration of the pH to ~ 12 shifts the equilibrium of both metal cations toward the formation of hydroxides, so that they can precipitate simultaneously; promoting the growth of CoFe₂O₄ NPs.⁹⁰

6.4.1 Results and discussion

The BF TEM images of Figure 6.3 illustrate the effect of varying the amount of CoCl₂ and FeCl₃ precursor in 40 ml water (Samples F1 – F4). In all cases, the NPs were identified as CoFe₂O₄ by SAED (Figure 6.3d, inset) and observed to range in size from ~ 10 nm up to ~ 50 nm (Figures 6.3a – d).

The associated XRD patterns of Figure 6.3e confirmed the presence of CoFe₂O₄ and α -Fe₂O₃ in Samples F1 – F4. The XRD patterns of Samples F1 and F2 exhibited peaks characteristic to both CoFe₂O₄ (JCPDS 1-1121) and α -Fe₂O₃. However, a relative decrease in the α -Fe₂O₃ peak intensities were seen in Samples F3 and F4, along with broad overlapping peaks at ~ 33 – 37°.

TEM investigation of Samples F5 and F6 revealed CoFe₂O₄ NPs < 30 nm and < 20 nm, respectively (Figure 6.4a & b, respectively). Further, the XRD patterns of Figure 6.4c chart the effect of increasing phosphate concentration on the CoFe₂O₄ and α -Fe₂O₃ phase proportions in Samples F4 – F6. The XRD pattern of F4 revealed an α -Fe₂O₃ peak intensity at ~ 33° comparable to the {311} CoFe₂O₄ peak intensity at ~ 37°, along with overlapping intermediate peak intensities. A comparative decrease in the α -Fe₂O₃ intensity was seen in Sample F5, reduced further in Sample F6. However, the overlapping peak intensities were absent from both Samples F5 and F6.

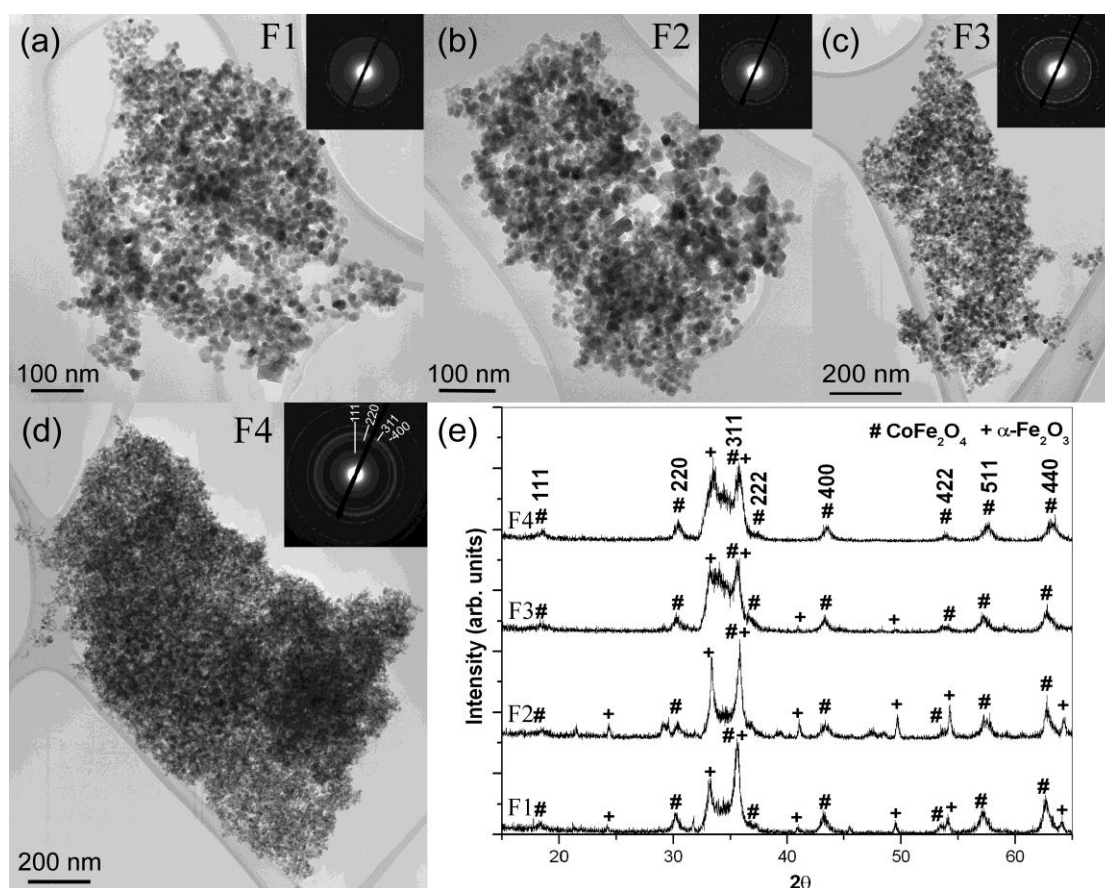


Figure 6.3 BF TEM images of hydrothermal products synthesised in 40 ml water at 200°C for 2 hours with (a) 0.2 ml FeCl_3 and 50 mg CoCl_2 ; (b) 0.1 ml FeCl_3 and 25 mg CoCl_2 ; (c) 0.1 ml FeCl_3 and 50 mg CoCl_2 ; and (d) 0.05 ml FeCl_3 and 25 mg CoCl_2 , with SAED indexed to CoFe_2O_4 (inset). (e) Associated XRD patterns of Samples F1 – F4 showing the formation of CoFe_2O_4 (JCPDS 1-1121) and α - Fe_2O_3 .

The TEM images of Figure 6.3 demonstrate CoFe_2O_4 NPs of similar size (~ 10 to 50 nm in diameter). The associated XRD data revealed that Samples F1 and F2, with a Fe : Co molar ratio of ~ 2 , comprised a significant proportion of α - Fe_2O_3 . The small size of the α - Fe_2O_3 NPs was consistent with a decrease in α - Fe_2O_3 particle size with increasing pH,¹⁹² in contrast to Sample S4 (Section 4.2.1.1). Reduction in the FeCl_3 content to a Fe : Co molar ratio of ~ 1 resulted in a decreased α - Fe_2O_3 proportion in Samples F3 and F4. Hence, the Fe : Co molar ratio is considered critical in achieving an adequate CoFe_2O_4 phase purity. The broad overlapping XRD peaks ($\sim 33 - 37^\circ$) were attributed tentatively to an unstable intermediate phase between hematite and spinel CoFe_2O_4 , possibly maghemite (γ - Fe_2O_3).¹⁹³⁻¹⁹⁶

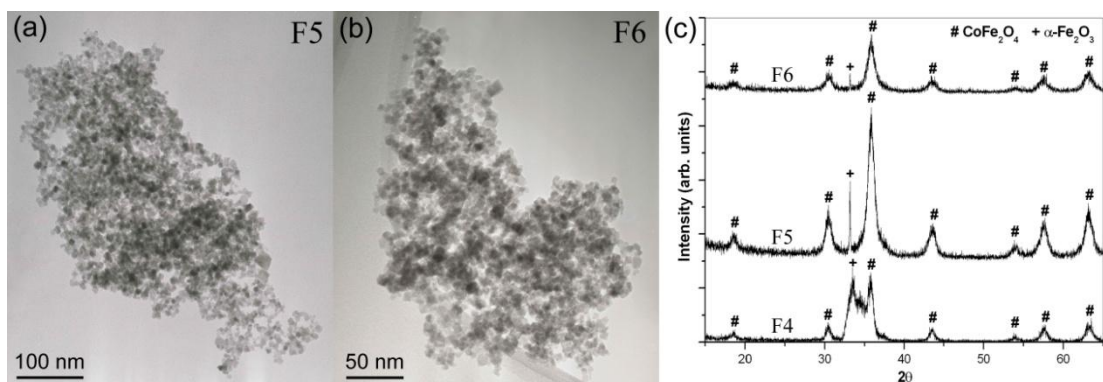


Figure 6.4 BF TEM images of hydrothermal products synthesised in 40 ml water at 200 °C for 2 hours with 0.05 ml FeCl₃, 25 mg CoCl₂ and (a) 3 mg NH₄H₂PO₄; (b) 6 mg NH₄H₂PO₄. (c) XRD patterns of Samples F4 – F6 showing the effect of phosphate on the development of CoFe₂O₄ and α-Fe₂O₃.

XRD data of Samples F5 and F6 demonstrated that the addition of NH₄H₂PO₄ reduced the peak intensities characteristic to α-Fe₂O₃. Phosphate absorption on the surface of α-Fe₂O₃ NPs can stabilise particle size and suppress particle formation in high phosphate conditions (Chapter 4 and 5). For this reason, it is suggested that NH₄H₂PO₄ has suppressed the α-Fe₂O₃ NP growth, resulting in a higher proportion of CoFe₂O₄ NPs with decreased size and increased CoFe₂O₄ phase purity.

6.5 Effect of CoFe₂O₄ NPs on the growth of α -Fe₂O₃ NRs

The CoFe₂O₄ NPs were considered potential candidates for creating hetero-nanostructures with α -Fe₂O₃ NRs, due the presence of iron in both phases. Accordingly, CoFe₂O₄ NPs (Sample F6 from Section 6.4) were centrifuged, cleaned with acetone and ultrasonically dispersed in the standard precursor solution for α -Fe₂O₃ NRs (0.2 ml FeCl₃ solution, further diluted in 40 ml water, 3mg NH₄H₂PO₄) in the standard 125 ml Teflon-lined stainless steel pressure autoclave, which was then sealed and heated at 200°C for 2 hours (Sample F6*).

6.5.1 Results and discussion

The BF TEM images of Figure 6.5a, c, d & e illustrate the effect of CoFe₂O₄ NPs on the growth of α -Fe₂O₃ NRs (Sample F6*). Figure 6.5a displays an individual α -Fe₂O₃ NR (identified by SAED) exhibiting a cavity halfway along its major axis, with a few CoFe₂O₄ NPs located within it. α -Fe₂O₃ NRs are also shown in Figure 6.5c, with NPs attached to their surface and tips. Again, one of the α -Fe₂O₃ NRs exhibits a cavity two thirds along its major axis with CoFe₂O₄ NPs located within it (Figure 6.5c, inset), as identified by characteristic lattice fringes corresponding to {111} planes ($d_{111} = 4.89\text{\AA}$). Figure 6.5d also shows a CoFe₂O₄ NP attached to the surface of an α -Fe₂O₃ NR. Closer examination revealed the CoFe₂O₄ NP to sit in a small cavity, similar in size to the NP, located on the surface of the α -Fe₂O₃ NR (Figure 6.5e).

The EDX spectra of Figure 6.5b & f, recorded using a spot size on the scale of the dashed area in Figures 6.5a & d, respectively, indicated the presence of cobalt in addition to the expected signals for iron and oxygen (and a Cu artefact signal arising from the specimen support grid). A phosphorus signal was also identified in the EDX spectrum of Figure 6.5f. In both cases the specimen was cleaned in acetone prior to chemical analysis.

It is considered that CoFe₂O₄ NPs promote the formation of cavities on the α -Fe₂O₃ NR surface. One possibility is that the cobalt atoms in the top few nm of the CoFe₂O₄ NP surface dissolve into solution as Co²⁺ cations at low pH values,^{190,191} leaving vacancies in the crystal lattice of the CoFe₂O₄ NP surface. When the CoFe₂O₄ NP attaches to α -Fe₂O₃ NR surface, the vacancies may be filled by surface Fe atoms of α -Fe₂O₃, resulting in a good accord at their interface, as evidenced by Figure 6.5e.

It is thought this bonding encourages α -Fe₂O₃ dissolution, resulting in the crater similar in size to the NP (Figure 6.5e). α -Fe₂O₃ dissolution could proceed by following the Ostwald rules of stages, whereby vacancies left by Co²⁺ cations and looser atomic packing in CoFe₂O₄ means that the equilibrium Fe concentration in the CoFe₂O₄ NP surface becomes lower than that of α -Fe₂O₃. The resulting concentration gradient leads to Fe³⁺ ions flowing from α -Fe₂O₃ to CoFe₂O₄ through the interface, prompting α -Fe₂O₃ dissolution along its surface to restore the equilibrium Fe³⁺ concentration. However, more work needs to be done to fully understand this process of α -Fe₂O₃ dissolution and cavity formation.

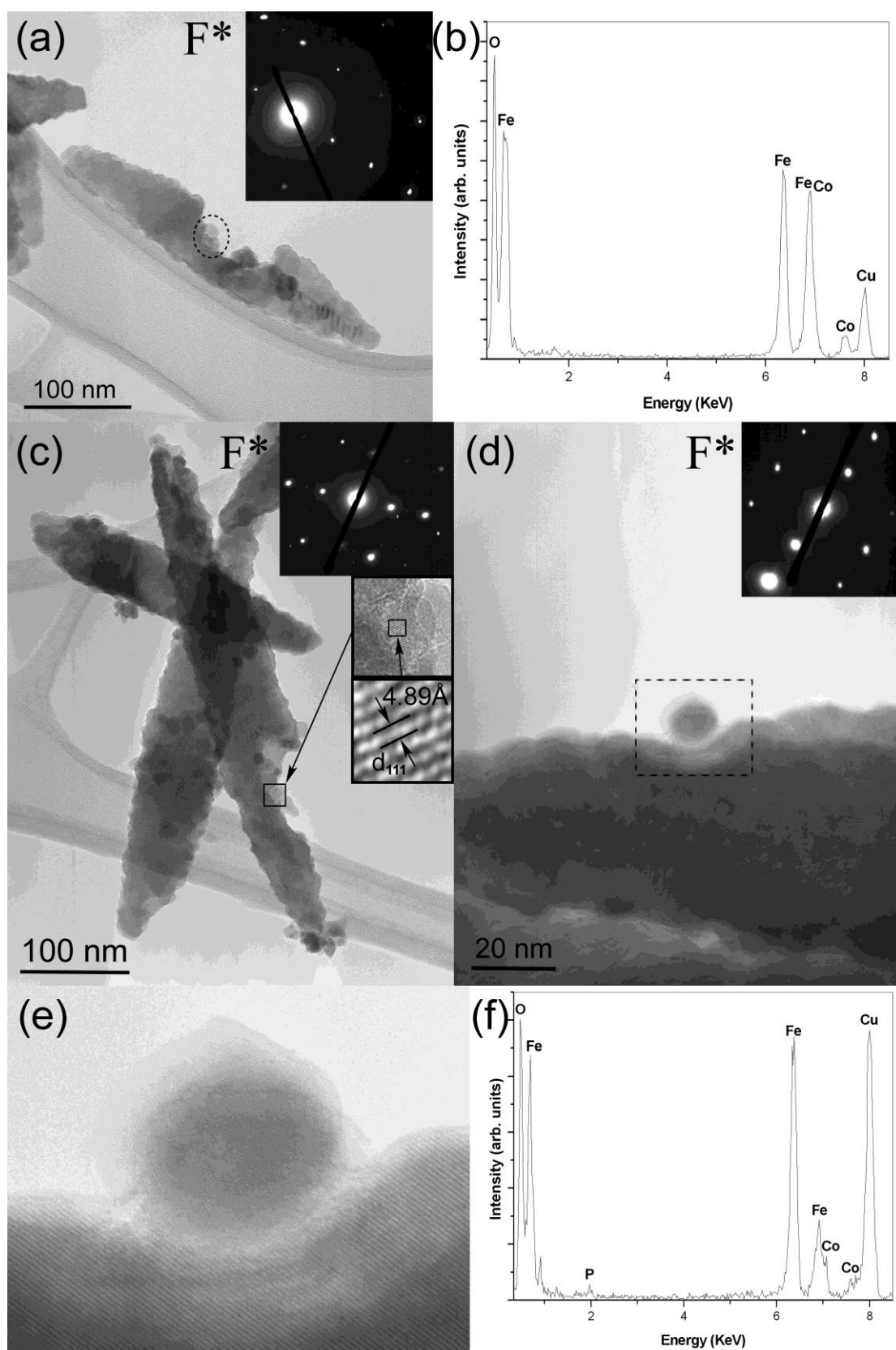


Figure 6.5 BF TEM images of α -Fe₂O₃ NRs synthesised in the presence of CoFe₂O₄ NPs (Sample F6*). (a) α -Fe₂O₃ NR exhibiting a cavity with CoFe₂O₄ NPs situated within it (outlined) and SAED (inset). (b) Associated EDX spectrum acquired from the outlined section shown in (a). (c) α -Fe₂O₃ NR exhibiting a cavity with CoFe₂O₄ NPs situated within it (outlined), as identified by lattice fringes (inset), and SAED (inset). (d) α -Fe₂O₃ NR with CoFe₂O₄ NP attached and SAED (inset). (e) High magnification of an individual CoFe₂O₄ NP attached to α -Fe₂O₃ NR, shown in (d). (f) Associated EDX spectrum acquired from the outlined section shown in (d) and magnified in (e).

6.6 Reaction product summary and process map

The schematic diagram of Figure 6.6 constitutes a ‘process map,’ illustrating the development of the size, shape and phases of the HS reaction products as a function of pH, FeCl₃, CoCl₂ and phosphate concentration. The precipitation of α -Fe₂O₃ NRs from the FeCl₃ salt solution occurred after 120 minutes of synthesis at 200°C in the presence of 3 mg phosphate surfactant at pH ~ 2 (Figure 6.6, regime(a)). Addition of Co₃O₄ (< 30 nm) and CoFe₂O₄ NPs (< 20 nm) to the precursor solution resulted in α -Fe₂O₃ NRs with Co₃O₄ and CoFe₂O₄ NPs attached to their surface, respectively, with α -Fe₂O₃ surface cavities apparent in the latter. Inclusion of 100 mg CoCl₂ in the precursor solution promoted an increase in the α -Fe₂O₃ NR size up to 950 nm long and 130 nm wide, with no evidence of cobalt incorporation within the α -Fe₂O₃ NRs. The precipitation of Co₃O₄ NPs from the CoCl₂ salt solution occurred after 120 minutes of synthesis at 200°C at pH ~ 8 (Figure 6.6, regime (b)). Addition of α -Fe₂O₃ NRs to the precursor solution resulted in α -Fe₂O₃ NRs with large Co₃O₄ NPs (< 100 nm) attached to their surface. Growth of CoFe₂O₄ and α -Fe₂O₃ NPs from a mixture of CoCl₂ and FeCl₃ salt solution with varied Fe : Co molar ratio and surfactant concentrations occurred after 120 minutes of synthesis at 200°C at pH ~ 12 (Figure 6.6, regime(c)). The reaction product solution with Fe : Co molar ratio of ~ 2 consisted of a significant proportion of α -Fe₂O₃, and reduction in FeCl₃ content to a Fe : Co molar ratio of ~ 1 resulted in a decreased α -Fe₂O₃ proportion. Addition of the phosphate surfactant promoted a further increase in CoFe₂O₄ phase purity and reduction in their particle size.

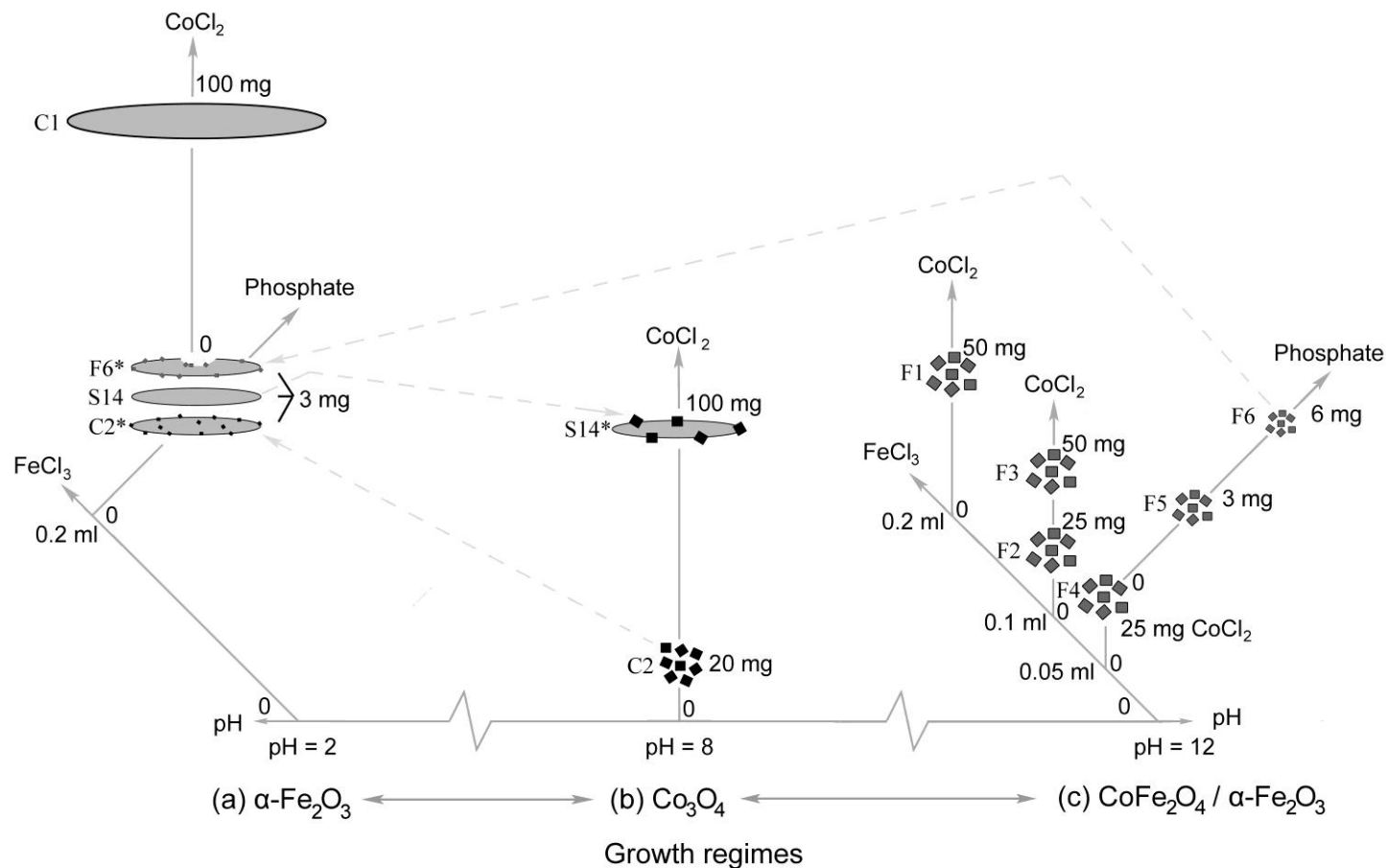


Figure 6.6 ‘Process map’ illustrating the development of the size, shape and phases of the hydrothermal products synthesised as a function of pH, FeCl_3 , CoCl_2 and phosphate concentration. The main growth regimes as a function of pH are (a) α - Fe_2O_3 NRs (pH = 2); (b) Co_3O_4 NPs (pH = 8); and (c) CoFe_2O_4 and α - Fe_2O_3 NPs (pH = 12). (a) Development of α - Fe_2O_3 NRs (Sample S14) with addition of 100 mg CoCl_2 (Sample C1); Co_3O_4 NPs (Sample C2*); and CoFe_2O_4 NPs (Sample F6*). (b) Development of Co_3O_4 NPs (Sample C2) with the addition of α - Fe_2O_3 NRs (Sample S14*). (c) Development of CoFe_2O_4 and α - Fe_2O_3 NPs as a function of CoCl_2 and FeCl_3 (Samples F1-F4); and phosphate concentration (Samples F5 & F6).

6.7 Summary

A feasibility study on the incorporation of ferromagnetic cobalt into α -Fe₂O₃ NRs during HS has been presented. A 'process map' for the HS of α -Fe₂O₃ NRs in the presence of CoCl₂, Co₃O₄ and CoFe₂O₄ has been constructed, as a function of pH, FeCl₃, CoCl₂ and phosphate surfactant concentration. Addition of CoCl₂ to the FeCl₃ precursor solution at low pH value resulted in an increase in size of the α -Fe₂O₃ NRs. Dispersion of α -Fe₂O₃ NRs in a CoCl₂ precursor solution, with pH ~ 8, resulted in the precipitation of Co₃O₄ NPs attached to the surface of α -Fe₂O₃ NRs. A low CoCl₂ concentration yielded the formation of small Co₃O₄ NPs at pH ~ 8 and their inclusion in the FeCl₃ precursor solution at low pH produced α -Fe₂O₃ NRs with Co₃O₄ NPs attached to their surface and tips, with some apparent Co₃O₄ NP dissolution. CoFe₂O₄ NPs were grown at pH ~ 12 with varying phase purity depending on the Fe : Co molar ratio, where a Fe : Co molar ratio of ~ 2 yielded a significant proportion of α -Fe₂O₃, which decreased with a Fe : Co molar ratio of ~ 1. Addition of the phosphate surfactant promoted a further increase in CoFe₂O₄ phase purity and reduction in the particle size. Dispersion of small CoFe₂O₄ NPs in the FeCl₃ solution at low pH resulted in α -Fe₂O₃ NRs with surface cavities and CoFe₂O₄ NPs attached to their surface. The CoFe₂O₄ NPs are considered to encourage the formation of the α -Fe₂O₃ NR surface cavities through promoting α -Fe₂O₃ dissolution. In all cases, there was no evidence for the incorporation of cobalt within the α -Fe₂O₃ NRs or the formation of hetero-nanostructures with the Co₃O₄ and CoFe₂O₄ NPs.

Chapter 7 Discussion

7.1 Introduction

In this chapter, the main aspects concerning the hydrothermal growth of acicular single crystalline α -Fe₂O₃ NRs are discussed. The HS technique and effect of various HS processing conditions on the development of these nanostructures are reviewed. Emphasis is given to the effect of the phosphate surfactant on phase transformation, size, shape and stability of the nanostructures. The kinetics and thermodynamics relating to the nucleation, growth and phase transformation of β -FeOOH and α -Fe₂O₃ nanostructures are considered. The HS growth mechanism of the acicular α -Fe₂O₃ NRs is discussed, with focus given to the role of the intermediate β -FeOOH phase and the specific mechanistics of anisotropic growth.

7.2 Hydrothermal synthesis and effect of processing conditions

HS has produced a range of crystalline nanostructures over a relatively short reaction time of 2 hours. The HS ‘process maps’ provided an overall impression of the growth of β -FeOOH and α -Fe₂O₃ NRs (Section 4.2.1.6), and α -Fe₂O₃ NRs in the presence of CoCl₂, Co₃O₄ and CoFe₂O₄ NPs (Section 6.6) using the standard 125 ml capacity Teflon-lined stainless steel pressure autoclave. The valve-assisted 50 ml capacity Teflon-lined stainless steel pressure autoclave allowed rapid quenching of HS suspensions in liquid nitrogen to provide descriptions of the localised development of high aspect ratio acicular α -Fe₂O₃ NRs. Hence, the pressure autoclaves provided distinct yet complementary evidence for investigating the hydrothermal growth of α -Fe₂O₃ NRs.

It is recognised that the autoclaves exhibited different temperature responses due to their respective dimensions and wall thicknesses, as evidenced by partial formation of α -Fe₂O₃ NRs (Sample S19) after 90 minutes of synthesis in comparison to fully formed α -Fe₂O₃ NRs (Sample Q200) after 80 minutes of synthesis, at the same reaction temperature of 200°C. Hence, the solution in the smaller valve-assisted

pressure autoclave experienced a higher heating rate, suggesting that any direct comparisons should be limited to precursor concentrations, pH or known temperatures.

The effect of HS processing conditions on the reaction products were investigated mainly using the standard pressure autoclave. The process variables included reaction temperature, reaction time, FeCl_3 and phosphate concentration at varied Fe : PO_4 molar ratios, pH value, $\alpha\text{-Fe}_2\text{O}_3$ seed content, CoCl_2 concentration and stage of phosphate addition. It was evident that increasing the HS reaction temperatures, or allowing heating over longer reaction times, promoted the precipitation and dissolution of the intermediate $\beta\text{-FeOOH}$ phase, and subsequent precipitation of the $\alpha\text{-Fe}_2\text{O}_3$ NPs and NRs. Since exposure over time increased the temperature of the solution, the growth reactions considered to be driven primarily by the reaction temperature.

The precursor concentrations had a significant effect on the size of the reaction products, with $\alpha\text{-Fe}_2\text{O}_3$ NRs decreasing in both size and aspect ratio when lowering the FeCl_3 and $\text{NH}_4\text{H}_2\text{PO}_4$ concentration. Similarly, there was a decrease in size of Co_3O_4 NPs with decreasing CoCl_2 concentration. However, CoFe_2O_4 NPs did not exhibit a marked reduction in size when the FeCl_3 and CoCl_2 concentrations at a Fe : Co molar ratio of ~ 1 were halved. Hence, a lower limit on the size of NPs in relation to the precursor concentration is thought to be dependent on a relationship between the NP nucleation rate, supply of elemental constituents and their stability under the HS conditions, and this will be discussed in more detail in Section 7.4.

The addition of $\alpha\text{-Fe}_2\text{O}_3$ seeds and CoCl_2 to the $\alpha\text{-Fe}_2\text{O}_3$ NR precursor solution had the opposite effect on the particle size of the $\alpha\text{-Fe}_2\text{O}_3$ NRs. The $\alpha\text{-Fe}_2\text{O}_3$ seeds were considered as centres of aggregation of the primary $\alpha\text{-Fe}_2\text{O}_3$ NPs, whilst Co^{2+} cations were suggested to effect with the OA or size of the primary $\alpha\text{-Fe}_2\text{O}_3$ NPs, resulting in fewer centres of aggregation. The more centres of aggregation, the lesser the supply of primary $\alpha\text{-Fe}_2\text{O}_3$ NPs to individual $\alpha\text{-Fe}_2\text{O}_3$ NRs. Hence, the sizes of the $\alpha\text{-Fe}_2\text{O}_3$ NRs were inversely proportionally to the number of centres of aggregation, whereby the addition $\alpha\text{-Fe}_2\text{O}_3$ seeds and CoCl_2 resulted in smaller and larger $\alpha\text{-Fe}_2\text{O}_3$ NRs, respectively.

Alteration of the initial pH value of the HS precursor solution had a significant effect on the phase and morphology of the reaction products. Co_3O_4 NPs would not precipitate at low pH values because atomic cobalt is too active to exist in acidic or neutral solutions.^{190,191} Similarly, a high pH of ~ 12 was required for the formation of

CoFe₂O₄ NPs. A slight increase in pH from ~ 2 to ~ 4 resulted in the reduction of the α -Fe₂O₃ NR aspect ratio. Hence, a good understanding of the effect of pH value exhibited by the precursor solution is essential for functional control over the precipitation and shape of the HS reaction products.

The phosphate surfactant and the stage of its addition also had a significant effect on the β -FeOOH, α -Fe₂O₃ and CoFe₂O₄ nanostructures, and this will be discussed in the next section.

7.3 Effect of phosphate surfactant on β -FeOOH, α -Fe₂O₃ and CoFe₂O₄ nanostructures

PO₄³⁻ containing surfactants were found to affect the phase and morphology of both β -FeOOH and α -Fe₂O₃ nanostructures. During the investigation of the α -Fe₂O₃ NR growth mechanism, strong phosphate anion absorption on the α -Fe₂O₃ crystal surfaces was found to stabilise the primary α -Fe₂O₃ NP size to < 10 nm. Similarly, the phosphate surfactant assisted with stabilising the particle size of CoFe₂O₄ NPs, resulting in the small NPs (< 30 nm) present in Samples F5 and F6. When the phosphate surfactant was added after β -FeOOH precipitation, PO₄³⁻ anion surface absorption was found to suppress subsequent β -FeOOH dissolution and promoted further β -FeOOH growth at 200°C (Sample S27*). Hence, the phosphate surfactant stabilised nanostructure particle size through surface absorption and this will be discussed in more detail in Section 7.4.

An increase in phosphate surfactant concentration resulted in an increase in α -Fe₂O₃ NP aspect ratio and loss of crystallinity when heated at 160°C in the standard 125 ml Teflon-lined stainless steel pressure autoclave (Samples S6 – S10). This PO₄³⁻ shape effect on α -Fe₂O₃ is now better understood through use of the 50 ml valve-assisted Teflon-lined stainless steel pressure autoclave used for the purpose of rapid quenching HS suspensions in liquid nitrogen. FTIR investigation of the quenched reaction products provided evidence for PO₄³⁻ absorption on the α -Fe₂O₃ NPs in the form of mono or bi-dentate (bridging) surface complexes on surfaces normal and parallel to the crystallographic α -Fe₂O₃ c-axis, respectively.

However, the stabilisation and shape effect of phosphate absorption on β -FeOOH, α -Fe₂O₃ and CoFe₂O₄ surfaces is found to depend on pH value. It was noted that the precursor solution for the formation of β -FeOOH and α -Fe₂O₃ NRs exhibited an initial pH of ~ 2, being much lower than their PZC of pH 8 and 8.5, respectively.^{160,163,164} Hence PO₄³⁻ anion adsorption, through strong electrostatic attraction, acts to inhibit the growth and dissolution of β -FeOOH, and promote the anisotropic growth of α -Fe₂O₃ NRs, as compared with phosphate-free environments.⁷ FTIR investigation of the rapidly quenched samples revealed bi-dentate PO₄³⁻ absorption on surfaces parallel to the crystallographic α -Fe₂O₃ c-axis of primary α -Fe₂O₃ NPs at low pH values (< 2). However, increasing the pH value was associated with mono-dentate mononuclear complexes with hydrogen bonding of phosphate

species to adjacent surface sites on faces parallel to the c-axis (Figure 7.1), being favoured over binuclear (bridging) complexes.^{187,188} The inference is that such hydrogen bonds of the mono-dentate surfactant complexes are easily displaced during α -Fe₂O₃ growth. Consequently, an increase in pH value results primarily in mono-dentate phosphate surface complexes, negating the preference of specific crystal surfaces for the attachment of primary α -Fe₂O₃ NPs, and hence inhibiting the anisotropic growth of α -Fe₂O₃ NRs.

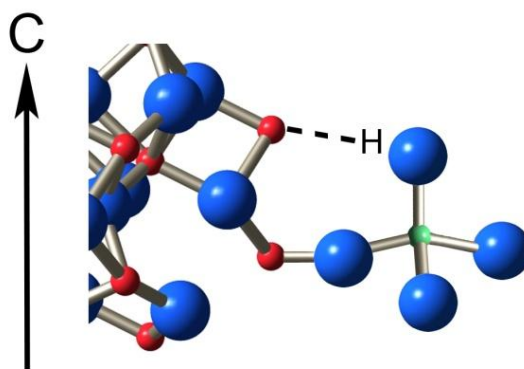


Figure 7.1 Schematic diagram of the hexagonal α -Fe₂O₃ crystal lattice showing mono-dentate phosphate adsorption with hydrogen bonding on a face parallel to the c-axis. Red (small), blue (large) and green (smallest) spheres correspond to iron, oxygen and phosphorus, respectively.

It was noted that the precursor solution for the formation of CoFe₂O₄ NPs exhibited an initial pH of ~ 12 , being much higher than the PZC of CoFe₂O₄ (pH 4).¹⁹⁷ When pH values are higher than the PZC of the particles, the surface is negatively charged. At these high pH values, the phosphate surfactant is thought to exist in solution as H₃PO₄⁰ (aq) complexes (with C_{3v} symmetry).¹⁸⁷ The hydrogen atoms may be attracted to the CoFe₂O₄ surface and hinder further growth through hydrogen bonding, thereby stabilising their size.

7.4 Nucleation and growth theory

The hydrothermal growth of nanostructures examined in this thesis involved homogeneous nucleation from aqueous media. When a spherical nucleus of radius r is formed, the change in energy of the system relates to the new bonds formed within the NP crystal lattice and the interfacial energy σ_{CL} between the crystal face and the liquid required to create the surface. The standard free energy change (ΔG^0) is represented by two terms having opposite contributions.¹⁹⁸

$$\Delta G^0 = -\frac{4}{3}\pi r^3 \Delta G_v + 4\pi r^2 \sigma_{CL} \quad (7.1)$$

where ΔG_v is the volume free energy resulting from bond formation.

A plot of ΔG against r shows a maximum at a critical radius r^* and free energy ΔG^* , as illustrated in Figure 7.2.

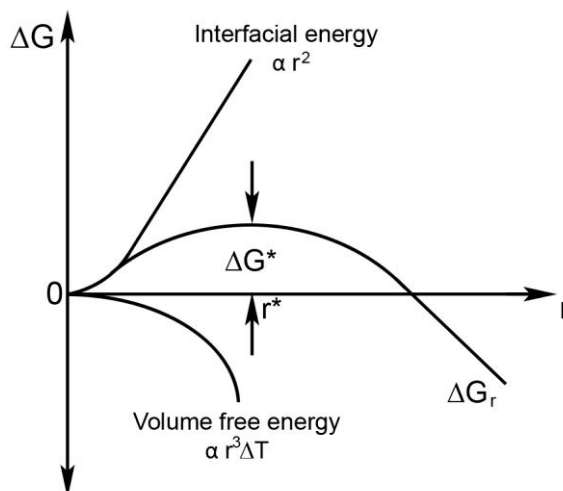


Figure 7.2 Plot of ΔG against r , showing the relationship between interfacial energy and volume free energy. ΔG^* is viewed as the activation energy barrier for the nucleation process.

For very small NPs, the surface energy term dominates. In this region of sizes the nuclei are formed and dispersed, without starting growth. For large NPs the volume free energy term dominates. The maximum value ΔG^* for a spherical cluster is:

$$\Delta G^* = \frac{16\pi\sigma_{CL}^3}{3\Delta G_v^2} \quad (7.2)$$

ΔG^* may be viewed as the activation energy barrier for the nucleation process to take place. The nucleus corresponding to the energy is termed the ‘critical nucleus’ *i.e.* a nucleus which will grow spontaneously, releasing energy. However, new bonds can only be formed if there is sufficient elemental supply, *i.e.* adequate precursor concentration. Accordingly, if the surface energy of a NP cannot be sufficiently reduced through the formation of new bonds and subsequent growth, the NP will dissolve, possibly assisting the Ostwald ripening of a larger NP. In contrast, if the surface energy is low enough when the elemental supply has been exhausted, the NP is thermodynamically stable. Hence, the size of a NP depends on the precursor concentration and the thermodynamic stability of the phase, as evidenced by the particle sizes of β -FeOOH, α -Fe₂O₃, Co₃O₄ and CoFe₂O₄ NPs grown from various FeCl₃ and CoCl₂ concentrations.

β -FeOOH was described as becoming partially thermodynamically stabilised through a reduction of surface energy by hydration. PO₄³⁻ anion absorption to β -FeOOH further reduces its surface energy, stabilising β -FeOOH NRs at smaller sizes in comparison to phosphate-free environments. Phosphate absorption is considered also to stabilise the β -FeOOH NRs against dissolution, hence suppressing the phase transformation to α -Fe₂O₃ in phosphate-rich environments, as evidenced by β -FeOOH NRs growing larger when the surfactant was added after β -FeOOH precipitation and heated at 200°C. The ΔG_v term for β -FeOOH is considered to dominate, suppressing dissolution and restricting Fe³⁺ supply for the nucleation and growth of the primary α -Fe₂O₃ NPs.

As mentioned in Section 7.3, strong phosphate anion absorption on α -Fe₂O₃ crystal surfaces at low pH values stabilised the primary α -Fe₂O₃ NP size to < 10 nm, compared with sizes of < 150 nm in phosphate free environments.⁷ At first, the ΔG_v term is considered to dominate, thereby promoting the growth of primary α -Fe₂O₃ NPs and reducing their surface energy. However, when a certain radius (< 10 nm) was reached, strong phosphate absorption reduces the surface energy sufficiently to prevent further growth, hence stabilising the size of the NP. At higher pH values and hence weaker phosphate absorption, the NP radius is considered to increase. The primary α -Fe₂O₃ NPs were observed to be the dominant α -Fe₂O₃ morphology with few β -FeOOH NPs present in Sample Q160. The elemental Fe³⁺ supply for nucleation or growth of primary α -Fe₂O₃ NPs is therefore thought to be limited. Hence, the formation of new bonds through primary α -Fe₂O₃ NP growth was not possible.

Accordingly, the surface energy was reduced through coalescence of the primary α - Fe_2O_3 NPs. Bi-dentate (bridging) phosphate surface absorption is thought to partially thermodynamically stabilise the α - Fe_2O_3 surfaces parallel to the α - Fe_2O_3 c-axis. Consequently, reduction of the surface energy, through primary α - Fe_2O_3 NP coalescence, is favoured on the α - Fe_2O_3 c-plane surfaces where displacement of the mono-dentate phosphate complexes is considered to be a lower energy process.

The addition of CoCl_2 to the precursor solution of α - Fe_2O_3 NRs is considered to possibly increase the size of the critical nuclei of the primary α - Fe_2O_3 NPs. A larger critical radius required for the primary α - Fe_2O_3 NPs to become established implies there would be fewer number of nucleation centres. Fewer centres of α - Fe_2O_3 NR aggregation would be present, increasing the supply of primary α - Fe_2O_3 NPs to individual α - Fe_2O_3 NRs and hence increasing their size.

7.5 Growth mechanism of β -FeOOH and α -Fe₂O₃ NRs

As mentioned in Section 5.3.2.2, the development of large single crystalline α -Fe₂O₃ NRs is a two stage process: 1) the growth and dissolution of intermediate β -FeOOH nanostructures, alongside precipitation of α -Fe₂O₃ NPs; and 2) the agglomeration and coarsening of α -Fe₂O₃ primary NPs into α -Fe₂O₃ NRs. However, comparison of the β -FeOOH and α -Fe₂O₃ NRs revealed that their anisotropic development proceeds through different growth mechanisms.

The tetragonal β -FeOOH crystal structure exhibited large channels along the crystallographic *c*-axis. Hence, the faces perpendicular to the *c*-axis are considered to be energetically favourable surfaces for elemental deposition or dissolution. Further, addition of the phosphate surfactant restricted the growth and dissolution of the β -FeOOH NRs, but had no marked effect on their 1D morphology. Accordingly, the β -FeOOH crystallographic structure is considered to dictate the anisotropic growth of the β -FeOOH NRs under conventional HS conditions, as illustrated in Figure 7.3.

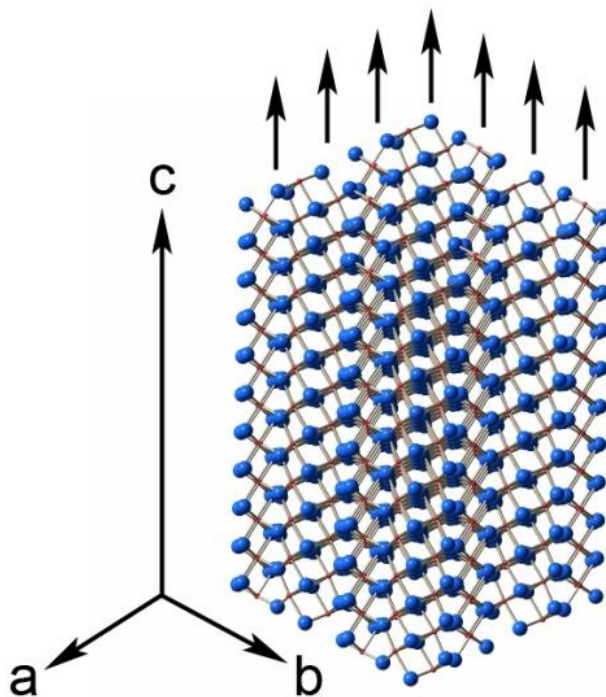


Figure 7.3 Schematic representation of the tetragonal β -FeOOH crystal structure showing preferential growth along the crystallographic *c*-axis.

A decrease in total surface energy is considered to be the driving force for the kinetics involved in β -FeOOH dissolution and subsequent primary α -Fe₂O₃ NP growth. Preferential phosphate absorption on specific α -Fe₂O₃ crystal faces acted to

stabilise particle size (< 10 nm) and promote the OA mechanism. This OA mechanism is considered equally applicable to the initial development of α -Fe₂O₃ NRs, as to the attachment of α -Fe₂O₃ primary NPs to well-defined crystalline α -Fe₂O₃ NRs, creating the filamentary features observed at the NR tips. Figure 7.4a illustrates how a single crystalline α -Fe₂O₃ NR can be viewed to comprise co-operately aligned filamentary features along its major axis (parallel to the crystallographic c-axis). The development of the α -Fe₂O₃ NR proceeds through attachment of primary α -Fe₂O₃ NPs to the tips of the filamentary features. Bi-dentate phosphate absorption stabilised the crystal faces parallel to the α -Fe₂O₃ c-axis, hindering surface accordance with the primary α -Fe₂O₃ NPs. For a reduction of the total surface energy through coalescence, the GRIGC mechanism^{178,179} compels the primary α -Fe₂O₃ NPs to the tips of the filamentary features, as illustrated in Figure 7.4b, where the mono-dentate phosphate surface complexes are more easily displaced (Figure 7.4c). The OA of primary α -Fe₂O₃ NPs to the filamentary features (parallel to crystallographic c-axis), encouraged by preferential phosphate absorption, is considered to dictate the anisotropic growth of the α -Fe₂O₃ NRs and mediate their unique acicular shape.

In summary, the overall growth mechanism of single crystalline acicular α -Fe₂O₃ NRs involved the anisotropic growth and dissolution of intermediate β -FeOOH NRs, governed by its crystallographic structure, and the OA of primary α -Fe₂O₃ NPs, mediated by preferential absorption of the phosphate surfactant.

In view of the above, the critical issues regarding the HS of 1D α -Fe₂O₃ nanostructures, as mentioned in Section 2.7, have been addressed.

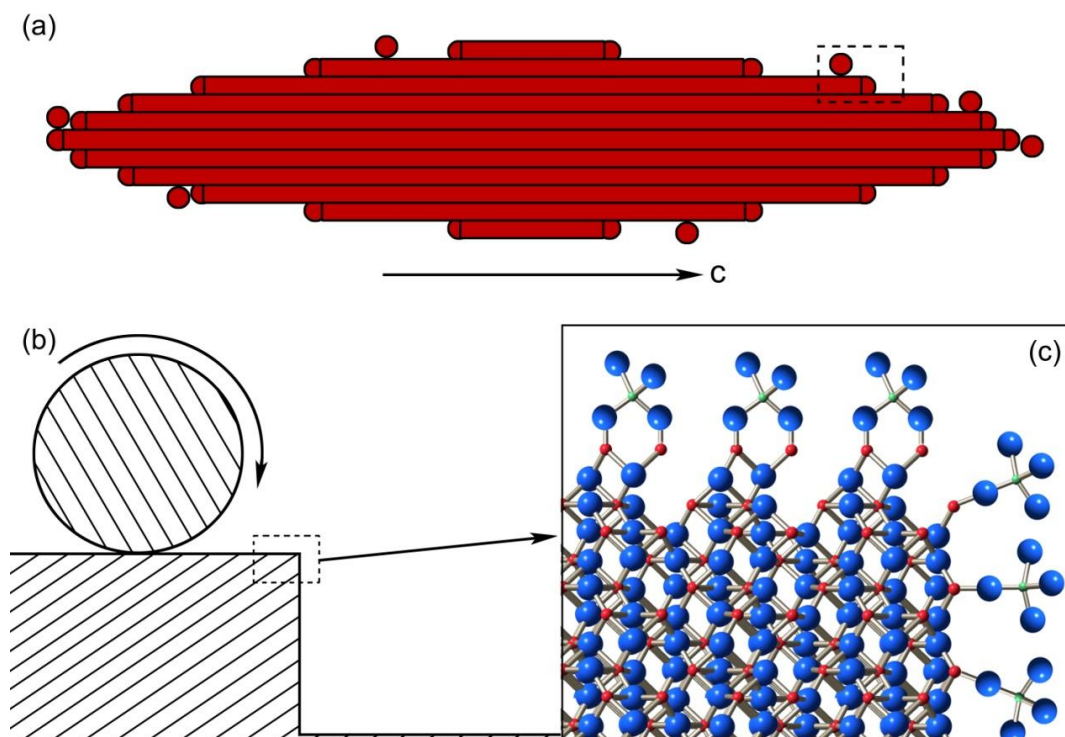


Figure 7.4 Schematic representation showing: (a) single crystal acicular α - Fe_2O_3 NR comprising filamentary features parallel to the crystallographic c-axis, with primary α - Fe_2O_3 NPs attached to its surface; (b) high magnification of the rotation (arrowed), based on the OA mechanism, of an individual primary α - Fe_2O_3 NP, shown in (a); and (c) hexagonal α - Fe_2O_3 crystal lattice showing mono-dentate phosphate adsorption on the c-plane and bi-dentate phosphate adsorption on faces parallel to the c-axis. Red (small), blue (large) and green (smallest) spheres correspond to iron, oxygen and phosphorus, respectively.

7.7 Summary

The main aspects concerning the hydrothermal growth of acicular single crystalline α - Fe_2O_3 NRs have been discussed. The standard and valve-assisted pressure autoclaves have provided HS ‘process maps’ and *in situ* descriptions of the development of α - Fe_2O_3 NRs, respectively. The size of the nanostructures decreases with decreasing precursor concentration. The addition of CoCl_2 and α - Fe_2O_3 seeds increase and reduce the particle size of the α - Fe_2O_3 NRs, respectively, by influencing the number of their aggregation sites. Alteration of the pH value of the precursor solution to ~ 2 , ~ 8 and ~ 12 is critical to the precipitation and growth of α - Fe_2O_3 NRs, Co_3O_4 NPs and CoFe_2O_4 NPs, respectively. The phosphate surfactant was identified to stabilise the size of the β - FeOOH NRs, primary α - Fe_2O_3 NPs and CoFe_2O_4 NPs through surface absorption. The mode of PO_4^{3-} absorption is considered to be dependent on pH, and hydrogen bonded mono-dentate PO_4^{3-} absorption on the α - Fe_2O_3 surface at pH ~ 4 is thought to reduce the OA of the primary α - Fe_2O_3 NPs, hindering the anisotropic growth of α - Fe_2O_3 NRs. The nucleation, growth and stabilisation of nanostructures have been discussed in terms of competition between the chemical free energy of new bonds formed within the crystal lattice and surface energy. Phosphate absorption is considered to stabilise the particle size of the nanostructures through the lowering of surface energy. In addition, high phosphate absorption stabilises the β - FeOOH NRs against dissolution, suppressing phase transformation to α - Fe_2O_3 in phosphate-rich environments. When the Fe^{3+} supply was exhausted and primary α - Fe_2O_3 NPs could no longer nucleate and grow, their coalescence was required to reduce the surface energy and restore the equilibrium of the system with increasing temperature. Coalescence was favoured on the α - Fe_2O_3 c-plane surfaces where the displacement of mono-dentate phosphate complexes is considered a lower energy process. The anisotropic development of β - FeOOH and α - Fe_2O_3 NRs occurs through different growth mechanisms. The β - FeOOH NR development proceeds along the crystallographic c-axis because the c-faces are considered to be energetically favourable for elemental deposition or dissolution. The anisotropic growth of α - Fe_2O_3 NRs is dictated by the OA of primary α - Fe_2O_3 NPs on filamentary features, lying parallel to the crystallographic c-axis, mediated by the preferential absorption of the phosphate surfactant, thereby promoting their acicular shape.

Chapter 8 Summary and conclusions

In summary, the effect of HS processing conditions on the reaction products has been investigated. A novel valve-assisted pressure autoclave for the purpose of rapid quenching of HS suspensions in liquid nitrogen has been developed, providing descriptions of the localised development of α -Fe₂O₃ NRs. Appraisal of the HS reaction products using a complementary combination of chemical, structural and surface characterisation techniques led to a detailed description of the growth mechanism of acicular α -Fe₂O₃ NRs. A feasibility study on the incorporation of ferromagnetic cobalt into α -Fe₂O₃ NRs for the purpose of improving their magnetic performance was presented.

In Chapter 4, the effect of various HS processing conditions on the β -FeOOH and α -Fe₂O₃ nanostructures was investigated. A comprehensive HS ‘process map’ for the formation of α -Fe₂O₃ NRs was constructed as a function of reaction temperature, time and phosphate concentration. Increasing reaction temperature promoted the phase transformation from β -FeOOH to α -Fe₂O₃. Phosphate additions increased the aspect ratio of the α -Fe₂O₃ NPs but hindered both β -FeOOH formation and dissolution. An HS processing temperature of 200°C and an Fe³⁺ : PO₄³⁻ molar ratio of 31.5 yielded well-crystallised acicular α -Fe₂O₃ NRs with an aspect ratio of ~7. The α -Fe₂O₃ particle size was found to decrease with decreasing FeCl₃ concentration. A small increase in pH resulted in a marked reduction in the α -Fe₂O₃ aspect ratio. Addition of the surfactant after β -FeOOH precipitation prevented the phase transformation of β -FeOOH to α -Fe₂O₃ and assisted with increasing the size of the β -FeOOH NRs. XRD and RHEED techniques both identified and distinguished between the different β -FeOOH and α -Fe₂O₃ HS reaction products. This investigation of the effect of the HS processing conditions has enabled the controlled growth of β -FeOOH to α -Fe₂O₃ nanostructures.

In Chapter 5, the application of a novel valve-assisted pressure autoclave for the purpose of rapid quenching of HS suspensions in liquid nitrogen facilitated descriptions of the localised development of α -Fe₂O₃ NRs. The ‘snapshot’ approach provided information on the localised development of high aspect ratio acicular α -

Fe₂O₃ NRs as a function of reaction time. Further, a more detailed description of the development of 1D α -Fe₂O₃ nanostructures, as a function of known reaction temperature, provided better understanding of the growth mechanism of α -Fe₂O₃ NRs. The release of Fe³⁺ ions back into solution through β -FeOOH dissolution supplied the nucleation and growth of primary α -Fe₂O₃ NPs which subsequently coalesce, with increasing temperature, into larger, acicular α -Fe₂O₃ NRs. The balance between bidentate phosphate absorption to faces parallel to the α -Fe₂O₃ c-axis, as distinct from mono-dentate phosphate absorption associated with the α -Fe₂O₃ c-plane, is considered critical in mediating the acicular shape of the α -Fe₂O₃ NRs. *i*TEM investigation of β -FeOOH and α -Fe₂O₃ NRs provided additional fundamental insight into the localised growth of these nanostructures, as a function of temperature. The heating of quenched HS samples *in situ* within the TEM provided direct evidence in support of the proposed mechanism for the formation of acicular α -Fe₂O₃ NRs.

In Chapter 6, a feasibility study on the incorporation of ferromagnetic cobalt into α -Fe₂O₃ NRs during HS was presented. A ‘process map’ for the HS of α -Fe₂O₃ NRs in the presence of CoCl₂, Co₃O₄ and CoFe₂O₄ was constructed, as a function of pH, and FeCl₃, CoCl₂ and phosphate surfactant concentration. Alteration of pH values of the precursor solution to ~ 8 and ~ 12 was required for the precipitation of Co₃O₄ and CoFe₂O₄ NPs, respectively. Dispersion of small Co₃O₄ and CoFe₂O₄ NPs in the FeCl₃ solution, at low pH, resulted in α -Fe₂O₃ NRs with NPs attached to their surface. The CoFe₂O₄ NPs were considered to encourage the formation of α -Fe₂O₃ NR surface cavities, through the promotion of α -Fe₂O₃ dissolution. In all cases, there was no evidence for the incorporation of cobalt within the α -Fe₂O₃ NRs or the formation of hetero-nanostructures with the Co₃O₄ and CoFe₂O₄ NPs.

In Chapter 7, the main aspects concerning the hydrothermal growth of acicular single crystalline α -Fe₂O₃ NRs were discussed. The overall growth mechanism of single crystalline acicular α -Fe₂O₃ NRs involved the anisotropic growth and dissolution of intermediate β -FeOOH NRs, governed by its crystallographic structure, and the OA of primary α -Fe₂O₃ NPs, mediated by preferential absorption of the phosphate surfactant. The critical issues regarding the HS of 1D α -Fe₂O₃ NRs were reviewed.

In conclusion:

- The relationship of the HS reaction temperature, reaction temperature and phosphate concentration with respect to the phase, size, morphology and crystallinity of the β -FeOOH and α -Fe₂O₃ reaction products has been established through the construction of a HS ‘process map’.
- Development of a novel valve-assisted pressure autoclave facilitated the rapid quenching of the HS reaction products and provided ‘snapshot’ descriptions closely representative of the *in situ* physical state of the nanostructures during growth as a function of reaction time and temperature.
- The growth and phase transformation of the β -FeOOH and α -Fe₂O₃ reaction products followed Ostwald’s rules of stages with increasing reaction temperature, whereby the less stable intermediate β -FeOOH phase precipitated and subsequently dissolute alongside the nucleation and growth of the more stable α -Fe₂O₃ phase.
- Absorption of the phosphate surfactant to surface of the β -FeOOH, α -Fe₂O₃, Co₃O₄ and CoFe₂O₄ nanostructures stabilised their particle size during growth. The phosphate surfactant suppressed β -FeOOH dissolution and promoted the anisotropic α -Fe₂O₃ growth at low pH values through mono- and bi-dentate absorption on surfaces normal and parallel to the α -Fe₂O₃ c-axis, respectively.
- The overall growth mechanism of single crystalline acicular α -Fe₂O₃ NRs involved the anisotropic growth and dissolution of intermediate β -FeOOH NRs, governed by its crystallographic structure, and the OA of primary α -Fe₂O₃ NPs, mediated by preferential absorption of the phosphate surfactant.

Chapter 9 Future work

Base on the obtained results, some suggestions for future work are proposed:

- Detailed investigation of the development of α -Fe₂O₃ NR surface cavities in the presence of CoFe₂O₄ NPs is required to allow the mechanism of cavity formation to be realised. The use of CoFe₂O₄ NPs to create cavities through α -Fe₂O₃ dissolution may allow α -Fe₂O₃ NRs to be sub-divided, which could be beneficial for improving their magnetic performance through the NR size effect.
- The addition of other water soluble chlorides, *e.g.* MnCl₂, NaCl and NiCl₂, needs to be investigated with the aim of producing Mn, Na and Ni-doped α -Fe₂O₃ NRs, respectively. Further, measurement and comparison of their functional properties should allow routes for the controlled doping of NRs to be identified.
- The reduction of α -Fe₂O₃ NRs, through annealing in an H₂ atmosphere, to the ferromagnetic iron oxide phases of γ -Fe₂O₃ and magnetite (Fe₃O₄) may improve their magnetic performance. However, particle agglomeration during the reduction process can be problematic and studies on the use of surfactant to inhibit coalescence would be beneficial. Investigation of the uniformity, purity and reproducibility of the reaction products is required. Further, *i*TEM examination of the reduction of nanostructures under hydrogen atmosphere using atomic resolution would give direct insight in the α -Fe₂O₃ - γ -Fe₂O₃ - Fe₃O₄ transformation mechanisms.
- Performing electron holography during *i*TEM magnetic field investigation allows for the appraisal of their magnetic properties on a localised scale. Direct comparison of the magnetic properties of α -Fe₂O₃ NRs, doped α -Fe₂O₃ NRs and Fe₃O₄ NRs is required to ensure their effect development for a variety of potential applications.

References

1. Iijima, S., Helical microtubes of graphitic carbon, *Nature*, 1991, 354, pp. 56-58.
2. Spaldin, N., *Magnetic Materials: Fundamentals and Device Applications*, First Edition, Cambridge University Press (2003).
3. Ozaki, M., Kratochvil, S., Matijevic, E., Formation of Monodispersed Spindle-Type Hematite Particles, *Journal of Colloid and Interface Science*, 1984, 102, pp. 146-151.
4. Xu, C., Teja, C. X., Continuous hydrothermal synthesis of iron oxide and PVA-protected iron oxide nanoparticles, *Journal of Supercritical Fluids*, 2008, 44, pp. 85-91.
5. Blood, P. J., Denyer, J. P., Azzopardi, B. J., Poliakoff, M., Lester, E., A versatile flow visualization technique for quantifying mixing in a binary system: application to continuous supercritical water hydrothermal synthesis (SWHS), *Chemical Engineering Science*, 2004, 59, pp. 2853-2861.
6. Caremans, T. P., Kirschhock, C. E. A., Verlooy, P., Paul, J. S., Jacobs, P.A., Martens, J.A. Prototype high-throughput system for hydrothermal synthesis and X-ray diffraction of microporous and mesoporous materials, *Microporous and Mesoporous Materials*, 2006, 90, pp. 62-68.
7. Almeida, T. P., Fay, M. W., Zhu, Y., Brown, P. D., Process map for the hydrothermal synthesis of α -Fe₂O₃ nanorods, *Journal of Physical Chemistry C*, 2009, 113, pp. 18689-18698.
8. Jorgensen, J. E., Jensen, T. R., Hanson, J.C., Hydrothermal synthesis of nanocrystalline ZnSe: An *in situ* synchrotron radiation X-ray powder diffraction study, *Journal of Solid State Chemistry*, 2008, 181, pp 1925-1929.
9. Meller, N., Kyritsis, K., Hall, C., The hydrothermal decomposition of calcium monosulfoaluminate 14-hydrate to katoite hydrogarnet and β -anhydrite: An in-situ synchrotron X-ray diffraction study, *Journal of Solid State Chemistry*, 2009, 182, pp 2743-2747.

10. Ellmer, K., Mientus, R., Rossner, H., In situ investigation by energy dispersive X-ray diffraction (EDXRD) of the growth of magnetron sputtered ITO films, *Surface and Coating Technology*, 2001, 142-144, pp. 1094-1099.
11. Nagarajan R., *Nanoparticles: Building Blocks for Nanotechnology*. ACS Symposium Series; American Chemical Society, 2008.
12. Website: nanoscience.massey.ac.nz/images/nanoscale.gif
13. Frenkel A. I., Hills C.W., Nuzzo R.G., A View from the Inside: Complexity in the Atomic Scale Ordering of Supported Metal Nanoparticles, *Journal of Physical Chemistry B*, 2001, 105, pp. 12689-12703.
14. Grassian V. H., When Size Really Matters: Size-Dependent Properties and Surface Chemistry of Metal and Metal Oxide Nanoparticles in Gas and Liquid Phase Environments, *Journal of Physical Chemistry C*, 2008, 112, pp. 18303-18313.
15. Zhang H., Banfield., J. F., Thermodynamic analysis of phase stability of nanocrystalline titania, *Journal of Physical Chemistry C*, 1998, 8(9), pp. 2073-2076.
16. Navrotsky A., Mazeina L., Majzlan, J., Size-Driven Structural and Thermodynamic Complexity in Iron Oxides, *Science*, 2008, 319, pp. 1635-1638.
17. Finnigan M. P., Zhang H., Banfield J. F., Phase Stability and Transformation in Titania Nanoparticles in Aqueous Solutions Dominated by Surface Energy, *Journal of Physical Chemistry C*, 2007, 111, pp. 1962-1968.
18. Hoffmann M., Hotze E., Wiesner M. R., *Environmental Nanotechnology: Applications and Impacts of Nanomaterials*, Wiesner M. R., Bottero J.Y., Eds. MacGraw-Hill, New York, 2007, pp. 155.
19. Roduner E., Size matters: why nanomaterials are different, *Chemical Society Reviews*, 2006, 35, pp. 583-592.
20. Kelly K. L., Coronado E., Zhao L. L., Schatz G. C., The Optical Properties of Metal Nanoparticles: The Influence of Size, Shape, and Dielectric Environment, *Journal of Physical Chemistry B*, 2003, 107, pp. 668-677.
21. Njoki P. N., Lim I. S., Mott D., Park H., Khan B., Mishra S., Sujakumar R., Luo J., Zhong C., Size Correlation of Optical and Spectroscopic Properties

- for Gold Nanoparticles, *Journal of Physical Chemistry C*, 2007, 111, pp. 14664-14669.
22. Dunin-Borkowski, R. E., McCartney, M. R., Pośfai, M., Frankel, R. B., Bazylini, D. A., Buseck, P. R., Off-axis electron holography of magnetotactic bacteria: magnetic microstructure of strains MV-1 and MS-1, *European Journal of Minerals*, 2001, 13, 6, pp.71–684.
 23. Huang, Y., Duan, X., Lieber, C. M., Directed Assembly of One-Dimensional Nanostructures into Functional Networks, *Science*, 2001, 291, pp. 630-633.
 24. Mallouk, T. E., Kovtyukhova, N. I., Nanowires as Building Blocks for Self-Assembling Logic and Memory Circuits, *Chemistry – A European Journal*, 2002, 8, pp. 4354-4363.
 25. Law, M., Sibuly, D. J., Johnson, J. C., Goldberger, J., Saykally, R. J., Yang, P., Nanoribbon Waveguides for Subwavelength Photonics Integration, *Science*, 2004, 305, pp. 1269-1273.
 26. Maier, S. A., Brongersma, M. L., Kik, P. G., Meltzer, S., Requichia, A.A. G., Atwater, H., Plasmonics - A Route to Nanoscale Optical Devices, *Advanced Materials*, 2001, 13, pp. 1501-1505.
 27. Maier, S. A., Kik, P. G., Atwater, H. A., Meltzer, S., Harel, E., Koel, B. E., Requichia, A. A, Local detection of electromagnetic energy transport below the diffraction limit in metal nanoparticle plasmon waveguides, *Nature materials*, 2003, 2, pp. 229-232.
 28. Fan, H., Lu, Y., Stump, A., Reed, S. T., Baer, T., Schunk, R., Perez-Luna, V., Lopez, G. P., Brinker, C. J., Rapid prototyping of patterned functional nanostructures, *Nature*, 2000, 405, pp. 56-60.
 29. Gao, H. J., Ji, B. H., Jager, I. L., Arzt, E., Fratzl, P., Materials become insensitive to flaws at nanoscale: Lessons from nature, *Proceedings of the National Academy of Sciences of the United States of America*, 2003, 100, pp. 5597-5600.
 30. Ji, B. H., Gao, H. J., Mechanical properties of nanostructure of biological materials, *Journal of the Mechanics and Physics of Solids*, 2004, 52, pp. 1963-1990.

31. Katz, E., Willner, I., Integrated Nanoparticle-Biomolecule Hybrid Systems: Synthesis, Properties, and Applications, *Angewandte Chemie International Edition*, 2004, 43, pp. 6042-6108.
32. Schultz, D. A., Plasmon resonant particles for biological detection, *Current Opinion in Biotechnology*, 2003, 14, pp. 13-22.
33. Salem, A. K., Searson, P. C., Leong, K. W., Multifunctional nanorods for gene delivery, *Nature materials*, 2003, 2, pp. 668-671.
34. Tkachenko, A. G., Xie, H., Coleman, D., Glomm, W., Ryan, J., Anderson, M. F., Franzen, S., Feldheim, D. L., Multifunctional Gold Nanoparticle–Peptide Complexes for Nuclear Targeting, *Journal of the American Chemical Society*, 2003, 125, pp. 4700-4701.
35. Xia, Y., Yang, P., Sun, Y., Wu, Y., Mayers, B., Gates, B., Yin, Y., Kim, F., Yan, H., One-Dimensional Nanostructures: Synthesis, Characterisation, and Applications, *Advanced Materials*, 2003, 15, pp. 353-389.
36. Liu, X. Q., Tao, S. W., Shen, Y. S., Preparation and characterization of nanocrystalline α -Fe₂O₃ by a sol-gel process, *Sensors & Actuators B*, 1997, 40, pp. 161-165.
37. Rostamnejadi, A., Salamati, H., Kameli, P., Ahmadvand, H., Superparamagnetic behavior of La_{0.67}Sr_{0.33}MnO₃ nanoparticles prepared via sol-gel method, *Journal of Magnetism and Magnetic Materials*, 2009, 321, pp. 3126-3131.
38. Pradeep, A., Priyadharsini, P., Chandrasekaran, G., Sol-gel route of synthesis of nanoparticles of MgFe₂O₄ and XRD, FTIR and VSM study, *Journal of Magnetism and Magnetic Materials*, 2008, 320, pp. 2774-2779.
39. Yener, D. O., Giesche, H., Synthesis of pure and Manganese-, Nickel-, and Zinc-Doped Ferrite Particles in Water-in-Oil Microemulsions, *Journal of American Ceramic Society*, 2001, 84(9), pp. 1987-1995.
40. Makovec, D., Kosak, A., Znidarsic, A., Drogenik, M., The synthesis of spinel-ferrite nanoparticles using precipitation in microemulsions for ferrofluid applications, *Journal of Magnetism and Magnetic Materials*, 2005, 289, pp. 32-35.
41. Kosak, A., Makovec, D., Drogenik, M., Znidarsic, A., In situ synthesis of magnetic MnZn-ferrite nanoparticles using reverse microemulsions, *Journal of Magnetism and Magnetic Materials*, 2004, 272-276, pp. 1542-1544.

42. Pillai, V., Shah, D. O., Synthesis of high-coercivity cobalt ferrite particles using water-in-oil microemulsions, *Journal of Magnetism and Magnetic Materials*, 1996, 163, pp. 243-248.
43. Zysler, R. D., Vasquez-Mansilla, M., Arciprete, C., Dimitrijewits, M., Rodriguez-Sierra, D., Saragovi, C., Structure and magnetic properties of thermally treated nanohematite, *Journal of Magnetism and Magnetic Materials*, 2001, 224, pp. 39-48.
44. Maaz, K., Karim, S., Mumtaz, A., Hasanain, S. K., Liu, J., Duan, J. L., Synthesis and magnetic characterization of nickel ferrite nanoparticles prepared by co-precipitation route, *Journal of Magnetism and Magnetic Materials*, 2009, 321, pp. 1838-1842.
45. Arulmurugan, R., Jeyadevan, B., Vaidyanathan, G., Sendhilnathan, S., Effect of zinc substitution on Co-Zn and Mn-Zn ferrite nanoparticles prepared by co-precipitation, *Journal of Magnetism and Magnetic Materials*, 2005, 288, pp. 470-477.
46. Vazquez- Vazquez, C., Lopez-Quintela, M. A., Solvothermal synthesis and characterisation of $\text{La}_{1-x}\text{A}_x\text{MnO}_3$ nanoparticles, *Journal of Solid State Chemistry*, 2006, 179, pp. 3229-3237.
47. Rosemary, M. J., Pradeep, T., Solvothermal synthesis of silver nanoparticles from thiolates, *Journal of Colloid and Interface Science*, 2003, 268, 81-84.
48. Chen, M., Xie, Y., Yao, Z., Liu, X. M., Qian, Y., Highly-oriented recrystallization of PbS nanoparticles in a solvothermal process, 2002, 74, pp. 109-111.
49. Yanez-Vilar, S., Sanchez-Andujar, M., Gomez-Aguirre, C., Mira, J., Senaris-Rodriguez, M. A., Castro-Garcia, S, A simple solvothermal synthesis of $M\text{Fe}_2\text{O}_4$ ($M = \text{Mn}, \text{Co}$ and Ni) nanoparticles, *Journal of Solid State Chemistry*, 2009, 182, pp. 2685-2690.
50. Wang, F., Fan, X., Pi, D., Wang, M., Hydrothermal synthesis of Nd^{3+} -doped orthoborate nanoparticles that emit in the near-infrared, *Journal of Solid State Chemistry*, 2004, 177, pp. 3346-3350.
51. Wang, Y., Xu, G., Ren, Z., Wei, X., Weng, W., Du, Piyi., Shen, G., Han, G., Low temperature polymer assisted hydrothermal synthesis of bismuth ferrite nanoparticles, 2008, 34, pp. 1569-1571.

52. Jing, Z., Wu, S., Synthesis and characterisation of monodisperse hematite nanoparticles modified by surfactants via hydrothermal approach, *Material Letters*, 2004, 58, pp. 3637-3640.
53. Hayashi, H., Noguchi, T., Islam, N. M., Hakuta., Hydrothermal synthesis of BaTiO₃ nanoparticles using a supercritical continuous flow reaction system, *Journal of Crystal Growth*, 2010, 312, pp. 1968-1972.
54. Li, Q., Wei, Y., Study on preparing monodispersed hematite nanoparticles by microwave-induced hydrolysis of ferric salts solution, *Material Research Bulletin*, 1998, 33(5), pp. 779-782.
55. Duong, G. V., Turtelli, R. S., Hanh, N., Linh, D. V., Reissner, M., Michor, H., Fidler, J., Wiesinger, G., Grossinger, R., Magnetic properties of nanocrystalline Co_{1-x}Zn_xFe₂O₄ prepared by forced hydrolysis method, *Journal of Magnetism and Magnetic Materials*, 2006, 307, pp. 313-317.
56. Mondal, A., Ram, S., Controlled phase transformations in Al³⁺ stabilized ZrO₂ nanoparticles via forced hydrolysis of metal cations in water, *Materials Letters*, 2003, 57, pp. 1696-1706.
57. Hirano, M., Miwa, T., Inagaki, M, Low-Temperature Direct Synthesis of Nanoparticles of Fluorite-Type Ceria-Zirconia Solid Solutions by ‘‘Forced Cohydrolysis’’ at 100°C, *Journal of Solid State Chemistry*, 2001, 158, pp. 112-117.
58. Kim, E. H., Lee, H. S., Kwak, B. K., Kim, B., Synthesis of ferrofluid with magnetic nanoparticles by sonochemical method for MRI contrast agent, *Journal of Magnetism and Magnetic Materials*, 2005, 289, pp. 328-330.
59. Boutonnet, M., Kizling, J., Stenius, P., Maire, G., The preparation of monodisperse colloidal metal particles from microemulsions, *Colloids and Surfaces*, 1982, 5, pp.209-255.
60. Leung, R., Hou, M. J., Manohar, C., Shah, D. O., Chun, P. W., *Macro- and Microemulsions*, ed. D.O. Shah (American Chemical Society, Washington, DC, 1985) p. 325.
61. Byrappa, K., Adschiri, T., Hydrothermal technology for nanotechnology, *Progress in Crystal Growth and Characterization of Materials*, 2007, 53, pp. 117-166.
62. Tian, Y., Zhao, J., Fu, W., Liu, Y., A facile route to synthesis of MoS₂ nanorods, *Materials Letters*, 2005, 59, pp. 3452-3455.

63. See, C. H., Harris, A. T., A Review of Carbon Nanotube Synthesis via Fluidized-Bed Chemical Vapor Deposition, *Industrial & Engineering Chemistry Research*, 2007, 46, pp. 997-1012.
64. Fan, W., Zhao, W., You, L., Song, X., Zhang, W., Yu, H., Sun, S., A simple method to synthesize single-crystalline lanthanide orthovanadate nanorods, *Journal of Solid State Chemistry*, 2004, 177, pp. 4399-4403.
65. Zhi, C., Bando, Y., Tan, C., Goldberg, D., Effective precursor for high yield synthesis of pure BN nanotubes, *Solid State Communications*, 2005, 135, pp. 67-70.
66. Yan, T., Zhang, D., Shi, L., Li, H., Facile synthesis, characterization, formation mechanism and photoluminescence property of Eu_2O_3 nanorods, *Journal of Alloys and Compounds*, 2009, 487, 483-488.
67. Thangadurai, P., Balaji, S., Manoharan, P. T., Growth and mechanism of CdS nanorods by microstructure analysis, *Materials Chemistry and Physics*, 2009, 114, pp. 420-424.
68. Liou, S-C., Hsiao, C-S., Chen, S-Y., Growth behavior and microstructure evolution of ZnO nanorods grown on Si in aqueous solution, *Journal of Crystal Growth*, 2005, 274, pp. 438-446.
69. Cao, G., Growth of Oxide Nanorod Arrays through Sol Electrophoretic Deposition, *Journal of Physical Chemistry B*, 2004, 108, pp. 19921-19931.
70. Schmidt, V., Wittemann, J. V., Gosele, U., Growth, Thermodynamics, and Electrical Properties of Silicon Nanowires, *Chemical Reviews*, 2010, 110, pp. 361-388.
71. Hou, Y., Kondoh, H., Che, R., Takeguchi, Ohta, T., Ferromagnetic FePt Nanowires: Solvothermal Reduction Synthesis and Characterization, *Small*, 2006, 2, pp. 235-238.
72. Zhao, Y. M., Zhu, Y. Q., Room temperature ammonia sensing properties of $\text{W}_{18}\text{O}_{49}$ nanowires, *Sensors and Actuators B: Chemical*, 2009, 137, pp. 27-31.
73. Wang, W., Xu, C., Zhen, L., Shao, W., Single-crystalline PbCrO_4 nanorods: Room temperature, surfactant free synthesis, characterization and optical property, *Journal of Crystal Growth*, 2007, 299, pp. 86-93.

74. Zhou, S. M., Feng, Y. S., Zhang, L. D., Sonochemical synthesis of large-scale single crystal CdS nanorods, *Materials Letters*, 2003, 57, pp. 2936-2939.
75. Kim, H. W., Lee, J. W., Shim, S. H., Study of Bi₂O₃ nanorods grown using the MOCVD technique, *Sensors and Actuators B*, 2007, 126, pp. 306-310.
76. Zheng, C., Chu, Y., Zhan, Y., Wang, G., Synthesis and characterization of SnO₂ nanorods, *Materials Letters*, 2005, 59, pp. 2018-2020.
77. Woodruff, J. H., Ratchford, J. B., Goldthorpe, I. A., McIntyre, P. C., Chidsey, C. E. D., Vertically Oriented Germanium Nanowires Grown from Gold Colloids on Silicon Substrates and Subsequent Gold Removal, *Nano Letters*, 2007, 7, pp. 1637-1642.
78. Chen, X., Zhu, T-J., Zhao, X-B., Synthesis and growth mechanism of rough PbTe polycrystalline thermoelectric nanorods, *Journal of Crystal Growth*, 2009, 311, pp. 3179-3183.
79. Wu, Y., Xue, C., Zhuang, H., Tian, D., Liu, Y., He, J., Sun, Lili., Wang, F., Ai, Y., Cao, Y., Synthesis of GaN nanorods through ammoniating Ga₂O₃/BN thin films deposited by RF magnetron sputtering, *Journal of crystal Growth*, 2006, 292, pp. 294-297.
80. Alexe, M., Hesse, D., Schmidt, V., Senz, S., Fan, H. J., Zacharias, M., Gosele, U., Ferroelectric nanotubes fabricated using nanowires as positive templates, *Applied Physics Letters*, 2006, 89, pp. 172907.
81. Niederberger, M., Muhr, H-J., Krumeich, F., Beri, F., Gunther, D., Nesper, R., Low-Cost Synthesis of Vanadium Oxide Nanotubes via Two Novel Non-Alkoxide Routes, *Chemistry of Materials*, 2000, 12, pp. 1995-2000.
82. Atkins. P.W, *Physical Chemistry*, Sixth Edition, Oxford University Press (2000).
83. Sun, R. Y., Sun, Q., Effect of nonvolatile solute on vapor-liquid equilibrium at fixed liquid composition, *Fluid Phase Equilibria*, 2002, 193, 135-145.
84. [http://en.wikipedia.org/wiki/Critical_point_\(thermodynamics\)](http://en.wikipedia.org/wiki/Critical_point_(thermodynamics)).
85. http://en.wikipedia.org/wiki/File:Freezing_point_depression_and_boiling_point_elevation.png.
86. Yoshimura, M., Suchanek, W., Byrappa, K., Soft Processing for Advanced Inorganic Materials, *Material Research Society Bulletin*, 25, 2000, pp. 17-24.

87. Byrappa, K., in: KirkeOthmer Encyclopedia of Chemical Technology, John Wiley and Sons, London, 2005.
88. Adschiri, T., Kanazawa, K., Arai, K., Rapid and Continuous Crystallisation of Metal Oxide Particles in Supercritical Water, *Journal of the American Ceramic Society*, 1992, 75, pp. 1019.
89. Cote, L., Teja, A. S., Wilkinson, A. P., Zhang, Z., Continuous hydrothermal synthesis and crystallization of magnetic oxides, *Journal of Material Research Society*, 2002, 17, pp. 2410-2416.
90. Cote, L., Teja, A. S., Wilkinson, A. P., Zhang, Z., Continuous hydrothermal synthesis of CoFe_2O_4 nanoparticles, *Fluid Phase Equilibria*, 2003, 210, pp. 307-317.
91. Cabanas, A., Darr, J. A., Lester, E., Poliakoff, M., A continuous and clean one-step synthesis of nano-particulate $\text{Ce}_{1-x}\text{Zr}_x\text{O}_2$ solid solutions in near-critical water, *Chemical Communications*, 2000, pp. 901-902.
92. Lester, E., Azzopardi, B. J., International Patent Application, 2005, WO 2005/077505.
93. Lester, E., Blood, P., Denyer, J., Giddings, D., Azzopardi, B., Poliakoff, M., Reaction Engineering: The supercritical water hydrothermal synthesis of nano-particles, *Journal of Supercritical Fluids*, 2006, 37, pp. 209-214.
94. Cornell, R. M., Schwertmann, U., *The Iron Oxides, Structure, Properties, Reactions, Occurrence and Uses*, Wiley-VCH, Weinheim, Germany, 2003 pp. 664.
95. Wells, A. F., *Structural Inorganic Chemistry*, 5th edition, Oxford University Press, Oxford, UK, 1991, pp. 1382.
96. Jolivet, J. -P, Tronc, E., Chaneac, C., Iron oxides: From molecular clusters to solid. A nice example of chemical versatility, *C. R. Geoscience*, 2006, 338, pp. 488-497.
97. Jolivet, J. -P, *Metal Oxide Chemistry and Synthesis. From Solution to Solid State*, Wiley, Chichester, 2000, pp. 321.
98. Matijevic, E., *Colloid science of ceramic powders*, *Pure and Applied Chemistry*, 1988, 60, pp. 1479-1491.
99. Music, S., Krehula, S., Popovic, S., Effect of HCl additions on forced hydrolysis of FeCl_3 solutions, *Materials Letters*, 2004, 58, pp. 2640-2645.

100. Riveros, P. A., Dutrizac, J. E., The precipitation of hematite from ferric chloride media, *Hydrometallurgy*, 1997, 46, 85-104.
101. Mackay, A. L., β -ferric oxyhydroxide-akaganeite, *Mineralogical Magazine*, 1962, 33, pp. 270-280.
102. Gallagher, K. J., The Atomic Structure of Tubular Subcrystals of β -Iron(III) Oxide Hydroxide, *Nature*, 1970, 226, pp. 1225.
103. Matijevic, E., Scheiner, P., Ferric hydrous oxide sols: III. Preparation of uniform particles by hydrolysis of Fe(III)-chloride, -nitrate, and -perchlorate solutions, *Journal of Colloid and Interface Science*, 1978, 63, pp. 509-522.
104. Barrios, E., Hernan, L., Morales, J., Tirado, J. L., Effect of grinding in synthetic akaganeite, *Journal of Colloid and Interface Science*, 1986, 113, pp. 212-217.
105. Watson, J. H. L., Cardell, R. R., The internal structure of colloidal crystals of β -FeOOH and remarks on their assemblies in schiller layers, *The Journal of Physical Chemistry*, 1962, 66, pp. 1757-1763.
106. Mazeina. L., Deore, S., Navrotsky, A., Energetics of Bulk and Nano-Akaganeite, $\hat{\alpha}$ -FeOOH: Enthalpy of Formation, Surface Enthalpy, and Enthalpy of Water Adsorption, *Chemistry of Materials*, 2006, 18, pp. 1830-1838.
107. Weiser. H. B., Milligan. W. O., X-ray Studies on the Hydrous Oxides. V. Beta Ferric Oxide Monohydrate, *Journal of the American Chemical Society*, 1935, 57, pp. 238.
108. Mackay, A. L., Mossbauer and X-ray data on β -FeOOH (akaganeite) *Mineralogical Magazine*. 1960, 32, pp. 545-557.
109. Stahl, K., Nielsen, K., Jiang, J., Lebech, B., Hanson, J. C., Norby, P., van Lanschot, J., On the akaganeite crystal structure, phase transformations and possible role in post-excavational corrosion of iron artifacts, *Corrosion Science*, 2003, 45, pp. 2563-2575.
110. Morrish, A. H., *Canted Antiferromagnetism: Hematite*, World Scientific, London, UK, 1994.
111. Pauling, L., Hendricks, S. B., The crystal structures of hematite and corundum, *Journal of the American Chemical Society*, 1925, 47, pp. 781-790.

112. Cudennec, Y., Lecerf, A., Topotactic transformations of goethite and lepidocrocite into hematite and maghemite, *Solid State Sciences*, 2005, 7, pp. 520-529.
113. Cornell, R. M., Schwertman, U., *The Iron Oxides*, 2nd edition, 2003, Wiley-VCH Verlag GmbH & Co. KGaA, Weinheim.
114. Pulgarin, C., Kiwi, J., Iron Oxide-Mediated Degradation, Photodegradation, and Biodegradation of Aminophenols, *Langmuir*, 1995, 11, pp. 519-526.
115. Pelino, M., Colella, C., Cantallini, C., Faccio, M., Ferri, G., D'Amico, A., Microstructure and electrical properties of an α -hematite ceramic humidity sensor, *Sensors and Actuators B: Chemical*, 1992, 7, pp. 464-469.
116. Wu, C., Yin, P., Zhu, X., OuYang, C., Xie, Y., Synthesis of Hematite (α -Fe₂O₃) Nanorods: Diameter-Size and Shape Effects on Their Applications in Magnetism, Lithium Ion Battery, and Gas Sensors, *Journal of Physical Chemistry B*, 2006, 110, pp. 17806-17812.
117. Widder, K. J., Senyei, A. E., Scarpelli, D. G., Magnetic microspheres: a model system for site specific drug delivery in vivo, *Proceedings of the Society for Experimental Biology and Medicine*, 1978, 58, pp. 141-146.
118. Garcon, G., Garry, S., Gosset, P., Zerimech, F., Martin, A., Hannotiaux, M., Shirali, P., Benzo(a)pyrene-coated onto Fe₂O₃ particles-induced lung tissue injury: role of free radicals, *Cancer Letters*, 2007, 167, pp. 7-15.
119. Lawaczeck, R., Menzel, M., Pietsch, H. V., Superparamagnetic iron oxide particles: contrast media for magnetic resonance imaging, *Applied Organometallic Chemistry*, 2004, 18, pp. 506-513.
120. Busch, M., Gruyters, M., Winter, H., Spin polarization and structure of thin iron oxide layers prepared by oxidation of Fe(1 1 0), *Surface Science*, 2006, 600, pp. 4166-4169.
121. Walter, D., Characterization of synthetic hydrous hematite pigments *Thermochimica Acta*, 2006, 445, pp. 195-199.
122. Scamehorn, J., An overview of Phenomena Involving Surfactant Mixtures, In *Phenomena in Mixed Surfactant Systems*, ACS Symposium Series, American Chemical Society, 1986, Washington, DC.
123. Rosen, M. J., *Surfactants and Interfacial Phenomena*, 2nd edition, Wiley-Interscience, New York, NY, 1989, pp. 69.

124. Rosen, M. J., Surfactants in emerging technologies, Surfactant Series, Marcel Dekker, Inc., New York, NY, 1987, Vol, 26.
125. Myers, D., Surfactant Science and Technology, VCH, New York, NY, 1988.
126. Adamson, A. W., Physical Chemistry of Surfaces, 5th edition, Wiley-Interscience, New York, NY, 1990.
127. Karsa, D. R., Industrial Applications of Surfactants III, Royal Society of Chemistry, London, 1990.
128. Murphy, C. J., Sau, T. K., Gole, A. M., Orendorff, C. J., Gao, J., Gou, L., Hunyadi, S., Li, T., Anisotropic Metal Nanoparticles: Synthesis, Assembly, and Optical Applications, *Journal of Physical Chemistry B*, 2005, 109, pp. 13857-13870.
129. Jia, B., Gao, L., Growth of Well-Defined Cubic Hematite Single Crystals: Oriented Aggregation and Ostwald Ripening, *Crystal Growth and Design*, 2008, 8, pp. 1372-1376.
130. Wang, S-B., Min, Y-L., Yu, S-H., Synthesis and Magnetic Properties of Uniform Hematite Nanocubes, *Journal of Physical Chemistry C Letters*, 2007, 111, pp. 3551-3554.
131. Suber, L., Santiago, A. G., Fiorani, D., Imperatori, P., Testa, A. M., Angiolini, M., Montone, A., Dormann, J. L., Structural and Magnetic Properties of α -Fe₂O₃ Nanoparticles, *Applied Organometallic Chemistry*, 1998, 12, pp. 347–351.
132. Liu, L., Kou, H-Z., Mo, W., Liu, H., Wang, Y., Surfactant-Assisted Synthesis of α -Fe₂O₃ Nanotubes and Nanorods with Shape-Dependent Magnetic Properties, *Journal of Physical Chemistry C*, 2006, 110, pp. 15218-15223.
133. Fan, H. M., You, G. J., Li, Y., Zheng, Z., Tan, H. R., Shen, Z. X., Tang, S. H., Feng, Y. P., Shape-Controlled Synthesis of Single-Crystalline α -Fe₂O₃ Hollow Nanocrystals and Their Tunable Optical Properties, *Journal of Physical Chemistry C*, 2009, 113, 9928–9935.
134. Zhong, S-L., Song, J-M., Zhang, S., Yao, H., Xu, A-W., Yao, W-T., Y, S-H., Template-Free Hydrothermal Synthesis and Formation Mechanism of Hematite Microrings, *Journal of Physical Chemistry C*, 2008, 112, pp. 19916-19921.

135. Cao, S-W, Zhu, Y-J, Surfactant-Free Preparation and Drug Release Property of Magnetic Hollow Core/Shell Hierarchical Nanostructures, *Journal of Physical Chemistry C*, 2008, 112, 12149-12156.
136. Yu, J., Yu, X., Huang, B., Zhang, X., Dai., Hydrothermal Synthesis and Visible-Light Photocatalytic Activity of Novel Cage-Like Ferric Oxide Hollow Spheres, *Crystal Growth and Design*, 2009, 9, pp. 1474-1480.
137. He, K., Xu, C-Y., Zhen, L., Shao, W-Z, Fractal growth of single-crystal α - Fe_2O_3 : From dendritic micro-pines to hexagonal micro-snowflakes, *Materials Letters*, 2008, 62, pp. 739-472.
138. Cao, M., Liu, T., Cao, S., Sun, G., Wu, X., Hu, C., Wang, Z. L., Single-Crystal Dendritic Micro-Pines of Magnetic α - Fe_2O_3 : Large-Scale Synthesis, Formation Mechanism, and Properties, *Angewandte Chemie*, 2005, 44, pp. 4197-4201.
139. Sugimoto, T, Sakata, K., Preparation of Monodisperse Pseudocubic α - Fe_2O_3 Particles from Condensed Ferric Hydroxide Gel, *Journal of Colloid and Interface Science*, 1992, 152, 587-590.
140. Sugimoto, T., Muramatsu, A., Sakata, K., Shindo, D, Characterization of Hematite Particles of Different Shapes, *Journal of Colloid and Interface Science*, 1993, 158, pp. 420-428.
141. Sugimoto, T., Khan, M. M., Muramatsu, A., Preparation of monodisperse peanut-type α - Fe_2O_3 particles from condensed ferric hydroxide gel, *Colloids and Surfaces A: Physicochemical and Engineering Aspects*, 1993, 70, pp. 167-169.
142. Sugimoto, T., Khan, M. M., Muramatsu, A., Itoh, H., Formation mechanism of monodisperse peanut-type α - Fe_2O_3 particles from condensed ferric hydroxide gel, *Colloids and Surfaces A: Physicochemical and Engineering Aspects*, 1993, 79, pp. 233-247.
143. Sugimoto, T, Wang, Y., Mechanism of the Shape and Structure Control of Mondispersed α - Fe_2O_3 Particles by Sulphate Ions, *Journal of Colloid and Interface Science*, 1998, 207, pp. 137-149.
144. Sugimoto, T., Itoh, H., Mochida, T., Shape Control of Monodisperse Hematite Particles by Organic Additives in the Gel-Sol System, *Journal of Colloid and Interface Science*, 1998, 205, pp 42-52.

145. Shindo, D., Park, G-S., Waseda, Y., Sugimoto, T., Internal Structure Analysis of Monodispersed Peanut-Type Hematite Particles Produced by the Gel-Sol Method, *Journal of Colloid and Interface Science*, 1994, 168, pp. 478-484.
146. Sasaki, N., Murakami, Y., Shindo, D., Sugimoto, T., Computer Simulations for the Growth Process of Peanut-Type Hematite Particles, *Journal of Colloid and Interface Science*, 1999, 213, pp. 121-125.
147. Kratochvil, S., Matijevic, E., Ozaki, M., Precipitation phenomena in $\text{FeCl}_3\text{-NaH}_2\text{PO}_2$ aqueous solutions at 245°C, *Colloid and Polymer Science*, 1984, 262, pp. 804–810.
148. Zhao, Y., Dunnill, C. W., Zhu, Y., Gregory, D. H., Kockenberger, W., Li, Y., Hu, W., Ahmad, I., McCartney, D. G., Low-Temperature Magnetic Properties of Hematite Nanorods, *Chemistry of Materials*, 2007, 19, 916-921.
149. Hu, X., Yu, J. C., Continuous Aspect-Ratio Tuning and Fine Shape Control of Monodisperse $\alpha\text{-Fe}_2\text{O}_3$ Nanocrystals by a Programmed Microwave-Hydrothermal Method, *Advanced Functional Materials*, 2008, 18, pp. 880-887.
150. Zic, M., Ristic, M., Music, S., Microstructural changes in particles detected during the transformation from $\beta\text{-FeOOH}$ to $\alpha\text{-Fe}_2\text{O}_3$ in dense aqueous suspensions, *Journal of Alloys and Compounds*, 2008, 464, pp. 81-88.
151. Zic, M., Ristic, M., Music, S., Effect of phosphate on the morphology and size of $\alpha\text{-Fe}_2\text{O}_3$ particles from dense $\beta\text{-FeOOH}$ suspensions, *Journal of Alloys and Compounds*, 2008, 466, pp. 498-506.
152. Cullity, B. D., Stock, S. R., *Elements of X-ray diffraction*, 3rd edition, Prentice Hall, Prentice-Hall, Inc., New Jersey, USA, 2001.
153. <http://www.microscopy.ethz.ch/bragg.htm>
154. Williams, D. B., Carter, C. B., *Transmission Electron Microscopy: A Textbook for Material Science*, Springer, USA, 1996.
155. Russell, G. J., *Practical reflection electron diffraction*, *Progress in Crystal Growth and Characterization of Materials*, 1982, 5, pp. 291-321.
156. Marlafeka, S., Bock, N., Cheng, T. S., Novikov, S. V., Winsor, A. J., Harrison, I., Foxon, C. T., Brown, P. D., A structural study of phase

- transitions within GaN layers grown by low-temperature molecular beam epitaxy, *Journal of Crystal Growth*, 2001, 230, pp. 415-420.
157. Watts, J. F., *An introduction to surface analysis by electron spectroscopy, Microscopy handbooks*. 1990, Royal Microscopical Society, Oxford University Press, USA, ISBN-10: 0198564252.
158. Banwell, C. N., McCash, E. M., *Fundamentals of molecular spectroscopy*, 1994, McGraw Hill, England, ISBN 0-07-707976-0.
159. Rodriguez, R. D., Demaille, D., Lacaze, E., Jupille, J., Chaneac, C., Jolivet, J., Rhombohedral Shape of Hematite Nanocrystals Synthesized via Thermolysis of an Additive-free Ferric Chloride Solution, *Journal of Physical Chemistry B*, 2007, 111, pp. 16866-16870.
160. Paterson, R., Rahman, H., The Ion Exchange Properties of Crystalline Inorganic Oxide-Hydroxides: Part II. Exclusion of Perchlorate from β -FeOOH by an Ion Sieve Mechanism, *Journal of Colloid and Interface Science*, 1984, 97, pp. 423-427.
161. Chitrakar, R., Tezuka, S., Sonoda, A., Sakane, K., Ooi, K., Hirotsu, T., Phosphate adsorption on synthetic goethite and akaganeite, *Journal of Colloid and Interface Science*, 2006, 298, pp. 602-608.
162. Sugimoto, T., Muramatsu, A., Formation Mechanism of Monodispersed α -Fe₂O₃ Particles in Dilute FeCl₃ Solutions, *Journal of Colloid and Interface Science*, 1996, 184, pp. 626-638.
163. Jeon, B-H., Dempsey, B. A., Burgos, W. D., Royer, R. A., Reactions of ferrous iron with hematite, *Colloids and Surfaces A: Physicochemical and Engineering Aspects*, 2001, 191, pp. 41-55.
164. Jeon, B-H., Dempsey, B. A., Burgos, W. D., Royer, R. A., Roden, E. E., Modeling the sorption kinetic of divalent metal ions to hematite, *Water Research*, 2004, 38, pp. 2499-2504.
165. Edwards, H. K., Evans, E., McCaldin, S., Blood, P., Gregory, D. H., Poliakov, M., Lester, E., Walker, G. S., Brown, P. D., Hydrothermally synthesised Fe₂O₃ nanoparticles as catalyst precursors for the CVD production of graphitic nanofibres, *Journal of Physics: Conference Series*, 2006, 26, pp. 195-198.

166. Hurle, D.T.J, editor. Handbook of crystal growth, 1a Fundamentals: Thermodynamics and Kinetics, Mutaftschiev, B. Chapter 4: Nucleation Theory Elsevier, Amsterdam, The Netherlands, 1993.
167. Murray, J., Kirwan, L., Loan, M., Hodnett, B. K., In-situ synchrotron diffraction study of the hydrothermal transformation of goethite to hematite in sodium aluminate solutions, *Hydrometallurgy*, 2009, 95, pp. 239-246.
168. Almeida, T. P., Fay, M. W., Zhu, Y., Brown, P. D., A valve-assisted snapshot approach to understand the hydrothermal synthesis of α -Fe₂O₃ nanorods, *CrystEngComm*, 2010, 12, pp. 1700–1704.
169. McIntyre, N. S., Zetaruk, D. G., X-ray Photoelectron Spectroscopic Studies of Iron Oxides, *Analytical Chemistry*, 1977, 49, pp. 1521-1529.
170. Amine, K., Yasuda, H., Yamachi, M., β -FeOOH, a new positive electrode material for lithium secondary batteries, *Journal of Power Sources*, 1999, 81-82, pp. 221-223.
171. Yamashita, T., Hayes, P., Analysis of XPS spectra of Fe²⁺ and Fe³⁺ ions in oxide materials, *Applied Surface Science*, 2008, 254, pp. 2441-2449.
172. Franke, R., Chasd, T., Streubel, P., Meisel, A., Auger parameters and relaxation energies of phosphorus in solid compounds, *Journal of Electron Spectroscopy and Related Phenomena*, 1991, 56, pp. 381-388.
173. Moulder, J. F.; Stickle, W. F.; Sobol, P. E.; Bomben, K. D. Handbook of X-ray Photoelectron Spectroscopy; Physical Electronics, Inc. USA, 1995.
174. Nakamoto, K. Infrared and Raman Spectra of Inorganic and Coordination Compounds – Part A: Theory and Applications in Inorganic Chemistry, 6th Edition, John Wiley & Sons, Inc. Hoboken, New Jersey, USA, 2009.
175. Aschauer, U., Jones, F., Richmond, W. R., Bowen, P., Rohlb, A. L., Parkinson, G. M., Hofmanna, H., Growth modification of hematite by phosphonate additives, *Journal of Crystal Growth*, 2008, 310, pp. 688-698.
176. Zhang, J., Huang, F., Lin, Z., Progress of nanocrystalline growth kinetics based on oriented attachment, *Nanoscale* 2009, 2, pp. 18-34.
177. Niederberger, M., Colfen, H., Oriented attachment and mesocrystals: Non-classical crystallization mechanisms based on nanoparticle assembly, *Physical Chemistry Chemical Physics*, 2006, 8, pp. 3271-3287.

178. Moldovan, D., Yamakov, V., Wolf, D., Phillpot, S. R., Scaling Behavior of Grain-Rotation-Induced Grain Growth, *Physical Review Letters*, 2002, 89, 20.
179. Leite, E. R., Giraldi, T. R., Pontes, F. M., Longo, E., Crystal growth in colloidal tin oxide nanocrystals induced by coalescence at room temperature, *Applied Physics Letters*, 2003, 83, pp. 1566-1568.
180. Tejedor-Tejedor, M., Anderson, M. A., Protonation of Phosphate on the Surface of Goethite As Studied by CIR-FTIR and Electrophoretic Mobility, *Langmuir* 1990, 6, pp. 602-611.
181. Persson, P., Nilsson, N., Sjöberg, S., Structure and Bonding of Orthophosphate Ions at the Iron Oxide–Aqueous Interface, *Journal of Colloid and Interface Science*, 1996, 177, pp. 263-275.
182. Kwon, K. D., Kubicki, J. D., Molecular Orbital Theory Study on Surface Complex Structures of Phosphates to Iron Hydroxides: Calculation of Vibrational Frequencies and Adsorption Energies, *Langmuir* 2004, 20, 9249-2954.
183. Arai, Y., Sparks, D. L., ATR–FTIR Spectroscopic Investigation on Phosphate Adsorption Mechanisms at the Ferrihydrite–Water Interface, *Journal of Colloid and Interface Science*, 2001, 241, pp. 317-326.
184. Rose, J., Flank, A., Masion, A., Bottero, J., Elmerich, P., Nucleation and Growth Mechanisms of Fe Oxyhydroxide in the Presence of PO₄ Ions. 2. P K-Edge EXAFS Study, *Langmuir* 1997, 13, pp. 1827-1834.
185. Wilhelmy, R. B.; Patel, R. C.; Matijevici, E., Thermodynamics and Kinetics of Aqueous Ferric Phosphate Complex Formation, *Inorganic Chemistry*, 1985, 24, pp. 3290-3297.
186. Saric, A.; Music, S.; Nomura, K.; Popovic, S., Microstructural properties of Fe–oxide powders obtained by precipitation from FeCl₃ solutions, *Materials Science and Engineering: B*, 1998, 56, pp. 43-52.
187. Elzinga, E. J., Sparks, D. L., Phosphate adsorption onto hematite: An in situ ATR-FTIR investigation of the effects of pH and loading level on the mode of phosphate surface complexation, *Journal of Colloid and Interface Science*, 2007, 308, pp. 53-70.
188. Borgnino, L., Giamcomelli, C. E., Avena, M. J., De Pauli, C. P., Phosphate adsorbed on Fe(III) modified montmorillonite: Surface complexation

- studied by ATR-FTIR spectroscopy, *Colloids and Surfaces A: Physicochemical and Engineering Aspects*, 2010, 353, pp. 238-244.
189. Gong, W., A real time in situ ATR-FTIR spectroscopic study of linear phosphate adsorption on titania surfaces, *International Journal of Mineral Processing*, 2001, 63, pp. 147-165.
190. Ni, Y., Ge, X., Zhang, Z., Liu, H., Zhu, Z., Ye, Q., A simple reduction-oxidation route to prepare Co_3O_4 nanocrystals, *Materials Research Bulletin*, 2001, 36, pp. 2383-2387.
191. Huang, J. H., Kargl-Simard, C., Oliazadeh, M., Alfantazi, A. M., pH-Controlled precipitation of cobalt and molybdenum from industrial waste effluents of a cobalt electrodeposition process, *Hydrometallurgy*, 2004, 75, pp. 77-90.
192. Sahu, K. K., Rath, Chandana, R., Mishra, N. C., Anand, S., Das, R. P., Microstructural and Magnetic Studies on Hydrothermally Prepared Hematite, *Journal of Colloid and Interface Science*, 1997, 185, pp. 402-410.
193. Jung, I-H., Deckerov, S. A., Pelton, A. D., Kim, H-M., Kang, Y-B., Thermodynamic evaluation and modeling of the Fe-Co-O system, *Acta Materialia*, 2004, 52, pp. 507-519.
194. Iida, S., Phase Diagram of Iron-Cobalt-Oxygen System. (I) Experimental Study, *Journal of the Physical Society of Japan*, 1956, 11, pp. 846-854.
195. De Guire, M. R., Prasanna, T. R. S., Kalonji, G., O'Handley, R. C., Phase Equilibria in the Iron Oxide-Cobalt Oxide-Phosphorous Oxide System, *Journal of American Ceramic Society*, 1987, 70, pp. 831-37.
196. De Vicente, J., Delgado, A. V., Plaza, R.C., Duran, J. D. G, Gonzalez-Caballero, F., Stability of Cobalt Ferrite Colloidal Particles. Effect of pH and Applied Magnetic Fields, *Langmuir*, 2000, 16, pp. 7954-7961.
197. Fu, W., Yang, H., Li, M., Li, M., Yang, N., Zou, G., Anatase TiO_2 nanolayer coating on cobalt ferrite NPs for magnetic photocatalyst, *Materials Letters*, 2005, 59, pp. 3530-3534.
198. Hurle, D.T.J, editor. Handbook of crystal growth, 2b Bulk Crystal Growth: Growth Mechanisms and Dynamics, Sarig, S. Chapter 19: Fundamentals of Aqueous Solution Growth, Elsevier, Amsterdam, The Netherlands, 1993.

Appendix

2 Theta information for β -FeOOH (JCPDS card no. 00-034-1266).

Pattern : 00-034-1266		Radiation = 1.540598		Quality : Not indexed		
Fe ₃ O(OH)		2θ	i	h	k	l
Iron Oxide Hydroxide Akaganeite-M, syn		11.842	40	1	1	0
		16.790	30	2	0	0
		23.849	5	2	2	0
		26.725	100	3	1	0
		34.003	25	4	0	0
		35.162	55	2	1	1
		36.146	2	3	3	0
		38.169	9	4	2	0
		39.220	35	3	0	1
		42.956	7	3	2	1
		43.769	7	5	1	0
		46.434	20	4	1	1
		48.863	4	4	4	0
		50.458	1	5	3	0
		52.047	15	6	0	0
		52.883	3	4	3	1
		55.087	1	6	2	0
		55.903	35	5	2	1
		61.099	9	0	0	2
		61.644	5	6	1	1
		62.278	3	7	1	0
		62.483	3	1	1	2
		63.799	1	2	0	2
		64.397	15	5	4	1
Lattice : Body-centered tetragonal S.G. : I4/m (87) a = 10.53500 c = 3.03000 Z = 8		Mol. weight = 88.85 Volume [CD] = 336.29 Dx = 3.510				
Sample preparation : A 0.1M Fe Cl ₃ solution was heated to 60 C for 8 days. The precipitate was separated by centrifuging, washed with H ₂ O and dried at 40 C. Additional pattern : To replace 13-157. Data collection flag : Ambient.						
Murad, E., Clay Miner., volume 14, page 273 (1979)						
Radiation : CoK α Lambda : 1.79020 SS/FOM : F24= 47(0.0196,26)		Filter : Monochromator crystal d-sp : Diffractometer				

Appendix

2 Theta information for α -Fe₂O₃ (JCPDS card no. 00-034-1266).

Pattern : 01-072-0469		Radiation = 1.540598		Quality : Calculated		
Fe ₂ O ₃		2th	I	h	k	l
Iron Oxide Hematite		24.128	312	0	1	2
		33.118	999	1	0	4
		35.612	699	1	1	0
		39.217	20	0	0	6
		40.829	191	1	1	3
		43.480	18	2	0	2
		49.419	343	0	2	4
		54.004	407	1	1	6
		56.127	5	2	1	1
		57.505	81	0	1	8
		62.386	253	2	1	4
		63.964	242	3	0	0
		65.971	2	1	2	5
		69.501	26	2	0	8
		71.821	92	1	0	10
		72.171	20	1	1	9
		75.106	2	2	1	7
		75.409	51	2	2	0
		77.661	18	0	3	6
		78.721	9	2	2	3
		79.437	1	1	3	1
		80.609	35	1	2	8
		82.822	42	0	2	10
		84.317	2	0	0	12
		84.867	59	1	3	4
		88.472	55	2	2	6
Lattice : Rhombohedral S.G. : R-3c (167) a = 5.03800 c = 13.77200 Z = 6		Mol. weight = 159.69 Volume [CD] = 302.72 Dx = 5.256 I/cor = 3.24				
ICSD collection code: 015840 Temperature factor: ATF Sample source or locality: Specimen from Elba, Italy. Data collection flag: Ambient.						
Blake, R.L., Hessevick, R.E., Zoltai, T., Finger, L.W., Am. Mineral., volume 51, page 123 (1966) Calculated from ICSD using POWD-12++ (1997)						
Radiation : CuK α 1 Lambda : 1.54060 SS/FOM : F26=1000(0.0001,29)		Filter : Not specified d-sp : Calculated spacings				

Appendix

2 Theta information for Co₃O₄ (JCPDS card no. 00-043-1003).

Pattern : 00-043-1003		Radiation = 1.540598		Quality : Calculated		
Co ₃ O ₄		2th	i	h	k	l
Cobalt Oxide		19.001	16	1	1	1
		31.272	33	2	2	0
		36.846	100	3	1	1
		38.547	9	2	2	2
		44.810	20	4	0	0
		49.082	1	3	3	1
		55.656	9	4	2	2
		59.355	32	5	1	1
		65.233	38	4	4	0
		68.630	1	5	3	1
		69.743	1	4	4	2
		74.119	3	6	2	0
		77.340	8	5	3	3
		78.405	4	6	2	2
		82.627	2	4	4	4
		85.762	1	5	5	1
		90.966	4	6	4	2
		94.099	11	7	3	1
		99.334	4	8	0	0
		102.516	1	7	3	3
		103.586	1	6	4	4
		107.908	2	8	2	2
		111.212	7	7	5	1
		112.339	2	6	6	2
		116.923	3	8	4	0
		120.486	1	9	1	1
		121.702	1	8	4	2
		126.716	1	6	6	4
		130.739	6	9	3	1
		138.001	10	8	4	4
<p>Lattice : Face-centered cubic</p> <p>S.G. : Fd3m (227)</p> <p>a = 8.08400</p> <p>Z = 8</p>		<p>Mol. weight = 240.80</p> <p>Volume [CD] = 528.30</p> <p>Dx = 6.055</p> <p>V/cor = 4.30</p>				
<p>General comments: Calculation of diffractometer peak intensities done with MICRO-POWD v. 2.2 (D. Smith and K. Smith) using default instrument broadening function (NBS Table), diffracted beam monochromator polarization correction, and atomic scattering factors corrected for anomalous dispersion. Cell parameters from 9-418. Atomic positions from Roth, W., <i>J. Phys. Chem. Solids</i>, 25 1-10 (1964): Co(1) in 8a, Co(2) in 16d, O in 32e with $x=.3881$. Isotropic thermal parameters from same source: Co (1), Co(2), and O, B=.413.</p> <p>Data collection flag: Ambient.</p>						
<p>Grier, D., McCarthy, G., North Dakota State University, Fargo, North Dakota, USA., ICDD Grant-in-Aid (1991)</p>						
<p>Radiation : CuKα1</p> <p>Lambda : 1.54056</p> <p>SS/FOM : F30=317(0.0032,30)</p>		<p>Filter : Monochromator crystal</p> <p>d-sp : Calculated spacings</p>				

Appendix

2 Theta information for CoFe₂O₄ (JCPDS card no. 00-001-1121).

Pattern : 00-001-1121		Radiation = 1.540598		Quality : Deleted			
CoFe ₂ O ₄		2th	i	h	k	l	
Cobalt Iron Oxide		18.127	8	1	1	1	
		30.273	40	2	2	0	
		35.744	100	3	1	1	
		37.281	5	2	2	2	
		43.473	15	4	0	0	
		53.888	8	4	2	2	
		57.168	45	5	1	1	
		62.728	65	4	4	0	
		71.403	3	6	2	0	
		73.997	13	5	3	3	
		79.870	3	4	4	4	
		86.907	5	6	4	2	
		89.934	20	7	3	1	
		94.381	4	8	0	0	
		102.170	2	6	6	0	
		105.145	8	7	5	1	
Lattice : Face-centered cubic S.G. : Fd3m (227) a = 8.39000 Z = 8		Mol. weight = 234.62 Volume [CD] = 590.59 Dx = 5.277 Dm = 5.300					
Deleted and rejected by: Deleted by 22-1086. Color: Black Melting point: 1570 Data collection flag: Ambient.							
New Jersey Zinc Co., Palmerton, PA, USA., Private Communication							
Radiation : MoKa Lambda : 0.70900 SS/FOM : F16= 7(0.1010,23)		Filter : Not specified d-sp : Not given					